

FUNDAMENTAL INSIGHTS INTO ELECTRON TRANSFER REACTIONS OF
CYCLOMETALATED RUTHENIUM DONOR-BRIDGE-ACCEPTOR COMPOUNDS

Eric J. Piechota

A dissertation submitted to the faculty at the University of North Carolina at Chapel Hill
in partial fulfillment of the requirements for the degree of Doctor of Philosophy in the
Department of Chemistry in the College of Arts and Sciences.

Chapel Hill
2019

Approved by:

Gerald J. Meyer

Andrew Moran

Jillian L. Dempsey

Joanna M. Atkin

James F. Cahoon

©2019
Eric J. Piechota
ALL RIGHTS RESERVED

ABSTRACT

Eric J. Piechota: Fundamental insights into electron transfer reactions in cyclometalated ruthenium donor-bridge-acceptor compounds
(Under the direction of Gerald J. Meyer)

Electron transfer reactions underlie the whole of chemistry: from C-H bond formation, to molecular electronics, and in complex proteins found in nature. Accordingly, much of chemistry relies on developing methods to understand and control such reactions to permit the rational design of molecules toward answering contemporary scientific questions. A common approach is the use of model systems which allow theoretical expectations to be tested experimentally. Chapter 1 establishes the framework on which the dissertation is focused through introducing theoretical expectations and predictions for intra- and interfacial electron transfer reactions through a general mathematical and physically intuitive approach. Additionally, the distinction between non-adiabatic and adiabatic reaction mechanisms is made.

This remainder of the Dissertation utilizes model systems of cyclometalated Ru^{II} donor-bridge-acceptor compounds to explore mechanisms and pathways through which electron transfer occurs. The donor-bridge-acceptor compounds are covalently linked through a synthetically modifiable aryl-thiophene bridge to an electron-rich triphenylamine unit. Chapter 2 introduces the steady-state spectroscopic, electrochemical, and spectroelectrochemical characterization of the compounds in fluid solution and anchored onto thin films of TiO₂. Further, Chapter 2 quantifies the donor-acceptor electronic coupling

using UV/Vis/NIR spectroscopy and identifies two pathways through which optical electron transfer can occur, either directly or indirectly.

Chapters 3 and 4 highlight the experimental distinction between adiabatic and non-adiabatic electron transfer using temperature dependent kinetics to determine the rate constant and barriers associated with intramolecular electron transfer. In Chapter 3, the kinetic data indicate that the free energy for the reaction is reduced when the electronic coupling is large. Chapter 4 quantifies the free energies of activation demonstrating that the free energy of activation was independent of reaction (non-)adiabaticity.

Chapters 5 and 6 investigate interfacial electron transfer from either a TiO_2 surface or a core/shell $\text{SnO}_2/\text{TiO}_2$ to a molecular acceptor, either the Ru center or triphenylamine unit. Electron transfer from the interface to the triphenylamine unit was found to be bridge independent and indicates that discrete sets of orbitals constitute an electron transfer pathway discussed in Chapter 5. Chapter 6 compares activation energies for interfacial electron transfer on $\text{SnO}_2/\text{TiO}_2$ toward determination of electron transfer occurs as an activated or tunneling process.

To learning something new every day

ACKNOWLEDGEMENTS

While speaking to Rachel, a fellow lab member, in early January 2019 about our plans for the Spring I said, “It’s going to be hard to thank the many people that have made this...*production*...possible.” That statement is still true. I’ve been very fortunate to have many friends, family, and colleagues that have shaped my scientific mindset and personal interests in ways they likely don’t realize. Indeed, everyone I’ve met has contributed in their own important way. Truly there have been many amazing individuals that have impacted my life before and during my graduate work and, at this milestone, it makes sense to take some time to revisit and reflect on the efforts of so many people that ultimately made this *production* a reality - if only to have an opportunity to thank them.

This reflection is inspired by an acceptance speech by Mr. Fred Rogers after receiving a Lifetime Achievement Award. In it, he asks the audience, “Would you just take, along with me, ten seconds to think of the people who have helped you become who you are...” and after the silence concludes, saying, “Whomever you’ve been thinking about, how pleased they must be to know the difference you feel they’ve made...”. It is my sincere hope that the many people who made this possible know that they have made a difference in my life. So if you would, please join me in a brief journey to acknowledge those who I feel have shaped it.

I’d like to begin with my parents, Mary and Frank, and my brother, Greg, for their help throughout my ‘formative’ years. A key aspect in my success now was their limitless

support throughout college career – and their belief in my choice to study Chemistry. The financial help and willingness to be there when they were needed, for rides or advice, made 2010-2014 a amazing time. Their support facilitated my participation in summer programs without needing to worry about working during school or being afraid to chase opportunities. Much of Greg’s (who happens to be a lifelong Carolina basketball fan who recently attended his first game against Duke in March 2019, Carolina won, 79-70) support stemmed from listening to me attempt to explain nuances of Chemistry, academia, publishing, and electron transfer over the phone or while throwing a football in the backyard during Thanksgiving and Christmas visits. Those conversations helped more than he knows and I hope that I can repay him in a similar way.

Many of my college friends have contributed in ways they likely do not know either. I feel that it is important that I highlight them as well. Their particular contributions have occurred over many years, at different times, and in very different places. So I shall try to be terse. The first group I’d like to highlight are my college ‘roommates’, as they were often the main motivators of my successes, and always happy to support me. The two that stand out are Matthew Libretti and Keighlyn Alber. They instilled in me a feeling of teamwork even though we had different majors, schedules, and interests. I’d like to think we all helped each other equally, but really I was more of a beneficiary of their help than they were of mine. It was their presence during my college career that provided relief and reassurance during many stressful times while at the same time participating in many celebrations, too.

Others that made my college journey possible helped in a different way by constantly reminding me to not take myself too seriously. These two are Jim Gallagher and Michael Chiesa. Still others helped by ensuring my apartment was a mess, that cell phones were a

poor way to communicate when yelling was much faster, and that the lines at the Phyrst and Café 210 were not as long as they seemed: Kara Kohler, Michelle Casella, and Kristen Mathious fit this bill. Together, my diverse group of friends made me realize that it is worth balancing social and studious lifestyles.

I've had many great teachers, professors, and advisors who I am glad to call friends. Collectively, they motivated my professional life and validated my choice to study Chemistry in college. In high school, Mrs. Caroline Gold inspired me, a solid 'B-' high school student, to study chemistry through her passion for it. And even though I wasn't a great student then, she was convinced I could major in chemistry and be successful. At Penn State Hazleton, Dr. Frank Novak was my first advisor who instilled in me an appreciation for Chemistry that I, thinking back, had no business understanding as a freshman. Nevertheless, we would talk almost weekly about electrochemistry and spectroscopy and I distinctly remember reading textbooks light-years above my level of understanding.

Perhaps the most influential faculty member I met during my time at Penn State was Dr. Ben Lear. If you asked him, he would likely deny his usefulness, remembering times instead that would probably not count as constructive. For example, having margaritas at 3 PM on a Wednesday. But, it is now my chance to say that his advising style was, to me, unarguably helpful. He made being an undergraduate researcher fun and educational. Scientifically, he immediately posed challenging questions when I joined his lab, and was always patient during discussions as I tried to tackle concepts. One day that stands out to me is when he offered to sit in the library together to comb through dusty chemical kinetics books to find an explanation for my data – we never did find one but it didn't matter because we had both learned something. Beyond working in the lab, he offered friendship and

mentored me in other important topics like cocktails, movies, and squash (though I could never beat him in a game.) More seriously, it wasn't until after moving to Chapel Hill that I realized that I had, by chance, independently developed an interest in electron transfer chemistry.

Now I'd like to take the time to thank individual members of Jerry's research group over the years (in no particular order): Tim Barr, Brian DiMarco, Evan Beauvilliers, Tyler Motley, Wesley Swords, Matt Brady, Sara Whelin, Erica James, Rachel Bangle, and Michael Turlington, and post-docs Ke Hu, Cassandra Ward, Jenny Schnider, Goucon Li, with a special thanks to Renato Sampaio and Ludovic Troain-Gautier – two inspirational post-docs that I worked closely with. Renato deserves special mentioning as an electron transfer enthusiast, too. We could waste an entire day discussing it. I'd also like to give special thanks to graduate students in my year: Catherine Burton and Andrew Maurer. Certainly Andrew, more than anyone else, has had to deal with sometimes silly ideas, bad math, and angry rants more than most. I'd also like to give a shout-out to Bruno Aramburu, a visiting student from Argentina, who I had the pleasure of working with for a short three months, and who, at the time of this writing, had just defended his own Dissertation.

In a way everyone I've listed contributed either during work or after and the level of friendship in the lab was, and will continue to be, encouraging and often feels like a second family. While I have limited experience in other groups, I feel that the dynamic is unique and powerful. Indeed, over the time I've been in this lab, it has always been close nit, collaborative, and members were always ready for a joke (though not always eager to hear mine). It always impressed me, the way that the members of the group were ready to discuss their results. More impressive are people's willingness to listen to colleagues throw ideas like

darts at a board while they tackle their on complicated research problems. Teamwork is certainly a strength of the group.

Next, I'd like to thank my advisor, Jerry Meyer, for the last four and a half years of advice, insight, and attention. His incredible knowledge of the literature, skillset in clear and concise writing, and genuine interest in each of our research projects is inspiring. Even though I've beat Jerry in squash, where he may have learned a move from me. As a testament to his expertise, I've never walked away from a research discussion without learning something new, either. An impressive feat, in my opinion, is that he managed to deal with me for over four years, let me 'follow my nose' in many different electrons transfer projects, and took interest when I would discuss very niche aspects of electron transfer theory. Maybe I wasn't the graduate student he expected, but working in his lab has impacted my scientific interests and focus on a fundamental level. I owe him a debt of gratitude for the last four years, both to him and the many members of the lab, for advising and help in research and my growth as a scientist.

As I'm rapidly approaching the end of my acknowledgements, I owe the largest thank-you possible to my wonderful, beautiful, and talented girlfriend, Anginelle. She's demonstrated incredible patience through my long working hours, limited exotic vacations, and my inability to dress professionally over the last three years. Yet, she has never failed to pack a lunch for the day or to be there for me during difficult times. She's walked our dog, Otto, after work nearly every day for the last two years – sacrificing her time at work to make sure I could accomplish what I needed to do. Not only that, she would also pick me up from work (even though she was tired) just for me to avoid taking the bus home. Of course, there were one or two days when we both left work early to adventure to Raleigh or take a long

weekend in Asheville, and we always made time to relax and laugh together. In this way, she's contributed not only to my successes in graduate school, but also to my intense interest in cooking, brunch (a cornerstone of our relationship), and to re-watching *The Office*. It is challenging to articulate my appreciation for what she's done for me in just a few sentences, and how she's helped and shaped by graduate student experience and life as a whole. And so, Anginelle: Thank you for everything; for all your help and all you do to make our lives function smoothly. I am a very lucky to have you in my life.

In wrapping up my acknowledgements, I am again reminded of the Fred Rogers quote on which this section is predicated. So many people have contributed to my life, my work in chemistry, and my personality that this short six-page reflection cannot possibly pay enough homage to them. I hope that those who made this *production* possible truly realize the impact they have had on me and my life. Thank you.

TABLE OF CONTENTS

LIST OF FIGURES	xix
LIST OF SCHEMES.....	xxvi
LIST OF TABLES	xxvii
Chapter 1. Intramolecular and interfacial electron transfer theory	1
1.1 Motivation.....	1
1.2 Electron transfer reactions.....	3
1.3 Marcus theory.....	5
1.4 Using potential energy surfaces and Marcus theory to understand electron transfer.....	7
1.4.1 Non-adiabatic potential energy surfaces	7
1.4.2 Gibbs energy of activation.....	9
1.4.3 Reorganization energy.....	10
1.4.4 Electronic coupling.....	13
1.5 Applications of potential energy surfaces in thermal and optical electron transfer.....	18
1.5.1 Interfacial electron transfer.....	18
1.5.2 Intramolecular electron transfer	21

1.5.3 Arrhenius and Eyring models	22
1.6 Genesis of the Marcus equation	23
1.6.1 Nuclear factors.....	23
1.6.2 Electronic and nuclear transmission coefficients	25
1.6.3 Adiabatic electron transfer	29
1.7 Conclusion	31
REFERENCES	32
Chapter 2. Optical intramolecular electron transfer in opposite directions through the same bridge that follows different pathways	39
2.1 Introduction	39
2.2 Results	42
2.3 Discussion	49
2.3.1 Electrochemistry.....	51
2.3.2 Mulliken-Hush H_{DA} calculations	53
2.3.3 Superexchange H_{DA} calculations.....	57
2.4 Conclusions	60
2.5 Experimental methods.....	62
2.5.1 Thin films and sensitization.....	62
2.5.2 Spectroscopic characterization	63
2.5.3 Solution spectroelectrochemistry	63

2.5.4 Surface spectroelectrochemistry	64
2.5.5 Chemical oxidation.....	65
2.6 Acknowledgements	65
2.7 Additional content.....	66
2.7.1 Chemical oxidation.....	66
2.7.2 Accounting for comproportionation	67
2.7.3 Deconvolution of the mixed-valent spectrum	70
2.7.4 Reconstructing the mixed-valent spectrum	71
2.7.5 Result of comproportionation correction and electrochemical modeling	72
2.7.6 Assignment of the TPA to cyclometalating ligand charge transfer transition.....	73
2.7.7 Spectroelectrochemical data of the x-series	75
2.7.8 Synthesis of the Studied Compounds	76
REFERENCES	77
Chapter 3. Kinetics teach that electronic coupling lowers the free energy change that accompanies electron transfer	85
3.1 Introduction	85
3.1.1 The theoretical prediction that electronic coupling, H_{DA} , lowers ΔG°	87
3.1.2 The kinetic approach	88
3.2 Results and discussions	91
3.2.1 The A-B-D compounds	91

3.2.2 Application of the kinetic approach	92
3.2.3 Free energy loss due to electronic coupling	98
3.3 Conclusions	102
3.4 Additional information	102
3.4.1 Experimental details	102
3.4.2 Sample preparation	102
3.4.3 UV-vis absorption	103
3.4.4 Transient absorption	103
3.4.5 Electrochemistry	104
3.4.6 Calculations	104
3.4.7 Calculation of H_{DA} through the generalized Mulliken-Hush model	105
3.4.8 Determination of H_{DA} for 1x and 1p	107
3.4.9 Kinetic model	109
3.4.10 Derivation of the Gibbs free energy surfaces	112
3.4.11 The adiabatic double minimum limit	115
3.4.12 Acknowledgements	117
REFERENCES	119
Chapter 4. Entropic barriers determine adiabatic electron transfer equilibrium	123
4.1 Introduction	123
4.2 Results	125

4.3 Discussion	128
4.3.1 Pre-exponential factors	129
4.3.2 Entropy of activation	133
4.3.3 Enthalpy of activation.....	135
4.3.4 Free energy of activation	136
4.3.5 <i>A priori</i> rate calculations	138
4.3.6 Reorganization energy.....	140
4.3.7 Standard thermodynamics	142
4.3.8 Origin of entropic barriers	143
4.4 Conclusions	146
4.5 Additional content.....	147
4.5.1 Calculation of the reorganization energy	147
4.5.2 Temperature dependence of the reorganization energy and adiabaticity factor	148
4.5.3 Nonadiabatic kinetics	150
4.5.4 Adiabatic kinetics	152
4.5.5 Marcus and Eyring model equivalence	154
4.6 Acknowledgements	158
REFERENCES	159
Chapter 5. A Kinetic pathway for interfacial electron transfer from a semiconductor to a molecule.....	165

5.1 Introduction	165
5.2 Results	168
5.2.1 Spectroscopic and redox properties	168
5.2.2 Bridge-mediated electronic coupling	170
5.2.3 Time-resolved absorption spectroscopy	171
5.2.4 Electron transfer kinetics	173
5.3 Discussion	174
5.4 Conclusions	177
5.5 Additional content and experimental details	178
5.5.1 Sensitized thin films	178
5.5.2 Spectroelectrochemistry	178
5.5.3 Transient absorption spectroscopy	178
5.5.4 Density functional theory calculations	179
5.5.5 H _{DA} Calculations	179
5.6 Acknowledgements	180
REFERENCES	182
Chapter 6. Barriers for interfacial back-electron transfer: a comparison between TiO ₂ and SnO ₂ /TiO ₂ core/shell structures	186
6.1 Introduction	186
6.2 Results	188

6.3 Discussion	194
6.3.1 The kinetic model:	195
6.3.2 Models for back-electron transfer	197
6.4 Conclusion	201
6.5 Additional Details	202
6.5.1 Materials	202
6.5.2 Preparation of SnO ₂ and TiO ₂ colloidal suspensions.	202
6.5.3 Preparation of TiO ₂ and SnO ₂ /TiO ₂ core/shell thin films.	203
6.5.4 UV–Vis absorption.....	204
6.5.5 Transient absorption	204
REFERENCES	205

LIST OF FIGURES

Figure 1.1. Gibbs free energy surfaces of reactants (blue) and products (red) calculated with equations x and y. The nuclear configuration along the abscissa represents the nuclear arrangement (molecule and solvent). The vertical transition from the minimum of the reactant to the product curve is the reorganization energy and the transition state, represented by ΔG^\ddagger , is where the product and reactant energies are equal.....	8
Figure 1.2. Four primary types of electron transfer reactions categorized by relationship between ΔG° and λ , except for self-exchange.	10
Figure 1.3. A molecular view of the reorganization energy corresponding to thermal and optical non-adiabatic electron transfer. (1)-(2): Beginning from the equilibrium configuration of the reactant (blue) absorption of light with $\Delta G^\circ = h\nu = \lambda$ generates the electronic configuration of the product (red) in the nuclear configuration of the reactants (Born-Oppenheimer approximation). (1)-(3): Thermal electron transfer over the transition state $G_{TS} = \Delta G^\ddagger = \lambda/4$ results in formation of the equilibrium electronic and nuclear configuration of the product.	11
Figure 1.4. Effect of electronic coupling on potential energy surfaces as categorized by Robin and Day. Class I electron transfer (top left) corresponds to $H_{DA} = 0$, electrons are valence-localized, with a maximum barrier for electron transfer ΔG^\ddagger (bottom left). In class II, $H_{DA} > 0$, electron density is partially delocalized (top middle), and electron transfer between reactants and products is discrete (and can be adiabatic), while the barrier is reduced $\Delta G_{ad}^\ddagger < \Delta G^\ddagger$ (bottom middle). In class III electron density is delocalized (top right) and electron transfer is not discrete. As a result, there is no barrier for electron transfer, $\Delta G^\ddagger = 0$ (bottom right), as the reactant minimum energy is equal to the energy of the transition state.	17
Figure 1.5. Three schematic representations of interfacial electron transfer. (left) A molecule, D, is immobilized onto a mesoporous substrate of TiO_2 . Following light excitation (1) electron transfer to the surface occurs from a localized molecular excited state to form D^+ (2) on the timescale of microseconds before the electron recombines with D^+ (3). (middle) A D-B-A molecule is immobilized onto a TiO_2 surface and, following excitation of D, injects an electron into the surface (2), after which a quasi-equilibrium between D and A may be established on the nanosecond timescale (4) which allows recombination to occur to either D^+ (3) or A^+ (5). (Right) Immobilization of D-B-A onto a core/shell film of $\text{SnO}_2/\text{TiO}_2$ increases the lifetime of the electron in the surface by virtue of the energy difference of the conduction band energies of SnO_2 and TiO_2 allowing the quasi-equilibrium to be established (4) before recombination via activated electron transfer (6) or tunneling (7) occurs to D^+ or A^+	20

Figure 1.6. Reactant (left) and product (right) potential energy surfaces of Marcus-inverted electron transfer reactions showing vibrational wavefunction sub-levels. Higher energy vibrational energies ($n = 7$ for reactants) and ($n = 16$ for products) show how excited-vibrational states facilitate inverted electron transfer. Adapted from Barbara et. al.⁵³ 24

Figure 1.7. (A and B) Nuclear factors for electron transfer reactions. The electron donor (blue) or acceptor (red) is influenced by inner-sphere-type vibrational Donor-Ligand modes ν_i with frequencies between 10^{12} - 10^{13} s⁻¹. Brown ovals (with tan oval backgrounds) show outer-sphere solvent rotational motion, ν_o , which are slower than vibrational motion with $\nu_o = 10^{10}$ - 10^{12} s⁻¹. (C) Electronic factors following from the Golden Rule where electronic coupling, H_{DA} , is represented by orbital overlap from the reactant and product wavefunctions. The electron transfer rate is limited by $\nu_{el} < \nu_n$ when the orbital overlap is weak whereas strong overlap can cause nuclear motion to be rate limiting, $\nu_n < \nu_{el}$ 27

Figure 1.8. (Top) The electronic transmission coefficient as a function of H_{DA} for the indicated values of nuclear frequencies, ν_n , with $\lambda = 1$ eV. (B) The electronic frequency (red dotted line) or the product of ν_n and κ_{el} as a function of H_{DA} . Red circles indicate the magnitude of electronic coupling necessary to achieve $\kappa_{el} = 1$, *i.e.* adiabatic electron transfer. When the colored lines (brown through green) deviate from ν_{el} (red dotted) electronic coupling becomes sufficiently large for the reaction to become limited by ν_n instead of ν_{el} . Values of ν_n were chosen to correspond to the timescales shown in the lower figure, from slow rotational motion to delocalized electronic motion. Vertical dotted lines corresponding to $H_{DA} = k_bT$ and $\lambda/2$ set boundary conditions establishing that coupling brought about by thermal energy fluctuations does not always result in adiabatic electron transfer and that $\Delta G^\ddagger > 0$ 28

Figure 2.1. Absorption spectra of the ester forms of the compounds in neat CH₃CN (left). Absorption spectra of the carboxylate forms of the compounds in CH₃OH containing tetrabutylammonium hydroxide (right)..... 43

Figure 2.2. Representative spectroelectrochemical data for **1p_E** (upper left), **2p_E** (lower left), **1x_E** (upper right) and **2x_E** (lower right) in CH₃CN containing 0.1M LiClO₄. Insets show single wavelength absorption changes as a function of applied potential, and all applied potentials are reported vs. NHE. 45

Figure 2.3. Spectroelectrochemical oxidation of **1p_C/nITO** (left) and **2p_C/nITO** (right). Insets show difference spectra taken relative to 0 mV of applied potential. Applied potentials are vs. NHE. 46

Figure 2.4. Plots of mole fractions for **1p_C/nITO** (left) and **2p_C/nITO** (right) in the ground, Ru^{II}-B-TPA (black), doubly-oxidized, Ru^{III}-B-TPA⁺ (red), and one-electron oxidized states (blue), as a function of applied electrochemical potential, where B represents the phenyl-thiophene bridge. The dashed lines represent the mole fractions for ideal ($\alpha = 1$) Nernstian behavior..... 47

Figure 2.5. Absorption spectra of 1pc/nITO (top) and 2pc/nITO (bottom) in their ground (black), one-electron oxidized (blue), and two-electron oxidized (red) states. The dashed blue line represents the comproportionation correction in the mixed valent state from spectral modeling which reveals intense IVCT-type transitions at 450 nm for 1pc/nITO and 1100 nm for 2pc/nITO	48
Figure 2.6. Representation of $E_{1/2}(\text{Ru}^{\text{III/II}})$ (red) and $E_{1/2}(\text{TPA}^{+/0})$ (blue) for the 8 compounds in fluid acetonitrile solution and immobilized nITO.....	52
Figure 2.7. Redox potential switch upon surface immobilization for 1pE and 1pc/nITO as well as 1xE and 1xC/nITO . The dashed lines connecting the redox potentials are guides to the eye.	53
Figure 2.8. UV-Vis-NIR absorption spectra of 1pE (left) and 2pE (right) in neat CH_3CN with Cu(II) titrated in as a chemical oxidant. Note the appearance of low energy IVCT transitions at ~1000 nm for both compounds.	56
Figure 2.9. Difference spectra of 1pE (left) and 2pE (right) as a function of added equivalents of Cu(II)	67
Figure 2.10. Plots of mole fractions of each species as a function of added Cu(II) for 1pE (A) and 2pE (C), and as a function of applied potential for 1pc/nITO (B) and 2pc/nITO (D).	68
Figure 2.11. Measured extinction coefficients after accounting for comproportionation for 1pE and 2pE (left) and 2pc/nITO (right).	70
Figure 2.12. Deconvoluted spectra of 1pE (top left), 1pc/nITO (top right), 2pE (bottom left), and 2pc/nITO (bottom right). Dashed red lines indicate the cumulative spectra of all Gaussian bands needed to fit the spectrum adequately.	71
Figure 2.13. Comparison of 1pE (left) and 2pE (right) spectra after being corrected for comproportionation. Note the large difference from similar spectra in the main text for 1pc/nITO and 2pc/nITO	72
Figure 2.14. Spectra of the free ligands in 0.1M $\text{LiClO}_4/\text{CH}_3\text{CN}$. (Left) Ligands containing a methoxy substituent that most closely resemble the 1-series . The green and black lines are ground-state spectra while the red and blue lines are oxidized by one electron. (right) ligands containing a CF_3 substituent that mimic the 2-series . The green and black lines are ground-state spectra while the blue and red are one-electron oxidized.	74
Figure 2.15. Comparison of ground-state spectra of 1pL (green) and one-electron oxidized 1pc/nITO (dashed blue line).	75
Figure 2.16. Spectroelectrochemical data of 1xC/nITO (left) and 2xC/nITO (right) in 0.1M $\text{LiClO}_4/\text{CH}_3\text{CN}$	76

Figure 3.1. The A-B-D compounds utilized. Four cyclometalated ruthenium (blue) compounds with carboxylic acid groups (for binding to TiO₂) and an aromatic bridge covalently bound to a triphenylamine unit (red). Methyl substituents in the R₃ position – xylyl bridge (**x**) – lowers electronic coupling relative to the phenyl-bridge (**p**, R₃ = H). The R₁ and R₂ substituents allow the E°(Ru^{III/II}) potentials to be controlled for the 1 and 2 series while E°(TPA⁺⁰) was held constant. 86

Figure 3.2. Potential energy surfaces and kinetic approach. (a), Gibbs free energy surfaces (GESs) that represent a redox equilibrium between A-B-D (blue) and A⁻-B-D⁺ (red) as the electronic coupling matrix element (H_{DA}) is increased from 0 (nonadiabatic) to over 3000 cm⁻¹ (adiabatic). Emphasis is placed herein on the reduction in the Gibbs free energy change, |ΔG°| > |ΔG°_{ad}|, that accompanies the transition from non-adiabatic to adiabatic electron transfer in the double minimum regime. (b) A ‘reaction coordinate’ diagram with potential energy surfaces of D-B-A reactants and D⁺-B-A⁻ products and semiconductor energetics. The kinetic approach used to quantify the thermal electron transfer reaction consists of a Ru^{II}-B-TPA compound anchored to the surface of mesoporous thin films of TiO₂ (the secondary acceptor). Light absorption induces excited-state electron injection from the Ru^{II} unit into the TiO₂ to form TiO₂(e⁻)-Ru^{III}-B-TPA. Within the time frame of charge recombination, the dynamic equilibrium Ru^{III}-B-TPA ⇌ Ru^{II}-B-TPA⁺ was quantified through a kinetic model that afforded the forward, k₁, and reverse, k₋₁, electron transfer rate constants..... 89

Figure 3.3. Electronic properties and transient absorption data. (Upper) The visible absorption spectra of **2x** (a) and **2p** (b) anchored to In₂O₃:Sn thin films. Highlighted in the shaded orange area are the intervalence transition bands. The insets show the molecular structure with the overlaid highest occupied molecular orbitals (HOMO) generated from DFT calculations. (Middle) Absorption difference spectra measured at the indicated delay times after laser excitation for **2x** (c) and **2p** (d). The insets show normalized single wavelength kinetic data monitored at 700 nm (that reports predominantly on TPA⁺ concentrations) and at 510 nm (due to Ru^{III}). (Bottom) Single wavelength data that reports on the time dependent TPA⁺ concentration as a function of temperature for **2x** (e) and **2p** (f). Overlaid in yellow are fits to the kinetic model used, as described in the Supplementary Information. The insets display Arrhenius plots of the forward, k₁, and reverse, k₋₁, rate constants. All experiments were performed in 0.1 M LiClO₄/acetonitrile solution. 94

Figure 3.4. Single wavelength data that reports on the time dependent TPA⁺ concentration as a function of temperature for **1x** (a) and **1p** (b). The insets display an Arrhenius plot of the forward, k₁ (red), and reverse, k₋₁ (blue), rate constants. Overlaid in yellow are fits to the kinetic model used, as described in this Supplementary Information. 95

Figure 3.5. van’t Hoff analysis and the influence of electronic coupling on Gibbs free energy. a) A van’t Hoff plot, ln K_{eq} vs 1000/T, of the redox equilibrium constants with overlaid best fit lines that demonstrates an adiabatic mechanism for (**1p**, **2p**) and nonadiabatic for (**1x**, **2x**). b) Effect of electronic coupling on the Gibbs

free energy for electron transfer calculated from numerical analysis of the GESs (equation (4)) with the indicated reorganization energies, λ . The solid lines represent the progression of the nonadiabatic ΔG° to the adiabatic value, $\Delta G^\circ_{\text{ad}}$, limited to the double minimum regime. The dotted lines denote fictitious $\Delta G^\circ_{\text{ad}}$ values for a GES collapsed to a single minimum. 98

Figure 3.6. Chemical oxidation of **1p** (left) and **2p** (right), in acetonitrile solutions, using $\text{Cu}(\text{ClO}_4)_2$ as the sacrificial oxidant. 109

Figure 3.7. Gibbs free energy surfaces generated from equation 22 for fixed $\lambda = 0.6$ eV and $\Delta G^\circ = 70$ mV with the indicated H_{DA} values. For $H_{\text{DA}} = 0.1$ eV an adiabatic double minimum GES occurs. At $H_{\text{DA}} = 0.2$ eV, the energy minimum of the donor, $G(\text{D})$, equals that of the transition state, $G(\text{TS})$. When H_{DA} values are greater than 0.2 eV, for instance $H_{\text{DA}} = 0.4$ eV, the acceptor and donor GES collapses to a single minimum. 116

Figure 3.8. a) Energy values abstracted for the acceptor and donor minima and the transition state with fixed $\lambda = 0.6$ eV and $\Delta G^\circ = 68$ mV, with varying H_{DA} . The inset highlights the H_{DA} value at which the acceptor and donor GESs collapses to a single minimum for different values of λ . b) H_{DA} values (in eV and kT) units necessary to collapse the GESs into a single minimum for multiple combinations of ΔG° and λ 117

Figure 4.1 van't Hoff plot of electron transfer equilibrium constants for the studied compounds.¹⁵ Adapted from Ref. 15. Uncertainty in $\ln(K_{\text{eq}})$ is ± 0.05 126

Figure 4.2. Arrhenius (top) and Eyring analysis (bottom) for the forward, $\text{TPA} \rightarrow \text{Ru}^{\text{III}}$, k_{TPA} , (open shapes) and reverse, $\text{Ru}^{\text{II}} \rightarrow \text{TPA}^+$, k_{Ru} (solid shapes) electron transfer rate constants for 1x, 1p (red triangles) and 2x, 2p (blue circles). Errors in the rate constants are $\pm 5\%$ 128

Figure 4.3 Electron transfer rates as a function of electronic coupling for a purely non-adiabatic reaction (Eq. 8, $\kappa_{\text{A}} = 0$, black), a non-adiabatic reaction with the adiabaticity parameter (Eq. 8, $\kappa_{\text{A}} > 0$, red) and a solvent-controlled adiabatic reaction (Eq. 10, dashed blue line). Parameters used in these calculations: $T = 298$ K, $\lambda = 1$ eV, $\tau_{\text{L}} = 0.2$ ps, $\Delta G^\ddagger = 24$ kJ mol⁻¹. 139

Figure 4.4. TD-DFT optimized structure of **2p** used to determine geometric distances for estimation of the reorganization energy. 148

Figure 5.1. The strategy utilized to demonstrate an electron transfer **pathway** from TiO_2 to a molecule. Pulsed laser excitation initiates excited state injection that yields an electron in TiO_2 , $\text{TiO}_2(e^-)$, and an oxidized molecule (not shown). The subsequent reaction of the $\text{TiO}_2(e^-)$ with the oxidized molecule shown is then quantified on nanosecond and longer time scales. The exceptional aspect of these molecules is that they vary only in the geometric torsion about the aromatic bridge (black), Bx = xylyl- or Bp = phenyl- thiophene. Hence a bridge dependence for this reaction

cannot be attributed to distance or driving force and must result from an interfacial electron transfer pathway that utilizes the bridge orbitals. 167

Figure 5.2. The interfacial density of states for **1x/TiO₂**, **1p/TiO₂**, **2x/TiO₂**, **2p/TiO₂** in 0.5 M LiClO₄/CH₃CN. The distributions shaded in blue correspond to Ru^{III/II} redox equilibria and that shaded in red corresponds to TPA⁺⁰. 169

Figure 5.3. The spectroscopic evidence for preferential interfacial electron transfer from TiO₂ to the Ru^{III} center through the xylyl bridge. (A) The transient absorption difference spectra measured at the indicated delay times after pulsed 532 nm excitation (0.2 mJ/cm²) of **2x/TiO₂** in 0.5 M LiClO₄/CH₃CN; and (b) the decay associated spectra (B) that show how the concentrations of Ru^{III} (blue) and of TPA⁺ (red) change with time. 172

Figure 5.4. Comparative kinetic analysis showing that reduction of TPA⁺ and Ru^{III} were the same for the phenyl bridge, $k_{RuIII}/k_{TPA} = 1$, and were significantly influenced by the xylyl bridge, $k_{RuIII}/k_{TPA} > 10$. Single wavelength kinetic data measured after pulsed 532-nm excitation (0.2 mJ/cm²) of A) **2x/TiO₂** and B) **1x/TiO₂** immersed in 0.5 M LiClO₄/CH₃CN solution at wavelengths that correspond mainly to recombination to Ru^{III} (blue), monitored at 510 nm, and TPA⁺ (red) monitored at 750 nm. The insets show recombination data for **2p/TiO₂** and **1p/TiO₂**, of Ru^{III} and TPA⁺ monitored at 550 nm and 740 nm, respectively. 174

Figure 6.1: Structure of the D-B-A sensitizers bearing either a **xylyl** bridge (R = CH₃, CF₃-**x**) or a **phenyl** bridge (R = H, CF₃-**p**) anchored on different metal oxides (TiO₂ or SnO₂/TiO₂ core/shell). The recombination reaction from electrons in the metal oxides to the oxidized Ru^{III} or the oxidized TPA⁺ is highlighted. 188

Figure 6.2: Absorption spectra of CF₃-**p** and CF₃-**x** recorded in methanol at room temperature. 189

Figure 6.3: Transient absorption difference spectra measured over the indicated time range after pulsed 532 nm light excitation of TiO₂|CF₃-**p** (a), TiO₂|CF₃-**x** (b), CS|CF₃-**p** (c) and CS|CF₃-**x** (d) thin films submerged in argon purged 0.1M LiClO₄ CH₃CN electrolyte. 191

Figure 6.4: The absorption change monitored at 730 nm after pulsed 532 nm excitation of TiO₂|CF₃-**p** (a), TiO₂|CF₃-**x** (b), CS|CF₃-**p** (c) and CS|CF₃-**x** (d) over the temperature ranges indicated. The dye-sensitized thin films were immersed in an argon purged 0.1M LiClO₄ CH₃CN electrolyte solution. 192

Figure 6.5: Arrhenius (left) analysis of back-electron transfer at the indicated dye-sensitized interfaces. The open shapes correspond to back-electron transfer from MO_x(e⁻) to Ru^{III} whereas the solid shapes correspond to back-electron transfer from MO_x(e⁻) to TPA⁺. A van't Hoff plot (right) obtained from the intramolecular equilibrium between MO_x(e⁻)|Ru^{III}-B-TPA and MO_x(e⁻)|Ru^{II}-B-TPA⁺. 194

Figure 6.6: Representation of two models previously used to rationalize the kinetics for back-electron transfer from SnO₂/TiO₂ core/shell nanoparticles to oxidized sensitizers or redox mediators. On the left, the conduction band edge band edge potential of TiO₂ is represented for illustration purposes as a solid red line. The band edge offset model between SnO₂ and TiO₂ is represented in the middle while the formation of a low energy Sn_xTi_yO₂ electronic state at the interface between the SnO₂ core and the TiO₂ shell is represented on the right..... 197

Figure 6.7: Activation energies for back-electron transfer from TiO₂(e⁻) to oxidized RuTPA,²⁸ triphenylamine derivatives 200

LIST OF SCHEMES

Scheme 1.1. Three types of electron transfer reactions.....	4
Scheme 1.2. Nuclear motion through the transition state associated with (non)adiabatic electron transfer reactions.	18
Scheme 2.1. Representation of the reversal of the electron transfer pathway following one-electron oxidation. ^a	41
Scheme 2.2. Nomenclature and structures of the 8 compounds studied.	42
Scheme 2.3. Representation of superexchange theory for bridge-mediated electron transfer (left) as well as for the ‘indirect’ electron transfer pathway when Ru ^{II} is oxidized prior to TPA (middle) and the ‘direct’ pathway when TPA is oxidized first (right).	51
Scheme 2.4. Potential energy surface diagram for 3-state optical electron transfer. ^a	54
Scheme 2.5. Previously reported cyclometalated Ru ^{II} mixed-valent compounds with the corresponding values of H _{DA} . Taken from ref. 46-48 and 52.	57
Scheme 2.6. Structures of the ligands prior to coordination to Ru ^{II}	73
Scheme 3.1 Square-scheme kinetic model for molecules that undergo excited-state acid-base chemistry.....	109
Scheme 3.2. Square-scheme kinetic model for interfacial (k _A , k _b) and intramolecular (k ₁ , k ₋₁) electron transfer for immobilized molecules.	110
Scheme 4.1. Redox equilibrium after excited state injection to TiO ₂	124
Scheme 4.2. Two-dimensional potential energy surfaces for asymmetric electron transfer.	137

LIST OF TABLES

Table 2.1. Spectroscopic and electrochemical properties of the compounds studied.	43
Table 2.2. Tabulated values of IVCT band parameters and the associated electronic coupling matrix elements.	56
Table 2.3. Parameters of the IVCT bands used to calculate H_{DA} .	71
Table 3.1. Thermodynamic and Electronic Coupling Parameters at Room Temperature.	91
Table 3.2. Arrhenius Parameters Extracted from Temperature Dependent Rate Constants.	96
Table 3.3. Calculated and experimental values for dipole-moments, degree of delocalization, electron transfer distances, and electronic coupling for the 2p compound.	107
Table 3.4 Rate and Equilibrium Constants from the Kinetic Analysis.	111
Table 4.1. Thermodynamic values for the indicated compounds in the redox equilibrium of Eq. 1.	126
Table 4.2. Activation parameters for intramolecular electron transfer in the xylyl-bridged (nonadiabatic) and phenyl-bridged (adiabatic) compounds.	128
Table 4.3. Standard and thermodynamic activation entropies for electron transfer.	134
Table 4.4. Calculated and observed rate constants of intramolecular electron transfer at 293 K.	140
Table 4.5. Rate constants for 2x calculated with reorganization energy as a temperature dependent and independent value.	149
Table 4.6. Temperature dependence of the adiabaticity parameter, κ_A , at $\lambda = 1.15$ eV.	150
Table 4.7. Experimental and calculated rate constants for electron transfer in the nonadiabatic limit in compound 1x .	151
Table 4.8. Experimental and calculated rate constants for electron transfer in the nonadiabatic limit for compound 2x .	152

Table 4.9 Experimental and calculated rate constants for electron transfer in the adiabatic limit in compound 1p	153
Table 4.10. Experimental and calculated rate constants for electron transfer in the adiabatic limit in compound 2p	153
Table 4.11. Errors for standard thermodynamic quantities from the van't Hoff analysis.....	154
Table 5.1. Reduction Potentials ^a and Rate Constants for 1-2/TiO ₂	170
Table 6.1: Activation parameters for the back-electron transfer reaction from TiO ₂ and SnO ₂ /TiO ₂ core/shell (CS) to the oxidized form of the indicated sensitizer.....	194

Chapter 1. Intramolecular and interfacial electron transfer theory

1.1 Motivation

Studies of electron transfer events within and between molecules has permeated the diverse fields of biology, physics, and chemistry which have captivated the minds of countless scientists over many generations. The ubiquity and fundamental insight provided by studying such reactions lends itself to the diversity of fields that are concerned with electron motion. In the field of Chemistry in particular, electron transfer reactions are studied, intentionally or not, in nearly every one of the sub-disciplines that comprise it and are present in nearly every physical medium. It is worth mentioning sub-disciplines of chemistry that have embraced this fundamental process. Biological chemistry, for example, studies electron transfer reactions between redox-active sites in an enzymes or proteins¹⁻², or between DNA base-pairs.³⁻⁴ Meanwhile, analytical and materials chemists interested in sensors⁵, microelectrodes⁶⁻⁷, or microscopy techniques⁸⁻⁹ are also concerned with electron transfer. Inorganic and physical chemists are inherently interested in electron transfer reactions within well-defined transition metal containing bioinorganic,¹⁰⁻¹⁴ or organometallic model complexes with time-resolved spectroscopies spanning over 21 orders of magnitude in time¹⁵⁻²³, or as theoretical problems studied with quantum theory²⁴⁻²⁵. Certainly, some examples have been (unintentionally) excluded as the field is too broad and detailed to motivate in any one document let alone be discussed comprehensively as one chapter of a dissertation. As such, this *Dissertation* serves only as a small piece of the overall ‘puzzle’ that is electron transfer.

Insofar as physical-inorganic chemists are concerned (where electron transfer is central to the field's scientific philosophy) an electron transfer 'puzzle' is often comprised of 1) determining the mechanism through which electron transfer occurs, 2) what principles govern it, and 3) what chemical factors contribute to it. However, like any challenging puzzle there exists extensive, exhaustive, and elaborate theoretical insights into what the best way to 'solve' it is. For studying electron transfer reactions the theoretical basis on which the field has grown (and continues to grow beyond) is that of theory of Libby and Marcus (who was recipient of the 1992 Nobel Prize for his contributions to electron transfer and proposition that thermodynamics and kinetics were intimately related).²⁶ Much of the beauty of Marcus theory the intuitive algebraic derivation without knowledge of the donor and acceptor chemical structure or properties. At the same time, it contains, implicitly, deep and fundamental chemical knowledge.

Since its inception, Marcus theory has spawned many theoretical treatments which have expanded the field greatly over the last sixty years. An initial significant experimental advance in this area was the validation of the 'Inverted Region' by Closs and Miller in 1984.²⁷ Indeed, despite the sophistication of modern electron transfer experiments and theories, the traditional theoretical groundwork has largely remained unchanged. Because of this, it is important to revisit the underlying microscopic principles that comprise Marcus theory, for example, on how to control the rate or direction of electron transfer or how to use steady-state experiments to calculate dynamic values. To this extent, the apparent simplicity, and applicability, of Marcus theory highlights the breadth of electron transfer reactions in the field of Chemistry. Moreover, the theory provides a pathway to show how electron transfer can be useful in chemical applications, such as in light-driven chemical reactions (photo-

redox catalysis), or more broadly on a macroscopic level, as in solar energy conversion schemes or in molecular electronics.²⁸⁻²⁹

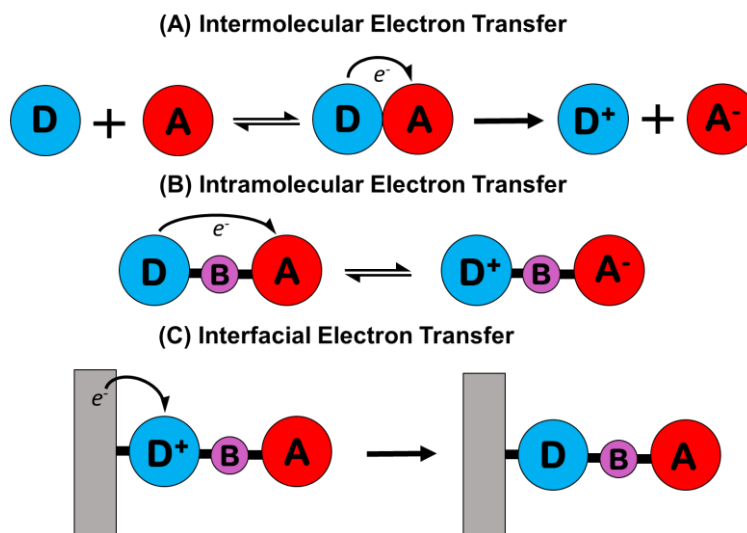
An attractive goal for solving electron transfer puzzles as Chemists lies in achieving the ability to predict *a priori* the rate constant for electron transfer in any given chemical system. Typically, this can be accomplished through utilization of experimental thermodynamic quantities such as spectroscopic absorption features, electrochemical reduction potentials, and environmental properties of the solvent and substrate. The intrinsic relationship between thermodynamic properties and the kinetics and dynamics of electron transfer is at the heart of Marcus theory. The combination of the two are used, individually or in tandem, to confirm a mechanism or calculate an expected rate of electron transfer with respect to the theoretical groundwork of the theory. Correspondingly, it seems prudent to introduce the underlying principles of Marcus theory that are present throughout this *Dissertation*.

1.2 Electron transfer reactions

A central concept in electron transfer chemistry is that of the roles of the molecules participating in the reaction. In fact, the applications of photo-redox catalysis, solar energy conversion, and molecular electronics highlight in particular three important classes of electron transfer reactions, Scheme 1.1. The first type is intermolecular electron transfer between an electron rich donor (D) and an acceptor (A) dissolved in fluid solution. In order for electron transfer to occur, the D and A reactants must collide to form an ‘encounter complex’ wherein electron transfer *may* occur. If it does occur, the newly formed products, D^+ and A^- can separate from the encounter complex to form individually solvated product species. This common reaction motif is often difficult to quantify as diffusive motion through

the solvent often controls the rate of electron transfer. Further, the transiently-formed transition state is difficult to isolate, and reactions distance between D and A are ill-defined.

Scheme 1.1. Three types of electron transfer reactions.



The second type of reaction is called intramolecular electron transfer where the D and A are linked by a chemical bridge (B) and surrounded by external solvent. This type of reaction is of particular interest because the transfer process does not depend on motion of the D and A through the solvent because they do not need to collide to form an encounter complex. Indeed, intramolecular reaction rates can exceed the diffusion limit imposed by the solvent. Similarly, this means that the distance separating the two centers is fixed and electron transfer occurs across that distance. Further, the interceding bridge can be made to be inert or an active participant in the electron transfer process³⁰, which is commonly observed in biological electron transfer and photosynthesis.³¹⁻³² Participation of filled or empty bridge orbitals permits intramolecular electron transfer to proceed over long distances.³³

Interfacial electron transfer is represented by the third type of reaction, where D-B-A compound is anchored onto a heterogeneous substrate. Immobilization of a transition metal

compound onto high-surface-area semi-conducting thin films of, *i.e.* TiO₂, SnO₂, Al₂O₃, or In₂O₃/SnO₂ nanoparticles³⁴⁻³⁶ is common practice in solar energy conversion schemes. In general, light is used to promote a donor to an excited state which injects an electron into the surface's conduction band.³⁷ Following injection, the electron can either recombine (as is depicted in Scheme 1.1 C) to the oxidized donor, D⁺, or continue through a circuit to do electrochemical work.³⁸ Of central interest in this reaction is the rate of interfacial electron transfer between the reduced surface and the oxidized donor, where long lifetimes for the injected electron are preferable.²² Immobilization of the molecules onto the surface defines the charge transfer distance and removes diffusion through the solvent. However, interfacial electron transfer reactions, as will be discussed below, display non-exponential kinetics and have ill-defined free energies as the recombining electron is present in a continuum of energy states.

1.3 Marcus theory

With the identity of the reactants and type of reaction specified, establishing the theoretical treatment can begin in earnest. Much of the phenomenal successes that Marcus theory has provided arose from calculating the electron transfer rate constant, k_{ET} , using the canonical semiclassical expression, Equation 1, which is arguably the most commonly invoked form of Marcus theory.³⁹

$$k_{ET} = \frac{2\pi}{\hbar} \frac{H_{DA}^2}{\sqrt{4\pi\lambda k_b T}} \exp\left(-\frac{(\Delta G^o + \lambda)^2}{4\lambda k_b T}\right) \quad (1)$$

The remarkable aspect of this theory is that the electron transfer rate constant is a function of only three variables: the driving force, or spontaneity of the reaction, ΔG^o , the reorganization energy, λ , and the electronic coupling or degree of quantum mechanical mixing, between D

and A wavefunctions, H_{DA} . In fact, Eq.1 is a special case of the more generic rate constant expression given in Eq. 2,⁴⁰

$$k_{et} = \nu_n \kappa_{el} \kappa_n g \quad (2)$$

for reactions where the magnitude of H_{DA} is small. The variables in Eq. 2 are physically meaningful; ν_n is a nuclear frequency, κ_{el} and κ_n are the electronic and nuclear transmission coefficients, and g is a factor that scales with the electronic coupling.⁴¹⁻⁴² The mechanistic regime in which H_{DA} is small is referred to as *non-adiabatic* electron transfer. By contrast, *adiabatic* electron transfer occurs when the electronic coupling is large. Indeed, the application of Marcus theory and the distinction between adiabatic and non-adiabatic electron transfer remains a contemporary issue.⁴³ Because the verbiage of the field is over 60 years old³⁹ many questions arise naturally which require extensive analysis of the literature to answer comprehensively.

This *Dissertation* seeks to address five questions using contemporary experimental and theoretical models: (1) What value of H_{DA} would change a reaction from non-adiabatic to adiabatic, (2) how drastic is the influence of H_{DA} on experimental and predicted electron transfer rate constants, (3) where and what are the limits of each theory, (4) what microscopic factors distinguish between (non-)adiabatic regimes of electron transfer, and (5) does reaction (non-)adiabaticity appear in heterogenous electron transfer reactions with relevance to solar energy conversion?

The answers to the above questions lie within in the individual terms that comprise Eq. 2 and can be found as major themes in each *Chapter*. Each variable in Eq. 2 contains significant chemical information that underlie the majority of theoretical expectations for

electron transfer reactions. A systematic deconvolution of the mathematical underpinnings of the three regimes of electron transfer will be presented: 1) non-adiabatic intramolecular and interfacial electron transfer, 2) adiabatic electron transfer, and 3) the transition between non-adiabatic and adiabatic electron transfer.

1.4 Using potential energy surfaces and Marcus theory to understand electron transfer

1.4.1 Non-adiabatic potential energy surfaces

Potential energy surfaces encapsulate the immensely complicated and sophisticated reality of molecular systems in an accessible fashion which allows the physical principles for electron transfer to be demonstrated graphically. In this section the focus will be on non-interacting redox centers that undergo, by definition, *non-adiabatic* electron transfer. In this regime, motion along the reaction coordinate will require that an electron will ‘hop’ from the reactant to product surface. The following section will build these potential energy surfaces and connect physical parameters of electron transfer reactions with illustrative diagrams.

Traditionally, such surfaces are presented in two dimensions: the energy of the reactant and product against the reaction coordinate which signifies the extent of the electron transfer reaction.⁴⁴⁻⁴⁵ In reality, there are $3N-6$ dimensional vibrational degrees of freedom for D and A molecules and external solvent.⁴⁶ Simplification to a single harmonic vibrational coordinate with fixed force constants for the reactant and product states is a hallmark of Marcus Theory as the force constants relate directly to the *reorganization energy*, λ , for the electron transfer reaction.⁴⁷⁻⁴⁸ Force constants calculated in this manner are phenomenologically identical to those as derived from Hooke’s Law, Eq. 3 and 4, and the

(3)

resulting curves are interpreted as increases in energy following distortion of the reactants potential energy surface from an equilibrium position.

$$G_R = \frac{1}{2}fX^2 = \lambda X^2 \quad (3)$$

$$G_P = \frac{1}{2}f(X - 1)^2 + \Delta G = \lambda(X - 1)^2 + \Delta G^0 \quad (4)$$

Here G_R and G_P are potential energies generally taken as free energies, f is the force constant for a particular chemical bond, X is the position along the reaction coordinate, and

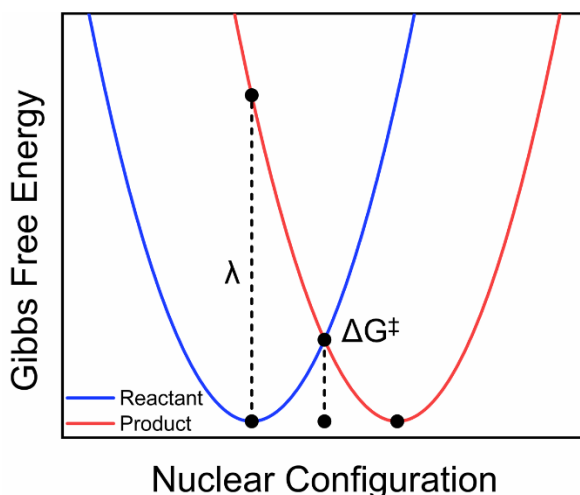


Figure 1.1. Gibbs free energy surfaces of reactants (blue) and products (red) calculated with equations x and y. The nuclear configuration along the abscissa represents the nuclear arrangement (molecule and solvent). The vertical transition from the minimum of the reactant to the product curve is the reorganization energy and the transition state, represented by ΔG^\ddagger , is where the product and reactant energies are equal.

ΔG^0 is the change in the Gibbs Free energy, driving force, for an electron transfer reaction.

Hence, vertex coordinates for the reactants and product energies are typically defined as (0,0)

and (1, ΔG) and the driving force for the reaction is reflected by the position of the product

surface minima. These two independent harmonic oscillator approximations allow for the

potential energy of the reactant and product surfaces to be evaluated as a function of progress

along the reaction coordinate through, for example, a vibrational mode. An example of a

generic surface is given in Figure 1, with the generic case of $\Delta G^0 = 0$.

A number of algebraic relationships are thus calculable from the resulting surfaces.⁴⁹ In this formalism, there are two additional points-of-interest beyond ΔG^0 , namely, the vertical energy difference of the product state in the equilibrium position of the ground-state at coordinates (0,0) and (0,1), and the energy where product and reactant surfaces are degenerate, at the midpoint along the reaction coordinate, $X = 0.5$. These two parameters contain information on the previously defined reorganization energy, λ , and the activation energy needed, ΔG^\ddagger , for the electron on the reactant surface to proceed to the product surface.

1.4.2 Gibbs energy of activation

The coordinate for which the energies of the reactant and product states are degenerate, shown in Fig 1. at $(0.5, \Delta G^\ddagger)$ provides an algebraic expression for ΔG^\ddagger by setting Eq. 3A and 3B equal, which results in Eq. 5.

$$\Delta G^\ddagger = \frac{(\Delta G^0 + \lambda)^2}{4\lambda} \quad (5)$$

The free energy barrier defines the energy of the transition state relative to the energies of the reactants and products for the reaction at the midpoint of the reaction coordinate, $X = 0.5$. In many cases, the free energy change, ΔG^0 , for the reaction can be determined experimentally from electrochemical redox potentials through Eq. 6.

$$\Delta G^0 = -nF\Delta E^0 = -nF[E_{1/2}(D^{0/-}) - E_{1/2}(A^{0/-})] \quad (6)$$

Where F is Faraday's constant, n is the number of electrons transferred, and $E_{1/2}$ represent the one electron reduction potentials for the donor and acceptor, respectively. A critical result of Eq. 2 is the prediction of a parabolic relationship between the barrier for electron transfer and the free energy for the reaction. A parabolic dependence of ΔG^\ddagger on ΔG° indicates that the barrier for a series of chemically similar D-A complexes with fixed λ will decrease, and concomitantly, the rate constant increases as the driving force increases, $-\Delta G^\circ < \lambda$. When $-\Delta G^\circ = \lambda$ the barrier is minimized, $\Delta G^\ddagger = 0$, and a maximal rate constant is achieved. The final

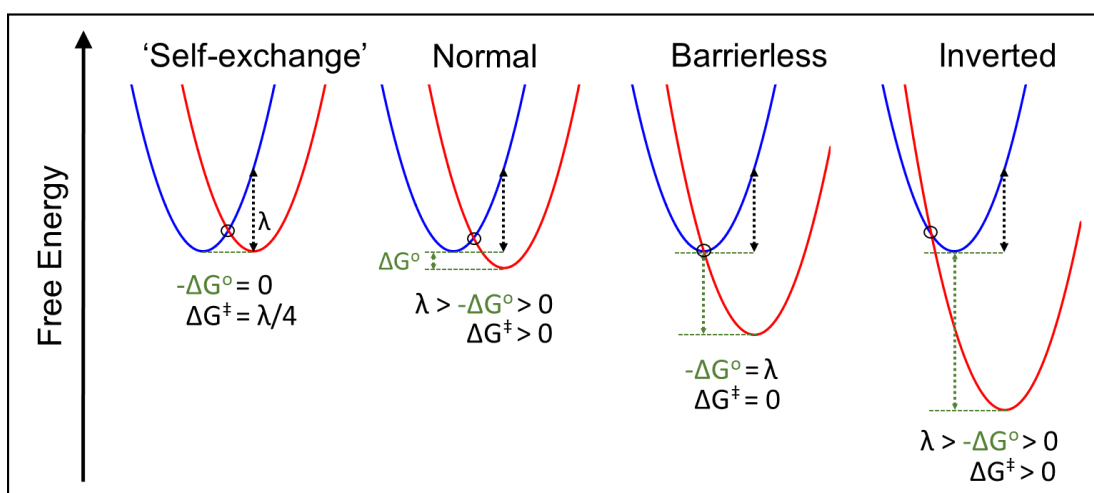


Figure 1.2. Four primary types of electron transfer reactions categorized by relationship between ΔG° and λ , except for self-exchange.

case, when $-\Delta G^\circ > \lambda$ driving force continues to increase, Eq. 5 would indicate that ΔG^\ddagger increases. As a result, electron transfer rate constants *decrease* for very exergonic reactions. This counter-intuitive, but profound, prediction is the origin of the Marcus inverted region, shown in Figure 1.2.

1.4.3 Reorganization energy

Using the constructed potential energy surfaces from Figure 1.1 the reorganization energy, λ , was defined as the energy difference between the product surface and the equilibrium position of the reactant surface.⁴⁹ Consider, for example instantaneous electron

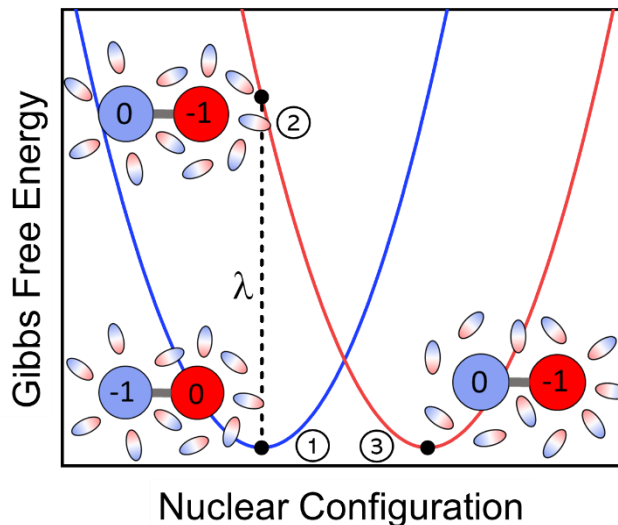


Figure 1.3. A molecular view of the reorganization energy corresponding to thermal and optical non-adiabatic electron transfer. (1)-(2): Beginning from the equilibrium configuration of the reactant (blue) absorption of light with $\Delta G^0 = h\nu = \lambda$ generates the electronic configuration of the product (red) in the nuclear configuration of the reactants (Born-Oppenheimer approximation). (1)-(3): Thermal electron transfer over the transition state $G_{TS} = \Delta G^\ddagger = \lambda/4$ results in formation of the equilibrium electronic and nuclear configuration of the product.

transfer from D to A in Fig. 1.3. Changes in the nuclear configuration have not occurred and the x-coordinate is still zero, which is a manifestation of the Born-Oppenheimer approximation (*i.e.* separation of nuclear and electronic motion timescales). Even still, electron transfer has altered the charge density distribution in the D-A compound. This results in an increase of potential energy because the compound and surrounding solvent has not moved to accommodate the new charge distribution. If motion were allowed along the reaction coordinate, the compound and surrounding solvent would move to minimize energy and reach the energy minimum of the product surface at $X = 1$. The essence of reorganization energy stated more rigorously is that it represents the potential energy of the system in the electronic configuration of the products while in the nuclear configuration of the reactants.

Because the reaction coordinate includes both nuclear and solvent degrees of freedom, in molecular terms the reorganization energy should be partitioned into a sum of inner-sphere

(λ_i , intramolecular bond length and angle changes) and outer-sphere (λ_o , solvent reorientation) terms so that $\lambda = \lambda_i + \lambda_o$. In order to gain insight into the individual contributions to the reorganization energy, revisiting the initial definition of the potential energy surfaces is useful.

A result of electron transfer to the product surfaces is the change in electron configuration of D and A, and changes in bond length and angle accompany relaxation toward the product minimum energy. The impact of changes in bond lengths is related to how the PES were constructed in using Hooke's Law. For a particular bond, j , with a force constant, f_j , the corresponding square of the change in bond length is the dominant contributor to λ_i given by Eq. 7.⁵⁰⁻⁵¹

$$\lambda_i = \frac{1}{2} \sum f_j \left(\frac{d_f - d_i}{2} \right)^2 \quad (7)$$

Here, d_f and d_i are the final and initial bond lengths, that is in the product and reactant state. Force constants for bonds have typical values of $\sim 200 \text{ N m}^{-1}$.^{50, 52} What Eq. 7 predicts is that there will be a large inner-sphere reorganization energy accompanying significant bond length changes.

Outer-sphere contributions to the reorganization energy correspond to the response of the solvent dielectric to the new electron configuration and charge density distribution.^{51, 53-54} As reviewed above and shown in Fig 1.3, the vertical transition originating at (0,0) represents the transfer of an electron from D to A while maintaining the reactant nuclear configuration. This results in a mixture of solvent dipole orientations either oriented around the now neutral donor or thermally averaged around the now negative acceptor. Initial theoretical treatments assumed that D and A were spherical and utilized solvent dielectric properties as they are

related to solvent response to new charge distributions. An initial calculation of λ_o can be garnered from treatment of the D and A as hard spheres according to dielectric continuum theory, Eq 8.^{51, 55-56}

$$\lambda_o = \frac{(\Delta e)^2}{4\pi\epsilon_o} \left(\frac{1}{2r_D} - \frac{1}{2r_A} - \frac{1}{R} \right) \left(\frac{1}{\epsilon_{op}} - \frac{1}{\epsilon_s} \right) \quad (8)$$

This approach requires the radii of the donor and acceptor spheres, r_D and r_A , as well as the internuclear distance, R . For intramolecular electron transfer, R is often larger than the sum of the two radii because the covalent bridge fixes the positions of the reacting species. Macroscopic solvent-dependent properties, namely the optical, ϵ_{op} , and static, ϵ_s , dielectric constants correlate with the polarity of the solvent the reaction occurs in.⁵⁷ Most polar aprotic solvents are reasonably well-suited to satisfy Eq. 8, however some exceptions can occur when non-polar and polar protic solvents are used.⁵⁸ For example, solvents capable of hydrogen bonding, such as alcohols and water, are often exceptions as they self-associate strongly and can often participate in specific solvent effects within the studied compound.

Typical structural changes associated with electron transfer for many transition metal compounds are minimal and as a result λ_i is often $< 10\%$ of the total λ . Practically, the implication is that the response of the solvent dielectric dominates the reorganization energy necessary to achieve most elementary electron transfer reactions.

1.4.4 Electronic coupling

An additional avenue for exploration of electron transfer theory with potential energy surfaces can be achieved by moving beyond situations where D and A centers are non-interacting and isolated. In reality, molecular orbitals facilitate charge transfer through spatial and energetic overlap which results in electron delocalization and mixing between the D and

A wavefunctions.⁵⁹⁻⁶⁰ Thus, it may be expected that the resulting delocalization alters the potential energy surfaces fundamentally - causing individual chemical identities and properties of the redox centers to become a weighted average when $\Delta G^0 \neq 0$. The physical quantity corresponding to this phenomenon is referred to as electronic coupling, H_{DA} .⁶¹ In this section the influence of electronic coupling on the potential energy surfaces is presented. Further, theoretical predictions and experimental measurement of coupling and the ramifications on the deviation from non-interacting (non-adiabatic) surfaces is discussed. Chapter 1 details the measurement and calculation of H_{DA} from spectroscopic data.

Quantifying the mixing between molecular orbitals is treated generally by Huckel theory for conjugated systems, and is similarly applied for potential energy surfaces.⁶² The same methodology is used for describing electronic coupling through constructing a 2×2 matrix of the Hamiltonians for the initial, G_D , final, G_A , and a mixing element, H_{DA} , Eq. 9. Taking advantage of the Kronecker delta for the overlap integral, S_{ij} , simplifies the matrix. A step-wise treatment is provided in Chapter 3.⁶³

$$\begin{bmatrix} G_D - E & H_{DA} \\ H_{AD} & G_A - E \end{bmatrix} = 0 \quad (9)$$

The determinant of Eq. 9 provides secular equations whose roots are Eq. 10, and after substituting H_{DD} and H_{AA} with Hooke's Law expressions, Eqs 3a, and 3b, results in Eq. 10.

$$G_{\pm} = \frac{(\lambda(2X^2 - 2X + 1) + \Delta G^0)}{2} \pm \frac{(\lambda(2X - 1) - \Delta G^0 + 4H_{DA}^2)^{\frac{1}{2}}}{2} \quad (10)$$

Note that when $H_{DA} = 0$, the resulting expressions are equivalent to Eq. 1A and 1B. The pertinent result of this equation is that for $H_{DA} > 0$ the surfaces are now split. Plots of Eq. 10 generates upper (G_+) and lower (G_-) energy surfaces which do not intersect except for in the

absence of electronic coupling. The lower surface, G_- , now contains two minima – a departure from the non-adiabatic case where minima were unique to the reactant and product states. It now becomes clear that electronic coupling modifies the potential energy surfaces at every point along the reaction coordinate.

A key question arising from the previous result lies in how much electronic coupling, measured by H_{DA} , is necessary to achieve a limit where the discrete identities and properties of D and A no longer exist.^{49, 64} An initial attempt to answer this question is to investigate the point along the nuclear coordinate where the non-interacting PES were previously degenerate - the transition state. The difference in energy between the minimum of the upper surface and lower surface at the position of the transition state on the reaction coordinate, $X = 0.5$, is given by Eq. 11.

$$G_+ - G_- = 2H_{DA} \quad (11)$$

As a result, the transition state energy (the point along the reaction coordinate where the reactant and product surfaces are degenerate) is predicted to decrease in the presence of electronic coupling resulting in a more general expression, Eq 12.

$$E_{TS} = \frac{\lambda}{4} - H_{DA} \quad (12)$$

Physically this corresponds to sufficiently strong orbital overlap delocalizing the electron density, in the case of $\Delta G^0 = 0$, evenly between the reactant and product state. However, the energy of the transition state is not the only point along the surface that is moving. In fact, as the reactant and product mix, the minima at $X = 0$ and $X = 1$ begin to decrease in energy and move toward $X = 0.5$ which provides a new expression for the Gibbs energy of activation, Eq. 13.

$$\Delta G^\ddagger = \frac{(\lambda - 2H_{DA})^2}{4\lambda} \quad (13)$$

This expression alone provides an interesting result that when $H_{DA} = \lambda/2$ the value of ΔG^\ddagger is zero. From the results of Eq. 13 it seems that, in practice, it is clear that the degree of electronic coupling implies a great intuition and expectation for an electron transfer reaction provided proper criteria are outlined.

There are three regimes of electron transfer reactions that are commonly inferred from the magnitude of the electronic coupling that mixes the potential energy surfaces constructed above which are commonly known as the Robin and Day classification.⁶⁵⁻⁶⁶ Figure 1.4 shows the three types of electron transfer. In the most basic situation for electron transfer $H_{DA} = 0$. Here, an electron is formally localized to either the donor or acceptor site and no mixing occurs. This type of reaction is known as Class I and is shown to the right of Figure 1A. Figure 1B shows the relative energetics of the transition state, product minimum energy, and the Gibb's free energy barrier and for a Class I reaction the energy of the transition state is that of the barrier. When the coupling is sufficiently large that $H_{DA} = \lambda/2$, a special case of Eq. 13 is achieved and discrete minima of the product and reactant no longer exist. Further, the identity of reactant and product potential energy surfaces are no longer distinguishable and the electron is delocalized across both surfaces. This is known as Class III electron transfer shown on the right of Figure 1A. Correspondingly, the transition state energy and reactant/product energy are equal and the barrier is zero - the minima of the lower surface having coalesced as shown on the right of Figure 1B. Unfortunately, the fact that the electron is delocalized in the Class III regime would formally mean that there is no electron transfer between the donor and acceptor.

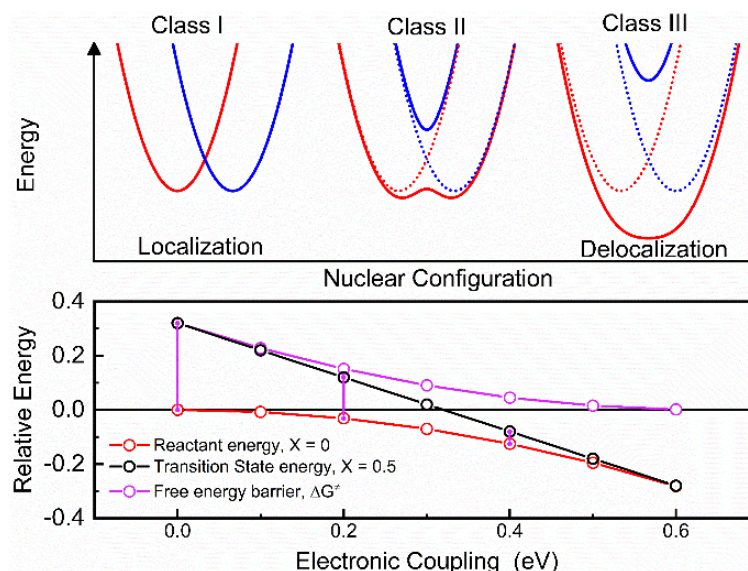
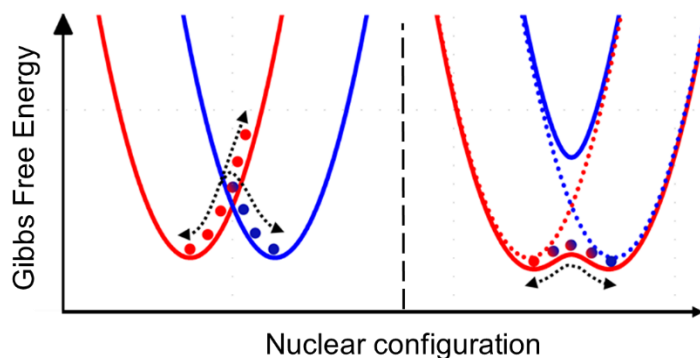


Figure 1.4. Effect of electronic coupling on potential energy surfaces as categorized by Robin and Day. Class I electron transfer (top left) corresponds to $H_{DA} = 0$, electrons are valence-localized, with a maximum barrier for electron transfer ΔG^\ddagger (bottom left). In class II, $H_{DA} > 0$, electron density is partially delocalized (top middle), and electron transfer between reactants and products is discrete (and can be adiabatic), while the barrier is reduced $\Delta G_{ad}^\ddagger < \Delta G^\ddagger$ (bottom middle). In class III electron density is delocalized (top right) and electron transfer is not discrete. As a result, there is no barrier for electron transfer, $\Delta G^\ddagger = 0$ (bottom right), as the reactant minimum energy is equal to the energy of the transition state.

Much more interesting to experimentalists are intermittent values of $0 < H_{DA} < \lambda/2$, which is known as Class II electron transfer shown in the middle of Figure 1.4. In this situation the coupling between the reactant and product is sufficient to perturb the shapes and energies of the surfaces. More crucial however is that discrete minima still exist, the free energy barrier is not zero, and electron transfer will still occur from the donor to the acceptor unlike in Class III electron transfer where the electron is equally delocalized between the D and A. Another interesting feature of Class II electron transfer is the prediction that ΔG^0 decreases in asymmetric compounds^{49, 67-69}, which is expanded upon in Chapter 2. Figure 1B demonstrates the expectation that the transition state energy decreases more rapidly than the energy of the reactant or product which results in the reduced barrier.

Further, the expectation that mixing the D and A surfaces generates two new surfaces allows for an initial, yet critically important, distinction between adiabatic and non-adiabatic electron transfer. In non-adiabatic electron transfer the electron can be thought to ‘hop’ between potential energy surfaces at the transition state, Scheme 1.2.⁷⁰ Essentially, the requirement is that the discrete potential energy surface of the reactants must move entirely to the surface of the products. When $H_{DA} > 0$, the new surfaces can allow for continuous motion of the reactant surface along the nuclear coordinate to reach a product configuration. This is one definition of adiabatic electron transfer. However, the magnitude of H_{DA} necessary for the reaction to proceed along one surface depends heavily on the relevant timescales of electron and nuclear motion which is considered below.

Scheme 1.2. Nuclear motion through the transition state associated with (non)adiabatic electron transfer reactions.



1.5 Applications of potential energy surfaces in thermal and optical electron transfer

1.5.1 Interfacial electron transfer

Traditional potential energy surfaces described above are readily applicable to electron transfer reactions occurring in homogenous solution. However, for heterogeneous electron transfer reactions between an immobilized molecule and a surface the potential energy landscape is much different. This difference arises because discrete energy levels, like those

seen in molecules, are no longer rigorously applicable for bulk surfaces. In any case, semi-conducting nanoparticles, i.e. TiO_2 , have a much higher density of states which comprise a continuum. This continuum of states is generally useful because unfilled energy levels act as electron acceptors. As such, many applications in molecular electronics, solar energy conversion, or solar fuels production take advantage of the increased density of unfilled states.

Unfilled states of semi-conductors are useful as electron acceptors because an electron can be 'injected' into the surface from a molecular excited state formed following the absorption of a photon, as demonstrated in Figure 1.5. Typically, following injection into the surface, an oxidized form of the molecule is formed. Following electron injection, the immobilized electron donor is oxidized, D^+ . Provided the lifetime of the injected electron is long enough, the immobilized compound may accumulate multiple charges which can drive chemical reactions or can be regenerated as in regenerative solar cells. However, injected electrons are known to recombine with D^+ on a microsecond timescale which may not be long enough for this to be realized. Circumventing this process can be approached through immobilizing donor-bridge-acceptor molecules on the surface which undergo intramolecular electron transfer as a means to move the oxidizing equivalent away from the surface. Essentially, an electron donor that does not participate in the injection process, but has enough energy to reduce D^+ acts as a molecular shuttle for the oxidizing equivalent to move away from the heterogeneous interface. If the equilibrium constant, K_{eq} , for the intramolecular equilibrium is small enough, $K_{\text{eq}} < 50$, and the lifetime of the injected electron long enough, a quasi-equilibrium can be established and recombination would occur to either of the discrete

redox sites within the molecule with different rate constants. Such an approach offers an opportunity to explore intramolecular equilibria without the need for sacrificial electron acceptors/donors as the TiO_2 surface acts initially as a long-lived electron acceptor. The kinetics with which the quasi-equilibrium is established can then be monitored was presented in Chapter 2. On the other hand, the recombination process can be monitored to discrete sites within the molecule depending on the identity of the bridge. Interfacial recombination

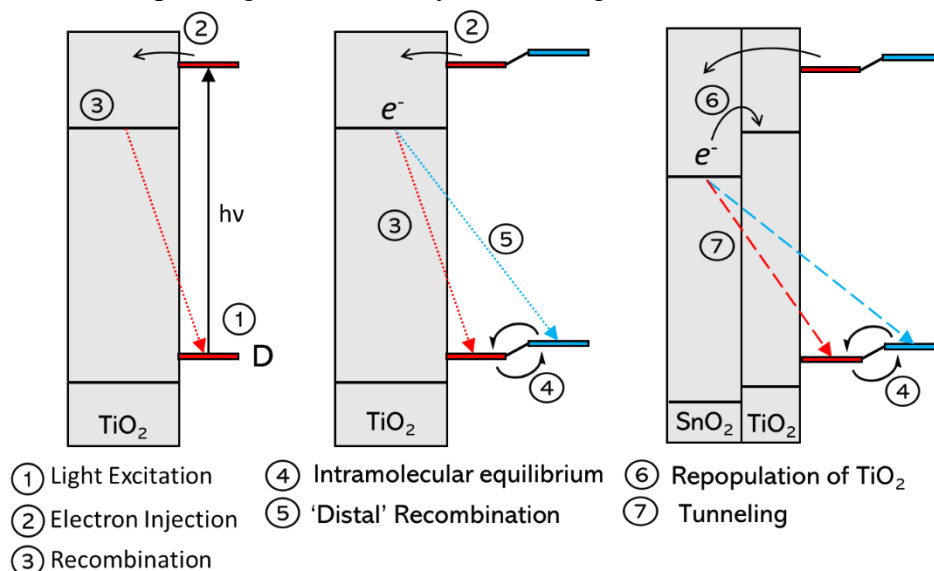


Figure 1.5. Three schematic representations of interfacial electron transfer. (left) A molecule, D, is immobilized onto a mesoporous substrate of TiO_2 . Following light excitation (1) electron transfer to the surface occurs from a localized molecular excited state to form D^+ (2) on the timescale of microseconds before the electron recombines with D^+ (3). (middle) A D-B-A molecule is immobilized onto a TiO_2 surface and, following excitation of D, injects an electron into the surface (2), after which a quasi-equilibrium between D and A may be established on the nanosecond timescale (4) which allows recombination to occur to either D^+ (3) or A^+ (5). (Right) Immobilization of D-B-A onto a core/shell film of $\text{SnO}_2/\text{TiO}_2$ increases the lifetime of the electron in the surface by virtue of the energy difference of the conduction band energies of SnO_2 and TiO_2 allowing the quasi-equilibrium to be established (4) before recombination via activated electron transfer (6) or tunneling (7) occurs to D^+ or A^+ .

kinetics is the subject of Chapter 5.

An additional approach used to inhibit recombination process down is the creation of core/shell materials of SnO_2 and TiO_2 . The conduction band of SnO_2 is lower in energy than

that of TiO_2 by approximately 300 mV and it would be thermodynamically favorable for the injected electron to reside in SnO_2 . Similarly, this would impose a large energy barrier for the reverse reaction, or the re-population of TiO_2 acceptor states. In principle, the recombination reaction would be slower for one or both of the following reasons: 1) the 300 mV barrier would decrease the rate at which electrons leave the TiO_2 surface, or 2) the electrons would tunnel through the barrier which has a low probability of occurring.⁷¹ Further, the increased distance between the oxidizing equivalent and the electron reduces the electronic coupling between them exponentially.⁷² The barriers for interfacial electron transfer from core/shell substrates and purely TiO_2 substrates is the subject of Chapter 6.

1.5.2 Intramolecular electron transfer

With molecules that have discrete energies and properties, a major application of potential energy surfaces lies in the ability to predict and rationalize how electronic coupling, reorganization energies, and free energy differences influence rate constants for intramolecular reactions. In the introduction, the semi-classical expression of Marcus was presented because it encompasses the great success achieved through theoretical calculations of rate constants and accounts for the three previously described factors. Properly applying Eq 1 to new kinetic data often requires answering the question: Is there strong electronic coupling between reactants and products and is the reaction adiabatic or non-adiabatic?²⁷ This question is typically difficult to answer because the relative timescales of molecular vibrational, solvent rotational/vibrational, and electronic motion become important and need to be considered simultaneously.^{48, 73} In fact, evaluating the (non)adiabaticity of a reaction can be reduced down to an interplay between electronic and nuclear motion and commonly utilized theories frequently implicitly assume one limit. This section will explore advanced

electron transfer models toward highlighting a continuum theory which interpolates between non-adiabatic and adiabatic electron transfer and emphasizes the importance of considering the timescales involved with each process.

1.5.3 Arrhenius and Eyring models

Classical models which quantify the rates of chemical reactions are those of Arrhenius and Eyring. The empirical observation that the reaction rate was exponentially dependent on temperature of Arrhenius, $k = A \exp(-E_a/RT)$, is still a cornerstone of kinetic analysis.

Arrhenius analysis predicts that an electron transfer reaction has a characteristic energy barrier, E_a , and frequency factor A (which is not solely dependent on the collision frequency)^{2, 74}. Later, Eyring invoked transition state theory to derive a similar model from first principles, Eq. 14.⁷⁵

$$k = \kappa \frac{k_b T}{h} \exp\left(\frac{-\Delta G^\ddagger}{k_b T}\right) = \frac{k_b T}{h} \exp\left(\frac{-\Delta S^\ddagger}{k_b T}\right) \exp\left(\frac{-\Delta H^\ddagger}{k_b T}\right) \quad (14)$$

where the activation energy, E_a , is instead the Gibbs free energy of activation which can be further reduced to the enthalpy and entropy of activation. Thus, the pre-exponential factor also contains a temperature independent entropy term as well as a frequency term of $k_b T/h$. There is also an additional term in κ , which is the transmission coefficient which can range from $0 < \kappa < 1$ whose interpretation can be loosely thought of as a probability that, upon achieving the transition state energy that reactants will proceed to products. Indeed, the pre-exponential factors correspond to the maximum rate of the reaction when the reaction is barrierless or, in cases where the barrier is non-zero, where $k_b T > \Delta H^\ddagger$.⁷⁶ A notable absence, however, from these models is an electronic coupling term.

1.6 Genesis of the Marcus equation

Unlike Arrhenius and Eyring, the semi-classical Marcus model contains an explicit term for the electronic coupling arising from first principles in the form of Fermi's Golden Rule which describes the rate constant of the transition of a particle in a two-level (reactant and product) system by Eq 15.⁷⁷

$$k = \frac{2\pi}{\hbar} |\langle p | H_{DA} | r \rangle|^2 \rho(E) \quad (15)$$

Here, $\rho(E)$ are the Frank-Condon weighted density of states which are thermally weighted probabilities that a system will gain enough energy through thermal fluctuations, $E_T = k_b T$, to overcome the enthalpy of activation, ΔH^\ddagger . Additionally, $|\langle p | H_{DA} | r \rangle|^2$ is similar to the Huckel formalism and represents the electronic wavefunctions for the reactant and product state that mix through electronic coupling. The result of the Fermi's golden rule approach is exactly that of the non-adiabatic Marcus equation, Eq 1. In this formalism the transmission coefficient, κ , of Eyring is absent from the expression. It is now worthwhile to reintroduce the generic expression for electron transfer rate constants from the introduction, $k_{ET} = \nu_n \kappa_e / \kappa_n g$ as the Golden Rule enables the dissection of the terms necessary to calculate k_{ET} .⁷⁸⁻⁷⁹

1.6.1 Nuclear factors

One of the central assumptions invoked when potential energy surfaces are constructed was that of the harmonic oscillator, and by extension, the Franck-Condon Principle. In the Golden Rule discussed above the product and reactant electronic wavefunctions were written separately from vibrational wavefunctions, which is a result of this Principle. The density of states, $\rho(E)$, which represents the nuclear factor, contains a term for the probability of occupying higher energy vibrational states in a harmonic potential energy well, Figure 1.6.

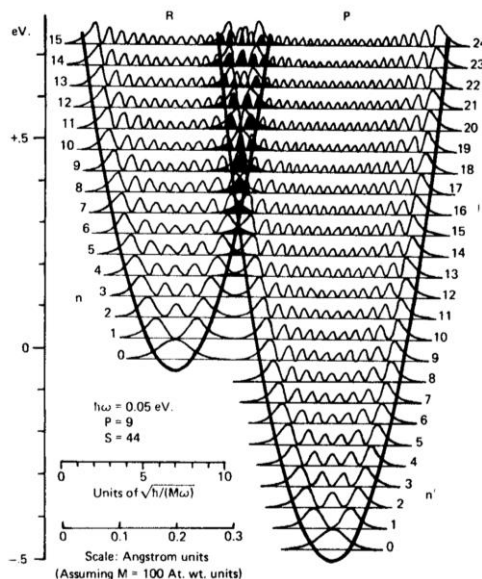


Figure 1.6. Reactant (left) and product (right) potential energy surfaces of Marcus-inverted electron transfer reactions showing vibrational wavefunction sub-levels. Higher energy vibrational energies ($n = 7$ for reactants) and ($n = 16$ for products) show how excited-vibrational states facilitate inverted electron transfer. Adapted from Barbara *et. al.*⁵³

Vibrational wavefunction overlap brought about by nuclear vibrational motion may provide alternative pathways for electron transfer to occur through nuclear tunneling. The influence of nuclear tunneling is most commonly observed at very low-temperatures and is critical for understanding inverted Marcus behavior. At high temperatures, however, $\kappa_n = \exp(-\Delta G^\ddagger/k_bT)$ and tunneling does not contribute significantly.⁸⁰⁻⁸¹ Full quantum mechanical expressions of the Marcus equation include coupling between vibrational states, however discussion of these expressions is beyond the scope of this Chapter. Further, the classical limit of Eq. 1 is usually sufficient around room temperature. To summarize briefly, control of electron transfer rate constants through vibrational overlap is important in situations where tunneling is the dominant pathway for electron transfer, *i.e.* at low temperatures and/or when spacing between vibrational energies are large.

1.6.2 Electronic and nuclear transmission coefficients

The unifying principle between the theories of Marcus and Eyring arises as an explicit equation for the transmission coefficient, κ , recalling that it represents probability of the reactants formally passing from the reactant surface, through the transition state, and onto the product surface. Such an approach is known as the Landau-Zener formalism which is given by Eq. 16^{50, 82}

$$\kappa_{el} = \frac{2P}{1+P} = \frac{2 \left(1 - \exp\left(\frac{\nu_{el}}{2\nu_n}\right)\right)}{2 - \exp\left(\frac{\nu_{el}}{2\nu_n}\right)} \approx \frac{\nu_{el}}{\nu_n + 0.5 \nu_{el}} \quad (16)$$

where ν_{el} and ν_n are electronic and nuclear frequencies, respectively, with ν_{el} appearing as the familiar pre-exponential factor expression from the non-adiabatic Marcus equation and is given by Eq 17.

$$\nu_{el} = \frac{2\pi}{\hbar} \frac{H_{DA}^2}{\sqrt{4\pi\lambda k_b T}} = \frac{2H_{DA}^2}{h} \left(\frac{\pi^3}{\lambda k_b T} \right)^{1/2} \quad (17)$$

The magnitude of the transmission coefficient is the origin of the distinction between and definition of *adiabatic* and *non-adiabatic* electron transfer reactions. If for a reaction $\kappa < 1$, the reaction is non-adiabatic while for an adiabatic reaction, $\kappa = 1$.⁸³ A Taylor series expansion of the exponential functions of Eq. 16 is the origin of an approximate expression that, for simplicity, can be evaluated by taking the ratio of the electronic and nuclear frequencies. Notably, the electronic coupling contains an exponential distance dependence that is dictated by the identity of the intervening bridge or solvent medium.⁸⁴⁻⁸⁶

For electron transfer reactions, the nuclear frequencies correspond to inner- and outer-sphere contributions in the same way the reorganization energies influence the barrier to electron transfer. The general expression for ν_n is given by Eq. 18,⁸⁷

$$\nu_n = \left(\frac{\nu_i^2 \lambda_i + \nu_o^2 \lambda_o}{\lambda_i + \lambda_o} \right)^{1/2} \quad (18)$$

with ν_i and ν_o representing inner- and outer-sphere motion. Equation 18 is an *effective* nuclear frequency that is weighted by the reorganization energies discussed previously in the Reorganization Energy section. For most intramolecular electron transfer reactions it is the outer-sphere reorganization energy that dominates because inner-sphere rearrangement is minimal and $\nu_n = \nu_o$. Examples of inner-sphere frequencies for intramolecular electron transfer can range from slow solvent rotational motion (10-100 cm⁻¹, 0.3-3×10¹² s⁻¹), low-energy metal-ligand vibrations, fast solvent relaxation, and thermal energy fluctuations (200-500 cm⁻¹, 6-15×10¹² s⁻¹) to high frequency aromatic carbon-carbon bonds and/or mixtures of intraligand and functional group vibrational modes (1000-3500 cm⁻¹, 3-10×10¹³ s⁻¹). Further, for many intramolecular electron transfer reactions $\lambda = \lambda_o \approx 1$ eV due to the increase in D-A separation from the inclusion of the chemical bridge. It is worth noting, however, for bimolecular reactions that that this is not always the case.

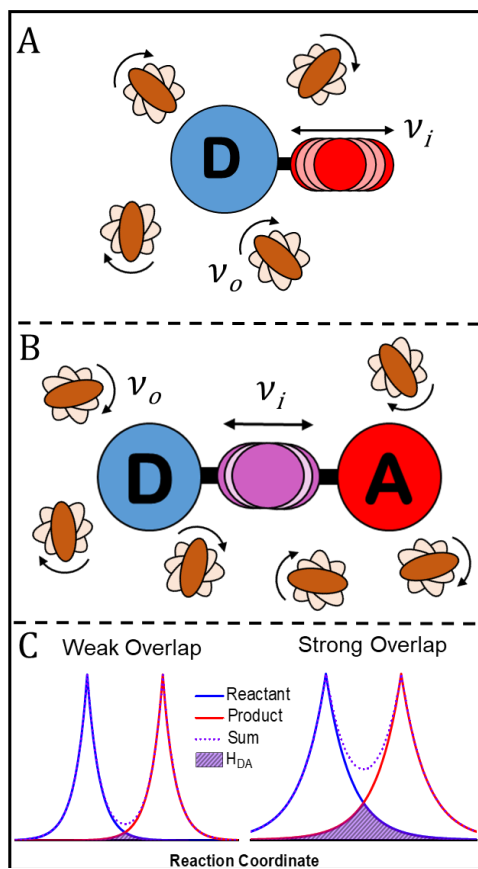


Figure 1.7. (A and B) Nuclear factors for electron transfer reactions. The electron donor (blue) or acceptor (red) is influenced by inner-sphere-type vibrational Donor-Ligand modes ν_i with frequencies between 10^{12} - 10^{13} s^{-1} . Brown ovals (with tan oval backgrounds) show outer-sphere solvent rotational motion, ν_o , which are slower than vibrational motion with $\nu_o = 10^{10}$ - 10^{12} s^{-1} . (C) Electronic factors following from the Golden Rule where electronic coupling, H_{DA} , is represented by orbital overlap from the reactant and product wavefunctions. The electron transfer rate is limited by $\nu_{el} < \nu_n$ when the orbital overlap is weak whereas strong overlap can cause nuclear motion to be rate limiting, $\nu_n < \nu_{el}$.

Whereas assumptions of small inner-sphere components are appropriate for many situations, molecules that undergo quantum mechanically forbidden spin changes or Jahn-Teller distortions, for example, are exceptions to the general trend that λ_o is dominant. Such reactions generally require large bond-length distortions in the inner coordination sphere ($\Delta d > 0.1$ Å) relative to bond lengthening in compounds which remain in high- or low-spin electron configurations or are rigid π -systems ($\Delta d < 0.05$ Å).⁵² Large inner-sphere components must be included in these cases because $\lambda_i \geq \lambda_o$ which results in ν_i contributing

to the effective frequency. Influence of inner-sphere components can be considerable, resulting in values of ν_n of $1\text{--}10 \times 10^{13}$. Interestingly, when $h\nu > 2k_bT$ (as is the case for C-C or C-H inner-sphere vibrational motion) quantum mechanical tunneling may be important as introduced above. Since inner-sphere dominated-reactions have high frequency factors, a large electron transfer rate constant (when κ_n is small) might be expected. However, quantum mechanical tunneling and, in some cases selection rules, significantly reduce the magnitude of electronic coupling between the potential wells.⁸⁸ As a result, numerical quantities calculated from Eq. 17 provide values where $\nu_{el} < \nu_n$. Hence, slow electron transfer rate constants, relative to ν_n , are achieved in practice.

Quantitative calculation of ν_{el} and ν_n can be used to predict the transmission coefficient that appears in the pre-exponential factor of Eq. 14. Figure 1.8 demonstrates the dependence of κ on H_{DA} in different situations where discrete solvent and vibrational nuclear frequencies control the nuclear configuration necessary for electron transfer to occur.

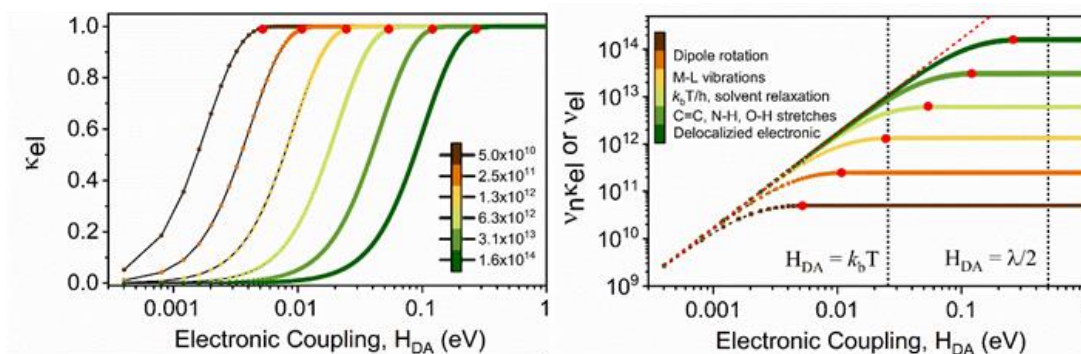


Figure 1.8. (Top) The electronic transmission coefficient as a function of H_{DA} for the indicated values of nuclear frequencies, ν_n , with $\lambda = 1$ eV. (B) The electronic frequency (red dotted line) or the product of ν_n and κ_{el} as a function of H_{DA} . Red circles indicate the magnitude of electronic coupling necessary to achieve $\kappa_{el} = 1$, *i.e.* adiabatic electron transfer. When the colored lines (brown through green) deviate from ν_{el} (red dotted) electronic coupling becomes sufficiently large for the reaction to become limited by ν_n instead of ν_{el} . Values of ν_n were chosen to correspond to the timescales shown in the lower figure, from slow rotational motion to delocalized electronic motion. Vertical dotted lines corresponding to $H_{DA} = k_bT$ and $\lambda/2$ set boundary conditions establishing that coupling brought about by thermal energy fluctuations does not always result in adiabatic electron transfer and that $\Delta G^\ddagger > 0$.

As above, the approach to calculating the pre-exponential factor for non-adiabatic electron transfer is presented as $\kappa\nu_n$. When $\kappa \ll 1$, the product $\kappa\nu_n = \nu_{el}$, as is evident from Eq 16 and the resulting reaction rate constant scales quadratically with electronic coupling. In the opposite situation when $\kappa = 1$, as in adiabatic electron transfer, the pre-exponential factor is simply ν_n . At intermediate values of κ , deviation from the explicit form of Eq. 14 becomes apparent with Figure 1.8 showing the dependence of $\kappa\nu_n$ on H_{DA} with ν_{el} shown as a dotted reference line to highlight the transition from when the reaction rate is solely dependent on ν_{el} to when it depends on ν_n . Vertical lines at $H_{DA} = k_bT$ and $H_{DA} = \lambda/2$ show that when the solvent medium response is slow ($\nu_o = 30 \text{ cm}^{-1}$), coupling brought about by thermal fluctuations is sufficient to enable adiabatic electron transfer and that discrete minima, and by extension non-zero ΔG^\ddagger that defines Class II electron transfer still exist. However, it is necessary to consider criteria on a molecule-by-molecule basis. The practical implications arising from both Figure 1.8 and the discussion indicate that the “nebulous” transmission coefficient ultimately determines the mechanism of electron transfer. In other words, it indicates whether electron transfer is *rate limited* by electronic motion when $\kappa \ll 1$, nonadiabatic, or whether it is instead rate limited by nuclear motion when $\kappa = 1$, adiabatic.

1.6.3 Adiabatic electron transfer

In situations where $\kappa = 1$, the electronic motion becomes competitive with, and may eventually out-compete, nuclear motion so that the nuclear configuration is the limiting factor for the electron transfer event.⁸⁹ Such a notion is contrary to the familiar Born-Oppenheimer approximation that their respective motional timescales are separable. This approximation laid the ground-work on which the non-adiabatic electron transfer potential energy surfaces were built, and in this limit the vibrational motions of the nuclei remain in

thermal equilibrium.^{48, 90} For adiabatic electron transfer it is no longer true that timescales for nuclear and solvent motion are separable.⁹¹ Instead, electronic and nuclear configurations are in thermal equilibrium. For adiabatic electron transfer reactions the motion of the electron and nuclei are now coupled and the electron is assumed to be in *equilibrium* with the nuclear configuration of the compound at all times.

Because the electron and nuclear degrees of freedom are no longer separable the motion of the solvent often dominates the nuclear frequency, ν_n . As such, electron transfer rate constants may become dependent on the ability of the solvent (or dielectric medium) to reorient during the reaction where a partially delocalized electron moves *gradually* from the D to the A. Whereas for non-adiabatic electron transfer solvent motion occurs on a rapid timescale and the electron transfer reaction would occur *suddenly* relative to ν_n because nuclear motion is not rate limiting.⁷⁰ Since the solvent does not contribute substantially to the non-adiabatic reactions, the independent of the weak electronic motion so static solvent properties (ϵ_{op} , ϵ_s) appear in the expression for λ , Eq 8.⁹² Adiabatic electron transfer, on the other hand, requires that solvent dynamically responds to the transferring electron and the expectation is that the pre-exponential factor depends on the *rate* at which solvent reorients in the presence of an electric field known as the longitudinal relaxation time, τ_L .⁹³⁻⁹⁵ Indeed, though a full introduction of solvent-controlled or solvent-friction-controlled electron transfer reactions is beyond the scope of this Dissertation, the change from non-adiabatic electron transfer to solvent-controlled electron transfer constitutes an important consideration in modern electron transfer experimental and theoretical treatments.

1.7 Conclusion

Marcus theory was and will continue to be a powerful tool in the treatment and theoretical determination of reaction rate constants and mechanisms through comparison with experimentally quantified values. This is mainly the result of the relative simplicity of the theory under the harmonic oscillator assumption and separability of timescales of nuclear and electronic motion. Moreover, the illustrative power of potential energy diagrams permit intuitive visualizations of electron transfer reactions which allow for tangible predictions to be formed off of fundamental assumptions. In tandem, these two methods provide an experimentalist with immense power to construct vivid images as to what is occurring on a molecular level during a chemical reaction.

REFERENCES

1. Page, C. C.; Moser, C. C.; Chen, X.; Dutton, P. L., Natural engineering principles of electron tunnelling in biological oxidation–reduction. *Nature* **1999**, *402*, 47.
2. Frauenfelder, H.; Wolynes, P., Rate theories and puzzles of heme protein kinetics. *Science* **1985**, *229* (4711), 337-345.
3. Lewis, F. D.; Wu, T.; Liu, X.; Letsinger, R. L.; Greenfield, S. R.; Miller, S. E.; Wasielewski, M. R., Dynamics of photoinduced charge separation and charge recombination in synthetic DNA hairpins with stilbenedicarboxamide linkers. *J. Am. Chem. Soc.* **2000**, *122* (12), 2889-2902.
4. Kelley, S. O.; Barton, J. K., Electron transfer between bases in double helical DNA. *Science* **1999**, *283* (5400), 375-381.
5. Shleev, S.; Tkac, J.; Christenson, A.; Ruzgas, T.; Yaropolov, A. I.; Whittaker, J. W.; Gorton, L., Direct electron transfer between copper-containing proteins and electrodes. *Biosensors and Bioelectronics* **2005**, *20* (12), 2517-2554.
6. Feldman, B. J.; Ewing, A. G.; Murray, R. W., Electron transfer kinetics at redox polymer/solution interfaces using microelectrodes and twin electrode thin layer cells. *J. Electroanal. Chem.* **1985**, *194* (1), 63-81.
7. Amatore, C. A.; Deakin, M. R.; Wightman, M., Electrochemical kinetics at microelectrodes part 1. Quasi-reversible electron transfer at cylinders. *J. Electroanal. Chem.* **1986**, *206* (1), 23-36.
8. Liu, B.; Bard, A. J.; Mirkin, M. V.; Creager, S. E., Electron transfer at self-assembled monolayers measured by scanning electrochemical microscopy. *J. Am. Chem. Soc.* **2004**, *126* (5), 1485-1492.
9. Velmurugan, J.; Sun, P.; Mirkin, M. V., Scanning electrochemical microscopy with gold nanotips: The effect of electrode material on electron transfer rates. *J. Phys. Chem. C* **2009**, *113* (1), 459-464.
10. Nocera, D. G.; Winkler, J. R.; Yocom, K. M.; Bordignon, E.; Gray, H. B., Kinetics of intermolecular and intramolecular electron transfer from ruthenium(ii) complexes to ferricytochrome c. *J. Am. Chem. Soc.* **1984**, *106* (18), 5145-5150.
11. Farver, O.; Pecht, I., Long-range intramolecular electron transfer in azurins. *Proceedings of the National Academy of Sciences* **1989**, *86* (18), 6968-6972.
12. Winkler, J. R.; Gray, H. B., Electron transfer in ruthenium-modified proteins. *Chem. Rev.* **1992**, *92* (3), 369-379.
13. McLendon, G., Long-distance electron transfer in proteins and model systems. *Acc. Chem. Res.* **1988**, *21* (4), 160-167.

14. Fukuzumi, S.; Karlin, K. D., Kinetics and thermodynamics of formation and electron-transfer reactions of Cu-O_2 and $\text{Cu}_2\text{-O}_2$ complexes. *Coord. Chem. Rev.* **2013**, *257* (1), 187-195.
15. Föhlisch, A.; Feulner, P.; Hennies, F.; Fink, A.; Menzel, D.; Sanchez-Portal, D.; Echenique, P. M.; Wurth, W., Direct observation of electron dynamics in the attosecond domain. *Nature* **2005**, *436*, 373.
16. Asbury, J. B.; Hao, E.; Wang, Y.; Lian, T., Bridge length-dependent ultrafast electron transfer from re polypyridyl complexes to nanocrystalline TiO_2 thin films studied by femtosecond infrared spectroscopy. *J. Phys. Chem. B* **2000**, *104* (50), 11957-11964.
17. Breton, J.; Martin, J. L.; Fleming, G. R.; Lambry, J. C., Low-temperature femtosecond spectroscopy of the initial step of electron transfer in reaction centers from photosynthetic purple bacteria. *Biochemistry* **1988**, *27* (21), 8276-8284.
18. Mataga, N.; Karen, A.; Okada, T.; Nishitani, S.; Kurata, N.; Sakata, Y.; Misumi, S., Picosecond dynamics of photochemical electron transfer in porphyrin-quinone intramolecular exciplex systems. *J. Phys. Chem.* **1984**, *88* (22), 5138-5141.
19. Shoute, L. C. T.; Mittal, J. P., Nanosecond laser flash photolysis study of the kinetics and mechanism of photoreduction of decafluorobenzophenone. *J. Phys. Chem.* **1993**, *97* (33), 8630-8637.
20. Hankache, J.; Wenger, O. S., Microsecond charge recombination in a linear triarylamine- $\text{Ru}(\text{bpy})_3^{2+}$ -anthraquinone triad. *Chem. Comm.* **2011**, *47* (36), 10145-10147.
21. Imbert, D.; Cantuel, M.; Bünzli, J.-C. G.; Bernardinelli, G.; Piguet, C., Extending lifetimes of lanthanide-based near-infrared emitters (Nd, Yb) in the millisecond range through $\text{Cr}(\text{III})$ sensitization in discrete bimetallic edifices. *J. Am. Chem. Soc.* **2003**, *125* (51), 15698-15699.
22. Sampaio, R. N.; Troian-Gautier, L.; Meyer, G. J., A charge-separated state that lives for almost a second at a conductive metal oxide interface. *Angew. Chemie.* **2018**, *130* (47), 15616-15620.
23. James, C. A.; Morris, D. E.; Doorna, S. K.; Arrington, C. A.; Dunbar, K. R.; Finnis, G. M.; Pence, L. E.; Woodruff, W. H., Photochemistry of deca(acetonitrile) dirhodium(II) cation: Evidence for kilosecond-lived photoinduced charge separation. *Inorganica Chim. Acta* **1996**, *242* (1), 91-96.
24. Saen-Oon, S.; Lucas, M. F.; Guallar, V., Electron transfer in proteins: Theory, applications and future perspectives. *Phys. Chem. Chem. Phys.* **2013**, *15* (37), 15271-15285.
25. Beratan, D.; Betts, J.; Onuchic, J., Protein electron transfer rates set by the bridging secondary and tertiary structure. *Science* **1991**, *252* (5010), 1285-1288.
26. Van Houten, J., A century of chemical dynamics traced through the Nobel prizes. 1992: Rudolph A. Marcus. *J. Chem. Ed.* **2002**, *79* (9), 1055.

27. Closs, G. L.; Miller, J. R., Intramolecular long-distance electron transfer in organic molecules. *Science* **1988**, *240* (4851), 440-447.
28. Ziessel, R. F., Photo-induced energy or electron transfer in supramolecular systems: Applications to molecular wires and light-harvesting sensors. *J. Chem. Ed.* **1997**, *74* (6), 673.
29. Gilbert, M.; Albinsson, B., Photoinduced charge and energy transfer in molecular wires. *Chem. Soc. Rev.* **2015**, *44* (4), 845-862.
30. Natali, M.; Campagna, S.; Scandola, F., Photoinduced electron transfer across molecular bridges: Electron- and hole-transfer superexchange pathways. *Chem. Soc. Rev.* **2014**, *43* (12), 4005-4018.
31. Groot, M.-L.; van Mourik, F.; Eijkelhoff, C.; van Stokkum, I. H. M.; Dekker, J. P.; van Grondelle, R., Charge separation in the reaction center of photosystem ii studied as a function of temperature. *Proceedings of the National Academy of Sciences* **1997**, *94* (9), 4389-4394.
32. Cardona, T.; Sedoud, A.; Cox, N.; Rutherford, A. W., Charge separation in photosystem ii: A comparative and evolutionary overview. *Biochim. Biophys. Acta* **2012**, *1817* (1), 26-43.
33. Wenger, O. S.; Leigh, B. S.; Villahermosa, R. M.; Gray, H. B.; Winkler, J. R., Electron tunneling through organic molecules in frozen glasses. *Science* **2005**, *307* (5706), 99-102.
34. Katoh, R.; Furube, A.; Yoshihara, T.; Hara, K.; Fujihashi, G.; Takano, S.; Murata, S.; Arakawa, H.; Tachiya, M., Efficiencies of electron injection from excited n3 dye into nanocrystalline semiconductor (zro2, tio2, zno, nb2o5, sno2, in2o3) films. *J. Phys. Chem. B* **2004**, *108* (15), 4818-4822.
35. Cappel, U. B.; Moia, D.; Bruno, A.; Vaissier, V.; Haque, S. A.; Barnes, P. R. F., Evidence for photo-induced charge separation between dye molecules adsorbed to aluminium oxide surfaces. *Sci. Rep.* **2016**, *6*, 21276.
36. O'Regan, B.; Grätzel, M., A low-cost, high-efficiency solar cell based on dye-sensitized colloidal tio2 films. *Nature* **1991**, *353* (6346), 737-740.
37. Fessenden, R. W.; Kamat, P. V., Rate constants for charge injection from excited sensitizer into sno2, zno, and tio2 semiconductor nanocrystallites. *J. Phys. Chem.* **1995**, *99* (34), 12902-12906.
38. Ardo, S.; Meyer, G. J., Photodriven heterogeneous charge transfer with transition-metal compounds anchored to tio2 semiconductor surfaces. *Chem. Soc. Rev.* **2009**, *38* (1), 115-164.
39. Marcus, R. A., On the theory of oxidation-reduction reactions involving electron transfer. *I. J. Chem. Phys.* **1956**, *24* (5), 966-978.
40. Sutin, N., Theory of electron transfer reactions: Insights and hindsights. In *Progress in inorganic chemistry: An appreciation of henry taube*, John Wiley & Sons, Inc.: Published Online, 2007; Vol. 30, pp 441-498.

41. Rips, I.; Jortner, J., Dynamic solvent effects on outer-sphere electron transfer. *J. Chem. Phys.* **1987**, *87* (4), 2090-2104.
42. Bolton, J. R.; Archer, M. D., Basic electron-transfer theory. In *Electron transfer in inorganic, organic, and biological systems*, American Chemical Society: 1991; Vol. 228, pp 7-23.
43. Rafiq, S.; Scholes, G. D., From fundamental theories to quantum coherences in electron transfer. *J. Am. Chem. Soc.* **2019**, *141* (2), 708-722.
44. Marcus, R. A., Electron transfer theory and its inception. *Phys. Chem. Chem. Phys.* **2012**, *14* (40), 13729-13730.
45. Libby, W. F., Theory of electron exchange reactions in aqueous solution. *J. Phys. Chem.* **1952**, *56* (7), 863-868.
46. Lewis, N. A., Potential energy diagrams: A conceptual tool in the study of electron transfer reactions. *J. Chem. Ed.* **1980**, *57* (7), 478.
47. Sutin, N., Theory of electron transfer reactions: Insights and hindsights. In progress in inorganic chemistry. In *Progress in inorganic chemistry*, Lippard, S. J., Ed. 2007.
48. Sutin, N., Nuclear, electronic, and frequency factors in electron transfer reactions. *Acc. Chem. Res.* **1982**, *15* (9), 275-282.
49. Brunschwig, B. S.; Sutin, N., Energy surfaces, reorganization energies, and coupling elements in electron transfer. *Coord. Chem. Rev.* **1999**, *187* (1), 233-254.
50. Brunschwig, B. S.; Creutz, C.; Macartney, D. H.; Sham, T. K.; Sutin, N., The role of inner-sphere configuration changes in electron-exchange reactions of metal complexes. *Faraday Discussions of the Chemical Society* **1982**, *74* (0), 113-127.
51. Chen, P.; Meyer, T. J., Medium effects on charge transfer in metal complexes. *Chem. Rev.* **1998**, *98* (4), 1439-1478.
52. Siders, P.; Marcus, R. A., Quantum effects in electron-transfer reactions. *J. Am. Chem. Soc.* **1981**, *103* (4), 741-747.
53. Barbara, P. F.; Meyer, T. J.; Ratner, M. A., Contemporary issues in electron transfer research. *J. Phys. Chem.* **1996**, *100* (31), 13148-13168.
54. Bader, J. S.; Berne, B. J., Solvation energies and electronic spectra in polar, polarizable media: Simulation tests of dielectric continuum theory. *J. Chem. Phys.* **1996**, *104* (4), 1293-1308.
55. Vaissier, V.; Barnes, P.; Kirkpatrick, J.; Nelson, J., Influence of polar medium on the reorganization energy of charge transfer between dyes in a dye sensitized film. *Phys. Chem. Chem. Phys.* **2013**, *15* (13), 4804-4814.

56. Moia, D.; Vaissier, V.; López-Duarte, I.; Torres, T.; Nazeeruddin, M. K.; O'Regan, B. C.; Nelson, J.; Barnes, P. R. F., The reorganization energy of intermolecular hole hopping between dyes anchored to surfaces. *Chemical Science* **2014**, 5 (1), 281-290.
57. Maroncelli, M.; MacInnis, J.; Fleming, G. R., Polar solvent dynamics and electron-transfer reactions. *Science* **1989**, 243 (4899), 1674-1681.
58. Hans, H., Dynamic solvent effects on electron-transfer reactions. *Angewandte Chemie International Edition in English* **1993**, 32 (3), 359-377.
59. Cave, R. J.; Newton, M. D., Generalization of the mulliken-hush treatment for the calculation of electron transfer matrix elements. *Chemical Physics Letters* **1996**, 249 (1), 15-19.
60. Cave, R. J.; Newton, M. D., Calculation of electronic coupling matrix elements for ground and excited state electron transfer reactions: Comparison of the generalized mulliken–hush and block diagonalization methods. *The Journal of Chemical Physics* **1997**, 106 (22), 9213-9226.
61. Hush, N. S., Intervalence-transfer absorption. Part 2. Theoretical considerations and spectroscopic data. In *Progress in inorganic chemistry*, 2007.
62. Hückel, E., Quantentheoretische beiträge zum problem der aromatischen und ungesättigten verbindungen. Iii. *Zeitschrift für Physik* **1932**, 76 (9), 628-648.
63. Creutz, C.; Newton, M. D.; Sutin, N., Metal—ligand and metal—metal coupling elements. *J. Photochem. Photobiol. A* **1994**, 82 (1), 47-59.
64. Brunschwig, B. S.; Creutz, C.; Sutin, N., Optical transitions of symmetrical mixed-valence systems in the class ii-iii transition regime. *Chemical Society Reviews* **2002**, 31 (3), 168-184.
65. Robin, M. B.; Day, P., Mixed valence chemistry-a survey and classification. In *Advances in inorganic chemistry and radiochemistry*, Emeléus, H. J.; Sharpe, A. G., Eds. Academic Press: 1968; Vol. 10, pp 247-422.
66. Day, P.; Hush, N. S.; Clark, R. J. H., Mixed valence: Origins and developments. *Philosophical Transactions of the Royal Society A: Mathematical, Physical and Engineering Sciences* **2008**, 366, 5-14.
67. Londergan, C. H.; Salsman, J. C.; Lear, B. J.; Kubiak, C. P., Observation and dynamics of “mixed-valence isomers” and a thermodynamic estimate of electronic coupling parameters. *Chem. Phys.* **2006**, 324 (1), 57-62.
68. Salsman, J. C.; Kubiak, C. P.; Ito, T., Mixed valence isomers. *J. Am. Chem. Soc.* **2005**, 127 (8), 2382-2383.
69. Ito, T.; Imai, N.; Yamaguchi, T.; Hamaguchi, T.; Londergan, C. H.; Kubiak, C. P., Observation and dynamics of “charge-transfer isomers”. *Angewandte Chemie International Edition* **2004**, 43 (11), 1376-1381.

70. Newton, M. D., Quantum chemical probes of electron-transfer kinetics: The nature of donor-acceptor interactions. *Chem. Rev.* **1991**, *91* (5), 767-792.
71. Knauf, R. R.; Kalanyan, B.; Parsons, G. N.; Dempsey, J. L., Charge recombination dynamics in sensitized $\text{SnO}_2/\text{TiO}_2$ core/shell photoanodes. *J. Phys. Chem. C* **2015**, *119* (51), 28353-28360.
72. Davis, W. B.; Ratner, M. A.; Wasielewski, M. R., Conformational gating of long distance electron transfer through wire-like bridges in donor-bridge-acceptor molecules. *J. Am. Chem. Soc.* **2001**, *123* (32), 7877-7886.
73. Hupp, J. T.; Weaver, M. J., The frequency factor for outer-sphere electrochemical reactions. *J. Electroanal. Chem.* **1983**, *152* (1), 1-14.
74. Hupp, J. T.; Weaver, M. J., Entropic driving-force effects upon preexponential factors for intramolecular electron transfer: Implications for the assessment of nonadiabaticity. *Inorg. Chem.* **1984**, *23* (2), 256-258.
75. Eyring, H., The activated complex in chemical reactions. *J. Chem. Phys.* **1935**, *3* (2), 107-115.
76. Marcus, R. A., On the frequency factor in electron transfer reactions and its role in the highly exothermic regime. *Int. J. Chem. Kinet.* **1981**, *13* (9), 865-872.
77. Ito, A.; Meyer, T. J., The golden rule. Application for fun and profit in electron transfer, energy transfer, and excited-state decay. *Phys. Chem. Chem. Phys.* **2012**, *14* (40), 13731-13745.
78. Jortner, J.; Bixon, M., Intramolecular vibrational excitations accompanying solvent-controlled electron transfer reactions. *J. Chem. Phys.* **1988**, *88* (1), 167-170.
79. Bixon, M.; Jortner, J., Quantum effects on electron-transfer processes. *Faraday Discussions of the Chemical Society* **1982**, *74* (0), 17-29.
80. Isied, S. S.; Vassilian, A.; Wishart, J. F.; Creutz, C.; Schwarz, H. A.; Sutin, N., The distance dependence of intramolecular electron-transfer rates: Importance of the nuclear factor. *J. Am. Chem. Soc.* **1988**, *110* (2), 635-637.
81. Brunschwig, B. S.; Logan, J.; Newton, M. D.; Sutin, N., A semiclassical treatment of electron-exchange reactions. Application to the hexaaquoiron(ii)-hexaaquoiron(iii) system. *J. Am. Chem. Soc.* **1980**, *102* (18), 5798-5809.
82. Zusman, L. D., Outer-sphere electron transfer in polar solvents. *Chem. Phys.* **1980**, *49* (2), 295-304.
83. Burshtein, A. I.; Georgievski, Y., Energy activation of adiabatic and nonadiabatic electron transfer. *J. Chem. Phys.* **1994**, *100* (10), 7319-7330.

84. Wenger, O. S., How donor–bridge–acceptor energetics influence electron tunneling dynamics and their distance dependences. *Accounts of Chemical Research* **2011**, *44* (1), 25-35.
85. Albinsson, B.; Mårtensson, J., Long-range electron and excitation energy transfer in donor–bridge–acceptor systems. *Journal of Photochemistry and Photobiology C: Photochemistry Reviews* **2008**, *9* (3), 138-155.
86. Glover, S. D.; Goeltz, J. C.; Lear, B. J.; Kubiak, C. P., Inter- or intramolecular electron transfer between triruthenium clusters: We'll cross that bridge when we come to it. *Coord. Chem. Rev.* **2010**, *254* (3), 331-345.
87. Weaver, M. J., Dynamical solvent effects on activated electron-transfer reactions: Principles, pitfalls, and progress. *Chem. Rev.* **1992**, *92* (3), 463-480.
88. Creutz, C., Nonadiabatic, short-range, intramolecular electron transfer from ruthenium(ii) to cobalt(iii) complexes. *J. Phys. Chem. B* **2007**, *111* (24), 6713-6717.
89. Sparpaglione, M.; Mukamel, S., Adiabatic vs. Nonadiabatic electron transfer and longitudinal solvent dielectric relaxation: Beyond the debye model. *J. Phys. Chem.* **1987**, *91* (15), 3938-3943.
90. M D Newton, a.; Sutin, N., Electron transfer reactions in condensed phases. *Annual Review of Physical Chemistry* **1984**, *35* (1), 437-480.
91. Sparpaglione, M.; Mukamel, S., Dielectric friction and the transition from adiabatic to nonadiabatic electron transfer. I. Solvation dynamics in liouville space. *J. Chem. Phys.* **1988**, *88* (5), 3263-3280.
92. Lear, B. J.; Glover, S. D.; Salsman, J. C.; Londergan, C. H.; Kubiak, C. P., Solvent dynamical control of ultrafast ground state electron transfer: Implications for class ii–iii mixed valency. *J. Am. Chem. Soc.* **2007**, *129* (42), 12772-12779.
93. Günter, G.; W., H.; G., H., Solvent dynamic in electron transfer reactions: An application of kramers theory to homogeneous organic electron self exchange. *Ber. Bunsenges. Phys. Chem.* **1990**, *94* (11), 1343-1348.
94. McManis, G. E.; Weaver, M. J., Solvent relaxation in thermal electron-transfer reactions: Some comparisons with real-time measurements of solvation dynamics. *Chemical Physics Letters* **1988**, *145* (1), 55-60.
95. Glover, S. D.; Lear, B. J.; Salsman, J. C.; Londergan, C. H.; Kubiak, C. P., Electron transfer at the class ii/iii borderline of mixed valency: Dependence of rates on solvent dynamics and observation of a localized-to-delocalized transition in freezing solvents. *Philos. Trans. Royal Soc. A* **2008**, *366* (1862), 177-185.

Chapter 2. Optical Intramolecular Electron Transfer in Opposite Directions Through the Same Bridge that Follows Different Pathways¹

2.1 Introduction

Covalently linked donor-bridge-acceptor compounds comprised of bimetallic, organometallic, or organic redox-active bridged centers have garnered intense interest for application in molecular wires and switches,¹⁻⁵ conductive metal-organic frameworks,⁶ logic gates,⁷⁻⁸ information storage,⁹ solar energy conversion.¹⁰⁻¹⁴ In one class of compounds, the bridge contains oligomers of π -electron rich units that allow quantum mechanical mixing (H_{DA}) of the donor and acceptor wave functions. This extended conjugation enhances light absorption and influences the yield and rate of electron transfer.¹⁵⁻¹⁶ Large bodies of theoretical and experimental¹⁰⁻¹² research have focused on how subtle changes in molecular structure control the degree of electronic coupling through substituent effects,¹⁷ geometry,¹⁸⁻¹⁹ or protonation state.²⁰ Surprisingly little research has investigated how the direction of electron transfer can dictate the discrete molecular orbitals, *i.e.* an orbital pathway, that participate in moving the electron between a donor and acceptor.²¹⁻²² Here we report systematic studies of this type showing that different pathways are accessed depending on the direction of optical electron transfer through a common bridge. Investigating directional thermal and optical electron transfer is both fundamentally meaningful and practically

¹This work was previously published in *Journal of the American Chemical Society*, 140 (23), 7176, with contributions from E. J. Piechota, L. Troian-Gautier, R. N. Sampaio, M. K. Brennaman, K. Hu, C. P. Berlinguette, and G. J. Meyer. Reprinted with permission. Copyright 2018 American Chemical Society.

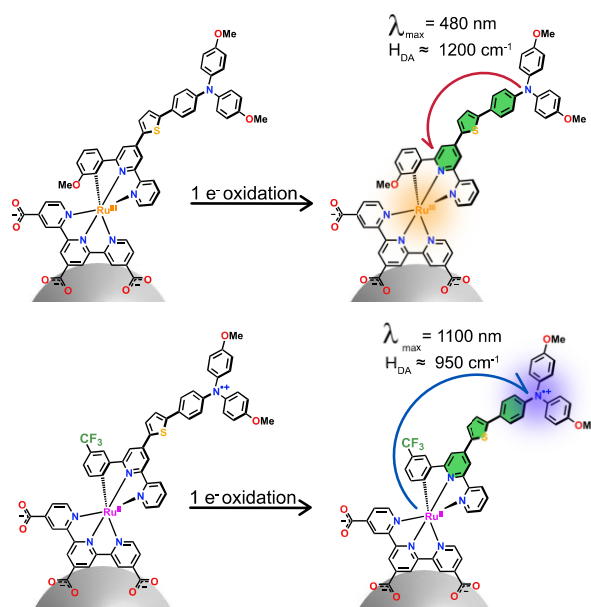
important. Indeed, for solar energy conversion it is often desirable to translate charge toward a catalytic site or to prevent unwanted thermal loss of injected electrons.

Natural and artificial photosynthesis achieve this charge separation through free energy gradients of spatially arranged redox-active centers.²³ In a similar way, for solar energy conversion and storage, light excitation of Ru^{II} polypyridyl compound results in electron injection into TiO₂ and formation of Ru^{III}. Subsequently, a covalently bound electron donor reduces the Ru^{III} and effectively relocates the hole away from the TiO₂ surface. In principle, the bridge would facilitate the charge separation and inhibit unwanted reverse reactions made possible through coupling of the two redox sites. As such, a systematic study where the direction of electron transfer was reversed around an identical molecular bridge presents a fundamentally important contribution to the literature.

Such an experimental approach is depicted in Scheme 2.1. Two Ru^{II} compounds covalently linked to a pendant triphenylamine (TPA), the structures of which are described further below, are immobilized onto metal oxide thin films. Through careful synthetic modification, the highest-occupied molecular orbital (HOMO) is varied between the two compounds, either being localized onto the Ru^{II} or on the triphenylamine (TPA) moiety. Upon electrochemical oxidation, mixed valent states are obtained and characterized by markedly different charge transfer spectroscopic features. These features are indicative of accessing discrete optical pathways that depend on the electron transfer direction *i.e.* which redox center the electron originates from. Experimentally observed spectroscopic features are reminiscent of intervalence charge transfer (IVCT) transitions and provide, through theoretical work by Mulliken and Hush, a direct measurement of H_{DA} through analysis of the IVCT band.²⁴⁻²⁷ This indicated very different electronic coupling mechanisms between Ru^{II}

and TPA, either ‘*direct*’ Ru^{II}/TPA coupling or ‘*indirect*’ coupling using unoccupied high-energy states, an effect commonly termed superexchange.²⁸

Scheme 2.1. Representation of the reversal of the electron transfer pathway following one-electron oxidation.^a



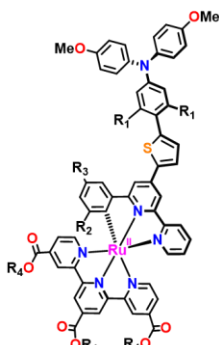
^aOrange and blue spheres represent the oxidation of the Ru metal center or TPA center. Arrows indicate optical electron transfer from the occupied orbitals to the corresponding empty (oxidized) orbitals. Text describing H_{DA} and λ correspond to the electronic coupling and energy of absorption in the UV/Vis/NIR spectrum.

This study utilizes eight bis-tridentate cyclometalated Ru^{II} compounds covalently bound to a pendant 4,4'-dimethoxy-substituted TPA through an aryl-thiophene bridge, Scheme 2.2. Substitution on the cyclometalating ring allowed for independent tuning of the Ru^{III/II} reduction potential, with either an electron donating methoxy group (**1**), or an electron withdrawing trifluoromethyl group (**2**).²⁹ The TPA unit was chosen because it provides an independent spectroscopic handle of the redox chemistry and has promising hole-transport properties for energy applications.³⁰⁻³¹ Spectroscopic and electrochemical characterization of the eight compounds indicated that the pendant TPA⁺⁰ potential varied minimally across the series.

The choice of bridge, either a phenyl-thiophene (**p**) or xylyl-thiophene (**x**) unit allowed for independent modification of the electronic coupling by enforcing a rotational energy barrier that tuned orbital overlap.³² Further, substitution in the *para* position of the pyridines that constitute the terpyridine ligand, either ethyl ester, (**E**) or carboxylate (**C**), enabled investigation both in fluid solution and anchored onto conductive thin films of Sn:In₂O₃ nanoparticles (nITO). Surface immobilization of the **1pc** series resulted in a negative shift in the TPA^{+/0} reduction potential relative to the solution value of **1p_E** that was absent for all xylyl bridged compounds.

Scheme 2.2. Nomenclature and structures of the 8 compounds studied.

Compound	Substituent			
	R ₁	R ₂	R ₃	R ₄
1p_E	-H	-OCH ₃	-H	-CH ₂ CH ₃
1x_E	-CH ₃	-OCH ₃	-H	-CH ₂ CH ₃
2p_E	-H	-H	-CF ₃	-CH ₂ CH ₃
2x_E	-CH ₃	-H	-CF ₃	-CH ₂ CH ₃
1p_C	-H	-OCH ₃	-H	-H
1x_C	-CH ₃	-OCH ₃	-H	-H
2p_C	-H	-H	-CF ₃	-H
2x_C	-CH ₃	-H	-CF ₃	-H



2.2 Results

The UV-visible absorption spectrum for the ester and carboxylate compounds in neat acetonitrile and methanol are presented in Figure 2.1. In all cases, appreciable absorption features extending beyond 700 nm were observed, with no significant absorbance beyond 800 nm.

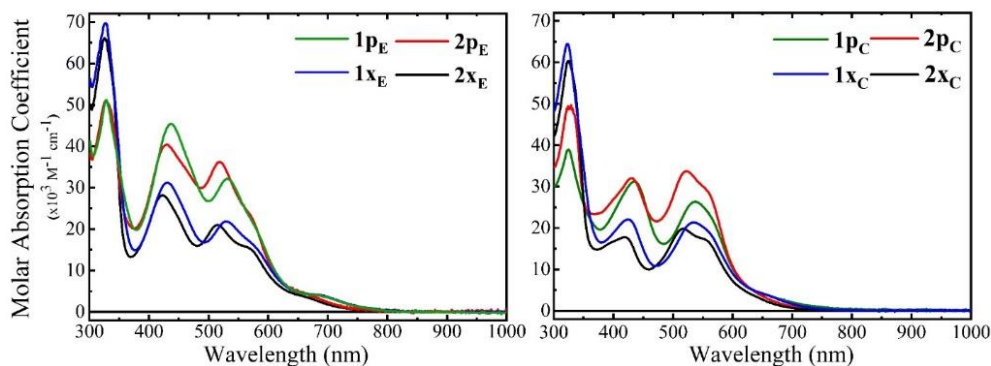


Figure 2.1. Absorption spectra of the ester forms of the compounds in neat CH_3CN (left). Absorption spectra of the carboxylate forms of the compounds in CH_3OH containing tetrabutylammonium hydroxide (right).

Table 2.1. Spectroscopic and electrochemical properties of the compounds studied.

Compound	λ_{max} , nm (ϵ , $\times 10^3 \text{ M}^{-1} \text{ cm}^{-1}$)	$E_{1/2}$ (mV vs. NHE)		ΔE (mV) ^c	K_c ^f
		$\text{Ru}^{\text{III/II}}$, α	$\text{TPA}^{+/0}$, α		
1pE ^a	328 (50.5), 437 (45.0), 531 (32.0)	950 ^c , 1.10	875 ^c , 1.05	75	19
2pE ^a	327 (50.5), 430 (40.4), 519 (36.0)	1110 ^c , 1.15	930 ^c , 1.14	180	1100
1xE ^a	327 (69.0), 431 (31.0), 530 (22.0)	960 ^c , 1.17	915 ^c , 1.03	45	6
2xE ^a	325 (65.0), 422 (28.0), 514 (21.0)	1085 ^c , 1.05	925 ^c , 1.05	160	420
1pC ^b	325 (39.6), 436 (31.3), 536 (26.7)	865 ^d , 1.41	940 ^d , 1.16	-75	0.05
2pC ^b	324 (49.3), 430 (32.0), 522 (33.7)	1050 ^d , 1.50	955 ^d , 1.15	90	33
1xC ^b	323 (63.3), 425 (22.0), 535 (21.5)	840 ^d , 1.23	920 ^d , 1.02	-80	0.04
2xC ^b	325 (61.0), 418 (17.8), 517 (19.8)	1010 ^d , 1.32	945 ^d , 1.17	65	13

^aRecorded in neat CH_3CN . ^bRecorded in CH_3OH with ~ 1 equiv of TBAOH. ^dMeasured in 0.1M $\text{LiClO}_4/\text{CH}_3\text{CN}$ solution. ^eMeasured after being anchored onto nITO in 0.1M $\text{LiClO}_4/\text{CH}_3\text{CN}$ solution. ^cCalculated relative to $E_{1/2}(\text{TPA}^{+/0})$ couple. ^fFrom Equation 3.

The extinction coefficients for **1pE** and **2pE** in CH_3CN were similar to those reported previously for the methyl ester derivatives in neat CH_3OH .³³ Absorption features observed between 500 and 600 nm were typical Ru^{II} metal-to-ligand charge transfer (MLCT) transitions.³⁴ The band at 450 nm was assigned to inter-ligand charge transfer (ILCT) transitions between the cyclometalating ligand and the pendant TPA.³⁵ We note, however, that the covalent Ru-C bond and C_1 -symmetric Ru^{II} center complicates traditional assignment of MLCT and ILCT transitions as the orbital mixing between the ligands and metal is

strong.³⁶ Absorption features below 400 nm correspond to $\pi \rightarrow \pi^*$ transitions of TPA, terpyridine, and the cyclometalating ligand. In general, the extinction coefficients of the **x**-series were found to be lower than that of the **p**-series at wavelengths greater than 400 nm. In the UV region (ca. 330 nm), the **x**-series exhibited higher extinction coefficients, $\epsilon = \sim 65 \times 10^3 \text{ M}^{-1} \text{ cm}^{-1}$, than those measured for the **p**-series, $\epsilon = \sim 50 \times 10^3 \text{ M}^{-1} \text{ cm}^{-1}$. The extinction coefficients and absorption maxima are presented in Table 2.1.

The $\text{Ru}^{\text{III/II}}$ and $\text{TPA}^{+/0}$ reduction potentials were measured in 0.1 M $\text{LiClO}_4/\text{CH}_3\text{CN}$ for the ester substituted compounds through spectroelectrochemical methods, Figure 2.2. Insets showing single wavelength absorption changes as a function of applied potential illustrate TPA^+ formation and Ru^{II} MLCT disappearance over the potential range. All electrochemical potentials reported here are given *vs.* NHE. For the compounds in fluid solution the application of positive potentials resulted in spectral changes indicative of two consecutive, one-electron oxidation events through the appearance of isosbestic points. Applying potentials between +800 and +950 mV resulted in the appearance of absorption bands beyond 700 nm, $\lambda_{\text{max}} = \sim 750 \text{ nm}$ indicative of TPA^+ formation which were observed prior to Ru^{II} oxidation events in all cases.³⁷ For **1pE** and **2pE**, bleaches in ground-state absorption were also observed below 700 nm, $\lambda_{\text{max}} \sim 450$ and 520 nm. However, growth beyond 800 nm was essentially absent in **1xE** and **2xE** within the same range of applied potentials. Applying potentials between +920 mV and +1100 mV resulted in spectral bleaches below 700 nm for **1pE**, **1xE**, **2pE**, and **2xE**, indicative of Ru^{III} formation by the loss of the MLCT transitions.

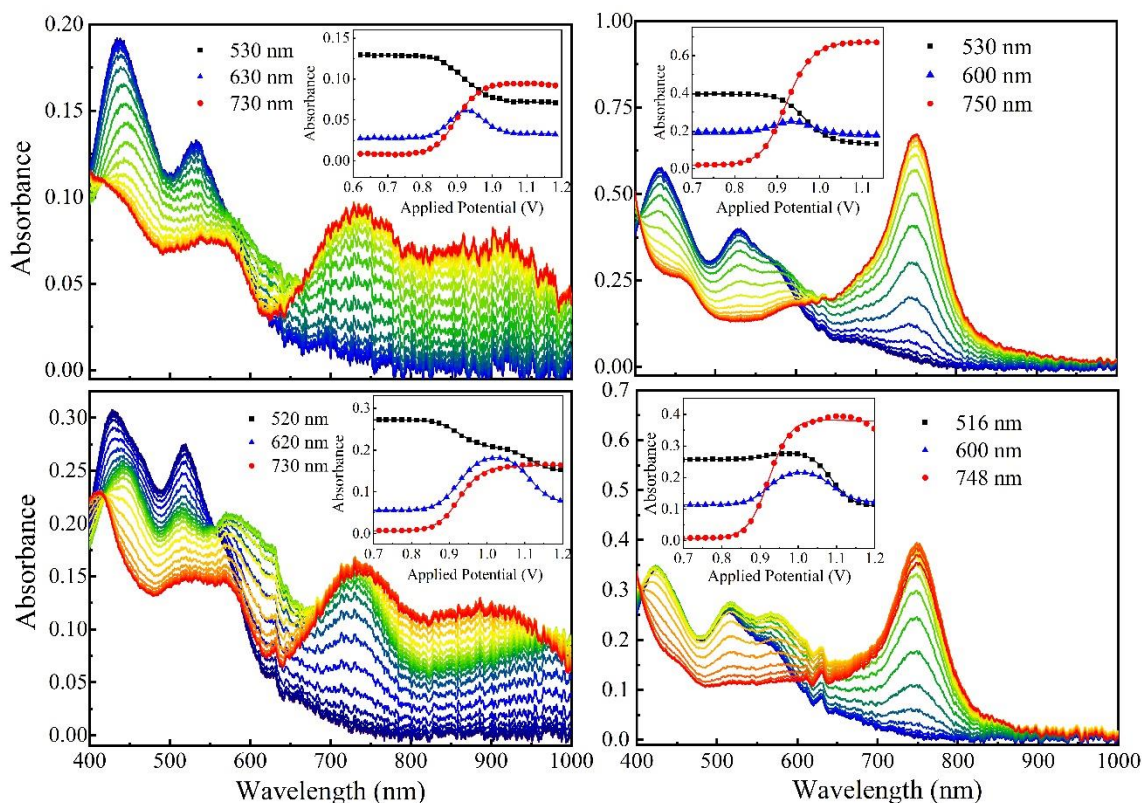


Figure 2.2. Representative spectroelectrochemical data for **1pE** (upper left), **2pE** (lower left), **1xE** (upper right) and **2xE** (lower right) in CH₃CN containing 0.1M LiClO₄. Insets show single wavelength absorption changes as a function of applied potential, and all applied potentials are reported vs. NHE.

The carboxylate derivatized compounds were anchored to mesoporous nITO thin films and the Ru^{III/II} and TPA⁺⁰ formal reduction potentials for **1pC/nITO**, **2pC/nITO**, **1xC/nITO**, and **2xC/nITO** were obtained through UV-Vis-NIR spectroelectrochemistry in a similar fashion as described above, and are shown in Figure 2.3. Similar solution-phase experiments were not possible for the carboxylate compounds due to limited solubility in CH₃CN. At applied potentials between +750 and +1100 mV, large absorption changes were observed throughout the visible and NIR regions, indicative of multiple redox events that occurred nearly simultaneously. Indeed, in many cases the growth of TPA⁺ at 750 nm was coincident with the bleach of Ru^{II} at ~500 nm. Upon application of potentials beyond +1150 mV vs. NHE, the TPA⁺ feature was observed to decrease which indicated an additional oxidation

event, presumably the second oxidation of the TPA moiety. Representative spectroelectrochemical data is shown in Figure 3 for **1p_C** (left) and **2p_C** (right). The corresponding data for **1x_C** and **2x_C** in the mixed valent state did not show appreciable absorption features indicative of electronic coupling, as discussed later. The reduction potentials, non-ideality factors, and electrochemical splitting are given in Table 2.1.

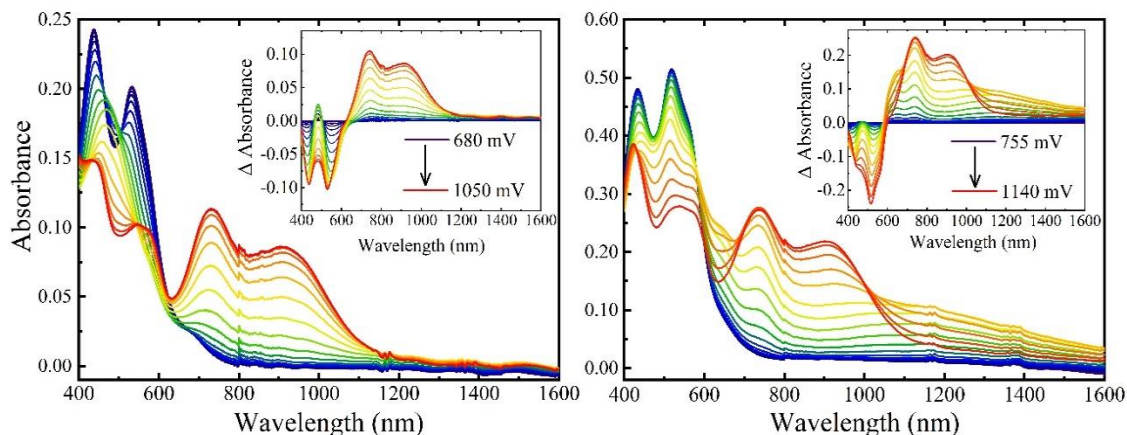


Figure 2.3. Spectroelectrochemical oxidation of **1p_C/nITO** (left) and **2p_C/nITO** (right). Insets show difference spectra taken relative to 0 mV of applied potential. Applied potentials are vs. NHE.

Formal reduction potentials were measured at the point of potential when equal concentrations of the reduced, [Red], and oxidized, [Ox], species were present. A modified Nernst equation was used to model changes in absorbance at single wavelengths corresponding to each redox event, Equation 1, where R is the gas constant and F is Faraday's constant.³⁸ In all cases, a non-ideality factor, α , was necessary to model the spectroelectrochemical data, $\alpha > 1$.

$$E = E_{1/2} - \frac{\alpha RT}{nF} \ln \left(\frac{[\text{Red}]}{[\text{Ox}]} \right) \quad (1)$$

In all cases, α was larger for compounds immobilized on nITO compared to the solution counterparts which represents deviations from Nernstian 59 mV steps to achieve a factor of ten change in concentration, as discussed later. However, in general, the modeled changes in

TPA⁺⁰ absorption features were more Nernstian than was the Ru^{III/II} redox chemistry.³⁹

Accurate modelling of the IVCT bands was difficult due to overlapping absorption features, small difference between Ru^{III/II} and TPA⁺⁰ reduction potentials, $\Delta E \sim 80$ mV, and non-ideal electrochemistry. A small electrochemical window existed where appreciable concentrations of the mixed valent forms were spectroscopically detectable, as predicted by the comproportionation constants, K_c , in Table 2.1 and defined in Eq 2.⁴⁰⁻⁴¹ In essence, K_c describes the relative thermodynamic stabilization of the one-electron oxidized mixed valent state relative to the ground state and doubly-oxidized state of the compounds, equation 2b.

$$K_c = \frac{nF}{RT} \exp(\Delta E) \quad (2a)$$

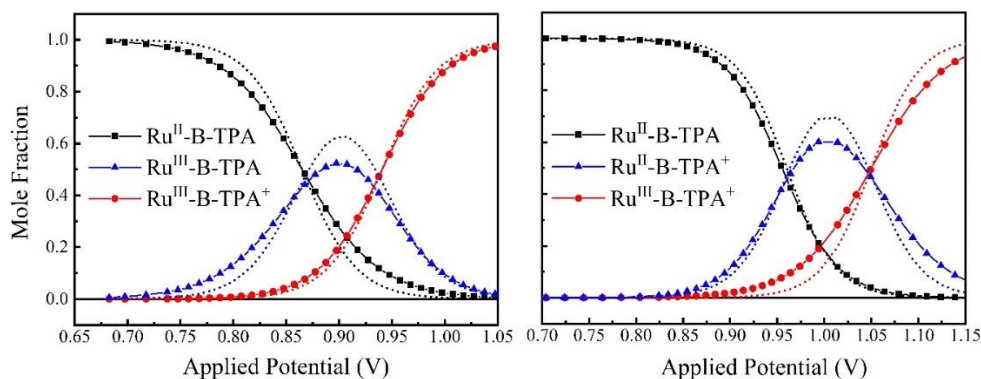
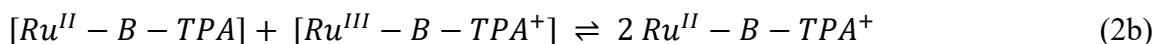


Figure 2.4. Plots of mole fractions for 1p_C/nITO (left) and 2p_C/nITO (right) in the ground, Ru^{II}-B-TPA (black), doubly-oxidized, Ru^{III}-B-TPA⁺ (red), and one-electron oxidized states (blue), as a function of applied electrochemical potential, where B represents the phenyl-thiophene bridge. The dashed lines represent the mole fractions for ideal ($\alpha = 1$) Nernstian behavior.

Figure 2.4 shows the mole fractions of the ground state and the singly-, and doubly-oxidized states as a function of applied potential. Without comproportionation corrections the concentration of the mixed valent state would be underestimated based on the assumption that all of the molecules were in a one-electron oxidized state. For example, before

comproportionation corrections, the extinction coefficient for the IVCT band in **2pc/nITO** was found to be $\epsilon_{\text{max}} = 7.5 \times 10^3 \text{ M}^{-1} \text{ cm}^{-1}$, yet increased by nearly 45% to $\epsilon_{\text{max}} = 10.8 \times 10^3 \text{ M}^{-1} \text{ cm}^{-1}$ after accounting for the true mixed valent compound concentration due to comproportionation and non-Nernstian electrochemistry. This is evident in Figure 4 as the mixed valent state (blue triangles) represents only 50% of the total number of molecules on the surface. This analysis also revealed that the transition observed at 480 nm had a larger extinction coefficient after correction, $\epsilon_{\text{max}} = 29.8 \times 10^3 \text{ M}^{-1} \text{ cm}^{-1}$, than the value, $\epsilon_{\text{max}} = 25 \times 10^3 \text{ M}^{-1} \text{ cm}^{-1}$, initially measured by the uncorrected spectra. Figure 5 shows the experimentally observed spectra for **1pc/nITO** and **2pc/nITO** after one-electron oxidation, as well as the spectrum corrected for comproportionation chemistry.

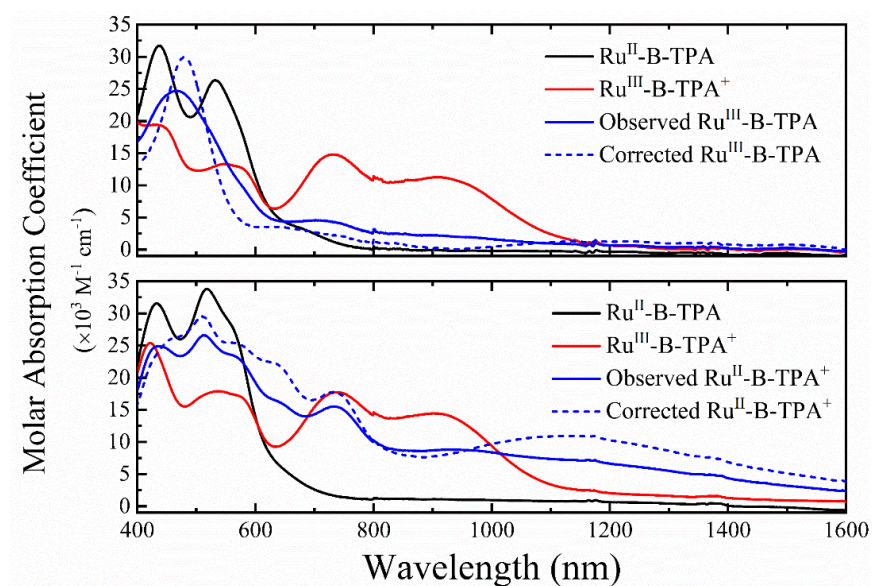


Figure 2.5. Absorption spectra of **1pc/nITO** (top) and **2pc/nITO** (bottom) in their ground (black), one-electron oxidized (blue), and two-electron oxidized (red) states. The dashed blue line represents the comproportionation correction in the mixed valent state from spectral modeling which reveals intense IVCT-type transitions at 450 nm for **1pc/nITO** and 1100 nm for **2pc/nITO**.

2.3 Discussion

The ground state, one-, and two-electron oxidized states of eight donor acceptor compounds of the type Ru^{II}-B-TPA with a phenyl- or xylyl-bridge were quantified in fluid solution and anchored to metal oxide thin films, Figures 2.2 and 2.3. These compounds were previously used for applications in dye-sensitized solar cells: the MLCT excited states quantitatively injected electrons into TiO₂ and subsequent hole transfer through the xylyl bridge to the TPA inhibited recombination with the injected electron. Interestingly, there was no kinetic advantage with respect to charge recombination for the phenyl bridged compounds.³² To minimize free energy losses associated with the hole transfer reaction, the Ru^{III/II} and TPA⁺⁰ reduction potentials were nearly the same and for these compounds, $|E_{1/2}(\text{Ru}^{\text{III/II}}) - E_{1/2}(\text{TPA}^{+/0})| \leq 180$ mV. Upon one-electron oxidation of Ru^{II}, electron transfer would, in principle, originate from the electron-rich TPA donor and occur to the electron deficient Ru^{III} center. However, the opposite was true when TPA⁺ was electrochemically generated prior to Ru^{II} oxidation. Hence the experimental approach used herein allowed optical electron transfer to be explored in opposite directions through the same bridge.

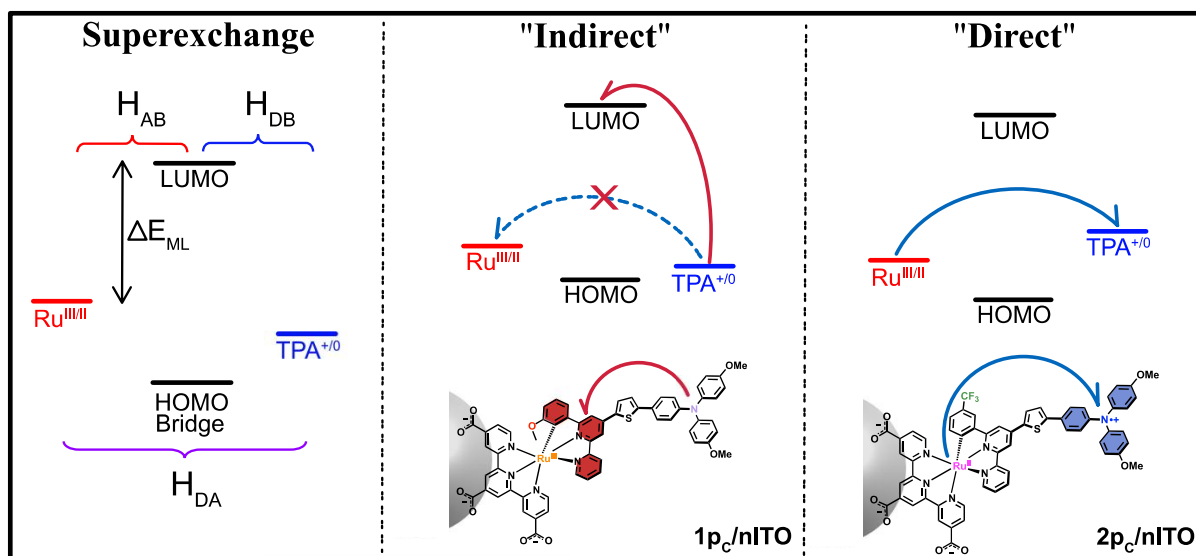
One would reasonably expect similar low-energy transitions regardless of the direction for symmetric compounds. Indeed, the most striking observation in the absorption spectra of the mixed valent compounds was the appearance of a low energy IVCT transition, $\lambda_{\text{max}} \sim 1000$ nm for Ru^{II}-B-TPA⁺ (**2p**c/nITO), that was substantially less pronounced for the opposite mixed valent state, Ru^{III}-B-TPA (**1p**c/nITO). Instead the mixed valent form of **1p**c/nITO displayed an intense absorption near 480 nm. However, the absorption spectra of the ground- and fully oxidized states were nearly identical spectroscopically. A low-energy IVCT transition is characteristic of *direct* electron transfer between the two redox active sites.²⁷ In contrast the higher energy visible absorption band is most consistent with TPA to

cyclometalating ligand charge transfer.⁴²⁻⁴³ Here the optical excitation proceeds from TPA-centered orbitals to an unoccupied high energy cyclometalating ligand orbital, implying *indirect* charge transfer. A depiction of the alternative pathways is provided in Scheme 2.1. An important point arises in distinguishing ‘direct’ and ‘indirect’ pathways which correspond to optical charge transfer transitions rather than thermal electron transfer reactions. Regardless, analysis of the mixed valent absorptions with a 2-state model provided very different electronic coupling parameters, as discussed further below.

In order to further understand the influence of different optical pathways on the electronic coupling, a common 2-state model was utilized to characterize the electronic coupling, H_{DA} , between Ru^{II} and TPA. The analysis indicated that H_{DA} was significantly different between these two discrete pathways. That is, that the electronic coupling seemed to depend on the electron transfer direction due to changes in the orbitals accessed during light absorption.

In addition to the two-state model, a 3-state superexchange model was also used. This model portions the *direct* coupling between Ru^{II} and TPA, H_{DA} , into step-wise electronic coupling elements between the Ru^{II} and bridge (H_{AB}) as well as the TPA and the bridge (H_{DB}), Scheme 2.3. The 3-state superexchange analysis revealed that the Ru^{II} /TPA coupling was pathway independent. Remarkably, even though the orbitals accessed during the optical charge transfer were found to ultimately depend on the electron transfer direction, H_{DA} was found to be independent of the direction. Evidence of these pathways and the electronic couplings responsible for them are described further below beginning first with the electrochemical properties of the compounds.

Scheme 2.3. Representation of superexchange theory for bridge-mediated electron transfer (left) as well as for the ‘indirect’ electron transfer pathway when Ru^{II} is oxidized prior to TPA (middle) and the ‘direct’ pathway when TPA is oxidized first (right).



2.3.1 Electrochemistry

Figure 2.6 provides a visual representation of the reduction potentials determined from spectroelectrochemical experiments. The $\text{Ru}^{\text{III/II}}$ reduction potentials were significantly (~ 100 mV) more negative when anchored to the oxide surface than in fluid solution. Such behavior has previously been reported and emanates from the inductive influence of the electron withdrawing ester groups relative to the carboxylates present on the oxide surface.³⁸ Interestingly, the $E_{1/2}(\text{TPA}^{+/0})$ potentials were nearly insensitive to substituents on the terpyridine ligand while the phenyl-bridged compounds showed a marked 75 mV positive shift. Such behavior is consistent with a through-bond inductive effect transmitted through the conjugated phenyl-bridge. An important lesson from these comparative studies is that the surface anchoring groups can in themselves alter interfacial energetics. A clear example is **1p_E**, where the TPA was oxidized first in solution while the Ru^{II} is oxidized first when anchored to the oxide, Figure 7. Such a redox ‘switch’ would not have been recognized if the

solution behavior of the ester (and presumably the carboxylic acid) were assumed to be the same as that for the carboxylate form present on the oxide surface.

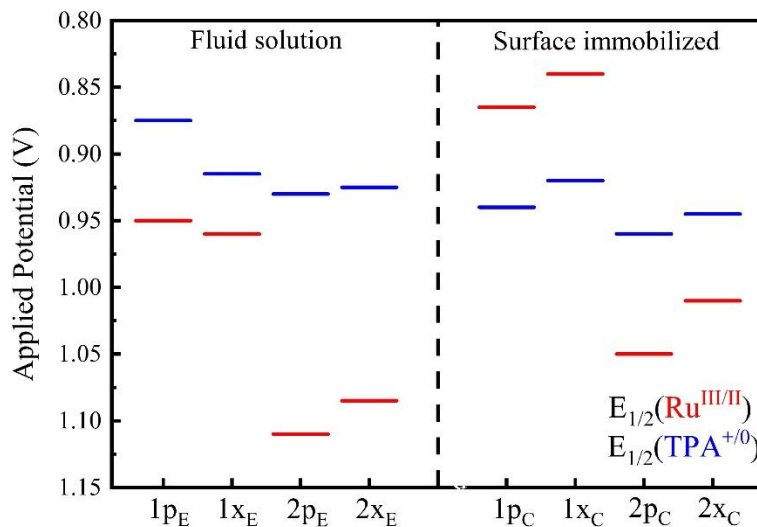


Figure 2.6. Representation of $E_{1/2}(\text{Ru}^{\text{III/II}})$ (red) and $E_{1/2}(\text{TPA}^{+/0})$ (blue) for the 8 compounds in fluid acetonitrile solution and immobilized nITO.

A subtler influence of the oxide surface was found in the non-Nernstian redox chemistry. In prior studies on TiO_2 , it was found that a much larger potential step was required to induce a factor of ten change in concentration of the $\text{Ru}^{\text{III}}/\text{Ru}^{\text{II}}$ ratio relative to that for TPA^+/TPA .³⁹ Both required more than the 59 mV predicted by the Nernst equation for a one-electron transfer process at room temperature. This behavior was attributed to an electric field effect wherein charges at the oxide interface create fields that influence the proximate Ru center to a greater degree than the more distant TPA.⁴⁴⁻⁴⁵ Similar effects of this type have been demonstrated for porphyrazines immobilized onto gold, where the first reduction potential was increased by $\sim +400$ mV based on proximity to the surface.⁴⁶ The present case was attributed to an electric field effect, rather than an inductive effect, as the non-ideality factor was insensitive to the coupling provided by the bridging ligand.⁴⁷ Small, but measurable,

deviations from Nernstian behavior were quantified for the ester derivatives in fluid acetonitrile electrolyte.

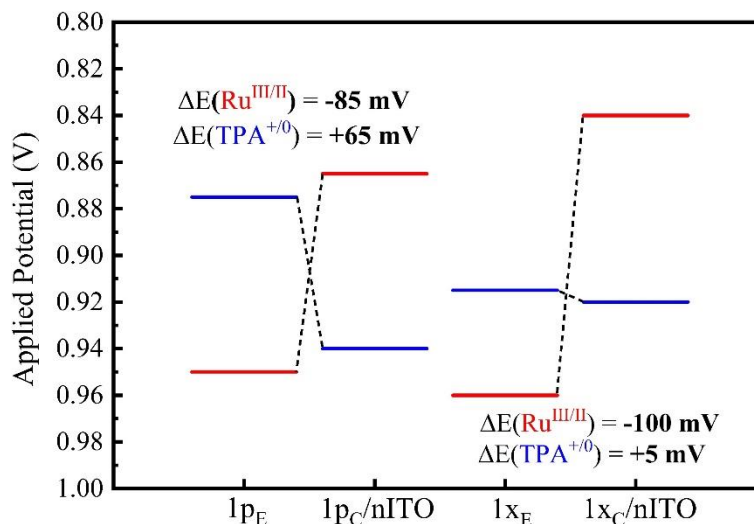


Figure 2.7. Redox potential switch upon surface immobilization for **1p_E** and **1p_C/nITO** as well as **1x_E** and **1x_C/nITO**. The dashed lines connecting the redox potentials are guides to the eye.

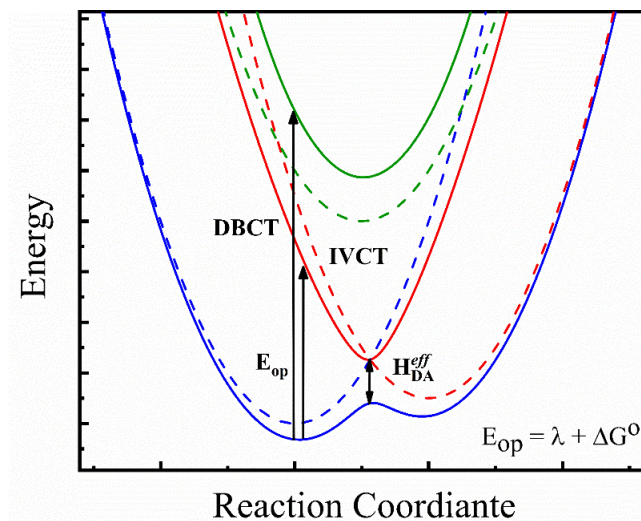
2.3.2 Mulliken Hush H_{DA} Calculations

The IVCT absorption band has traditionally been used to determine the strength of orbital interactions between the ‘donor’ and ‘acceptor’ potential energy surfaces along a reaction coordinate. The magnitude of H_{DA} was calculated using the semi-classical theory of Mulliken and Hush, Equation 3. Here the macroscopic parameters of the IVCT transition, namely the full-width at half-max $\Delta\nu_{1/2}$ (cm^{-1}), molar absorption coefficient at the absorbance maximum, ϵ_{max} , transition energy E_{op} (cm^{-1}), as well as the distance between centers, r , allows for direct calculation of coupling matrix elements.⁴⁸ Spectral deconvolution and subsequent least-squares analysis with multiple Gaussian functions afforded band parameters and successfully minimized the influence of overlapping absorption bands that would otherwise have overestimated the FWHM and ϵ_{max} values of the IVCT transition.

$$H_{DA} = \frac{0.0206}{r} \sqrt{E_{op} \epsilon_{max} \Delta v_{1/2}} \quad (3)$$

Constructing one-dimensional approximations of the potential energy surfaces for the product and reactant states presents a powerful tool to visualize electronic transitions arising as a result of mixed valent redox states. Scheme 3 represents a 3-state model, discussed in more detail below, and represents the reactant (blue), product (red), and bridge (green) states in the absence (dashed) and presence (solid) of electronic coupling, H_{DA} .⁴² Experimentally, $E_{op} = \Delta G^\circ + \lambda$, where ΔG° is the standard free energy change and λ is the reorganization energy. Unlike the 2-state model, where the splitting between the product and reactants surfaces is $2H_{DA}$, in a 3-state model this difference corresponds to H_{DA} . Energetically high-lying bridge states mediate electronic coupling between the energy surfaces through donor-bridge charge transfer (DBCT) transition, with electronic coupling H_{DB} .

Scheme 2.4. Potential energy surface diagram for 3-state optical electron transfer.^a



^aDBCT (donor-to-bridge charge transfer) corresponds to the high energy TPA \rightarrow ligand or generic metal-to-ligand charge transfer transition. IVCT (intervalence charge transfer) corresponds to a low energy transition between TPA and Ru^{III} . Effective coupling, H_{DA}^{eff} arises from mixing between all three surfaces which enables the optical transitions to be observed.

The calculation of H_{DA} by Eq. 3 requires an estimate of the charge transfer distance, r , which was assumed to be the geometric distance between the Ru^{II} metal center and central nitrogen atom of the TPA group. Electronic coupling calculated by this method presents a lower-limit of the coupling.⁴⁹⁻⁵¹ A distance of 14 Å and 13 Å for ‘direct’ and ‘indirect’ electron transfer was garnered from density functional theory optimized structures, respectively.

These analyses yielded values of H_{DA} on the order of 950 cm^{-1} for **2pc**/nITO. In the case of **1pc**/nITO, the higher energy IVCT type band gave $H_{DB} \sim 2500\text{ cm}^{-1}$. We emphasize that the calculated coupling for **1pc**/nITO represents TPA to cyclometalating ligand coupling, Scheme 2.2. A crude estimate of H_{DA} was possible for the low energy transition observed in the mixed valent spectrum **1pc**/nITO in the near-IR, $\epsilon_{max} \sim 1300\text{ M}^{-1}\text{ cm}^{-1}$, and gave $H_{DA} \leq 250\text{ cm}^{-1}$. As a control experiment, the magnitude of H_{DA} was determined in a similar way for the compounds in fluid solution by oxidation with $Cu(ClO_4)_2$ and are presented in Table 2.2 with spectra provided in Figure 2.8. Both **1pe** and **2pe** had similar spectral signatures to that of **2pc**/nITO with IVCT bands appearing $\sim 1000\text{ nm}$, with $H_{DA} \approx 950\text{ cm}^{-1}$. By contrast the x-series compounds did not display any indication of IVCT transitions at concentrations used herein, and H_{DA} was estimated to be $< 100\text{ cm}^{-1}$.³² Additionally, while K_c values have been reported to correlate strongly with electronic coupling, careful analysis has provided evidence that this approach is not always applicable.⁵²⁻⁵³

Table 2.2. Tabulated values of IVCT band parameters and the associated electronic coupling matrix elements.

Compound	E_{OP} (nm), (ϵ , $\times 10^3$ M cm $^{-1}$) ^b	$\Delta\nu_{1/2}$ (cm $^{-1}$) ^c	H_{DA} (cm $^{-1}$) ^e	H_{DB} (cm $^{-1}$)
1p ^E ^a	1025 (9.0)	4480	920 ^c	-
2p ^E ^a	1000 (11.4)	4080	1000 ^c	-
1pC/nITO	480 (29.8)	4000	-	2500 ^d
2pC/nITO	1110 (10.5)	4460	950 ^c	-

^aMeasured by chemical oxidation with Cu(II). ^bDetermined from spectral modeling after correcting for comproportionation. ^cCalculated for direct IVCT from the low-energy bands. ^dElectronic coupling between the TPA center and the cyclometalating ligand, H_{DB} . ^eFrom deconvoluted spectral analysis.

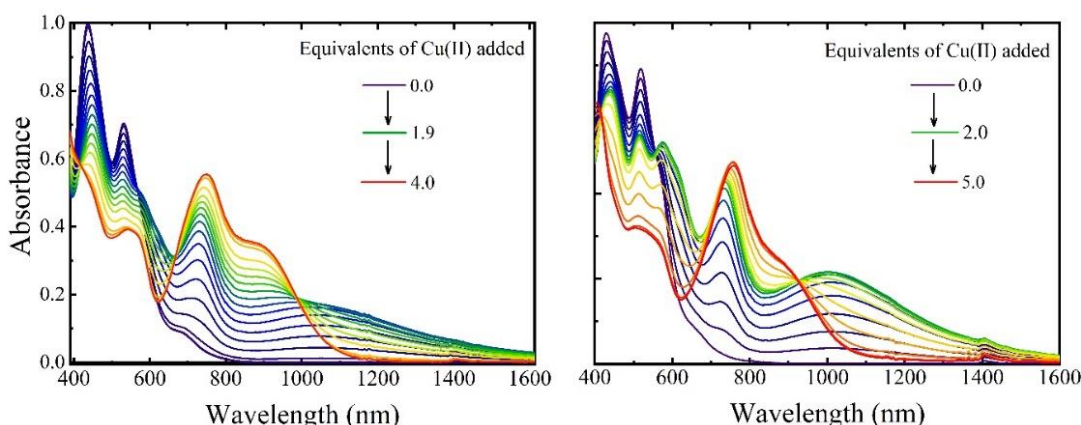
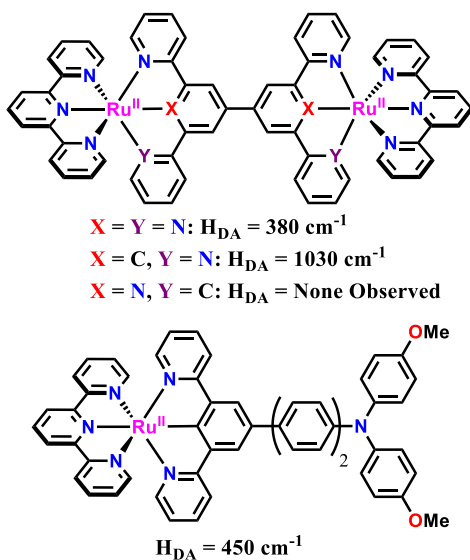


Figure 2.8. UV-Vis-NIR absorption spectra of **1pE** (left) and **2pE** (right) in neat CH₃CN with Cu(II) titrated in as a chemical oxidant. Note the appearance of low energy IVCT transitions at ~1000 nm for both compounds.

The calculated electronic coupling values presented in Table 2.2 for phenyl-bridged compounds that undergo direct ET are among the highest reported for this class of compounds.⁵⁴⁻⁵⁶ It is worthwhile to place the studied compounds in the context of other bis-tridentate Ru^{II} compounds with similar cyclometalating motifs to briefly address what factors contribute to the strong electronic interactions. Sauvage and others have shown that electronic coupling between centers was enhanced when the N atom of the central pyridine ring in 2,2',2''-terpyridine was replaced with a carbon atom, 2.5.⁵⁷⁻⁵⁹ However, when a *peripheral* nitrogen was replaced with a carbon atom, there was no evidence for coupling between the metal centers. Other investigations of Ru^{II}-B-TPA compounds, where B = phenyl, has also shown appreciable coupling on the order of $H_{DA} \sim 450$ cm $^{-1}$.⁶⁰⁻⁶¹ In this regard, it is surprising

that electronic coupling is strong in the present compounds, $H_{DA} \sim 1000 \text{ cm}^{-1}$, considering that the Ru-C bond is in a peripheral position. This highlights the importance of thiophene as an effective mediator of electronic coupling, which has recently garnered much experimental interest.^{35, 62-64}

Scheme 2.5. Previously reported cyclometalated Ru^{II} mixed-valent compounds with the corresponding values of H_{DA} . Taken from ref. 46-48 and 52.



2.3.3 Superexchange H_{DA} Calculations

The McConnell relationship for superexchange has been widely invoked for many cases of long range electron transfer where the redox orbitals are degenerate in energy; an energetic situation that holds approximately for these compounds.⁶⁵⁻⁶⁶ When ET is mediated by the high-lying bridge LUMO transiently, the electronic coupling, H_{DA} , can be calculated through Equation 4 as derived by Ratner and co-workers.^{67,68}

$$H_{DA} = \frac{H_{DB}H_{BA}}{E - E_B} \quad (4)$$

This expression treats the electronic coupling between the donor and acceptor sites as the product of multi-site, or stepwise, electronic coupling elements between the donor and the bridge, H_{DB} , and between the bridge and the acceptor, H_{BA} .⁶⁹⁻⁷⁰ The quantity $E-E_B$ corresponds to the energy separation between the donor or acceptor, E , and the bridging ligand, E_B , and is frequently referred to as the tunneling energy gap.⁷¹⁻⁷³ It is difficult to measure experimentally, but can be related to the redox potentials of the individual donor, bridge, and, acceptor units.⁷⁴

For optical investigations of moderately coupled mixed valent charge transfer compounds where the bridge orbitals mediate ET, the Creutz, Newton, and Sutin model depicted in Scheme 3 provides the *effective* coupling through Equation 5.⁴⁸ The same methodology was used for the phenyl bridged compounds studied herein.

$$H_{DA}^{eff} = \frac{H_{AB}H_{DB}}{2\Delta E_{ML}} \quad (5)$$

In this expression the term ΔE_{ML} refers to the difference between the metal and bridge states and is given by Equation 6,

$$\frac{1}{\Delta E_{ML}} = \frac{1}{2} \left(\frac{1}{\Delta E_{MLCT}} + \frac{1}{\Delta E_{MLCT} - \Delta E_{IVCT}} \right) \quad (6)$$

where ΔE_{MLCT} and ΔE_{IVCT} are the spectroscopically observed energies for the metal to cyclometalating ligand and the IVCT energy, respectively.²⁶ Note the factor of 2 in Equation 6 arises from degeneracy factor for symmetric compounds and is not necessary in this analysis. Similar approaches often approximate this factor as differences in free energy or ionization potentials.⁷⁵⁻⁷⁶ Unfortunately, the measurement of electrochemical redox potentials of cyclometalating ligands often result in irreversible electrochemistry. Onset reduction potentials typically begin at -1.9 V vs. NHE.^{36, 77}

The value of ΔE_{IVCT} is readily available from the compounds that exhibit direct IVCT and is $\sim 10^3 \text{ cm}^{-1}$. Inspection of the UV-Vis provides the value of ΔE_{MLCT} for Ru to the cyclometalating ligand, $\lambda_{\text{max}} = 23.5 \times 10^3 \text{ cm}^{-1}$ (425 nm), which was observed at higher energy relative to Ru to terpyridine MLCT, $\sim 520 \text{ nm}$, presumably due to the electron rich nature of the covalent Ru-C bond.²⁹ From these values ΔE_{ML} was found to be 2.2 eV. Electronic coupling between the metal and the ligand, H_{AB} , was calculated from Equation 5 with typical linewidths for polypyridyl MLCT transitions, $\Delta\nu_{1/2} = 4000 \text{ cm}^{-1}$ and common values for metal-ligand coupling values, H_{AB} , range from $3\text{-}6 \times 10^3 \text{ cm}^{-1}$ for Ru^{II} to bipyridyl MLCT transitions.⁴⁸ This analysis provided $H_{AB} = 8400 \text{ cm}^{-1}$, such a large degree of coupling is startling, but is not unreasonable considering that strong σ -donating and π -back bonding effects are operative for a covalent Ru-C bond. The magnitude of H_{DB} is provided in Table 2 for **1pc/nITO**.

With all the necessary quantities in hand, the effective coupling for $\text{TPA} \rightarrow \text{Ru}^{\text{III}}$ ET was calculated, $H_{DA}^{\text{eff}} = 1200 \text{ cm}^{-1}$, which is likely an upper limit for the coupling arising from underestimating ΔE_{ML} and/or overestimating H_{AB} . However, the value calculated here is consistent with the results of Creutz, Newton, and Sutin.⁴⁸ A critical experimental detail that indicates an alternative optical pathway may be operative is the absence of an appreciable low energy transition for **1pc/nITO** relative to **2pc/nITO**, Figure 5. Indeed, since the coupling is large, $H_{DA}^{\text{eff}} = 1200 \text{ cm}^{-1}$, then the appearance of a low-energy transition would be expected under the experimental conditions. Phrased differently this raises an interesting question: Why is a low-energy transition absent in **1pc/nITO** despite having a comparable effective electronic coupling? This is likely the result of the alternative orbital pathway that proceeds virtually through the ligand LUMO in superexchange interaction.

In addressing the alternative pathway it is likely that the bridge previously defined as phenyl-thiophene is influenced by the electron donating/withdrawing ability of the -OCH₃ or -CF₃ substituents on the cyclometalating ring. Qualitatively, one would expect the donating nature of the -OCH₃ to destabilize the bridge LUMO relative to -CF₃.⁷⁸ Therefore, the tunneling energy gap, ($E-E_b$, equation 3) should be larger for **1pC**/nITO and thus less contribution from a superexchange pathway would be expected. This is contrary to experiment where the indirect path was operative for electron transfer. Therefore, it seems that inductive effect of the two groups does not appear to be significant.

From this analysis, an important distinction exists for optical *versus* thermal electron transfer. In thermal electron transfer processes, the tunneling energy gap represents the energetic difference between the donor or acceptor orbitals and the bridge HOMO or LUMO at the transition state of the reaction.⁷⁹ On the other hand, mixing between states during optical ET necessarily occurs between high-lying unoccupied bridge orbitals while the system is in the nuclear geometry of the ground state. In principle, the bridge-centered HOMO also contributes to the total superexchange interaction, though it is difficult to quantify the impact without spectroscopic handles such as ligand to metal charge transfer transitions.⁷⁰ Indeed, cyclometalation of the Ru^{II} center moves the energy of the bridge HOMO closer to that of the Ru^{III/II} state, which provides access to more energetically favorable thermal pathways whereas for optical transitions a LUMO-mediated superexchange mechanism is most prominent.^{32, 56,}

⁸⁰ Thus, thermal and optical electron transfer occur through very different mechanisms.

2.4 Conclusions

The electrochemical redox potentials and spectroscopic features of eight cyclometalated Ru^{II} compounds immobilized on a surface and in fluid solution were reported. Electrochemical

experiments indicated that ΔG° between the two centers was small enough to enable interchange of the molecular HOMO between Ru^{II} and TPA. Upon one-electron oxidation, appreciable amounts of the mixed valent state were formed. Compounds containing a phenyl bridge displayed intense IVCT transitions that were absent for the xylyl-bridged compounds. The electronic coupling between the Ru^{II} and TPA redox active centers was determined using a combination of Mulliken-Hush and a 3-state superexchange-type analysis.

This analysis indicated that modifying the direction of electron transfer in model donor-bridge-acceptor compounds with an identical molecular bridge can provide access to different orbital transitions that may facilitate electron transfer. Such orbital pathways are evident in the steady-state electronic spectra of the one-electron oxidized forms of the conjugated phenyl-bridged compounds. Intense IVCT transitions provided direct approaches to measuring and characterizing the electronic coupling between the Ru^{II} and TPA redox centers. Use of a 2-state model, indicated that the electronic coupling between the Ru^{II} and TPA centers ultimately depended on the direction, *i.e.* what orbitals the transition originated from. However, the use of a 3-state model indicated that electronic coupling was independent of the charge transfer direction.

The origins of the different spectral features can be qualitatively understood through the molecular orbitals and electron densities. Each redox state possesses significantly different orbital character between the Ru^{II} d-orbitals and nitrogen sp^3 orbitals. To a first approximation, the Ru^{II} d π orbitals mix significantly with the cyclometalating ligand π^* orbitals and this degree of mixing is expected to decrease dramatically when the Ru^{II} is oxidized to Ru^{III} . By comparison, the amine orbitals are not as diffuse and upon oxidation of TPA, direct charge transfer from Ru^{II} occurs to the empty orbitals of the TPA unit because of the large electron

density associated with the Ru^{II} and the corresponding cyclometalating ligand states. In the opposite case, the absence of electron density in the Ru^{III} d π orbitals cannot be accessed directly by the TPA electron density which results in a charge transfer pathway that more easily proceeds from the amine to the cyclometalating ligand proximal to the Ru^{III} center.

A systematic study of 8 Ru^{II}-B-TPA compounds both in solution and anchored onto a conductive surface was carried out. Spectroscopic and electrochemical experiments revealed that, following one-electron oxidation, charge transfer proceeded in different directions across a common bridge. This study demonstrated that electronic coupling between the two redox active centers is independent of which center is oxidized first. This was accomplished through explicit inclusion of high energy bridge-centered orbitals. Taken together, these observations present a fundamental contribution to the study of hybrid inorganic/organic materials that have potential applications in energy conversion or storage, or as electrochromic materials.

2.5 Experimental methods

2.5.1 Thin films and sensitization

Colloidal nITO was prepared by previously published literature methods and deposited onto 1-cm wide optically transparent F doped SnO₂ glass slides *via* doctor blading. The resulting films were usually 3 μ m thick. The newly deposited films were annealed following the procedure of Farnum *et. al.* to yield oxidized nITO, which appeared pale yellow to the unaided eye.⁸¹ Films were sensitized by immersion in stock solutions of a carboxylate derivative of one of the compounds in neat methanol for 10-20 minutes. The resulting thin films had peak absorbance values of 0.6 or lower in their electronic ground states over the range of wavelengths measured.

2.5.2 Spectroscopic characterization

UV-Visible absorption spectra were measured using a Varian Cary 60 spectrometer in a 1 cm path length cuvette. The molar extinction coefficients for the ester derivatives were determined in neat acetonitrile. However, the carboxylic acid derivatives were not soluble in acetonitrile and only sparingly soluble in neat methanol. To completely dissolve the compounds, 1 equivalent of ~1.5 M tetrabutylammonium hydroxide (TBAOH) in water was added to the methanol solution. In a typical experiment, stock solutions of 25 mL were prepared with 1 equivalent of base which was approximately 0.5 μ L of the stock TBAOH solution, except for 1pC, which required 5 μ L. The resulting change in volume was considered negligible.

2.5.3 Solution spectroelectrochemistry

Formal reduction potentials in bulk solution were determined in CH_3CN containing 100 mM LiClO_4 as the supporting electrolyte in a standard 3-electrode set up. The working electrode was a Pt honeycomb microelectrode with a Pt counter (Pine Research Instruments), and a nonaqueous pseudo Ag/AgCl reference electrode. The half-wave potential of the $\text{Fc}(+/0)$ was measured in 100 mM LiClO_4 in CH_3CN both before and after the experiment to account for potential drift.. The pseudo-reference electrode was externally referenced to NHE by using the measured value of the $\text{Fc}(+/0)$ redox couple and adding a standard value of +630 mV.⁸² Spectra were collected using a Avantes AvaLight DHc light source with an Avantes StarLine AvaSpec-2048 UV/Vis spectrometer while the electrochemical potential was applied using a Pine Wavenow potentiostat. All of the devices were controlled by Aftermath software (Pine Research Instruments).

The resulting potential-dependent spectra were analyzed by subtracting the ground-state spectrum of the molecule at each applied potential, resulting in so-called “difference spectra”. The difference spectra, which represented changes due to the applied potentials, displayed positive values of absorbance indicative of feature growth and negative values of absorbance which indicate ground-state bleaching. Single wavelength data were selected at maxima of growths and bleaches, isosbestic points, and intermediate wavelengths and fit to the Nernst equation to give the formal reduction potential of each oxidation event.

2.5.4 Surface spectroelectrochemistry

UV/Vis/NIR spectroelectrochemistry of the carboxylate substituted molecules anchored onto thin films of nITO on FTO slides were monitored using a Varian Cary 5000 spectrometer while simultaneously applying a potential. The slides were immersed in 100 mM LiClO₄/CH₃CN solutions at a 45° angle in a 1 cm path length cuvette at low surface coverages. Electrochemical potentials were applied by a BASi epsilon potentiostat using the EClipse software in a standard 3-electrode arrangement. In the experiments, the FTO glass served as the working electrode with a Pt gauze counter and a Ag/AgCl pseudo-reference electrode. Potentials were applied stepwise on the order of 10-20 mV/step and held for a minimum of 15 seconds before a scan was taken to ensure electrochemical equilibrium, after which data were recorded. Spectra were recorded until changes were minimized. The same methodology to standardize the applied potentials was used as previously stated. The Cary 5000 was operated in the standard dual beam set up with reduced slit height, fixed slit-band widths, and a grating and detector changeover at 850 nm. Notably, a “spectral discontinuity” was occasionally observed during the experiment, which is not uncommon, and was corrected for by adjusting the appropriate slit-band widths. Background spectra collected

from 350 nm to a minimum of 1700 nm were of bare FTO and solvent to account for the NIR absorbance of CH₃CN. Measuring beyond 2000 nm was not possible due to intense cuvette absorption. Separate background spectra of nITO were recorded due to its behavior as a function of applied bias.

2.5.5 Chemical oxidation

Redox titrations of **1p_e** and **2p_e** were performed on ester derivatives in neat acetonitrile using Cu(ClO₄)₂•6H₂O as the sacrificial oxidant in the form of the Cu(II/I) redox couple.⁸³⁻⁸⁴ In all experiments, a stock solution of 0.6 mM Cu(ClO₄)₂ was used. Aliquots of 20 μL were added to a 1 cm path length cuvette containing 3.0 mL of ~1 μM ester compound with a Hamilton syringe and carefully stirred to ensure equilibrium was established. Spectra were recorded using a Varian Cary 5000 spectrometer, in a similar fashion described as above, until subsequent spectral changes were negligible. The resulting spectra were corrected as a function of total volume over the course of the titration.

2.6 Acknowledgements

This material is based upon work solely supported as part of the UNC EFRC: Center for Solar Fuels, an Energy Frontier Research Center funded by the U.S. Department of Energy, Office of Science, Office of Basic Energy Sciences under Award Number DE-SC0001011. L. T.-G. acknowledges personal fellowships from the Belgian American Educational Foundation (BAEF) as well as the Bourse d'Excellence Wallonie-Bruxelles (WBI.World). The authors thank Tyler C. Motley for helpful discussions.

2.7 Additional content

2.7.1 Chemical oxidation

Solution phase oxidation was performed in CH_3CN . A common chemical oxidant, $\text{Cu}(\text{ClO}_4)_2 \cdot 6\text{H}_2\text{O}$, was used which has been previously shown to result in oxidation of TPA-type compounds with no observable chemical side reactions or appreciable amounts of visible light absorption at the concentrations used herein.^{83, 85} The formal reduction potential of the $\text{Cu}(\text{II/I})$ redox couple was previously measured to be 1.33 V vs. NHE in acetonitrile, which was sufficiently positive of the $\text{TPA}^{+/0}$ and $\text{Ru}^{\text{III/II}}$ redox potentials determined electrochemically.⁸⁴ In all experiments, a stock solution of 0.6 mM $\text{Cu}(\text{ClO}_4)_2$ was used. Aliquots of 20 μL were added using to a 1 cm path length cuvette containing 3.0 mL of $\sim 1 \mu\text{M}$ ester compound with a Hamilton syringe and carefully stirred to ensure equilibrium was established. Spectra were recorded using a Varian Cary 5000 spectrometer until subsequent spectral changes were negligible. Difference spectra are given in Figure S1. The same approach was not possible for 1x_E or 2x_E due to exceptionally slow equilibration after addition of $\text{Cu}(\text{II})$. In either case, the spectral data observed were extremely similar to what was observed electrochemically. Additionally, the $\text{Cu}(\text{II/I})$ redox couple did not achieve the same result in CH_3OH .

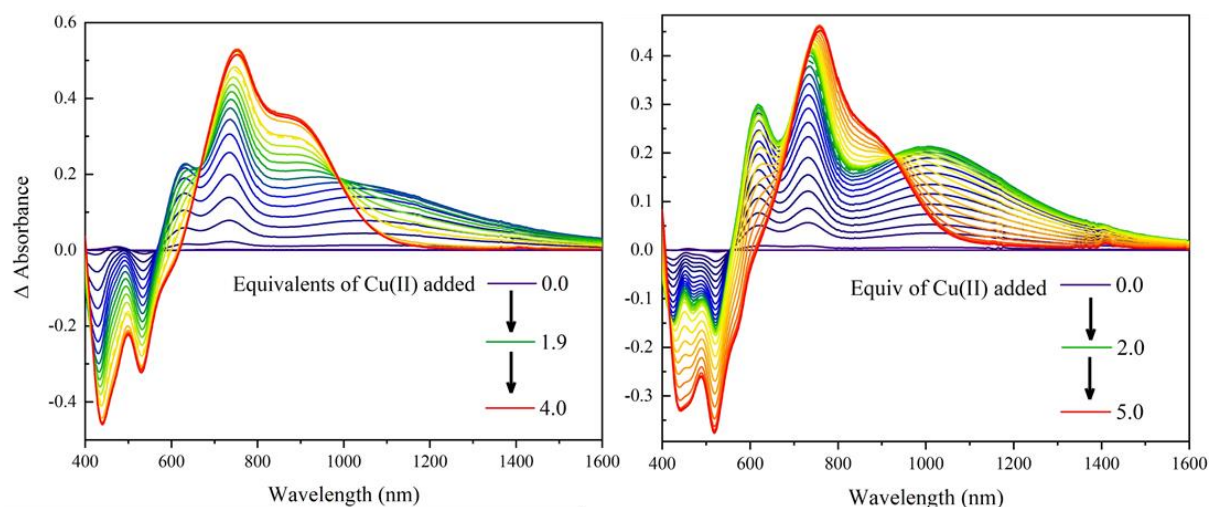


Figure 2.9. Difference spectra of **1pE** (left) and **2pE** (right) as a function of added equivalents of Cu(II).

2.7.2 Accounting for comproportionation

The analysis of mixed-valent (MV) spectra has been discussed by D'Alessandro and Keene wherein they presented a “check-list” of factors to consider. This included (1) accounting for comproportionation chemistry, (2) full spectral deconvolution to isolate the IVCT band, and (3) taking advantage of the statistical moments of the band. Herein, the approach outlined by D'Alessandro and Keene was used to analyze the data for the studies in fluid solution and on a surface.⁴¹

The concentration of molecules in the MV state for a general redox equilibrium is given by the comproportionation constant, K_c , Equation 6.

$$K_c = \exp \left(\left(\Delta E_{1/2}(\text{Ru(III/II)}) - \Delta E_{1/2}(\text{TPA(+ / 0)}) \right) \frac{nF}{RT} \right) \quad (6)$$

Here, $\Delta E_{1/2}$ refers to the measured formal reduction potentials of $\text{Ru}^{\text{III/II}}$ and $\text{TPA}^{+/0}$, F is Faraday's constant, R is the ideal gas constant and T is the absolute temperature. The electrochemically determined values for K_c are given in Tables 2.1.

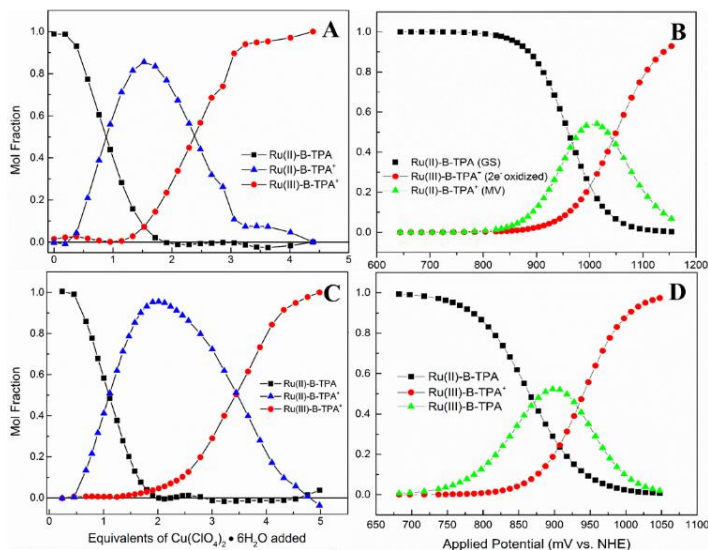


Figure 2.10. Plots of mole fractions of each species as a function of added Cu(II) for **1pE** (A) and **2pE** (C), and as a function of applied potential for **1pc/nITO** (B) and **2pc/nITO** (D).

The proportion of molecules in the MV state scales as $\sqrt{K_c}/(2 + \sqrt{K_c})$, and represents the theoretical limit.⁴¹ Using the values of the redox potentials garnered from electrochemistry, it was found that the fraction of molecules in MV state is 91% and 95% for **1pE** and **2pE**, respectively. The same analysis for the surface anchored compounds yielded 65% and 75% for **1pc/nITO** and **2pc/nITO**. Experimental results that deconvolute the mol fractions of the ground-, one-, and two-electron oxidized forms of the molecules from chemical and electrochemical oxidation are presented in Figure S2.

Two approaches were necessary to model the spectra in fluid solution and immobilized on nITO. In solution, the isosbestic points present during the titration were utilized, while for the surface a modified Nernst equation was employed. The results of the solution model indicated good agreement with theory, where it was found spectroscopically that 86% and

95% of molecules were in the MV state for **1p_E** and **2p_E**. We focused mainly on the immobilized molecules where the Nernst equation can predict the mole fraction of each species present over a range of applied potentials with Eq. 7.

$$\chi = \frac{1}{1 + 10^{\frac{E_{app} - E_{1/2}}{59\alpha}}} \quad (7)$$

Here, χ is the mole fraction, E_{app} is the applied potential, and $E_{1/2}$ and α retain their original identities. Applying this equation to the one-electron and two-electron oxidized species at appropriate applied potentials gave the fraction of species in the MV state. Alarming, this analysis indicated that just 52% for **1pc/nITO** and 60% for **2pc/nITO** of molecules were in the MV state at the electrochemical mid-point between the Ru(III/II) and TPA(^{•+}/0) redox potentials. This collective analysis highlights the importance of comprotonation when quantitatively evaluating MV spectra. This analysis resulted in quantifying the extinction coefficients of the low-energy IVCT bands following both chemical and electrochemical oxidation. Note that for **2pc/nITO**, the absorbance at low surface concentrations was most likely uncorrected potential dependant absorbance of the nITO thin films. This effect was eventually dominated by one-electron oxidation and the transition to the two-electron oxidized

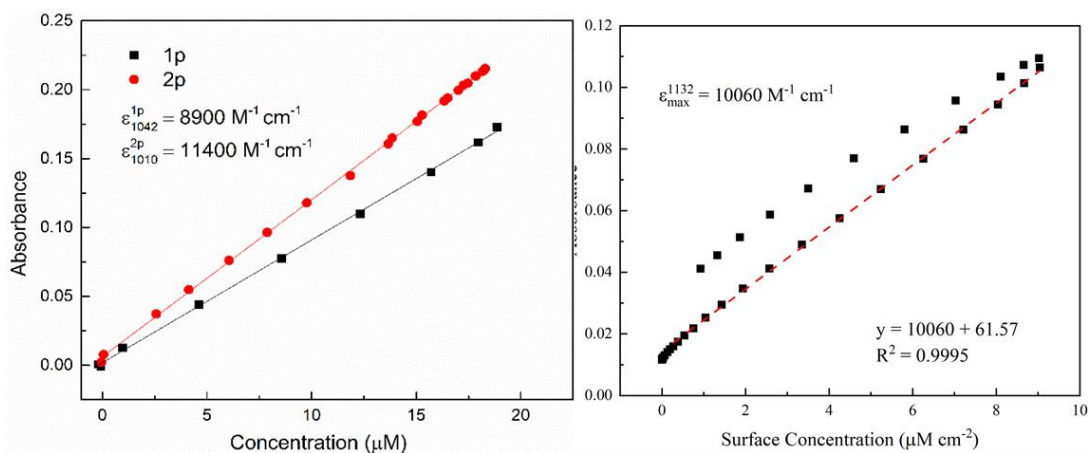


Figure 2.11. Measured extinction coefficients after accounting for comproportionation for **1p_E** and **2p_E** (left) and **2p_C/nITO** (right).

state is also observed when the absorbance begins to decrease. Figure 2.11 shows the Beer's law analysis to extract the extinction coefficients for the IVCT transition.

2.7.3 Deconvolution of the mixed-valent spectrum

The mixed-valent spectrum for each specie was fit to a sum of Gaussian peaks with care taken so as to not over-parametrize the fitting function. In most cases, the spectra were fit satisfactorily with less than 7 Gaussian peaks spanning 400 and 1600 nm. We note that the peaks did not necessarily correspond to discrete transitions except in the case of the IVCT band, and were instead used to ensure minimization of error in the properties of the IVCT transition, as it was often difficult to quantitatively analyze peaks between 400-800 nm due to many overlapping transitions as the true character of the transitions are heavily mixed due to

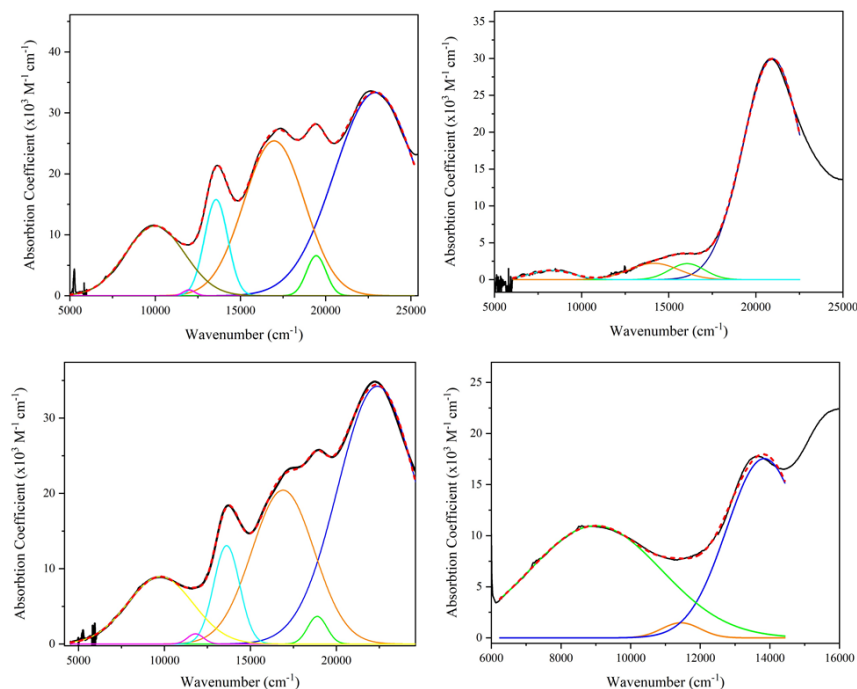


Figure 2.12. Deconvoluted spectra of **1pE** (top left), **1pc/nITO** (top right), **2pE** (bottom left), and **2pc/nITO** (bottom right). Dashed red lines indicate the cumulative spectra of all Gaussian bands needed to fit the spectrum adequately.

strong orbital interactions between the metal orbitals and cyclometalating ligand through the Ru-C bond.

Table 2.3. Parameters of the IVCT bands used to calculate H_{DA} .

	1pE	2pE	1pc/nITO	2pc/nITO
y_0	0	0	0	0
E_{op} (cm ⁻¹)	9760	9998	20952	8995
FWHM (cm ⁻¹)	4477	4077	4011	4456
Area	4.26×10^7	4.98×10^7	1.28×10^8	$5.2e \times 10^7$

2.7.4 Reconstructing the mixed-valent spectrum

Each oxidation state had spectral features that allowed for independent measurement of their relative concentrations. Using mole fractions of these species allowed the spectrum of the MV state to be reconstructed using equation 8.

$$A(x) = a(x)S_1 + b(x)S_2 + c(x)S_3 \quad (8)$$

Here, the coefficients a , b , and c represent the mole fractions at a particular applied potential or equivalent of Cu(II) (x), and S_1 , S_2 , and S_3 represent the discrete absorption spectra of the ground state, and the one- and two-electron oxidized states, respectively. By using the observed absorption spectrum at any point, $A(x)$, the ground state spectrum, S_1 , and doubly oxidized state spectrum, S_3 , the spectrum of S_2 was calculated and treated with a traditional Beer-Lambert Law analysis to extract the extinction coefficients. Note that in order to quantitatively analyze the coefficients for the immobilized molecules, the concentration was instead cast as the surface coverage, Γ (mol/cm²), which is related to the absorbance through $A = 1000\Gamma\epsilon$.^{38, 86} In the case of **1pc/nITO**, the low energy band is likely an artefact stemming from uncorrected near IR absorption of nITO.

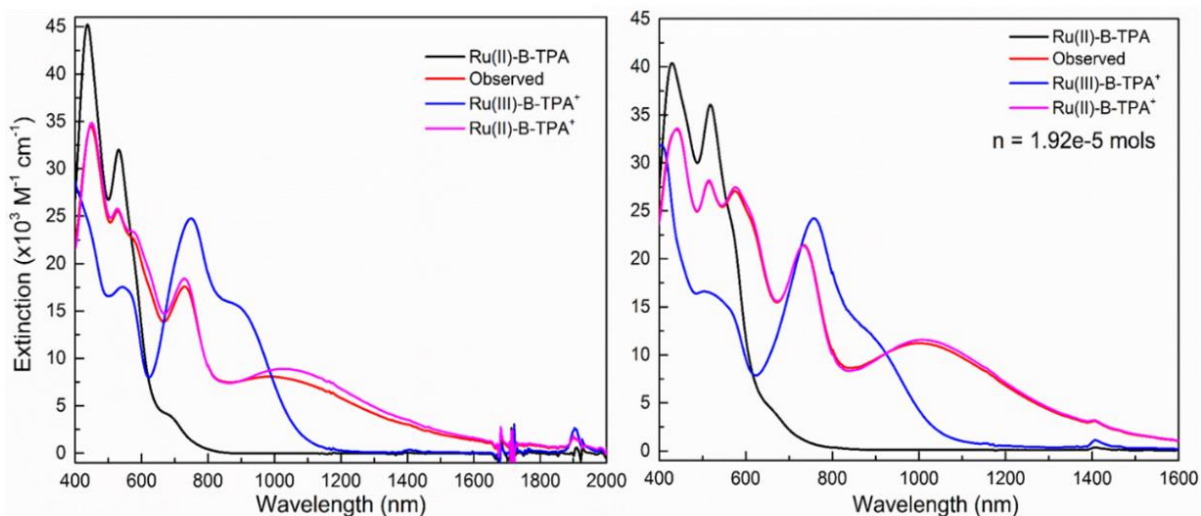


Figure 2.13. Comparison of **1pE** (left) and **2pE** (right) spectra after being corrected for comproportionation. Note the large difference from similar spectra in the main text for **1pc/nITO** and **2pc/nITO**.

2.7.5 Result of comproportionation correction and electrochemical modeling

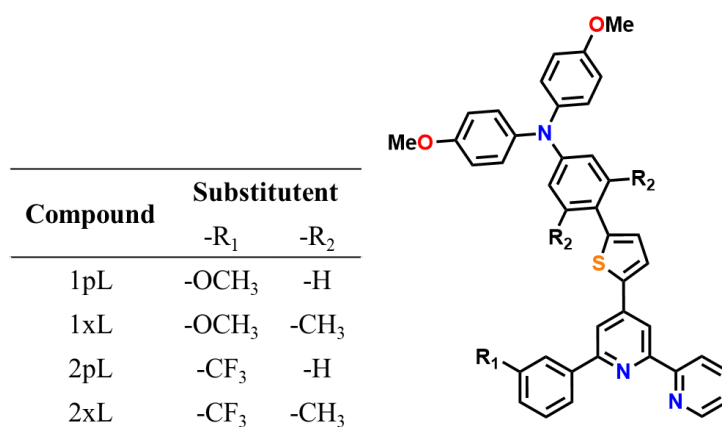
After accounting for comproportionation and reconstructing the spectrum of the MV, the solution-phase studies were only marginally affected, Figure 2.13. On the other hand, correction of the immobilized spectra revealed broad spectral features that were small in the

raw experimental data, mainly beyond 800 nm in the NIR region, Figure 6 in the main text. The results here again highlight the power and necessity of proper comproportionation considerations when analyzing spectral changes associated with redox chemistry of surface bound molecules. Without proper treatment, results taken at face-value may be subject to unexpected errors.

2.7.6 Assignment of the TPA to cyclometalating ligand charge transfer transition

In order to assign the origin of the high energy intraligand charge transfer transitions (ILCT), spectroelectrochemical experiments were carried out on the free ligands, shown in Scheme 2.6, in CH₃CN containing 0.1M LiClO₄.

Scheme 2.6. Structures of the ligands prior to coordination to Ru^{II}.



The results of the spectroelectrochemical experiments are shown in Figure 2.14. The ground state spectra of **1xL** and **2xL** were similar, with intense transitions observed at 300 nm with $\epsilon = 47,000$ and $45,000 \text{ M}^{-1} \text{ cm}^{-1}$, respectively. No other appreciable features were observed beyond 400 nm. For **1pL** and **2pL**, the extinction coefficients decreased at 300 nm to $35,000 \text{ M}^{-1} \text{ cm}^{-1}$ and $22,000 \text{ M}^{-1} \text{ cm}^{-1}$, respectively. Additionally, a transition was observed at 410 nm in both cases. This transition was initially assigned as the TPA to cyclometalating ligand

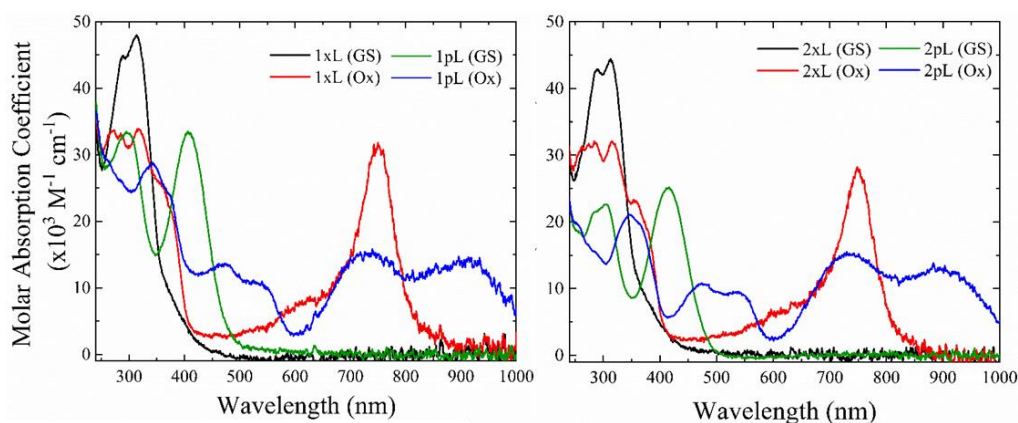


Figure 2.14. Spectra of the free ligands in 0.1M LiClO₄/CH₃CN. (Left) Ligands containing a methoxy substituent that most closely resemble the **1-series**. The green and black lines are ground-state spectra while the red and blue lines are oxidized by one electron. (right) ligands containing a CF₃ substituent that mimic the **2-series**. The green and black lines are ground-state spectra while the blue and red are one-electron oxidized.

transition. Indeed, the origin of TPA-centered ILCT transitions is well understood through considering the electron density of the TPA unit. Similar transitions have been observed, and assigned as ILCTs, for Ru^{II}-B-TPA³⁹ compounds in addition to other organometallic complexes.⁸⁷⁻⁹⁰

One-electron oxidation of the ligands resulted in broad spectral changes, including the appearance of transitions consistent with the TPA⁺ cation (see text). In the phenyl-bridged cases, the 410 nm transition was observed to decrease and was absent in the oxidized state. The disappearance of the 410 nm transition, along with the concurrent appearance of TPA⁺ transitions beyond 600 nm, was consistent with those seen for **1p_c/nITO** and **2p_c/nITO**. In the absence of the Ru^{II} center, this observation is in line with the assignment of a charge transfer transition that originates from TPA-centered molecular orbitals. Contrastingly, the xylyl-bridged ligands showed markedly different characteristic TPA⁺ features that indicate decreased conjugation across the ligand (*i.e.* a decrease in electronic coupling). Surface immobilized compounds of **1x** and **2x** (**1x_c/nITO** and **2x_c/nITO**) displayed similar characteristics.

Comparing the one-electron oxidized form of **1p_c/nITO** to **1pL**, Figure 2.15, aided in the assignment of a superexchange-type analysis that utilized the high-energy cyclometalating ligand orbitals.

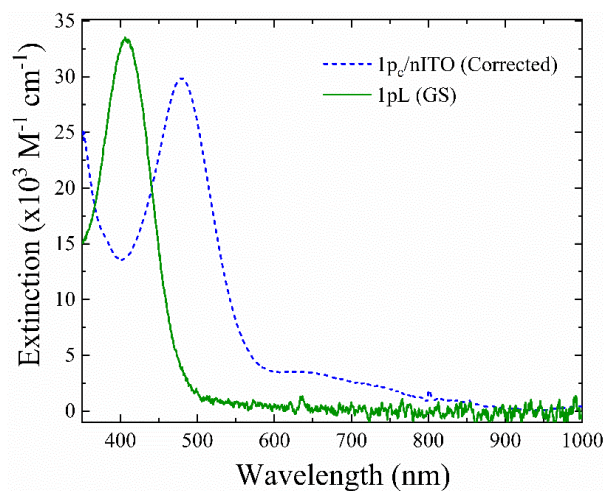


Figure 2.15. Comparison of ground-state spectra of **1pL** (green) and one-electron oxidized **1p_c/nITO** (dashed blue line).

Briefly, the as-assigned ILCT in **1p_c/nITO** was red shifted by 0.48 eV relative to **1pL** in solution. The observed decrease in optical transition energy is most readily explained as an inductive effect resulting from the oxidation of Ru^{II} to Ru^{III}, as the carbene bond contains mixes the metal and ligand based orbitals. As a result, the ligand LUMO energy decreases and the TPA → cyclometalating ligand transition energy decreases concurrently which represents a shift in the ILCT transition from the ground-state to the one-electron oxidized state.

2.7.7 Spectroelectrochemical data of the x-series

Control experiments were performed on **1x_c/nITO** and **2x_c/nITO** in CH₃CN containing 0.1M LiClO₄ electrolyte. The pertinent results of these experiments are the absence of low- and high-energy transitions following one-electron oxidation. These data indicate that in this series of compounds there is no significant electronic coupling and, hence, the spectra represent additive spectra of the Ru^{II} and TPA center independently. It was apparent that the electronic

coupling was diminished as a result of changing the bridge from phenyl-thiophene to xylyl-thiophene. Figure 2.16 shows the experimental data.

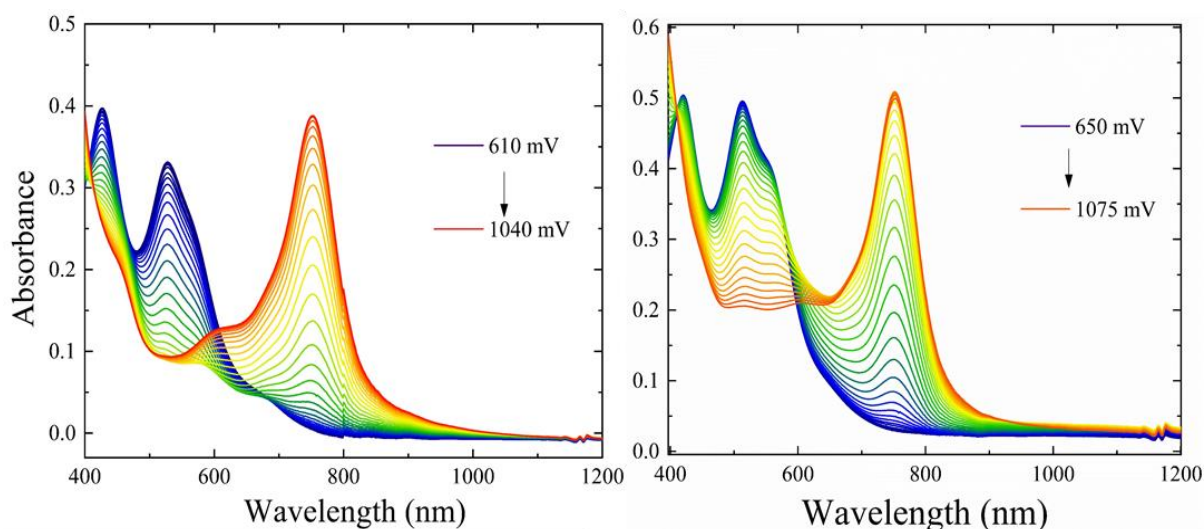


Figure 2.16. Spectroelectrochemical data of **1x**_C/nITO (left) and **2x**_C/nITO (right) in 0.1M LiClO₄/CH₃CN.

2.7.8 Synthesis of the studied compounds

All molecules were synthesized by following published literature procedures.^{32-33, 39} In general, the yields were increased by 20-30% after employing freeze-pump-thaw techniques to degas reaction mixtures. Characterization of the products following each step matched the previously reported spectral characteristics. Solvents and starting reagents were commercially available and were used as received.

REFERENCES

1. Mas-Torrent, M.; Rovira, C.; Veciana, J., Surface-confined electroactive molecules for multistate charge storage information. *Adv. Mater.* **2013**, *25* (3), 462-468.
2. Mortimer, R. J., Electrochromic materials. *Chem. Soc. Rev.* **1997**, *26* (3), 147-156.
3. Browne, W. R.; Feringa, B. L., Light switching of molecules on surfaces. *Annu. Rev. Phys. Chem.* **2009**, *60* (1), 407-428.
4. Wu, Z.; Cui, P.; Zhang, G.; Luo, Y.; Jiang, J., Self-adaptive switch enabling complete charge separation in molecular-based optoelectronic conversion. *J. Phys. Chem. Lett.* **2018**, *9* (4), 837-843.
5. He, B.; Wenger, O. S., Photoswitchable organic mixed valence in dithienylcyclopentene systems with tertiary amine redox centers. *J. Am. Chem. Soc.* **2011**, *133* (42), 17027-17036.
6. Murase, R.; Leong, C. F.; D'Alessandro, D. M., Mixed valency as a strategy for achieving charge delocalization in semiconducting and conducting framework materials. *Inorg. Chem.* **2017**, *56* (23), 14373-14382.
7. Magri, D. C.; Brown, G. J.; McClean, G. D.; de Silva, A. P., Communicating chemical congregation: A molecular and logic gate with three chemical inputs as a “lab-on-a-molecule” prototype. *J. Am. Chem. Soc.* **2006**, *128* (15), 4950-4951.
8. de Silva, A. P.; Gunaratne, H. Q. N.; McCoy, C. P., Molecular photoionic and logic gates with bright fluorescence and “off-on” digital action. *J. Am. Chem. Soc.* **1997**, *119* (33), 7891-7892.
9. Cui, B.-B.; Zhong, Y.-W.; Yao, J., Three-state near-infrared electrochromism at the molecular scale. *J. Am. Chem. Soc.* **2015**, *137* (12), 4058-4061.
10. Chen, H.-Y.; Ardo, S., Direct observation of sequential oxidations of a titania-bound molecular proxy catalyst generated through illumination of molecular sensitizers. *Nature Chemistry* **2017**, *10*, 17-23.
11. Troian-Gautier, L.; DiMarco, B. N.; Sampaio, R. N.; Marquard, S. L.; Meyer, G. J., Evidence that $\delta s_{\frac{1}{2}}$ controls interfacial electron transfer dynamics from anatase TiO_2 to molecular acceptors. *J. Am. Chem. Soc.* **2018**, *140* (8), 3019-3029.
12. Khoudiakov, M.; Parise, A. R.; Brunschwig, B. S., Interfacial electron transfer in $\text{Fe}(\text{CN})_6^{4-}$ -sensitized TiO_2 nanoparticles: A study of direct charge injection by electroabsorption spectroscopy. *J. Am. Chem. Soc.* **2003**, *125* (15), 4637-4642.
13. Yang, M.; Thompson, D. W.; Meyer, G. J., Charge-transfer studies of iron cyano compounds bound to nanocrystalline TiO_2 surfaces. *Inorg. Chem.* **2002**, *41* (5), 1254-1262.

14. Alibabaei, L.; Brennaman, M. K.; Norris, M. R.; Kalanyan, B.; Song, W.; Losego, M. D.; Concepcion, J. J.; Binstead, R. A.; Parsons, G. N.; Meyer, T. J., Solar water splitting in a molecular photoelectrochemical cell. *Proc. Natl. Acad. Sci. U.S.A.* **2013**, *110* (50), 20008-20013.
15. Robson, K. C. D.; Koivisto, B. D.; Gordon, T. J.; Baumgartner, T.; Berlinguette, C. P., Triphenylamine-modified ruthenium(ii) terpyridine complexes: Enhancement of light absorption by conjugated bridging motifs. *Inorg. Chem.* **2010**, *49* (12), 5335-5337.
16. Kreitner, C.; Mengel, A. K. C.; Lee, T. K.; Cho, W.; Char, K.; Kang, Y. S.; Heinze, K., Strongly coupled cyclometalated ruthenium triarylamine chromophores as sensitizers for dsscs. *Chem. Eur. J* **2016**, *22* (26), 8915-8928.
17. Ding, Y.; Jiang, Y.; Zhang, W.; Zhang, L.; Lu, X.; Wang, Q.; Zhou, G.; Liu, J.-m.; Kempa, K.; Gao, J., Influence of heterocyclic spacer and end substitution on hole transporting properties based on triphenylamine derivatives: Theoretical investigation. *J. Phys. Chem. C* **2017**, *121* (31), 16731-16738.
18. Spettel, K. E.; Damrauer, N. H., Exploiting conformational dynamics of structurally tuned aryl-substituted terpyridyl ruthenium(ii) complexes to inhibit charge recombination in dye-sensitized solar cells. *J. Phys. Chem. C* **2016**, *120* (20), 10815-10829.
19. Benniston, A. C.; Harriman, A., Charge on the move: How electron-transfer dynamics depend on molecular conformation. *Chem. Soc. Rev.* **2006**, *35* (2), 169-179.
20. Kennedy, S. R.; Goyal, P.; Kozar, M. N.; Yennawar, H. P.; Hammes-Schiffer, S.; Lear, B. J., Effect of protonation upon electronic coupling in the mixed valence and mixed protonated complex, [ni(2,3-pyrazinedithiol)2]. *Inorg. Chem.* **2016**, *55* (4), 1433-1445.
21. Tang, J.-H.; Wu, S.-H.; Shao, J.-Y.; Nie, H.-J.; Zhong, Y.-W., Ruthenium-amine electronic coupling bridged through phen-1,3-diyl versus phen-1,4-diyl: Reverse of the charge transfer direction. *Organometallics* **2013**, *32* (16), 4564-4570.
22. Harriman, A.; Heitz, V.; Sauvage, J. P., Pathways for photoinduced electron transfer within a mixed-metal bisporphyrin. *J. Phys. Chem.* **1993**, *97* (22), 5940-5946.
23. Cailliez, F.; Müller, P.; Firmino, T.; Pernot, P.; de la Lande, A., Energetics of photoinduced charge migration within the tryptophan tetrad of an animal (6–4) photolyase. *J. Am. Chem. Soc.* **2016**, *138* (6), 1904-1915.
24. Hush, N. S., Intervalence-transfer absorption. Part 2. Theoretical considerations and spectroscopic data. In *Progress in inorganic chemistry*, John Wiley & Sons, Inc.: 2007; pp 391-444.
25. Creutz, C.; Taube, H., Direct approach to measuring the franck-condon barrier to electron transfer between metal ions. *J. Am. Chem. Soc.* **1969**, *91* (14), 3988-3989.

26. Brunschwig, B. S.; Sutin, N., Energy surfaces, reorganization energies, and coupling elements in electron transfer. *Coord. Chem. Rev.* **1999**, *187* (1), 233-254.
27. Brunschwig, B. S.; Creutz, C.; Sutin, N., Optical transitions of symmetrical mixed-valence systems in the class ii-iii transition regime. *Chem. Soc. Rev.* **2002**, *31* (3), 168-184.
28. Evans, C. E. B.; Naklicki, M. L.; Rezvani, A. R.; White, C. A.; Kondratiev, V. V.; Crutchley, R. J., An investigation of superexchange in dinuclear mixed-valence ruthenium complexes. *J. Am. Chem. Soc.* **1998**, *120* (50), 13096-13103.
29. Robson, K. C. D.; Koivisto, B. D.; Yella, A.; Spornova, B.; Nazeeruddin, M. K.; Baumgartner, T.; Grätzel, M.; Berlinguette, C. P., Design and development of functionalized cyclometalated ruthenium chromophores for light-harvesting applications. *Inorg. Chem.* **2011**, *50* (12), 5494-5508.
30. Malagoli, M.; Brédas, J. L., Density functional theory study of the geometric structure and energetics of triphenylamine-based hole-transporting molecules. *Chem. Phys. Lett.* **2000**, *327* (1-2), 13-17.
31. Ellis, H.; Schmidt, I.; Hagfeldt, A.; Wittstock, G.; Boschloo, G., Influence of dye architecture of triphenylamine based organic dyes on the kinetics in dye-sensitized solar cells. *J. Phys. Chem. C* **2015**, *119* (38), 21775-21783.
32. Hu, K.; Blair, A. D.; Piechota, E. J.; Schauer, P. A.; Sampaio, R. N.; Parlane, F. G. L.; Meyer, G. J.; Berlinguette, C. P., Kinetic pathway for interfacial electron transfer from a semiconductor to a molecule. *Nat. Chem.* **2016**, *8* (9), 853-859.
33. Robson, K. C. D.; Spornova, B.; Koivisto, B. D.; Schott, E.; Brown, D. G.; Berlinguette, C. P., Systematic modulation of a bichromic cyclometalated ruthenium(ii) scaffold bearing a redox-active triphenylamine constituent. *Inorg. Chem.* **2011**, *50* (13), 6019-6028.
34. Kreitner, C.; Heinze, K., Excited state decay of cyclometalated polypyridine ruthenium complexes: Insight from theory and experiment. *Dalton Trans.* **2016**, *45* (35), 13631-13647.
35. Koivisto, B. D.; Robson, K. C. D.; Berlinguette, C. P., Systematic manipulation of the light-harvesting properties for tridentate cyclometalated ruthenium(ii) complexes. *Inorg. Chem.* **2009**, *48* (20), 9644-9652.
36. Wadman, S. H.; Lutz, M.; Tooke, D. M.; Spek, A. L.; Hartl, F.; Havenith, R. W. A.; van Klink, G. P. M.; van Koten, G., Consequences of n,c,n'- and c,n,n'-coordination modes on electronic and photophysical properties of cyclometalated aryl ruthenium(ii) complexes. *Inorg. Chem.* **2009**, *48* (5), 1887-1900.
37. Amthor, S.; Noller, B.; Lambert, C., Uv/vis/nir spectral properties of triarylamines and their corresponding radical cations. *Chem. Phys.* **2005**, *316* (1-3), 141-152.

38. Ardo, S.; Achey, D.; Morris, A. J.; Abrahamsson, M.; Meyer, G. J., Non-nernstian two-electron transfer photocatalysis at metalloporphyrin–tio₂ interfaces. *J. Am. Chem. Soc.* **2011**, *133* (41), 16572-16580.
39. Hu, K.; Robson, K. C. D.; Beauvilliers, E. E.; Schott, E.; Zarate, X.; Arratia-Perez, R.; Berlinguette, C. P.; Meyer, G. J., Intramolecular and lateral intermolecular hole transfer at the sensitized tio₂ interface. *J. Am. Chem. Soc.* **2014**, *136* (3), 1034-1046.
40. Sutton, J. E.; Sutton, P. M.; Taube, H., Determination of the comproportionation constant for a weakly coupled mixed-valence system by titration of the intervalence transfer band: .Mu.-(4,4'-bipyridyl)-bis(pentaammineruthenium)(5+). *Inorg. Chem.* **1979**, *18* (4), 1017-1021.
41. D'Alessandro, D. M.; Keene, F. R., Current trends and future challenges in the experimental, theoretical and computational analysis of intervalence charge transfer (ivct) transitions. *Chem. Soc. Rev.* **2006**, *35* (5), 424-440.
42. Kubiak, C. P., Inorganic electron transfer: Sharpening a fuzzy border in mixed valency and extending mixed valency across supramolecular systems. *Inorg. Chem.* **2013**, *52* (10), 5663-5676.
43. Lambert, C.; Noll, G.; Schelter, J., Bridge-mediated hopping or superexchange electron-transfer processes in bis(triarylamine) systems. *Nat. Mater.* **2002**, *1* (1), 69-73.
44. Zaban, A.; Ferrere, S.; Gregg, B. A., Relative energetics at the semiconductor/sensitizing dye/electrolyte interface. *J. Phys. Chem. B* **1998**, *102* (2), 452-460.
45. Yang, W.; Vlachopoulos, N.; Boschloo, G., Impact of local electric fields on charge-transfer processes at the tio₂/dye/electrolyte interface. *ACS Energy Letters* **2017**, *2* (1), 161-167.
46. Vesper, B. J.; Salaita, K.; Zong, H.; Mirkin, C. A.; Barrett, A. G. M.; Hoffman, B. M., Surface-bound porphyrazines: Controlling reduction potentials of self-assembled monolayers through molecular proximity/orientation to a metal surface. *J. Am. Chem. Soc.* **2004**, *126* (50), 16653-16658.
47. Ardo, S.; Meyer, G. J., Characterization of photoinduced self-exchange reactions at molecule–semiconductor interfaces by transient polarization spectroscopy: Lateral intermolecular energy and hole transfer across sensitized tio₂ thin films. *J. Am. Chem. Soc.* **2011**, *133* (39), 15384-15396.
48. Creutz, C.; Newton, M. D.; Sutin, N., Metal—ligand and metal—metal coupling elements. *J. Photochem. Photobiol. A* **1994**, *82* (1), 47-59.
49. Karki, L.; Lu, H. P.; Hupp, J. T., Electroabsorption studies of intervalence charge transfer in (nc)5fecnos(nh₃)5-: Experimental assessment of charge-transfer distance, solvent reorganization, and electronic coupling parameters. *J. Phys. Chem.* **1996**, *100* (39), 15637-15639.

50. Cave, R. J.; Newton, M. D., Calculation of electronic coupling matrix elements for ground and excited state electron transfer reactions: Comparison of the generalized mulliken–hush and block diagonalization methods. *J. Chem. Phys.* **1997**, *106* (22), 9213-9226.
51. Zheng, J.; Kang, Y. K.; Therien, M. J.; Beratan, D. N., Generalized mulliken–hush analysis of electronic coupling interactions in compressed π -stacked porphyrin–bridge–quinone systems. *J. Am. Chem. Soc.* **2005**, *127* (32), 11303-11310.
52. Winter, R. F., Half-wave potential splittings $\delta e/2$ as a measure of electronic coupling in mixed-valent systems: Triumphs and defeats. *Organometallics* **2014**, *33* (18), 4517-4536.
53. D'Alessandro, D. M.; Keene, F. R., A cautionary warning on the use of electrochemical measurements to calculate comproportionation constants for mixed-valence compounds. *Dalton Trans.* **2004**, (23), 3950-3954.
54. Zhong, Y.-W.; Gong, Z.-L.; Shao, J.-Y.; Yao, J., Electronic coupling in cyclometalated ruthenium complexes. *Coord. Chem. Rev.* **2016**, *312*, 22-40.
55. Shen, J.-J.; Shao, J.-Y.; Gong, Z.-L.; Zhong, Y.-W., Cyclometalated osmium–amine electronic communication through the p-oligophenylene wire. *Inorg. Chem.* **2015**, *54* (22), 10776-10784.
56. Shen, J.-J.; Zhong, Y.-W., Long-range ruthenium-amine electronic communication through the para-oligophenylene wire. *Sci. Rep.* **2015**, *5*, 13835-13843.
57. Beley, M.; Collin, J. P.; Sauvage, J. P., Highly coupled mixed-valence dinuclear ruthenium and osmium complexes with a bis-cyclometalating terpyridine analog as bridging ligand. *Inorg. Chem.* **1993**, *32* (21), 4539-4543.
58. Patoux, C.; Launay, J.-P.; Beley, M.; Chodorowski-Kimmes, S.; Collin, J.-P.; James, S.; Sauvage, J.-P., Long-range electronic coupling in bis(cyclometalated) ruthenium complexes. *J. Am. Chem. Soc.* **1998**, *120* (15), 3717-3725.
59. Barigelletti, F.; Flamigni, L.; Balzani, V.; Collin, J.-P.; Sauvage, J.-P.; Sour, A.; Constable, E. C.; Thompson, A. M. W. C., Rigid rod-like dinuclear ru(ii)/os(ii) terpyridine-type complexes. Electrochemical behavior, absorption spectra, luminescence properties, and electronic energy transfer through phenylene bridges. *J. Am. Chem. Soc.* **1994**, *116* (17), 7692-7699.
60. Yao, C.-J.; Zhong, Y.-W.; Nie, H.-J.; Abruña, H. D.; Yao, J., Near-ir electrochromism in electropolymerized films of a biscyclometalated ruthenium complex bridged by 1,2,4,5-tetra(2-pyridyl)benzene. *J. Am. Chem. Soc.* **2011**, *133* (51), 20720-20723.
61. Yang, W.-W.; Zhong, Y.-W.; Yoshikawa, S.; Shao, J.-Y.; Masaoka, S.; Sakai, K.; Yao, J.; Haga, M.-a., Tuning of redox potentials by introducing a cyclometalated bond to bis-tridentate ruthenium(ii) complexes bearing bis(n-methylbenzimidazolyl)benzene or -pyridine ligands. *Inorg. Chem.* **2012**, *51* (2), 890-899.

62. Jahnke, A. C.; Spulber, M.; Neuburger, M.; Palivan, C. G.; Wenger, O. S., Electronic coupling mediated by furan, thiophene, selenophene and tellurophene in a homologous series of organic mixed valence compounds. *ChemComm* **2014**, 50 (74), 10883-10886.
63. Morseth, Z. A.; Pho, T. V.; Sheridan, M. V.; Meyer, T. J.; Schanze, K. S.; Reynolds, J. R.; Papanikolas, J. M., Interfacial dynamics within an organic chromophore-based water oxidation molecular assembly. *ACS Appl. Mater. Interfaces* **2017**, 9 (19), 16651-16659.
64. Cruz, C. D.; Christensen, P. R.; Chronister, E. L.; Casanova, D.; Wolf, M. O.; Bardeen, C. J., Sulfur-bridged terthiophene dimers: How sulfur oxidation state controls interchromophore electronic coupling. *J. Am. Chem. Soc.* **2015**, 137 (39), 12552-12564.
65. McConnell, H. M., Intramolecular charge transfer in aromatic free radicals. *J. Chem. Phys.* **1961**, 35 (2), 508-515.
66. Lambert, C.; Risko, C.; Coropceanu, V.; Schelter, J.; Amthor, S.; Gruhn, N. E.; Durivage, J. C.; Brédas, J.-L., Electronic coupling in tetraanisylarylenediamine mixed-valence systems: The interplay between bridge energy and geometric factors. *J. Am. Chem. Soc.* **2005**, 127 (23), 8508-8516.
67. Closs, G. L.; Miller, J. R., Intramolecular long-distance electron transfer in organic molecules. *Science* **1988**, 240 (4851), 440-447.
68. Ratner, M. A., Bridge-assisted electron transfer: Effective electronic coupling. *J. Phys. Chem.* **1990**, 94 (12), 4877-4883.
69. Albinsson, B.; Mårtensson, J., Long-range electron and excitation energy transfer in donor–bridge–acceptor systems. *J. Photochem. Photobiol. C* **2008**, 9 (3), 138-155.
70. Natali, M.; Campagna, S.; Scandola, F., Photoinduced electron transfer across molecular bridges: Electron- and hole-transfer superexchange pathways. *Chem. Soc. Rev.* **2014**, 43 (12), 4005-4018.
71. Wenger, O. S.; Leigh, B. S.; Villahermosa, R. M.; Gray, H. B.; Winkler, J. R., Electron tunneling through organic molecules in frozen glasses. *Science* **2005**, 307, 99-102.
72. Wenger, O. S., How donor–bridge–acceptor energetics influence electron tunneling dynamics and their distance dependences. *Acc. Chem. Res.* **2011**, 44 (1), 25-35.
73. Gray, H. B.; Winkler, J. R., Long-range electron transfer. *Proc. Natl. Acad. Sci. U.S.A.* **2005**, 102 (10), 3534-3539.
74. Hankache, J.; Wenger, O. S., Photoinduced electron transfer in covalent ruthenium-anthraquinone dyads: Relative importance of driving-force, solvent polarity, and donor-bridge energy gap. *Phys. Chem. Chem. Phys.* **2012**, 14 (8), 2685-2692.

75. Lewis, F. D.; Liu, J.; Weigel, W.; Rettig, W.; Kurnikov, I. V.; Beratan, D. N., Donor-bridge-acceptor energetics determine the distance dependence of electron tunneling in DNA. *Proc. Natl. Acad. Sci. U.S.A.* **2002**, *99* (20), 12536-12541.
76. Hu, Y.; Mukamel, S., Superexchange and electron transfer in the photosynthetic reaction center. *Chem. Phys. Lett.* **1989**, *160* (4), 410-416.
77. Kreitner, C.; Heinze, K., The photochemistry of mono- and dinuclear cyclometalated bis(tridentate)ruthenium(ii) complexes: Dual excited state deactivation and dual emission. *Dalton Trans.* **2016**, *45* (13), 5640-5658.
78. Schäfer, J.; Holzapfel, M.; Mladenova, B.; Kattnig, D.; Krummenacher, I.; Braunschweig, H.; Grampp, G.; Lambert, C., Hole transfer processes in meta- and para-conjugated mixed valence compounds: Unforeseen effects of bridge substituents and solvent dynamics. *J. Am. Chem. Soc.* **2017**, *139* (17), 6200-6209.
79. Hupp, J. T.; Neyhart, G. A.; Meyer, T. J.; Kober, E. M., Energy relationships in optical and thermal electron transfer. Temperature dependence of an intervalence transfer absorption band. *J. Phys. Chem.* **1992**, *96* (26), 10820-10830.
80. Constable, E. C.; Housecroft, C. E., The electronic structure of some ruthenium(ii) complexes related to $[\text{Ru}(\text{bipy})_3]^{2+}$: An investigation of the stepwise replacement of n,n-donors by c,n-donors. *Polyhedron* **1990**, *9* (15), 1939-1947.
81. Farnum, B. H.; Morseth, Z. A.; Brennaman, M. K.; Papanikolas, J. M.; Meyer, T. J., Application of degenerately doped metal oxides in the study of photoinduced interfacial electron transfer. *J. Phys. Chem. B* **2015**, *119* (24), 7698-7711.
82. Pavlishchuk, V. V.; Addison, A. W., Conversion constants for redox potentials measured versus different reference electrodes in acetonitrile solutions at 25°C. *Inorg. Chim. Acta* **2000**, *298* (1), 97-102.
83. Sreenath, K.; Suneesh, C. V.; Gopidas, K. R.; Flowers, R. A., Generation of triarylamine radical cations through reaction of triarylamines with Cu(II) in acetonitrile. A kinetic investigation of the electron-transfer reaction. *J. Phys. Chem. A* **2009**, *113* (23), 6477-6483.
84. Quinton, C.; Alain-Rizzo, V.; Dumas-Verdes, C.; Clavier, G.; Miomandre, F.; Audebert, P., Design of new tetrazine-triphenylamine bichromophores – fluorescent switching by chemical oxidation. *Eur. J. Org. Chem.* **2012**, *2012* (7), 1394-1403.
85. Sumalekshmy, S.; Gopidas, K. R., Reaction of aromatic amines with $\text{Cu}(\text{ClO}_4)_2$ in acetonitrile as a facile route to amine radical cation generation. *Chem. Phys. Lett.* **2005**, *413* (4–6), 294-299.
86. Brigham, E. C.; Meyer, G. J., Ostwald isolation to determine the reaction order for $\text{TiO}_2(\text{e}^-)|\text{s}^+ \rightarrow \text{TiO}_2|\text{s}$ charge recombination at sensitized TiO_2 interfaces. *J. Phys. Chem. C* **2014**, *118* (15), 7886-7893.

87. Chen, L.; Mallick, S.; Tan, Y. N.; Meng, M.; Liu, C. Y., Charge transfer properties of triarylamine integrated dimolybdenum dyads. *Inorg. Chem.* **2017**, *56* (13), 7470-7481.
88. Larsen, C. B.; van der Salm, H.; Clark, C. A.; Elliott, A. B. S.; Fraser, M. G.; Horvath, R.; Lucas, N. T.; Sun, X.-Z.; George, M. W.; Gordon, K. C., Intraligand charge-transfer excited states in re(i) complexes with donor-substituted dipyridophenazine ligands. *Inorg. Chem.* **2014**, *53* (3), 1339-1354.
89. Adams, B. S.; Shillito, G. E.; van der Salm, H.; Horvath, R.; Larsen, C. B.; Sun, X.-Z.; Lucas, N. T.; George, M. W.; Gordon, K. C., Alteration of intraligand donor-acceptor interactions through torsional connectivity in substituted re-dppz complexes. *Inorg. Chem.* **2017**, *56* (21), 12967-12977.
90. Huff, G. S.; Lo, W. K. C.; Horvath, R.; Turner, J. O.; Sun, X.-Z.; Weal, G. R.; Davidson, H. J.; Kennedy, A. D. W.; McAdam, C. J.; Crowley, J. D.; George, M. W.; Gordon, K. C., Excited states of triphenylamine-substituted 2-pyridyl-1,2,3-triazole complexes. *Inorg. Chem.* **2016**, *55* (23), 12238-12253.

Chapter 3. Kinetics teach that electronic coupling lowers the free energy change that accompanies electron transfer²

3.1 Introduction

Electron flow in natural photosynthesis is controlled, to a large extent, by the spatial arrangement of redox active species in the electron transport chain whose formal reduction potentials provide a free energy gradient.¹⁻⁶ In artificial photosynthesis, this same strategy has been employed to vectorially translate electrons away from interfaces or toward catalytic sites.⁷⁻¹¹ In each case, ideal electron flow occurs rapidly and quantitatively in one desired forward direction, without a significant loss in the Gibbs free energy, ΔG° . In reality, electron transfer exists as an equilibrium with forward and reverse reactions regulated by the free energy that separates the redox active species, $|\Delta G^\circ|$. When $|\Delta G^\circ|$ approaches zero, the reverse reactions become more significant resulting in electron flow in undesired directions. Strong electronic coupling between redox centers facilitates rapid electron transfer, but theoretical considerations indicate that this will result in a free energy loss.¹²⁻¹³ Many scientists in the growing fields of artificial photosynthesis for electrical power generation or solar fuel production do not consider the influence of electronic coupling on ΔG° . This is largely due to the fact that the theory that relates electronic coupling and ΔG° has received

²This work was previously published in *Proceedings of the National Academy of Sciences of the United States of America*, 115 (28), 7248 with contributions from R. N. Sampaio, E. J. Piechota, L. Troian-Gautier, A. B. Maurer, K. Hu, P. A. Schauer, A. D. Blair, C. P. Berlinguette, and G. J. Meyer. Reprinted with permission. Copyright The National Academy of Sciences of the United States of America 2018.

little experimental attention.¹⁴⁻¹⁵ Herein, we describe a new kinetic approach for quantifying the influence of electronic coupling on ΔG° that was applied to donor-bridge-acceptor compounds of the type shown in Fig. 3.1.

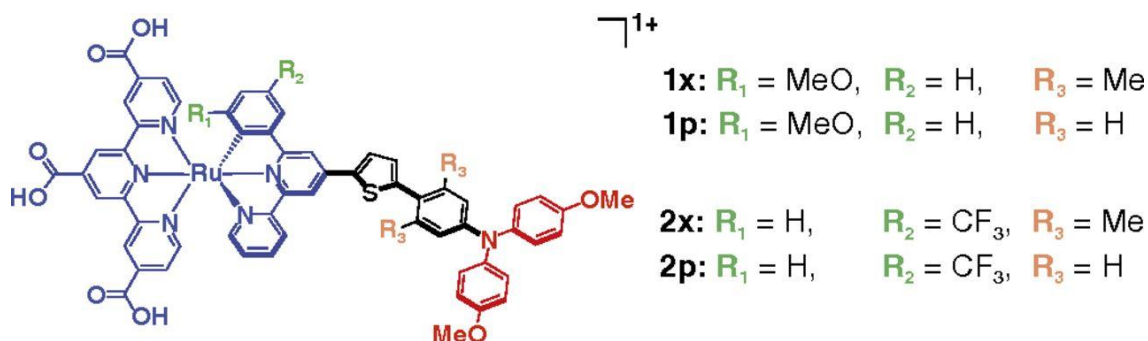


Figure 3.1. The A-B-D compounds utilized. Four cyclometalated ruthenium (blue) compounds with carboxylic acid groups (for binding to TiO_2) and an aromatic bridge covalently bound to a triphenylamine unit (red). Methyl substituents in the R_3 position – xylyl bridge (**x**) – lowers electronic coupling relative to the phenyl-bridge (**p**, $R_3 = \text{H}$). The R_1 and R_2 substituents allow the $E^\circ(\text{Ru}^{\text{III/II}})$ potentials to be controlled for the 1 and 2 series while $E^\circ(\text{TPA}^{+/0})$ was held constant.

The four cyclometalated ruthenium compounds shown contain an aromatic thiophene bridge to a TPA donor group. Electron withdrawing ($-\text{CF}_3$) or donating ($-\text{OMe}$, methoxy) substituents on the cyclometalating phenyl ring were used to tune the $\text{Ru}^{\text{III/II}}$ potentials while the identity of the $\text{TPA}^{+/0}$ was fixed. These compounds are ideal for fundamental study of thermal intramolecular electron transfer reactions that are thermodynamically unfavored (**1x**, **1p**), $\Delta G^\circ > 0$, or favored (**2x**, **2p**), $\Delta G^\circ < 0$ due primarily to redox and spectroscopic properties necessary to differentiate between a product and reactant. In either case, the electron transfer was explored in terms of the electronic coupling via synthetic modifications on the thiophene bridge. For compounds (**1p**, **2p**), a *phenyl* bridge unit preserves planarity along Ru^{II} and TPA centers and thus strong electronic coupling promotes adiabatic electron transfer. Compounds (**1x**, **2x**), on the contrary, contain a *xylyl* bridge unit where the aromatic

ring is twisted perpendicularly out of plane from the Ru^{II} center, such that H_{DA} is decreased, resulting in nonadiabatic electron transfer. This synthetic strategy represents an ideal approach where electronic coupling is the only isolated variable being explored. The 14 Å geometric distance, garnered from density functional theory (DFT) optimized structures, between the amine N and the Ru center is the same for all four compounds such that the through space electronic coupling is constant. The intense color changes associated with the redox chemistry enabled small concentrations of the intermediates to be detected spectroscopically. The combined optical, redox, and structural properties of these compounds are the most optimal available in the literature for determination of how electronic coupling influences the free energy change.¹⁶

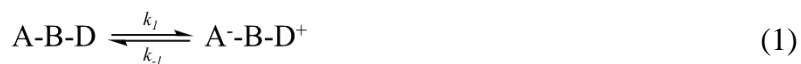
3.1.1 The theoretical prediction that electronic coupling, H_{DA} , lowers ΔG°

Consider a simplified A-B-D compound in which the quantum mechanical interaction between an electron acceptor (A) and an electron donor (D) wavefunctions is controlled by the bridge (B) that links them. The degree of mixing is quantified by the electronic coupling matrix element H_{DA} . Marcus theory holds that the many-fold potential surfaces for electron-transfer can be represented as parabolic Gibbs free energy surfaces (GESs) with fixed force constants, for the A-B-D ‘reactants’ and the A⁻-B-D⁺ ‘products’, that are a function of a single reaction coordinate, Equation 1 and Figure 3.2.^{12-13, 17} Robin and Day have categorized the degree of electronic coupling between A and D in three distinct classes, Figure 3.2A.¹⁸ When the bridge is insulating and no coupling occurs during the electron transfer, D and A retain their original identities and electron transfer occurs by a jump from the reactant to the product GES (Class I or nonadiabatic). At the opposite extreme where the bridge facilitates strong electronic coupling, the D and A GESs collapse to a single minimum

GES (adiabatic Class III). Most common electron transfer reactions in biology and chemistry, however, occurs with intermediate electronic coupling in the double minimum GES (adiabatic Class II). Note that as H_{DA} increases in the progression from non-adiabatic to adiabatic Class II electron transfer, $|\Delta G^0|$ decreases to an adiabatic value, ΔG^0_{ad} , i.e. $|\Delta G^0| > |\Delta G^0_{ad}|$. This would indicate that the equilibrium and thus the directionality of electron transfer can be controlled by the nature of the bridge and its ability to promote electronic coupling. It is therefore of interest to test this prediction experimentally under a variety of conditions that include both weak and strong¹⁴⁻¹⁵ coupling.

3.1.2 The kinetic approach

The approach reported here exploits the *dynamic* aspect of equilibrium reactions through a broadly applicable kinetic model. Although equilibrium, as a ‘balance of opposing forces’, oftentimes invokes the false perception that the competing forces stop altogether as solution concentrations become time invariant,¹⁹ in fact, a *dynamic* equilibrium is emphasized in introductory science class rooms where the opposing forces are rate constants, Eq. 1, whose values can be quite large and depend only on the absolute temperature.²⁰



Rate constants provide a direct measure of the equilibrium constant, K_{eq} , that may also be computed from the difference in the acceptor (A) and the donor (D) formal reduction potentials, $\Delta E^0 = E^0(A^{0/-}) - E^0(D^{+/0})$ through Faraday’s constant (F), Equation 2.

$$K_{eq} = e^{\frac{F\Delta E^0}{RT}} = e^{\frac{-\Delta G^0}{RT}} = \frac{k_1}{k_{-1}} \quad (2)$$

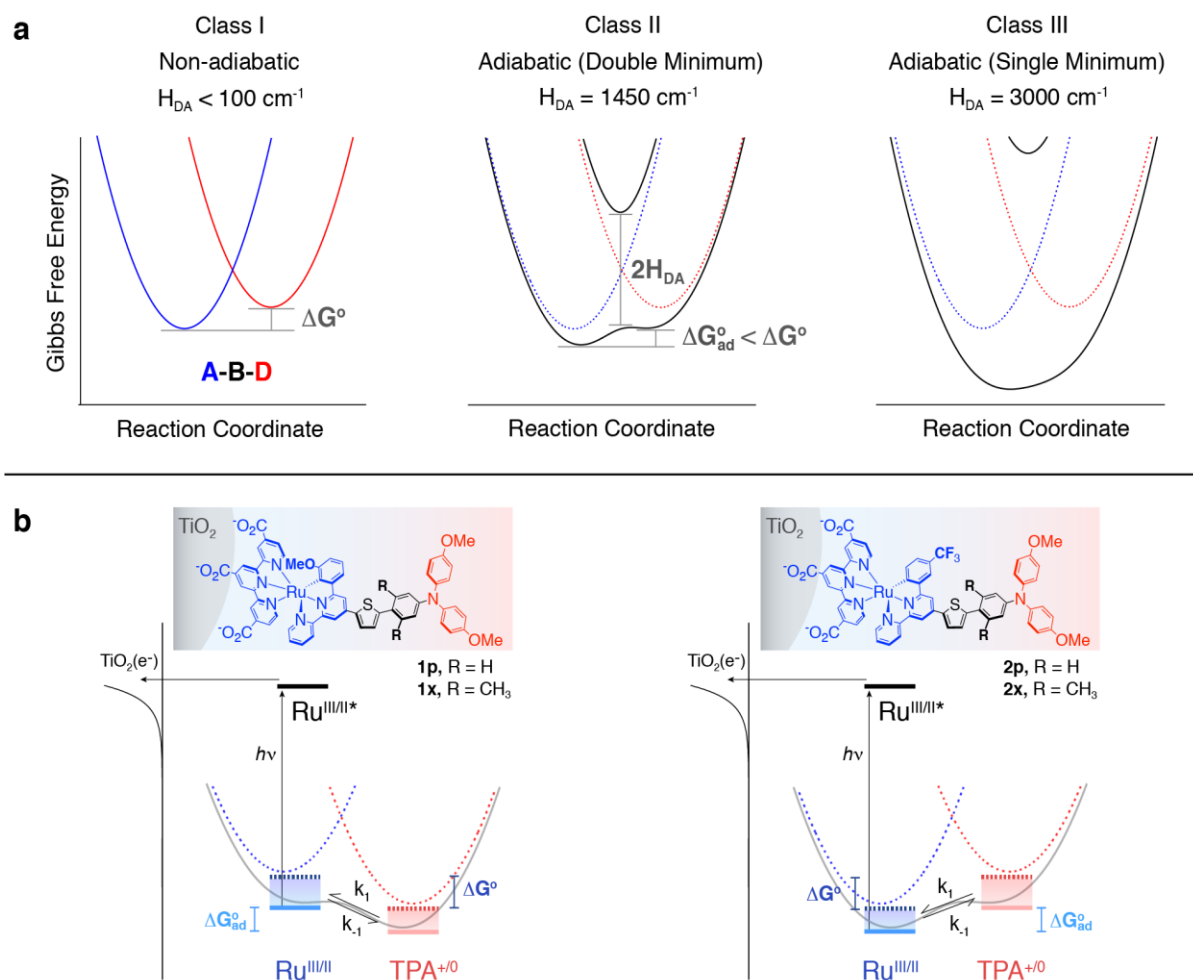


Figure 3.2. Potential energy surfaces and kinetic approach. (a), Gibbs free energy surfaces (GESs) that represent a redox equilibrium between A-B-D (blue) and A⁻B-D⁺ (red) as the electronic coupling matrix element (H_{DA}) is increased from 0 (nonadiabatic) to over 3000 cm^{-1} (adiabatic). Emphasis is placed herein on the reduction in the Gibbs free energy change, $|\Delta G^\circ| > |\Delta G_{ad}^\circ|$, that accompanies the transition from non-adiabatic to adiabatic electron transfer in the double minimum regime. (b) A ‘reaction coordinate’ diagram with potential energy surfaces of D-B-A reactants and D⁺-B-A⁻ products and semiconductor energetics. The kinetic approach used to quantify the thermal electron transfer reaction consists of a Ru^{II}-B-TPA compound anchored to the surface of mesoporous thin films of TiO₂ (the secondary acceptor). Light absorption induces excited-state electron injection from the Ru^{II} unit into the TiO₂ to form TiO₂(e⁻)-Ru^{III}-B-TPA. Within the time frame of charge recombination, the dynamic equilibrium $\text{Ru}^{III}\text{-B-TPA} \rightleftharpoons \text{Ru}^{II}\text{-B-TPA}^+$ was quantified through a kinetic model that afforded the forward, k_1 , and reverse, k_{-1} , electron transfer rate constants.

While relations like those given in Equation 2 can be found in most introductory science books, direct estimates of K_{eq} values through independent electrochemical measurements of

ΔE° are only strictly correct for nonadiabatic electron transfer. Strong electronic interactions of the donor and acceptor redox orbitals at the instant of electron transfer will result in adiabatic electron transfer that is expected to decrease $|\Delta G^\circ|$ as was described above.^{12-13, 17} Indeed, under such conditions ΔE° is no longer an accurate indicator of the equilibrium or the true free energy change. An alternative approach is to use kinetic data, yet previous attempts to quantify dynamic equilibria with pulsed-laser or line-broadening techniques have met limited success and have not provided temperature dependent K_{eq} values.^{14-15, 21-23} Kubiak has previously demonstrated the influence of H_{DA} on ΔG° through the use of steady-state vibrational spectroscopy on ‘mixed-valence isomers’ which has shown that $|\Delta G^\circ|$ in strongly coupled systems was smaller relative to values expected in the absence of electronic coupling.¹⁴⁻¹⁵

The kinetic strategy utilizes a pulsed laser to initiate electron transfer to a secondary acceptor whose recombination kinetics are sufficiently slow such that the approach to $A-B-D \rightleftharpoons A^{\cdot-}-B-D^+$ equilibrium can be time resolved spectroscopically. In particular, Fig. 2 shows four A-B-D compounds employed in this work. The cyclometalated ruthenium(II) compounds bearing a pendant triphenylamine (TPA), of the general form $Ru^{II}-B-TPA$, were anchored to the surface of TiO_2 anatase nanocrystallites that serves as the secondary acceptor. Upon light absorption by the Ru^{II} constituent, a charge transfer excited-state injects an electron into TiO_2 to form $TiO_2(e^-)-Ru^{III}-B-TPA$, where $Ru^{III}-B-TPA$ represents the A-B-D state of interest. Following electron injection, the TPA donor may transfer an electron to the oxidized Ru^{III} acceptor to give $Ru^{II}-B-TPA^+$, which establishes the $A^{\cdot-}-B-D^+$ state.¹⁶ For all four compound studied in this work, the $Ru^{III}-B-TPA$ is the initial A-B-D state after excited-state electron injection, such that electron transfer from the TPA donor to the Ru^{III} acceptor is

thermodynamically unfavored for (**1x**, **1p**), and favored for (**2x**, **2p**) (see Table 1). The millisecond lifetime of the injected $\text{TiO}_2(e^-)$ electron and the intense color changes associated with the $\text{Ru}^{\text{III/II}}$ and $\text{TPA}^{+/0}$ redox chemistry, enabled the $\text{Ru}^{\text{III}}\text{-B-TPA} \rightleftharpoons \text{Ru}^{\text{II}}\text{-B-TPA}^+$ *dynamic* equilibria to be measured spectroscopically and quantified through the proposed kinetic model. It is recognized that this light-initiated reaction technically yields a ‘quasi-equilibrium’ since true equilibrium is achieved only when the injected electrons recombine with the oxidized compound. Nevertheless, related photochemical strategies have been widely utilized in fluid solution to characterize excited-state “equilibrium” reactions, most notably for the determination of excited-state $\text{p}K_{\text{a}}^*$ values of photo-acids and photo-bases in aqueous solutions.²⁴⁻²⁶ Consequently, this kinetic approach is expected to be of general utility for characterization of free energy changes that accompany electron transfer in chemistry and biology.

3.2 Results and discussions

3.2.1 The A-B-D compounds

Table 3.1. Thermodynamic and Electronic Coupling Parameters at Room Temperature.

Compound	Electrochemistry ^{a,b}			Kinetics ^{a,c}	$H_{\text{DA}} (\text{cm}^{-1})^{\text{d}}$
	$E^{\circ}(\text{TPA}^{+/0})$	$E^{\circ}(\text{Ru}^{\text{III/II}})$	$-\Delta G^{\circ}/F$	$-\Delta G^{\circ}/F$	
1x	940	860	-80 (0.044)	-80 (0.044)	< 100 (0.01)
1p	940	860	-80 (0.044)	-62 (0.089)	1450 (0.18)
2x	940	1010	+70 (16)	+68 (15)	< 100 (0.01)
2p	940	1030	+90 (35)	+54 (8.4)	1450 (0.18)

^aValues given in mV vs. NHE. ^bCalculated with equation (2), using the electrochemical data, where F is Faraday’s constant. Values in parenthesis are the equilibrium constants, K_{eq} , calculated from $-\Delta G^{\circ} = RT \ln K_{\text{eq}}$. ^cCalculated with equation (2), using the kinetic data. Values in parenthesis are the equilibrium constants, K_{eq} . ^dValues in parenthesis are given in eV.

All four compounds were available from our previous studies and their measured redox properties are summarized in Table 3.1.¹⁶ Of note is the fact that the $E^{\circ}(\text{TPA}^{+/0}) = 0.94 \text{ V vs. NHE}$ for all four compounds and $E^{\circ}(\text{Ru}^{\text{III/II}})$ was 1.03 V for **2p**, 1.01 V for **2x**, and 0.86 V for

1x and **1p**. For **2p** in particular, where the TPA redox center was oxidized first, the more positive $E^{\circ}(\text{Ru}^{\text{III/II}})$ value likely emanates from an inductive influence from the oxidized TPA group transmitted through the strongly coupled *phenyl*-bridge. Nevertheless, $\Delta E^{\circ} = E^{\circ}(\text{Ru}^{\text{III/II}}) - E^{\circ}(\text{TPA}^{+/0})$ was insensitive to the bridge identity for **1p** and **1x** and changed by 20 meV for **2p** and **2x**, Table 3.1.

Representative UV-vis absorption spectra of **2x** and **2p** anchored to an oxide surface show extinction coefficients for the *phenyl*-bridged **2p** compound that were about 30-50% larger than those measured for its *xylyl*-bridged analogue **2x**; consistent with greater electronic coupling afforded by the *phenyl* bridge.^{16, 27} Density functional theory calculations (Fig. 3.3a and 3.3b insets) reveal that the highest occupied molecular orbital (HOMO) for **2p** is more delocalized over the thiophene bridge and has both Ru and TPA character, while the HOMO for **2x** was localized predominantly on the TPA group. The appearance of an intervalence transition ‘IT’ absorption band centered around 1100 nm in the one-electron oxidized mixed-valent $\text{Ru}^{\text{II}}\text{-B-TPA}^{+}$ state enabled quantitative analysis of the electronic coupling. Application of the 2-state generalized Mulliken-Hush expression²⁸⁻³⁰ provided: $H_{\text{DA}} = 1450 \text{ cm}^{-1}$ for **2p**; and $H_{\text{DA}} < 100 \text{ cm}^{-1}$ for **2x**. Electronic coupling values for (**1x**, **1p**) were estimated to be equivalent to those measured for (**2x**, **2p**), respectively, which indicated that for the different compounds, the common identity of the bridge unit, either *xylyl* or *phenyl*, is what primarily determines the degree of electronic coupling. The details of this analysis are given in the Section 3.4.9.

3.2.2 Application of the kinetic approach

The transient spectra measured after pulsed green light excitation of **2x** and **2p** are given in Fig. 3c-d, respectively. The room temperature spectra reveal the appearance of an

absorption band at ~ 750 nm that is characteristic of the oxidized donor TPA^+ that could be time resolved for **2x**, but not for **2p**. Hence the transient spectra alone provide direct evidence that the redox equilibrium is established more quickly for the adiabatic electron transfer reaction. In fact, the transient spectra recorded at any delay time after light excitation of **2p** were superposable when normalized, demonstrating that equilibrium was achieved on a sub-10 ns time scale at room temperature, whereas at lower temperatures, the appearance of TPA^+ could be partially time resolved (see below). The insets show kinetic data that corresponds to recombination of the injected electron with TPA^+ and the Ru^{III} center, the latter of which is much faster for the *xylyl* bridge.¹⁶

Temperature dependent kinetic data, over an 80 degree range, that report on the transient TPA^+ concentration for compounds **2x** and **2p**, Figure 3.3e through 3.3f, are shown with overlaid kinetic fits. Under all conditions, the transient data fully recovered to initial values within 10 ms with no evidence of net photochemistry. The kinetic model utilized has previously been reported for excited-state acid base equilibria²⁴⁻²⁶ and was constrained here with kinetic data from a model compound, that did not contain the pendant TPA group, which took into account the non-exponential nature of the interfacial back electron transfer reaction (see Supplementary Information). The insets show the classical Arrhenius analysis of the k_1 and k_{-1} values extracted from the kinetic data. The observed temperature dependence, evident for all four compounds, is indicative of a significant activation barrier that provides clear evidence that the electronic coupling was insufficient to collapse the PES to a single minimum, i.e. Class III behavior, Fig. 3.2a.

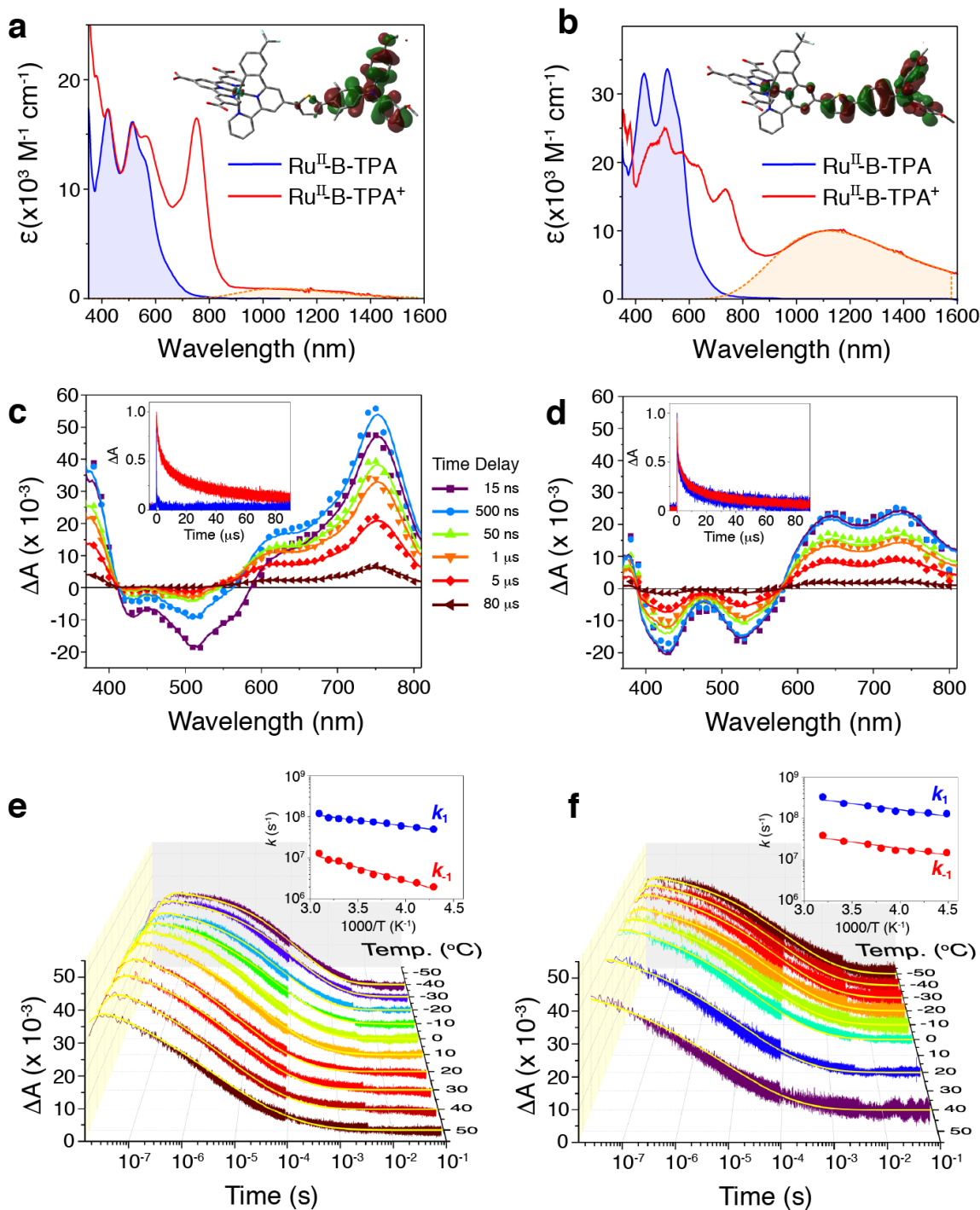


Figure 3.3. Electronic properties and transient absorption data. (Upper) The visible absorption spectra of **2x** (a) and **2p** (b) anchored to $\text{In}_2\text{O}_3:\text{Sn}$ thin films. Highlighted in the shaded orange area are the intervalence transition bands. The insets show the molecular structure with the overlaid highest occupied molecular orbitals (HOMO) generated from DFT calculations. (Middle) Absorption difference spectra measured at the indicated delay times after laser excitation for **2x** (c) and **2p** (d). The insets show normalized single wavelength kinetic data

monitored at 700 nm (that reports predominantly on TPA^+ concentrations) and at 510 nm (due to Ru^{III}). (Bottom) Single wavelength data that reports on the time dependent TPA^+ concentration as a function of temperature for **2x** (e) and **2p** (f). Overlaid in yellow are fits to the kinetic model used, as described in the Supplementary Information. The insets display Arrhenius plots of the forward, k_1 , and reverse, k_{-1} , rate constants. All experiments were performed in 0.1 M $\text{LiClO}_4/\text{acetonitrile}$ solution.

For **1p** and **2p**, the two forward and reverse rate constants displayed the same temperature dependence. In sharp contrast, the introduction of the methyl substituents in **2x**, decreased the forward rate constant by over an order of magnitude, while k_{-1} also decreased significantly and became more temperature dependent. Kinetic data are shown in Figure 3.4

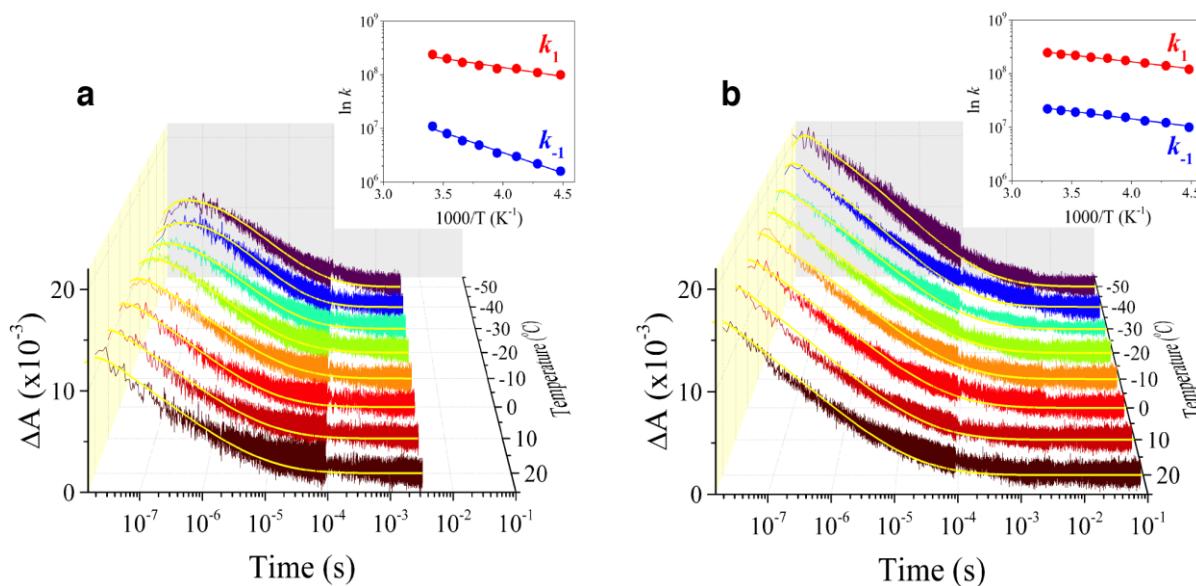


Figure 3.4. Single wavelength data that reports on the time dependent TPA^+ concentration as a function of temperature for **1x** (a) and **1p** (b). The insets display an Arrhenius plot of the forward, k_1 (red), and reverse, k_{-1} (blue), rate constants. Overlaid in yellow are fits to the kinetic

An expectation from transition state theory that the rate constant for the thermodynamically uphill reaction would increase with increasing H_{DA} was realized. The generality of this finding held true for the endothermic equilibrium of **1x** where kinetic analysis demonstrated that the uphill reaction, $\text{Ru}^{\text{III}}\text{-B-TPA} \rightarrow \text{Ru}^{\text{II}}\text{-B-TPA}^+$, became more temperature dependent. This is understood by an increased H_{DA} that lowers the barrier for the

uphill reaction to a greater extent than for the exothermic reaction. For both *xylyl*-bridged compounds (**1x**, **2x**), the slow unfavored reaction rate constant approached the same value of that for the favored reaction as the temperature was raised. Classical Arrhenius analysis was also performed to measure the barriers and pre-exponential factors for electron transfer, Table 3.2. The similar pre-exponential factors, $\ln(A)$, indicate that differences in the observed equilibrium kinetics do not originate from changes in dynamic crossing events but are instead, controlled by the reduction of the activation barrier, E_a , for the uphill process, $\text{Ru}^{\text{III}}\text{-B-TPA} \rightarrow \text{Ru}^{\text{II}}\text{-B-TPA}^+$ for **1p**, and $\text{Ru}^{\text{II}}\text{-B-TPA}^+ \rightarrow \text{Ru}^{\text{III}}\text{-B-TPA}$ for **2p**. Kinetic barriers are discussed in detail in Chapter 4.

Table 3.2. Arrhenius Parameters Extracted from Temperature Dependent Rate Constants.

Compound	$\text{Ru}^{\text{III}}\text{-B-TPA} \rightarrow \text{Ru}^{\text{II}}\text{-B-TPA}^+$		$\text{Ru}^{\text{II}}\text{-B-TPA}^+ \rightarrow \text{Ru}^{\text{III}}\text{-B-TPA}$		Enthalpy ^a	Entropy ^b
	$\ln(A)$	E_a	$\ln(A)$	E_a	(ΔH°)	(ΔS°)
	k_1 (<i>uphill</i>)		k_{-1} (<i>downhill</i>)			
1x	22.0 ± 0.3	14.4 ± 0.6	21.8 ± 0.3	6.44 ± 0.6	$+7.9 \pm 0.2$	1.5 ± 0.8
1p	21.2	4.86 ± 0.2	19.1 ± 0.1	5.40 ± 0.3	0.0 ± 0.3	-18 ± 0.6
	k_1 (<i>downhill</i>)		k_{-1} (<i>uphill</i>)			
2x	20.5 ± 0.2	5.45 ± 0.3	20.8 ± 0.3	12.5 ± 0.7	-7.0 ± 0.6	-2.6 ± 2.4
2p	21.7	5.84 ± 0.7	19.6 ± 0.4	6.07 ± 0.8	0.0 ± 0.2	17 ± 2.4

^aValues in kJ mol^{-1} . ^bValues in $\text{J mol}^{-1} \text{K}^{-1}$. Arrhenius equation, $k = A\exp(-E_a/RT)$. Classical van't Hoff representations²⁰ of the temperature dependent equilibrium data given in Fig. 3.4a and Equation 3.

$$\ln K_{eq} = -\frac{\Delta G^\circ}{RT} = -\frac{\Delta H^\circ}{RT} + \frac{\Delta S^\circ}{R} \quad (3)$$

provide a vividly clear demonstration that K_{eq} was closer to unity for the *phenyl*-bridged (**1p**, **2p**) compounds, and hence $|\Delta G^\circ|$ was smaller for the more strongly coupled equilibrium. This finding is completely in line with theoretical predictions and the pioneering work of Kubiak and coworkers.¹⁴⁻¹⁵ Before discussing the broader impacts of this finding it is worthwhile to consider more carefully the specific data in Fig. 3.4a.

The van't Hoff plot demonstrates an adiabatic equilibrium for the *phenyl*-bridged compounds and a nonadiabatic one for the *xylyl*-bridged compounds. In other words, there is no evidence for thermal energy transfer at constant pressure for the *phenyl*-bridged compounds, i.e. $q_p = \Delta H^\circ = 0$, Table 2. In contrast, the strong temperature dependence for **1x** and **2x** emanates from an enthalpically favored ($\Delta H^\circ = -7.0$ kJ/mol) and unfavored ($\Delta H^\circ = +7.9$ kJ/mol) electron transfer equilibrium, respectively. These data represent a notable contribution to the literature as calorimetric characterization of intramolecular electron transfer is difficult to obtain and most discussions of adiabatic vs. nonadiabatic electron transfer are subjective, i.e. adiabaticity is inferred from rate constants or other observations.

Extrapolation of the *xylyl*-bridged data in the van't Hoff plot to higher temperatures suggests that a common equilibrium constant would be reached for the *xylyl*- and *phenyl*-bridged compounds around 350 K. At this temperature, thermal motion in the *xylyl* bridge is expected to provide sufficient coupling to access an adiabatic electron transfer pathway, however, the boiling point of CH₃CN precluded experimental confirmation of this. Though the possibility of this slope change at higher temperature for *xylyl*-bridged compounds is in principle possible, a preliminary intercept-analysis from the van't Hoff equation was revealing. Nevertheless, we note that some degree of caution should be emphasized.²⁰ Use of Eq. 3 and the experimental data provided standard entropy changes, ΔS° for the electron transfer reactions. In the x-series, the absolute entropic contribution to the total Gibb's Free Energy change was, $|\Delta S^\circ| = 2 \pm 3$ J mol⁻¹ K⁻¹, indicating only a slight contribution to the total Gibb's Free Energy at the experimental temperatures studied. Strikingly, however, $|\Delta S^\circ| = +17 \pm 3$ J mol⁻¹ K⁻¹ for the both **1p** and **2p** which indicates that entropy is the main contributor to the overall free energy. This is currently the subject of ongoing research. The

enthalpies and entropies for the adiabatic and non-adiabatic reactions are presented in Table 3.2.

3.2.3 Free energy loss due to electronic coupling

Significantly, the van't Hoff data, Figure 3.5a, reveal that $|\Delta G^\circ|$ was smaller for the adiabatic equilibrium of both *phenyl*-bridged compounds over the entire 80 degree temperature range. This finding naturally raises two interrelated questions of relevance to maximizing the free energy stored in artificial photosynthesis: 1) *How much free energy can be lost due to coupling?* and 2) *What amount of coupling is necessary to collapse the double minimum GES into a single minimum?* The second question could be rephrased to ask, *when*

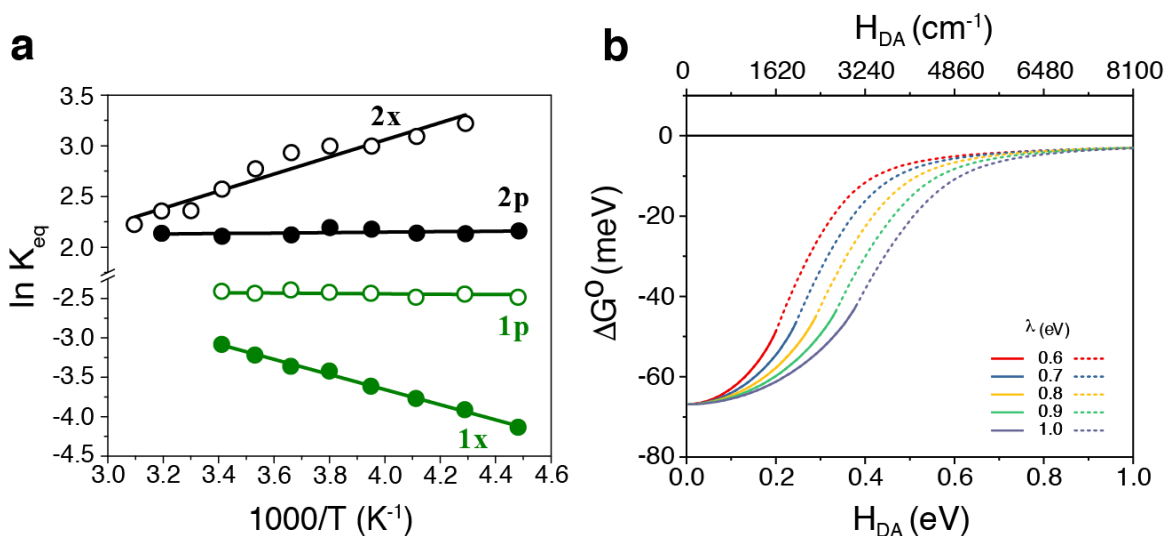


Figure 3.5. van't Hoff analysis and the influence of electronic coupling on Gibbs free energy. a) A van't Hoff plot, $\ln K_{eq}$ vs $1000/T$, of the redox equilibrium constants with overlaid best fit lines that demonstrates an adiabatic mechanism for (**1p**, **2p**) and nonadiabatic for (**1x**, **2x**). b) Effect of electronic coupling on the Gibbs free energy for electron transfer calculated from numerical analysis of the GESs (equation (4)) with the indicated reorganization energies, λ . The solid lines represent the progression of the nonadiabatic ΔG° to the adiabatic value, ΔG°_{ad} , limited to the double minimum regime. The dotted lines denote fictitious ΔG°_{ad} values for a GES collapsed to a single minimum.

does H_{DA} become so large that the electron is delocalized over both redox centers such that equilibrium no longer has any physical meaning? The answers to these questions depend on

the magnitudes of ΔG° , H_{DA} and the reorganization energy, λ .¹²⁻¹³ Fortunately, the lower GES can be calculated exactly with Equation 4 that has been previously reported.¹²⁻¹³

$$G_+ = \frac{[\lambda(2X^2 - 2X + 1) + \Delta G^\circ]}{2} + \frac{[(\lambda(2X - 1) - \Delta G^\circ)^2 + 4H_{DA}^2]^{\frac{1}{2}}}{2} \quad (4)$$

The first derivative of the lower GES expression provides x-intercepts that indicate the reaction coordinate X positions for the two minima and the transition state (provided that one exists) which can then be analyzed. An example is given below.

Consider **2x** and **2p** whose GESs, shown in Fig. 3.2, were generated from Equation 4 with $\lambda = 0.6$ eV and $\Delta G^\circ = -70$ meV, $H_{DA} = 0$ eV for **2x**, and $H_{DA} = 0.18$ eV (1450 cm^{-1}) for **2p**. When H_{DA} is increased in the progression from 0 to 1 eV, the nonadiabatic $\Delta G^\circ = -70$ mV characteristic of **2x** remains essentially constant until about $H_{DA} = 0.040$ eV. With increasing H_{DA} values, the adiabatic ΔG°_{ad} monotonically decreases and eventually the GES collapses to a single minimum, at the point where the solid lines become dashed in Fig. 3.4b, i.e. Class II \rightarrow Class III behavior. At this point about 25% of the free energy is lost. Interestingly, the double minimum GES survives at much larger H_{DA} when λ is increased to 1.0 eV. Additionally, Fig. 3.8 and Fig. 3.7 shows that H_{DA} value necessary for collapse increases linearly with λ . We note that Dutton has shown that a λ of 0.6 eV for proteins and 1.0 eV for aqueous solution is sufficient to model much electron transfer data regardless of the medium that separates the D and A.³¹⁻³³ When $|\Delta G^\circ|$ is greater than 70 meV, Class III behavior occurs at weaker electronic coupling. Indeed, for self-exchange reactions, when $\Delta G^\circ = 0$, the double minimum survives to $H_{DA} = 0.5$ eV for $\lambda = 0.6$ eV, Supplementary Fig. 3.4b. However, in self-exchange reactions, the products and reactants are the same and a free

energy gradient for vectorial electron transport is lost. Nevertheless, concentration gradients have been successfully used to transport charge toward an electrode for solar cell applications.³⁴ In summary, this analysis indicates that the magnitude of $|\Delta G^0|$ lost to electronic coupling is significant and should be considered in artificial photosynthesis design. As the open circuit photovoltage, V_{oc} , represents the maximum Gibbs free energy a regenerative solar cell can produce, the loss of > 10 mV is highly significant. Indeed, a 3 mV loss in V_{oc} was recently reported when a donor-acceptor adduct was formed and it is likely that this enhanced coupling turned on an adiabatic pathway.³⁵

It is worthwhile to consider how natural photosynthesis utilizes electronic coupling to control the flow of electrons. In purple bacteria, H_{DA} is sufficient for adiabatic electron transfer in the special pair and the subsequent electron transfer steps are nonadiabatic.^{2-4, 6} Other photosystems also show decreased electronic coupling when the redox active groups are more spatially separated from the excited-state.²⁻⁶ Presumably these photosystems evolved to efficiently transfer electrons when a kinetic competition with excited-state decay existed and the subsequent vectorial electron transfer steps occurred nonadiabatically to minimize free energy loss.^{2-4, 6} The particular interfaces have been used in artificial photosynthesis, specifically in dye-sensitized solar cells.¹⁶ It was found that the strong coupling afforded by the *phenyl* bridge resulted in more delocalized orbitals that promoted faster recombination of the injected electrons with the oxidized molecules.¹⁶ It's now clear that a weakly coupled secondary donor should be employed with a small free energy gradient to translate the charge further from the interface. Therefore, natural and artificial photosynthesis utilize adiabatic pathways for electron transfer reactions that occur in kinetic competition with fast excited-state relaxation processes and nonadiabatic pathways to shuttle

redox equivalents to catalytic or other redox active sites. The data reported herein indicates that the magnitude of the electronic coupling should be carefully tuned so as to minimize free energy loss.

The demonstration of a smaller K_{eq} – or reduced $|\Delta G^0|$ – values for electron transfer reactions that follow adiabatic, relative to nonadiabatic, pathways has broad implications. Taube indicated that adiabatic electron transfers were possible whenever $H_{DA} > 2k_bT$,³⁶⁻³⁷ and thus are potentially relevant to many classes of electron transfer in biology and chemistry including redox titrations that are commonly performed in undergraduate laboratories. Such bimolecular chemistry, and others in general, involves diffusion of the D and the A to form an encounter complex prior to electron transfer.^{13, 38} The free energy change associated with the formation of the encounter complex is small in polar solvents and is usually neglected, but becomes more significant in low dielectric media.³⁹ If coupling within the encounter complex is strong at the instance of electron transfer, an adiabatic pathway may be operative that is expected to decrease the yield of products from that calculated based on formal reduction potentials. Indeed, a recent literature report of light driven bimolecular electron transfer in acetonitrile and ionic liquids with H_{DA} values between $\sim 100 - 1500 \text{ cm}^{-1}$ showed that the rate constants could only be satisfactorily modeled when the ΔG^0 values were lower than those measured electrochemically.⁴⁰ This behavior is consistent with coupling lowering the free energy change. Indeed, when any encounter complex is sufficiently coupled, such as those that occur by an inner-sphere mechanism where an atom, ion or molecule, bridge the donor and acceptor, a loss in free energy should be expected.

3.3 Conclusions

In summary, light initiated kinetic measurements have provided temperature dependent equilibrium constants for fundamental adiabatic *and* nonadiabatic electron transfer. It was found that the absolute value of ΔG° decreased for the adiabatic equilibria as was predicted theoretically decades ago.¹²⁻¹³. A virtue of adiabatic electron transfer is that equilibrium is rapidly achieved, but the data described herein show that this comes with a loss in free energy and more delocalized wavefunctions that can promote reactions in undesired directions. Subtle structural changes were found to dramatically influence electron transfer reactions on the adiabatic/nonadiabatic borderline, and the results presented here teach how this influences basic chemical equilibrium. The data indicate that adiabatic pathways provide a more rapid approach to equilibrium that comes at the expense of some free energy loss.¹⁹ On the other hand, the slower nonadiabatic path ultimately conserves more free energy in redox equilibrium and in vectorial transport chains for natural and artificial photosynthesis.

3.4 Additional information

3.4.1 Experimental details

All materials and reagents were used as received from the indicated commercial suppliers: acetonitrile (CH_3CN ; Burdick & Jackson, spectrophotometric grade); Lithium perchlorate (LiClO_4 ; Sigma Aldrich, $\geq 99.99\%$); glass microscope slides (Fisher Scientific, 1 mm thick); fluorine-doped SnO_2 -coated glass (FTO; Hartford Glass Co. Inc., 2.3 mm thick, $15 \Omega/\square$). All compounds were synthesized as previously described.¹⁶

3.4.2 Sample preparation

Mesoporous thin films of TiO_2 nanocrystals and conductive tin doped indium oxide, $\text{In}_2\text{O}_3:\text{Sn}$, nanoparticles were prepared as described previously.⁴¹⁻⁴² The thin films were

immersed in $\sim 1 \times 10^{-4}$ M solution of the compounds and their absorbance values were monitored to obtain the desired surface coverage. Saturation coverages were necessary for electrochemical experiments with TiO₂ thin films while those on In₂O₃:Sn were performed at < 50% saturation coverages. To avoid intermolecular electron transfer reactions during transient absorption measurements, the absorbance of the thin films was controlled to assure < 50% surface coverage with TiO₂. Unless otherwise stated, all experiments were performed in 0.1 M LiClO₄/acetonitrile solutions and samples were purged with argon gas for a minimum of 30 min prior to experiments.

3.4.3 UV-vis absorption

The steady-state UV-visible absorption spectra were carried out with an Agilent Cary 5000 UV/Vis/NIR spectrophotometer at room temperature.

3.4.4 Transient absorption

Nanosecond transient absorption experiments were performed on an apparatus as previously described.^{16, 41} Variable temperature transient absorption data were obtained with a UniSoku CoolSpek (USP-203-B) liquid nitrogen cryostat. Kinetic measurements were taken after thermal equilibration at each temperature for at least 10 minutes.

Spectral modeling of the transient spectra obtained from kinetic analysis were performed using a least-square fitting (written in Mathematica 10) to the independently measured spectra of the singly oxidized Ru^{III} or TPA⁺ and the ground-state UV-vis spectra. The variable temperature kinetic data were analyzed through a kinetic model described further below.

3.4.5 Electrochemistry

Spectroelectrochemical measurements were performed with an integrated UV-vis spectroelectrochemical system from Pine Research Instrumentation. Briefly, an Avalight Deuterium/Halogen (Avantes) was used as the light source and the AvaSpec ULS2048 UV-vis (Avantes) was the spectrophotometer. The WaveNow (Pine) operated as the potentiostat. The experimental setup consisted of a standard three-electrode cell with the sensitized thin films of TiO₂ or In₂O₃:Sn as the working electrodes, a Pt counter electrode (BAS), and a nonaqueous Ag/AgCl pseudoreference electrode (Pine). The ferrocenium/ferrocene (Fc⁺⁰) half-wave potential (+ 630 mV vs NHE)⁴³ was used to calibrate the pseudoreference electrode before and after experiments and to convert all measured potentials to the normal hydrogen electrode (NHE). Each applied potential was typically held for ~2 min before UV-vis absorption spectrum was recorded. Fractional curves of each redox species were analyzed as a function of the applied potential. Integration of the Ru^{III} and TPA⁺ fractional curves yielded their respective Nernstian redox distributions. The formal reduction potentials, E°(Ru^{III/II}) or E°(TPA⁺⁰), were taken as the equilibrium potential where equal concentration of the two redox states were present. For NIR data, a BAS model CV-50W potentiostat was used in parallel with an Agilent Cary 6000i UV/Vis/NIR spectrophotometer at room temperature.

3.4.6 Calculations

Ground-state geometries of **2p** and **2x** and their singly oxidized states were optimized using B3LYP and 6-31G(d) basis set. The effective charge transfer distance was calculated from the dipole moment change between the ground- and intervalence excited-state of the

singly oxidized Ru^{II}-Bp-TPA⁺, $r_{da} = \Delta\mu_{eg}/e$. Calculations were carried using Gaussian 09 Package.⁴⁴

3.4.7 Calculation of H_{DA} through the generalized Mulliken-Hush model

The H_{DA} values previously reported for **2x** ($H_{DA} < 100 \text{ cm}^{-1}$) and **2p** ($H_{DA} > 1000 \text{ cm}^{-1}$) were calculated using the traditional Mulliken-Hush expression, Equation 5,¹²

$$H_{DA} = \frac{2.06 \times 10^{-2} (v_{max} \epsilon_{max} \Delta v_{1/2})^{1/2}}{d} \quad (5)$$

with spectroscopy information of the IT transition and the geometric distance $d = r_0 = 14 \text{ \AA}$, that separates the Ru^{II} and TPA centroids. Although the geometrical distance is oftentimes used to calculate H_{DA} through the traditional Mulliken-Hush expression in reality it represents only a lower limit for H_{DA} . Indeed, the electron transfer distance during intervalence (IT) transitions can be appreciably lower than r_0 if the Bridge allows enough electronic coupling between the redox centers,⁴⁵⁻⁴⁷ so that d decreases as H_{DA} is increased. The traditional Mulliken-Hush expression, equation 1, is conceivably a more accessible alternative for H_{DA} calculations as it can be estimated based on geometrical distances.

The generalized Mulliken-Hush model casts H_{DA} in terms of the more fundamental adiabatic quantities: adiabatic transition dipole moment, μ_{eg} , and change in dipole moment, $\Delta\mu_{eg}$, and thus does not required an independent measure of the Donor-Acceptor charge transfer distance.^{28-30, 48} In this work, the H_{DA} values were calculated using the 2-state generalized Mulliken-Hush expression, Equation 6,

$$H_{DA} = \left| \frac{\mu_{eg} v_{max}}{\mu_D - \mu_A} \right| = \left| \frac{\mu_{eg} v_{max}}{[(\Delta\mu_{eg})^2 + 4(\mu_{eg})^2]^{1/2}} \right| \quad (6)$$

where ν_{max} is the energy of the intervalence transition maximum and $(\mu_D - \mu_A)$ is the nonadiabatic change in dipole moment. The latter, is connected to the adiabatic quantities through Equation 7^{28-30, 46}

$$(\mu_D - \mu_A)^2 = (\Delta\mu_{eg})^2 + 4(\mu_{eg})^2 \quad (7)$$

where the change in dipole-moment $(\mu_D - \mu_A)$ is directly related to the effective (nonadiabatic) electron transfer distance, Equation 8,⁴⁶

$$r_{DA} = (\mu_D - \mu_A)/e \quad (8)$$

which is generally smaller than r_0 . The electron delocalization between the two redox centers, with increasing H_{DA} values, reduces the change in dipole moment $(\mu_D - \mu_A)$ to an *adiabatic* value, $\Delta\mu_{eg}$, Equation 9,

$$\Delta\mu_{eg} = (1 - 2c_b^2)(\mu_D - \mu_A) \quad (9)$$

where c_b^2 is the degree of delocalization, which is direct link between the localized nonadiabatic and delocalized adiabatic quantities.⁴⁶

In the progression of a nonadiabatic to adiabatic electron transfer reaction, the increased electron delocalization reduces the effective charge transfer distance, r_{DA} , to values⁴⁶

$$r_{del} = \Delta\mu_{eg}/e \text{ or } er_{del} = (1 - 2c_b^2) er_{DA} \quad (10)$$

Collectively, equations 2-6 permit a more truthful prediction of H_{DA} . Nevertheless, the generalized Mulliken-Hush expression, equation 11, can also be related to Equation 5,

$$H_{DA} = \left| \frac{\mu_{eg} \nu_{max}}{(\mu_D - \mu_A)} \right| = \left| \frac{\mu_{eg} \nu_{max}}{er_{DA}} \right| = \frac{2.06 \times 10^{-2} (\nu_{max} \epsilon_{max} \Delta\nu_{1/2})^{1/2}}{r_{DA}} \quad (11)$$

In this work, the transition dipole-moment, μ_{eg} , was obtained by integrating the IT band obtained from spectroelectrochemical measurements (Fig. 3b in the main text) and the energy of the IT transition maximum, ν_{max} , was also obtained from experimental data in Fig. 3b. DFT calculations were used to optimized the structure of the one-electron oxidized **2p** (Ru^{II} -B-TPA⁺), from which the ground-state dipole moment was obtained, μ_g . Further TD-DFT calculations on the previous optimized structure provided identification of the IT transition. A single point energy calculation of the specified IT transition provided the dipole moment of the excited-state IT transition, μ_e . The adiabatic dipole-moment difference was calculated as $\Delta\mu_{eg} = \mu_e - \mu_g = -40.5$ D. Finally, the electronic coupling was calculated from Equation 2. with input values from both theoretical calculations and experimental data. All values are summarized in Table 3.3.

Table 3.3. Calculated and experimental values for dipole-moments, degree of delocalization, electron transfer distances, and electronic coupling for the **2p** compound.

Compound	$ \mu_{eg} $ (D) ^a	$ \Delta\mu_{eg} $ (D) ^b	$ (\mu_D - \mu_A) $ (D) ^c	c_b^{2d}	r_0 (Å) ^e	r_{DA} (Å) ^f	r_{del} (Å) ^g	H_{DA} (cm ⁻¹) ^h
Bp	7.05	40.5	42.8	0.03	14	8.9	8.4	1450

^a Calculated from the integrated area of the IT absorption band. ^b Adiabatic ground-excited state dipole-moment difference computed from DFT and TD-DFT calculations. ^c Nonadiabatic change in dipole-moment calculated from equation 3. ^d degree of delocalization calculated from equation 5. ^e Geometrical distance estimated from the separation between the Ru^{II} and TPA centroids based on the optimized molecular structure from DFT calculations. ^f Effective nonadiabatic (localized) electron transfer distance calculated from equation 3. ^g Delocalized electron transfer distance calculated using equation 6. ^h Electronic coupling calculated from equation 2.

3.4.8 Determination of H_{DA} for **1x** and **1p**

The ethyl ester derivatized **1p** compound, *i.e.* when the H^+ on the carboxylic acid functional groups are replaced by CH_2CH_3 groups, served as model compounds to analyze the electronic coupling for the corresponding carboxylic acid analogue. In work currently under review, it was found that the ethyl ester derivatized compounds of the **1-series** exhibited the first oxidation state centered at the TPA redox unit. On the contrary, the

carboxylic acid forms are characteristic of Ru^{II} being the first to be oxidized. Note that in all cases, the identity of the bridge unit is the same. However, for reasons better discussed in this submitted work, the ethyl ester derivatized (**1x**, **1p**) compounds are better models to quantify the H_{DA} Values.

Chemical oxidation of **1p** and **2p**, in acetonitrile solutions, with $\text{Cu}(\text{ClO}_4)_2$ is shown in Figure 3.7. Equimolar addition of the sacrificial oxidant $\text{Cu}(\text{ClO}_4)_2$ afforded the one electron oxidized form, $\text{Ru}^{\text{II}}\text{-B-TPA}^+$, of the compounds. The magnitudes of H_{DA} were evaluated using the traditional Mulliken-Hush analysis, Equation 1, considering the geometrical distance of 14 Å. For both compounds, the calculated electronic coupling values were within experimental error identical, $H_{\text{DA}} \sim 1000 \text{ cm}^{-1}$. This observation provides compelling evidence that the common identity of the bridge unit between these two different compounds, **1p** vs. **2p**, is the primary element that controls the degree of electronic coupling between the Donor and Acceptor redox centers. Therefore, in this current work, $H_{\text{DA}} = 1450 \text{ cm}^{-1}$ for **1p**, as follows the calculation through the Generalized Mulliken-Hush expression performed for **2p**.

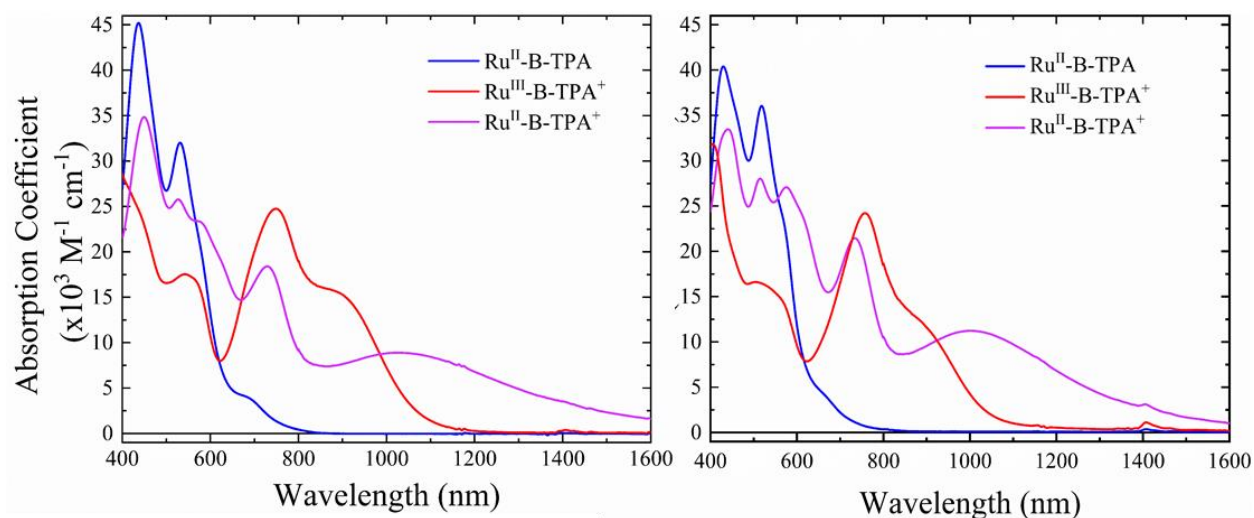


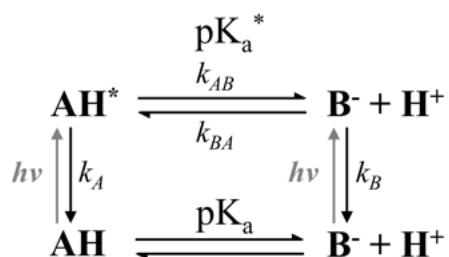
Figure 3.6. Chemical oxidation of **1p** (left) and **2p** (right), in acetonitrile solutions, using $\text{Cu}(\text{ClO}_4)_2$ as the sacrificial oxidant.

Since the xylyl bridge does not promote significant electronic coupling, $H_{\text{DA}} < 150 \text{ cm}^{-1} < kT$, as found for **2x**, the same is expected for **1x**.

3.4.9 Kinetic model

The strategy utilized in this work to quantify dynamic equilibrium constants K_{eq} , is analogous to that previously described for acid-base equilibria in the determination of excited-state pK_a^* values^{24-26, 49}, shown as a square-scheme in Scheme 3.1,

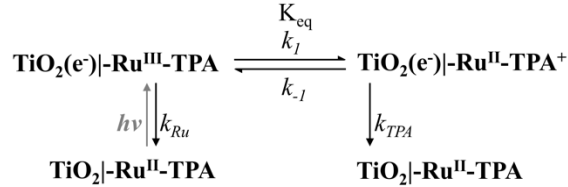
Scheme 3.1 Square-scheme kinetic model for molecules that undergo excited-state acid-base chemistry.



where the solution to the coupled differential equations that describe the square kinetic Scheme 1, is used to obtain the rate constants. The implementation of the approach shown in

Fig. 31b in the main text was adapted from acid-base chemistry and applied to interfacial and intramolecular electron transfer equilibria shown in Scheme 3.2,

Scheme 3.2. Square-scheme kinetic model for interfacial (k_A , k_b) and intramolecular (k_1 , k_{-1}) electron transfer for immobilized molecules.



where k_1 and k_{-1} are the forward and backward rate constant respectively. After excited-state electron injection $\text{TiO}_2\text{-Ru}^{\text{II}*}\text{-TPA} \rightarrow \text{TiO}_2(e^-)\text{-Ru}^{\text{III}}\text{-TPA}$, the ground-state is recovered with rate constants for charge recombination, k_{Ru} and k_{TPA} , to the oxidized Ru^{III} or TPA^+ respectively. The coupled differential rate equations that mathematically describes Scheme 3.2 are

$$\frac{d[\text{Ru}^{\text{III}}]}{dt} = -(k_{Ru} + k_1)[\text{Ru}^{\text{III}}] + k_{-1}[\text{TPA}^+] \quad (12)$$

$$\frac{d[\text{TPA}^+]}{dt} = -(k_{TPA} + k_{-1})[\text{TPA}^+] + k_1[\text{Ru}^{\text{III}}] \quad (13)$$

For clarity, the transient states $\text{TiO}_2(e^-)\text{-Ru}^{\text{III}}\text{-TPA}$ and $\text{TiO}_2(e^-)\text{-Ru-TPA}^+$ were abbreviated to Ru^{III} and TPA^+ . The non-exponential nature of charge recombination reactions on sensitized TiO_2 thin films were modeled as a distribution of recombination rate constants that resulted in stretched exponential behaviors, Equation 14,⁵⁰⁻⁵²

$$f(t) = Ae^{-(k t)^\beta} \quad (14)$$

where β is inversely related to the width of and underlying Levy distribution of rate constants. Consequently, the mono-exponential rate constants, k_{Ru} and k_{TPA} , in equations 15 and 16 were adjusted accordingly

$$\frac{d[Ru^{III}]}{dt} = -(\beta_{Ru}(k_{Ru})^{\beta_{Ru}} t^{\beta_{Ru}-1} + k_1)[Ru^{III}] + k_{-1}[TPA^+] \quad (15)$$

$$\frac{d[TPA^+]}{dt} = -(\beta_{TPA}(k_{TPA})^{\beta_{TPA}} t^{\beta_{TPA}-1} + k_{-1})[TPA^+] + k_1[Ru^{III}] \quad (16)$$

Equations 15 and 16 describe the time-dependent concentrations of $[Ru^{III}]$ and $[TPA^+]$ and were directly related to the absorbance changes through a modified Beer-Lambert law, $\Delta A = \Gamma \Delta \epsilon / 1000$.⁵³ The parameters k_{Ru} and β_{Ru} were obtained from variable temperature transient absorption experiments of a cyclometalated ruthenium(II) compound without the TPA donor under the same experimental conditions. These values were substituted into equations 15 and 16 as input parameters. Finally, with these two constraints the set of coupled differential equations 15 and 16 were solved numerically with a code written in Mathematica 10 that provided synthetic decays that were minimized with respect to data shown in Fig. 3.2e-f and Figure 3.5a-b. The abstracted forward and backward rate constants, k_1 and k_{-1} , were later used in the analysis discussed in the main text.

The results of the kinetic model were presented in Table 3.4. Forward, k_1 , and reverse, k_{-1} , are given at each temperature for all four compounds. Included in the table are the equilibrium constants measured at each temperature as given by Equation 2.

Table 3.4 Rate and Equilibrium Constants from the Kinetic Analysis.

	1x			2x			1p			2p		
Temp. (K)	k_{-1} $\times 10^7$	k_1 $\times 10^6$	K_{eq}	k_{-1} $\times 10^6$	k_1 $\times 10^7$	K_{eq}	k_{-1} $\times 10^8$	k_1 $\times 10^7$	K_{eq}	k_{-1} $\times 10^7$	k_1 $\times 10^8$	K_{eq}
220	6.0	1.0	0.017	-	-	-	1.2	1.0	0.083	1.5	1.3	8.7
230	7.2	1.6	0.022	2.0	5.0	25.0	1.4	1.2	0.086	1.6	1.4	8.8

240	8.0	2.0	0.025	2.5	5.5	22.0	1.6	1.3	0.081	1.7	1.4	8.2
250	8.7	2.4	0.028	3.0	6.0	20.0	1.7	1.5	0.088	1.7	1.5	8.8
260	9.0	2.9	0.032	3.5	7.0	20.0	1.9	1.7	0.089	1.9	1.7	8.9
270	9.2	3.2	0.035	4.0	7.5	18.8	2.0	1.8	0.090	2.4	2.0	8.3
280	9.5	3.8	0.040	5.0	8.0	16.0	2.2	1.9	0.086	-	-	-
290	10	4.5	0.045	6.5	8.5	13.1	2.3	2.1	0.091	2.8	2.3	8.2
300	12	6.0	0.050	8.5	9.0	10.6	2.5	2.2	0.088	-	-	-
310	-	-	-	9.0	9.5	10.6	-	-	-	3.9	3.3	8.5
320	-	-	-	13	12	9.2	-	-	-	-	-	-

3.4.10 Derivation of the Gibbs free energy surfaces

Discussions on electron transfer theory and the energy surfaces of reactants and products can be found in the original work of Sutin and Brunschwig.¹²⁻¹³ Simplified models were derived assuming reactants/donors (D) and products/acceptors (A) potential curves behave as harmonic oscillators with identical force constants, equations 17 and 18.

$$G_D = \frac{kx^2}{2} \quad (17)$$

$$G_A = \frac{k(x-a)^2}{2} + \Delta G^0 \quad (18)$$

where k is the reduced force constant, x is the reaction coordinate, and a and ΔG^0 are the displacements of the configuration and energy, respectively, of the final-state (product) minimum relative to the initial-state (reactant) minimum. Equations 17 and 18 can be rewritten in terms of the reduced nuclear coordinate $X = x/a$. The effect of this transformation is to move the nonadiabatic minima to $X = 0$ and $X = 1$,

$$G_D = \frac{ka^2}{2} X^2 \quad (19)$$

$$G_A = \frac{ka^2}{2} (X-1)^2 + \Delta G^0 \quad (20)$$

where the constant $ka^2/2 = \lambda$ is the reorganization energy. Eq. 19 and 20 represent the zero-order potential energy surfaces for the electron transfer reaction.

The first-order potential surfaces introduce electronic coupling that causes quantum chemical mixing of donor (D) and acceptor (A) states. The coupling brakes the degeneracy of the system at the intersection of the zero-order surfaces leading to the formation of two new surfaces, named the first-order (or the adiabatic) state of the system. If one assumes that electronic coupling corresponds to a small perturbation, derivation of the equations that describe the new potential energy surfaces is analogous to that from quantum mechanics in the time-independent perturbation theory,

$$H |\Psi\rangle = G |\Psi\rangle \quad (21)$$

where $H = H_0 + \gamma V$ is the Hamiltonian containing the first-order perturbation. Recasting equation 21 in its matrix form

$$\begin{pmatrix} H_{DD} & 0 \\ 0 & H_{AA} \end{pmatrix} |\Psi\rangle = G |\Psi\rangle \quad \text{Unperturbed system}$$

$$\begin{pmatrix} H_{DD} & H_{DA} \\ H_{DA} & H_{AA} \end{pmatrix} |\Psi\rangle = G |\Psi\rangle \quad \text{Perturbed system}$$

where $H_{DD} = \langle \Psi_D | H | \Psi_D \rangle$, $H_{AA} = \langle \Psi_A | H | \Psi_A \rangle$ and $H_{DA} = \langle \Psi_D | H | \Psi_A \rangle$. Equation 21 represents the Schrödinger equation of the perturbed system and for a non-trivial solution $\det[M] = 0$ gives the secular equations below.

$$\begin{pmatrix} H_{DD} & H_{DA} \\ H_{DA} & H_{AA} \end{pmatrix} |\Psi\rangle = G I |\Psi\rangle \quad (22)$$

$$\begin{pmatrix} H_{DD} & H_{DA} \\ H_{DA} & H_{AA} \end{pmatrix} |\Psi\rangle = G \begin{pmatrix} 1 & 0 \\ 0 & 1 \end{pmatrix} |\Psi\rangle$$

$$\begin{pmatrix} H_{DD} - G & H_{DA} \\ H_{DA} & H_{AA} - G \end{pmatrix} |\Psi\rangle = 0$$

$$\det \begin{pmatrix} H_{DD} - G & H_{DA} \\ H_{DA} & H_{AA} - G \end{pmatrix} = 0$$

The roots of the equation 22 are

$$G_{\pm} = \frac{(H_{DD} + H_{AA})}{2} \pm \frac{[(H_{DD} - H_{AA})^2 + 4H_{DA}^2]^{\frac{1}{2}}}{2} \quad (23)$$

Remembering that H_{DD} and H_{AA} are the zero-order energies of the system in its initial and final state, respectively, Eq. 17 and 18 can be substituted in Eq. 23 to give¹²

$$G_{\pm} = \frac{(\lambda(2X^2 - 2X + 1) + \Delta G^0)}{2} \pm \frac{[(\lambda(2X - 1) - \Delta G^0)^2 + 4H_{DA}^2]^{\frac{1}{2}}}{2} \quad (24)$$

Equation 22 represents the new potential energy surfaces of the adiabatic system, where G_+ and G_- are the lower and upper surfaces, respectively. The lines in Figure 3.4b were constructed by inputting a known value of ΔG^0 into equation 24. For each value of λ , H_{DA} was varied from 0 to 1 eV. The first derivative of each lower potential energy surface yielded the position of the reactant and product minimum. By placing these values back into equation 22, the energy minima were obtained and later used to calculate the adiabatic Gibbs free energy difference, ΔG_{ad}^0 . The equilibrium constants were calculated using the relationship

$$K_{eq} = e^{-\frac{\Delta G_{ad}^0}{RT}}.$$

A simplified approach for direct calculation of ΔG_{ad}^0 with experimental quantities was proposed by Brunschwig and Sutin¹². With the assumptions that $H_{AB} < (\lambda + \Delta G^0)/2$ and $|\Delta G^0| < \lambda$, the positions of the product and reactant minima can be approximated to

$$X_{min,D} = \frac{H_{DA}^2}{(\lambda + \Delta G^0)^2} \quad (25)$$

$$X_{min,A} = 1 - \frac{H_{DA}^2}{(\lambda - \Delta G^0)^2} \quad (26)$$

Equations 23 and 24 were substituted into the lower surface, G_+ , equation 22 to give the energy values corresponding to the minima. The difference between them gives the Gibbs free energy corrected for the donor-acceptor interaction, i.e., the adiabatic Gibbs free energy, ΔG_{ad}^0 ,

$$\Delta G_{ad}^0 = \Delta G^0 \left[1 - \frac{2H_{DA}^2}{(\lambda^2 - \Delta G^{0^2})} \right] \quad (27)$$

3.4.11 The adiabatic double minimum limit

As the electronic coupling between acceptor (A) and donor (D) increases in the progression from nonadiabatic to adiabatic GES, the double minimum regime eventually collapses into a true single minimum, Figure 3.8. Under the condition of very large H_{DA} , the electron is sufficiently delocalized over the redox centers of interest such that equilibrium no longer has any physical meaning. In order to more quantitatively understand the adiabatic

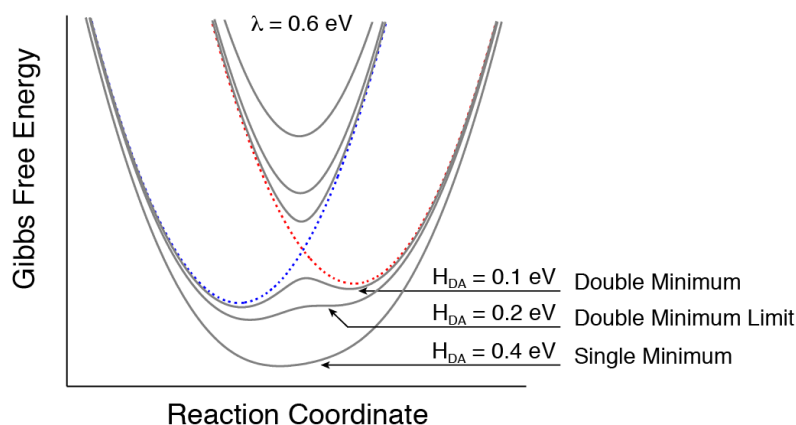


Figure 3.7. Gibbs free energy surfaces generated from equation 22 for fixed $\lambda = 0.6$ eV and $\Delta G^\circ = 70$ mV with the indicated H_{DA} values. For $H_{DA} = 0.1$ eV an adiabatic double minimum GES occurs. At $H_{DA} = 0.2$ eV, the energy minimum of the donor, $G(D)$, equals that of the transition state, $G(TS)$. When H_{DA} values are greater than 0.2 eV, for instance $H_{DA} = 0.4$ eV, the acceptor and donor GES collapses to a single minimum.

double minimum limit in terms of H_{DA} , GESs were generated with multiple combinations of ΔG° and λ with varying H_{DA} , and were then analyzed.

As previously described, the energies of the product and reactant minima and the transition state can be obtained through the first derivative analysis of lower GES given in equation 22, $dG_+/dX = 0$. It will be assumed that the distinct reactant and product minima survives whenever the energy of the donor minimum is equal or lower than the energy of the transition state, i.e. $|G(D)| \leq |G(TS)|$, Fig. 2 and 3a. For example, when $\lambda = 0.6$, the double minimum GES survives at $H_{DA} \leq 0.2$ eV. For simplicity, the values of H_{DA} necessary to collapse the GESs into a single minimum will be termed the H_{DA} cutoff.

The construction of the GESs are highly sensitive to the input values of ΔG° and λ and so is the H_{DA} cutoff. Figure 3.9a displays the energies of the acceptor and donor minima and the transition state with varying H_{DA} for fixed $\lambda = 0.6$ eV and $\Delta G^\circ = 70$ mV. The double minimum limit is highlighted when $G(D) = G(TS)$. Moreover, the H_{DA} cutoff increases linearly with λ for a fixed $\Delta G^\circ = 70$ mV.

Figure 3.9b presents a compilation of multiple H_{DA} *cutoff* for different combinations of ΔG° and λ . At first, it's evident that the double minimum survives at higher H_{DA} values when ΔG° approaches to zero; condition often seen for self-exchange electron transfer reactions. Similarly, the H_{DA} *cutoff* becomes larger as the reorganization energy increase.

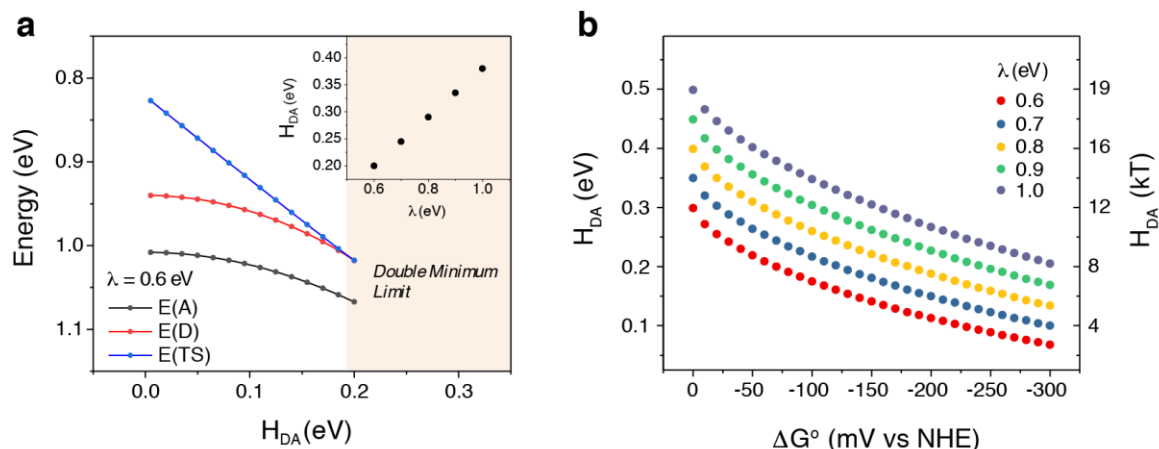


Figure 3.8. a) Energy values abstracted for the acceptor and donor minima and the transition state with fixed $\lambda = 0.6$ eV and $\Delta G^\circ = 68$ mV, with varying H_{DA} . The inset highlights the H_{DA} value at which the acceptor and donor GESs collapses to a single minimum for different values of λ . b) H_{DA} values (in eV and kT) units necessary to collapse the GESs into a single minimum for multiple combinations of ΔG° and λ .

3.4.12 Acknowledgements

The University of North Carolina (UNC) authors gratefully acknowledge support from the Division of Chemical Sciences, Office of Basic Energy Sciences, Office of Energy Research, U.S. Department of Energy (Grant DE-SC0013461). L. T.-G. would like to acknowledge the Belgian American Educational Foundation (BAEF) as well as the Bourse d'excellence Wallonie-Bruxelles International (WBI.World) for postdoctoral funding. The University of British Columbia authors are grateful to the Canadian Natural Science and Engineering Research Council (RGPIN 337345-13), Canadian Foundation for Innovation

(229288), Canadian Institute for Advanced Research (BSE-BERL-162173), and Canada Research Chairs for financial support.

REFERENCES

1. Winkler, J. R.; Gray, H. B., Electron flow through metalloproteins. *Chem. Rev.* **2014**, *114* (7), 3369-3380.
2. Cardona, T.; Sedoud, A.; Cox, N.; Rutherford, A. W., Charge separation in photosystem ii: A comparative and evolutionary overview. *Biochim. Biophys. Acta* **2012**, *1817* (1), 26-43.
3. Romero, E.; Novoderezhkin, V. I.; van Grondelle, R., Quantum design of photosynthesis for bio-inspired solar-energy conversion. *Nature* **2017**, *543* (7645), 355-365.
4. Feher, G.; Allen, J. P.; Okamura, M. Y.; Rees, D. C., Structure and function of bacterial photosynthetic reaction centres. *Nature* **1989**, *339* (6220), 111-116.
5. Whitmarsh, J.; Govindjee, Photosystem ii. *eLS* **2001**.
6. Barber, J., Electron-transfer theory in question. *Nature* **1988**, *333* (6169), 114-114.
7. Gust, D.; Moore, T. A.; Moore, A. L., Mimicking photosynthetic solar energy transduction. *Acc. Chem. Res.* **2001**, *34* (1), 40-48.
8. Gust, D.; Moore, T. A.; Moore, A. L., Solar fuels via artificial photosynthesis. *Acc. Chem. Res.* **2009**, *42* (12), 1890-1898.
9. Wasielewski, M. R., Photoinduced electron transfer in supramolecular systems for artificial photosynthesis. *Chem. Rev.* **1992**, *92* (3), 435-461.
10. Kärkäs, M. D.; Verho, O.; Johnston, E. V.; Åkermark, B., Artificial photosynthesis: Molecular systems for catalytic water oxidation. *Chem. Rev.* **2014**, *114* (24), 11863-12001.
11. Ashford, D. L.; Gish, M. K.; Vannucci, A. K.; Brennaman, M. K.; Templeton, J. L.; Papanikolas, J. M.; Meyer, T. J., Molecular chromophore–catalyst assemblies for solar fuel applications. *Chem. Rev.* **2015**, *115*, 13006-13049.
12. Brunschwig, B. S.; Sutin, N., Energy surfaces, reorganization energies, and coupling elements in electron transfer. *Coord. Chem. Rev.* **1999**, *187* (1), 233-254.
13. Sutin, N., Theory of electron transfer reactions: Insights and hindsights. In *Progress in inorganic chemistry: An appreciation of henry taube*, John Wiley & Sons, Inc.: Published Online, 2007; Vol. 30, pp 441-498.
14. Ito, T.; Imai, N.; Yamaguchi, T.; Hamaguchi, T.; Londergan, C. H.; Kubiak, C. P., Observation and dynamics of “charge-transfer isomers”. *Angew. Chem. Int. Ed.* **2004**, *43* (11), 1376-1381.
15. Londergan, C. H.; Salsman, J. C.; Lear, B. J.; Kubiak, C. P., Observation and dynamics of “mixed-valence isomers” and a thermodynamic estimate of electronic coupling parameters. *Chem. Phys.* **2006**, *324* (1), 57-62.

16. Hu, K.; Blair, A. D.; Piechota, E. J.; Schauer, P. A.; Sampaio, R. N.; Parlane, F. G. L.; Meyer, G. J.; Berlinguette, C. P., Kinetic pathway for interfacial electron transfer from a semiconductor to a molecule. *Nat. Chem.* **2016**, 8 (9), 853-859.
17. Marcus, R. A., Electron transfer reactions in chemistry. Theory and experiment. *Reviews of Modern Physics* **1993**, 65 (3), 599-610.
18. Day, P.; Hush, N. S.; Clark, R. J. H., Mixed valence: Origins and developments. *Phil. Trans. R. Soc. A* **2008**, 366, 5-14.
19. "Equilibrium", Equilibrium. In *Merriam-Webster.com*, Merriam-Webster, 2017.
20. Oxtoby, D. W.; Gillis, H. P.; Butler, L. J., *Principles of modern chemistry*. 8th ed.; Cengage Learning: 2015.
21. Walker, G. C.; Barbara, P. F.; Doorn, S. K.; Dong, Y.; Hupp, J. T., Ultrafast measurements on direct photoinduced electron transfer in a mixed-valence complex. *J. Phys. Chem.* **1991**, 95 (15), 5712-5715.
22. Nelsen, S. F.; Ismagilov, R. F.; Trieber, D. A., Adiabatic electron transfer: Comparison of modified theory with experiment. *Science* **1997**, 278, 846-849.
23. Lindeman, S. V.; Rosokha, S. V.; Sun, D.; Kochi, J. K., X-ray structure analysis and the intervalent electron transfer in organic mixed-valence crystals with bridged aromatic cation radicals. *J. Am. Chem. Soc.* **2002**, 124 (5), 843-855.
24. Laws, W. R.; Brand, L., Analysis of two-state excited-state reactions. The fluorescence decay of 2-naphthol. *J. Phys. Chem.* **1979**, 83 (7), 795-802.
25. Demas, J. N., Chapter 4 - more complex systems. In *Excited state lifetime measurements*, Demas, J. N., Ed. Academic Press: 1983; pp 43-69.
26. O'Donnell, R. M.; Sampaio, R. N.; Li, G.; Johansson, P. G.; Ward, C. L.; Meyer, G. J., Photoacidic and photobasic behavior of transition metal compounds with carboxylic acid group(s). *J. Am. Chem. Soc.* **2016**, 138 (11), 3891-3903.
27. Robson, K. C. D.; Koivisto, B. D.; Gordon, T. J.; Baumgartner, T.; Berlinguette, C. P., Triphenylamine-modified ruthenium(ii) terpyridine complexes: Enhancement of light absorption by conjugated bridging motifs. *Inorg. Chem.* **2010**, 49 (12), 5335-5337.
28. Cave, R. J.; Newton, M. D., Generalization of the mulliken-hush treatment for the calculation of electron transfer matrix elements. *Chemical Physics Letters* **1996**, 249 (1), 15-19.
29. Rust, M.; Lappe, J.; Cave, R. J., Multistate effects in calculations of the electronic coupling element for electron transfer using the generalized mulliken-hush method. *J. Phys. Chem. A* **2002**, 106 (15), 3930-3940.

30. Cave, R. J.; Edwards, S. T.; Kouzelos, J. A.; Newton, M. D., Reduced electronic spaces for modeling donor/acceptor interactions. *J. Phys. Chem. B* **2010**, *114* (45), 14631-14641.
31. Moser, C. C.; Keske, J. M.; Warncke, K.; Farid, R. S.; Dutton, P. L., Nature of biological electron transfer. *Nature* **1992**, *355* (6363), 796-802.
32. Page, C. C.; Moser, C. C.; Chen, X.; Dutton, P. L., Natural engineering principles of electron tunnelling in biological oxidation-reduction. *Nature* **1999**, *402* (6757), 47-52.
33. Osyczka, A.; Moser, C. C.; Daldal, F.; Dutton, P. L., Reversible redox energy coupling in electron transfer chains. *Nature* **2004**, *427* (6975), 607-612.
34. Moia, D.; Leijtens, T.; Noel, N.; Snaith, H. J.; Nelson, J.; Barnes, P. R. F., Dye monolayers used as the hole transporting medium in dye-sensitized solar cells. *Adv. Mater.* **2015**, *27* (39), 5889-5894.
35. O'Regan, B. C.; Walley, K.; Juozapavicius, M.; Anderson, A.; Matar, F.; Ghaddar, T.; Zakeeruddin, S. M.; Klein, C. d.; Durrant, J. R., Structure/function relationships in dyes for solar energy conversion: A two-atom change in dye structure and the mechanism for its effect on cell voltage. *J. Am. Chem. Soc.* **2009**, *131* (10), 3541-3548.
36. Sutton, J. E.; Taube, H., Metal to metal interactions in weakly coupled mixed-valence complexes based on ruthenium ammines. *Inorg. Chem.* **1981**, *20* (10), 3125-3134.
37. Reynolds, W. L.; Lumry, R. W., *Mechanisms of electron transfer*. The Ronald Press Co.: New York, 1966.
38. Marcus, R. A.; Sutin, N., Electron transfers in chemistry and biology. *Biochim. Biophys. Acta* **1985**, *811* (3), 265-322.
39. Troian-Gautier, L.; Beauvilliers, E. E.; Swords, W. B.; Meyer, G. J., Redox active ion-paired excited states undergo dynamic electron transfer. *J. Am. Chem. Soc.* **2016**, *138* (51), 16815-16826.
40. Wu, B.; Maroncelli, M.; Castner, E. W., Photoinduced bimolecular electron transfer in ionic liquids. *J. Am. Chem. Soc.* **2017**.
41. Argazzi, R.; Bignozzi, C. A.; Heimer, T. A.; Castellano, F. N.; Meyer, G. J., Enhanced spectral sensitivity from ruthenium(ii) polypyridyl based photovoltaic devices. *Inorg. Chem.* **1994**, *33* (25), 5741-5749.
42. Farnum, B. H.; Morseth, Z. A.; Lapidus, A. M.; Rieth, A. J.; Hoertz, P. G.; Brennaman, M. K.; Papanikolas, J. M.; Meyer, T. J., Photoinduced interfacial electron transfer within a mesoporous transparent conducting oxide film. *J. Am. Chem. Soc.* **2014**, *136* (6), 2208-2211.
43. Pavlishchuk, V.; Addison, A. W., Conversion constants for redox potentials measured versus different reference electrodes in acetonitrile solutions at 25°C. *Inorg. Chim. Acta.* **2000**, *298*, 97-102.

44. Frisch, M. J.; Trucks, G. W.; Schlegel, H. B.; Scuseria, G. E.; Robb, M. A.; Cheeseman, J. R.; al, e., *Gaussian 09, revision b.01*. Gaussian, Inc.: Wallingford CT, 2010.
45. D'Alessandro, D. M.; Keene, F. R., Current trends and future challenges in the experimental, theoretical and computational analysis of intervalence charge transfer (ivct) transitions. *Chem. Soc. Rev.* **2006**, *35* (5), 424-440.
46. Brunschwig, B. S.; Creutz, C.; Sutin, N., Electroabsorption spectroscopy of charge transfer states of transition metal complexes. *Coord. Chem. Rev.* **1998**, *177* (1), 61-79.
47. Demadis, K. D.; Hartshorn, C. M.; Meyer, T. J., The localized-to-delocalized transition in mixed-valence chemistry. *Chem. Rev.* **2001**, *101* (9), 2655-2686.
48. Mulliken, R. S.; Person, W. B., *Molecular complexes*. Wiley: New York, 1969.
49. Loken, M. R.; Hayes, J. W.; Gohlke, J. R.; Brand, L., Excited-state proton transfer as a biological probe. Determination of rate constants by means of nanosecond fluorometry. *Biochemistry* **1972**, *11* (25), 4779-4786.
50. Nelson, J., Continuous-time random-walk model of electron transport in nanocrystalline TiO_2 electrodes. *Phys. Rev. B* **1999**, *59* (23), 15374-15380.
51. Nelson, J.; Haque, S.; Klug, D.; Durrant, J., Trap-limited recombination in dye-sensitized nanocrystalline metal oxide electrodes. *Phys. Rev. B* **2001**, *63* (20), 205321.
52. Barzykin, A. V.; Tachiya, M., Mechanism of charge recombination in dye-sensitized nanocrystalline semiconductors: Random flight model. *J. Phys. Chem. B* **2002**, *106* (17), 4356-4363.
53. Trammell, S. A.; Meyer, T. J., Diffusional mediation of surface electron transfer on TiO_2 . *J. Phys. Chem. B* **1998**, *103* (1), 104-107.

Chapter 4. Entropic barriers determine adiabatic electron transfer equilibrium³

4.1 Introduction

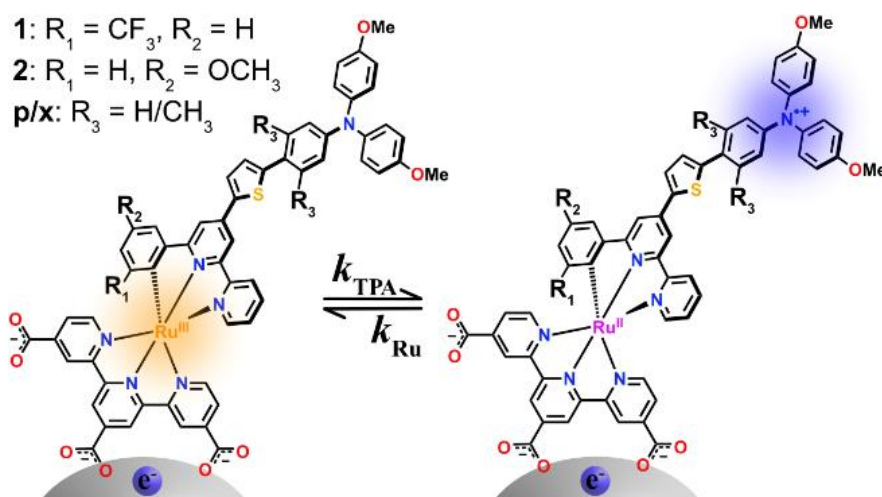
Thermodynamic activation energies ultimately underlie the population and lifetimes of electron transfer products of light initiated reactions in molecular excited states as well as subsequent thermal reactions important for energy conversion, storage, and catalysis.¹⁻⁶ Despite a large body of research on the influence of donor-acceptor electronic coupling, H_{DA} , on inter- and intramolecular electron transfer kinetics, a comparative study of activation barriers for strongly and weakly coupled electron transfer reactions remain elusive. Weakly coupled (non-adiabatic) electron transfer reactions have been well-studied in proteins and bimolecular cases with great success.⁷⁻¹² In contrast, kinetic data for strongly coupled (adiabatic) intramolecular electron transfer reactions is rather limited, despite the existence of a sophisticated theoretical framework.¹³⁻¹⁴ Thus, studies of structurally similar compounds that can be synthetically modified to exhibit strong or weak coupling present an opportunity to elucidate the influence of coupling on the enthalpic and entropic barriers for electron transfer.

A recently reported experimental approach has provided direct kinetic data on the influence of electronic coupling on the standard Gibbs free energy change, ΔG° , for some specific acceptor-bridge-donor (A-B-D) compounds that undergo intramolecular electron

³ This work was previously published in *The Journal of Physical Chemistry C*, 123 (6), 3416 with contributions from Eric J. Piechota, Renato N. Sampaio, Ludovic Troian-Gautier, Andrew B. Maurer, Curtis P. Berlinguette, and Gerald J. Meyer. Reproduced with permission. Copyright 2019.

transfer on the nanosecond timescale.¹⁵ Kinetic data for four A-B-D compounds based on a bis(tridentate)cyclometalated Ru^{II} center covalently linked to a triphenylamine (TPA) through either a phenyl- or xylyl-thiophene bridge were utilized, **Scheme 4.1**. Compounds were anchored onto mesoporous TiO₂ thin films and, following light excitation, ultrafast electron injection into TiO₂ led to the generation of Ru^{III}. As a result, a quasi-equilibrium between Ru^{III/II} and TPA⁺⁰ was established and the kinetics of electron transfer between TPA and Ru^{III} centers were measured.¹⁵

Scheme 4.1. Redox equilibrium after excited state injection to TiO₂.



Equilibrium constants permitted the spectroscopic determination of the forward (k_{TPA} , TPA \rightarrow Ru^{III}) and reverse (k_{Ru} , Ru^{II} \rightarrow TPA⁺) electron transfer rate constants corresponding to the equilibrium reaction defined by Eq. 1. The driving force was controlled by substituents on the cyclometalating ligand to either inhibit ($\Delta G^\circ > 0$ for 1) or promote ($\Delta G^\circ < 0$ for 2) electron transfer from TPA to the Ru^{III} center created after excited state injection into TiO₂.¹⁶



Indeed, prior analysis of the intervalence charge transfer bands in the one-electron oxidized forms of the compounds revealed that the phenyl bridge promoted strong electronic coupling, H_{DA} , between the Ru^{II} and TPA centers and adiabatic ($H_{DA} > 1000\text{ cm}^{-1}$) electron transfer while the methyl groups of the xylyl bridge disrupted conjugation that presumably resulted in non-adiabatic transfer, $H_{DA} \leq 150\text{ cm}^{-1}$.¹⁷

Here we report Eyring analysis of these data that provides the enthalpy and entropy of activation. For adiabatic electron transfer the barrier was predominantly determined by entropic factors rather than enthalpic contributions. Interestingly, the free energy barriers, ΔG^\ddagger , were nearly the same for the adiabatic and non-adiabatic electron transfer. This was in stark contrast to an experimentalists assumption that enhanced coupling decreases the barrier for electron transfer.¹⁸⁻¹⁹ The implication(s) of these experimental advances on electron transfer are discussed.

4.2 Results

The kinetic data used in this study was collected from a previous report that focused on the change in the free energy that accompanies electron transfer in the (non-)adiabatic limits without regard to the barriers. Thin films of TiO_2 were sensitized to visible light with compounds **1x**, **1p**, **2x**, and **2p** as surface coverages less than half the saturation value. The films were then immersed in 100 mM $LiClO_4/CH_3CN$ solutions. Pulsed laser excitation resulted in rapid ($k_{inj} > 10^8\text{ s}^{-1}$) excited-state electron injection and a quasi-equilibrium as described in Scheme 4.1 and Eq. 1. Equilibration was quantified on a nanosecond and longer timescales over a 220-330 K range. Additional experimental details are provided in ref. 13.¹⁵

A van't Hoff analysis of the kinetic data for the compounds revealed that when the bridge orbitals promoted strong D-A electronic coupling the reaction was adiabatic, $\Delta H^\circ = 0\text{ kJ mol}^{-1}$

^{1,15} When the bridge was more insulating, the reaction was non-adiabatic, $\Delta H^\circ \neq 0 \text{ kJ mol}^{-1}$, Figure 1 and Table 3.1. This analysis also indicated that when $H_{\text{DA}} > 1000 \text{ cm}^{-1}$, the driving force for the reaction, $|\Delta G^\circ|$, was reduced in accordance with theoretical predictions.¹⁵ Standard entropies for the reaction were also garnered from the intercept of the van't Hoff analysis. Interestingly, it was apparent that in the **p**-series a large entropy term, $|\Delta S^\circ| = 18 \text{ J mol}^{-1} \text{ K}^{-1}$ was noted in stark contrast to the **x**-series which had only a marginal standard entropy change, $|\Delta S^\circ| = 2 \text{ J mol}^{-1} \text{ K}^{-1}$.

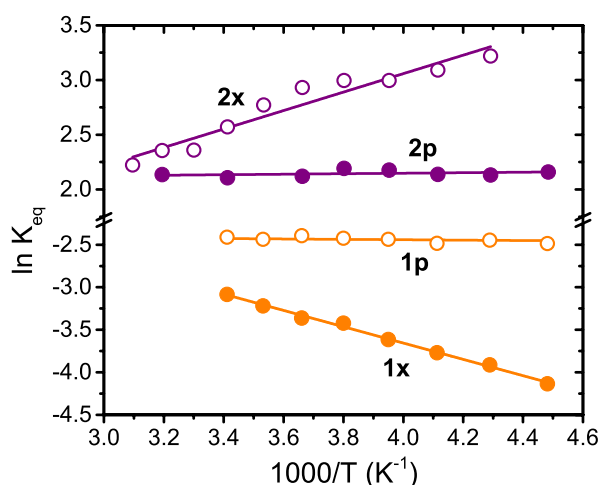


Figure 4.1 van't Hoff plot of electron transfer equilibrium constants for the studied compounds.¹⁵ Adapted from Ref. 15. Uncertainty in $\ln(K_{\text{eq}})$ is ± 0.05 .

Table 4.1. Thermodynamic values for the indicated compounds in the redox equilibrium of Eq. 1.

Cmpd	$\Delta H^{\circ\text{a,b,c}}$	$\Delta S^{\circ\text{a,c,e}}$	$\Delta G^{\circ\text{b,d,e}}$	E° (TPA ⁺⁰) ^a	E° (Ru ^{III/II}) ^a
1x	$+7.9 \pm 0.2$	$+1.5 \pm 0.2$	$+7.4 \pm 0.2$	940	860
1p	0.0 ± 0.2	-18 ± 0.2	$+5.9 \pm 0.2$	940	860
2x	-7.0 ± 0.2	-2.6 ± 0.2	-6.2 ± 0.2	940	1010
2p	0.0 ± 0.2	$+17 \pm 0.2$	-5.2 ± 0.2	940	1030

^aFrom Ref 13. ^bkJ mol⁻¹ ^cJ mol⁻¹ K⁻¹ ^dT = 298 K. ^eUncertainties were calculated from a least-squares analysis. Note: thermodynamic values are defined relative to the TPA⁺⁰ redox couple.

Moving away from standard thermodynamic quantities, it is clear that the kinetic barriers will also provide insight following theoretical predictions: 1) the activation barriers are reduced in the presence of strong coupling, and 2) pre-exponential factors provide quantitative insights into reaction adiabaticity through the entropy of activation. Initial treatment of the temperature dependent data with the Arrhenius expression revealed very different pre-exponential factors between the xylyl- and phenyl-bridged compounds indicative of dynamical differences between the two mechanisms. Arrhenius analysis provided activation energies (E_a) and pre-exponential factors, $\ln(A)$, while Eyring analysis provided enthalpies (ΔH^\ddagger), entropies (ΔS^\ddagger) and Gibbs Free (ΔG^\ddagger) energies of activation for the forward and reverse electron transfer reactions by Eq. 2.

$$\ln\left(\frac{k}{T}\right) = -\frac{\Delta H^\ddagger}{R} \frac{1}{T} + \frac{\Delta S^\ddagger}{R} + \ln\left(\frac{k_b}{h}\right) \quad (2)$$

where k is the rate constant for a particular reaction, k_b is the Boltzmann's constant, and h is Planck's constant.

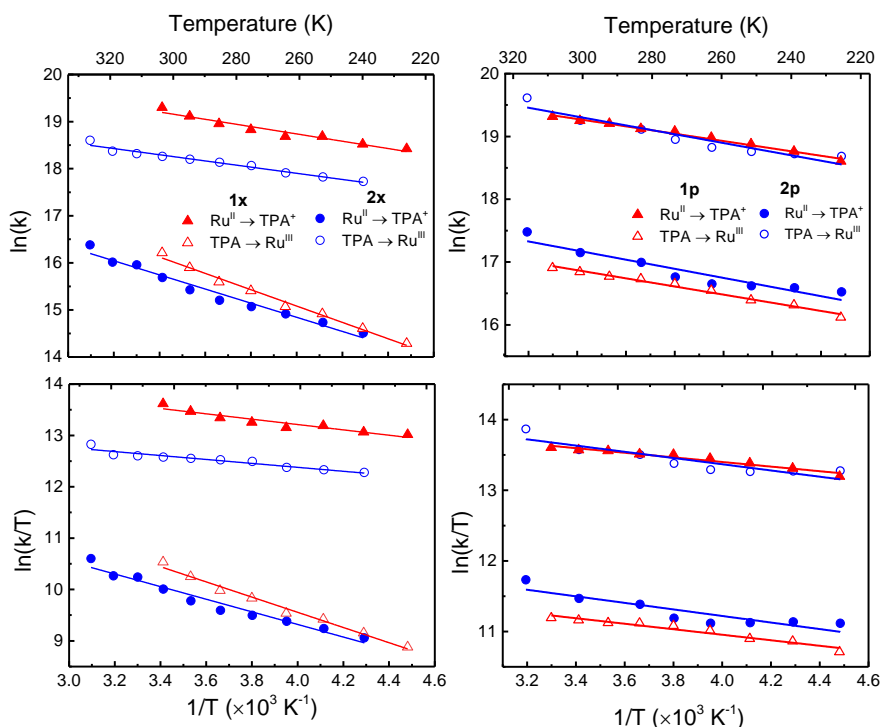


Figure 4.2. Arrhenius (top) and Eyring analysis (bottom) for the forward, $\text{TPA} \rightarrow \text{Ru}^{\text{III}}$, k_{TPA} , (open shapes) and reverse, $\text{Ru}^{\text{II}} \rightarrow \text{TPA}^+$, k_{Ru} (solid shapes) electron transfer rate constants for **1x**, **1p** (red triangles) and **2x**, **2p** (blue circles). Errors in the rate constants are $\pm 5\%$.

The overlaid solid lines demonstrate a good fit of the kinetic data to the Arrhenius and Eyring models, Figure 2. The extracted thermodynamic activation energies for each reaction are summarized in **Table 2**, and Arrhenius analysis results are included. For clarity, k_{TPA} is the rate constant for the reaction $\text{TPA} \rightarrow \text{Ru}^{\text{III}}$ while k_{Ru} is the reverse process, $\text{Ru}^{\text{II}} \rightarrow \text{TPA}^+$. The driving force for the equilibrium reaction, as written, is uphill for **1x** and **1p** and downhill for **2x** and **2p**. That is to say that k_{Ru} and k_{TPA} can represent thermodynamically uphill or downhill reactions depending on the cyclometalating substituent.

Table 4.2. Activation parameters for intramolecular electron transfer in the xylyl-bridged (nonadiabatic) and phenyl-bridged (adiabatic) compounds.

	1x		2x		1p		2p	
	k_{TPA}	k_{Ru}	k_{TPA}	k_{Ru}	k_{TPA}	k_{Ru}	k_{TPA}	k_{Ru}
$\Delta H^{\ddagger a,d}$	12.3 \pm 0.6	4.3 \pm 0.6	3.2 \pm 0.3	10.2 \pm 0.7	3.2 \pm 0.2	2.7 \pm 0.2	3.6 \pm 0.7	3.8 \pm 0.7
$\Delta S^{\ddagger b,d}$	-70 \pm 2	-70 \pm 2	-80 \pm 3	-80 \pm 1	-94 \pm 2	-75 \pm 2	-70 \pm 3	-89 \pm 1
$\Delta G^{\ddagger a,c,d}$	32.8 \pm 0.9	25.3 \pm 0.8	27.0 \pm 0.5	34 \pm 1	30.4 \pm 0.3	25 \pm 0.2	24 \pm 1	30 \pm 1
$E_a^{a,d}$	14.4 \pm 0.6	6.4 \pm 0.6	5.4 \pm 0.3	12.5 \pm 0.7	5.4 \pm 0.2	4.8 \pm 0.2	5.8 \pm 0.7	6.0 \pm 0.8
$\ln(A)$	22.0 \pm 0.3	21.8 \pm 0.3	20.5 \pm 0.3	20.8 \pm 0.2	19.1 \pm 0.1	21.3 \pm 0.3	21.7 \pm 0.3	19.6 \pm 0.4

^akJ mol⁻¹ ^bJ mol⁻¹ K⁻¹. ^cT = 298 K. ^dUncertainties were calculated from the results of least-squares analysis of the data.

4.3 Discussion

A van't Hoff analysis of the kinetic data afforded standard enthalpies and entropies for electron transfer between the $\text{Ru}^{\text{III/II}}$ and $\text{TPA}^{+/0}$ centers. For the phenyl-bridged compounds, the electron transfer reaction was adiabatic, $\Delta H^\circ = 0$ kJ mol⁻¹. Compounds that contained a xylyl-bridge, which disrupted conjugation, the reaction was non-adiabatic, $\Delta H^\circ \neq 0$ kJ mol⁻¹. The analysis also indicated that the Gibbs free energy, ΔG° , accompanying electron transfer was reduced in the phenyl bridged compounds relative to the weakly coupled xylyl-bridged

compounds, *i.e.* $|\Delta G^{\circ}_{\text{ad}}| < |\Delta G^{\circ}|$. Further, the standard entropy change ΔS° was substantially different between the two kinetic limits. Spectroelectrochemical experiments and interfacial electron transfer recombination kinetics indicated two discrete redox reactions to either $\text{Ru}^{\text{III/II}}$ or $\text{TPA}^{+/0}$ regardless of the bridge structure.^{17, 20} This observation implies that, despite strong electronic coupling in the phenyl-bridged compounds, $H_{\text{DA}} > 1000 \text{ cm}^{-1}$, the redox chemistry was localized and discrete minima for reactants and products exist. Hence, entropic and enthalpic *barriers* for electron transfer were measurable.²⁰

Many previously reported models for electron transfer partition the entropy and enthalpy of activation into a pre-exponential factor and a Boltzmann-weighted exponential term, respectively. The magnitude of the activation entropy is further dependent on the adiabaticity of the reaction and, in some cases, the kinetic model applied. As such, we first consider the common models of Eyring and Marcus and account for the influence of coupling on the pre-exponential factors. We then apply these models to the kinetic data reported herein to quantify entropies, enthalpies, and free energies of activation for adiabatic and non-adiabatic electron transfer. Determination of H_{DA} is briefly addressed and calculations of the total reorganization energy, λ , are presented. Finally, the entropic barriers are discussed in the context of vibrational entropy and solvent dynamical effects on the electron transfer reactions.

4.3.1 Pre-exponential factors

It is critical to establish criteria for appropriate use of pre-exponential factors. Within this section, such criteria are presented and discussed in context of the studied compounds. Arrhenius analysis, $k_{\text{et}} = A \exp(-E_a/k_b T)$, takes the ratio of forward and reverse pre-

(3)

exponential factors to provide information on the standard entropy change, ΔS° , through Eq. 3.²¹

$$\frac{A_{TPA}}{A_{Ru}} = \frac{\exp(S_{TPA}/k_b)}{\exp(S_{Ru}/k_b)} = \exp\left(\frac{\Delta S^\circ}{k_b}\right) \quad (3)$$

Where A_{TPA} and A_{Ru} are the pre-exponential factors for $Ru^{II} \rightarrow TPA^+$ and $TPA \rightarrow Ru^{III}$ electron transfer reactions. In this case, however, no explicit expression is written for ΔS^\ddagger . Analysis of the pre-exponential factors yielded standard entropies that were in good agreement with the results of the van't Hoff treatment. Values extracted from the van't Hoff analysis are given in Table 1 and those from Arrhenius analysis in Table 3.3.

In transition state theory, the pre-exponential factor yields ΔS^\ddagger directly as it is temperature independent, Eq. 4. Here, κ_{el} is the transmission coefficient, T is the temperature, and $\Delta G^\ddagger = \Delta H^\ddagger - T\Delta S^\ddagger$. Notably H_{DA} and λ do not appear in the rate expression explicitly. When $\kappa_{el} = 1$ this approach is elegant and applied easily provided that the reaction is truly adiabatic.

$$k_{et} = \kappa_{el} \frac{k_b T}{h} e^{\left(-\frac{\Delta G^\ddagger}{k_b T}\right)} = \kappa_{el} \frac{k_b T}{h} e^{\left(-\frac{\Delta H^\ddagger}{k_b T} + \frac{\Delta S^\ddagger}{k_b}\right)} \quad (4)$$

Hence, a subtle yet important detail is properly accounting for non-adiabaticity.²²⁻²³

Adiabaticity has previously been accounted for through the Landau-Zener electronic transmission coefficient, κ_{el} , calculated through Eq. 5, which uses electronic, ν_{el} , and nuclear, ν_n , frequency factors²⁴

$$\kappa_{el} = \frac{2[1 - \exp(\nu_{el}/2\nu_n)]}{2 - \exp(\nu_{el}/2\nu_n)} = \exp\left(\frac{\Delta S_{el}^\ddagger}{k_b}\right) \quad (5)$$

with ν_{el} given by Eq. 6.

$$\nu_{el} = \frac{2\pi}{\hbar} \frac{H_{DA}^2}{\sqrt{\lambda k_b T}} \quad (6)$$

Here ν_n is a vibrational frequency taken as k_bT/h , as in transition state theory, or in some cases as high frequency modes if they dominate the reaction coordinate, and λ is the reorganization energy.²⁵ This factor represents the probability of the reaction proceeding from the reactant surface, through the transition state, and ultimately to the product potential energy surface. Generally, when $\nu_{el} \gg 2\nu_n$, the reaction is adiabatic, $\kappa_{el} = 1$, and rate limited by ν_n . For $\lambda = 1$ eV and $\nu_n = k_bT/h$, adiabaticity is achieved at $H_{DA} = 300 \text{ cm}^{-1} ((3/2)k_bT)$, that is $\kappa_{el} > 0.9$. Of course, the additional entropic contributions from κ_{el} arise as a result of the limited orbital mixing, i.e. *delocalization*, between the redox centers which necessitates a particular electronic structure to be achieved in order to undergo electron transfer.

Marcus and Sutin have derived Eq. 7 which partitions the measured activation entropy into a sum of nuclear and electronic entropies. In other words, ΔS^\ddagger is a sum of nuclear and electronic entropy contributions.^{5, 23}

$$\Delta S^\ddagger = \Delta S_n^\ddagger + \Delta S_{el}^\ddagger = \Delta S_n^\ddagger + k_b \ln(\kappa_{el}) \quad (7)$$

where ΔS_n^\ddagger is the inherent nuclear entropy arising from solvent and vibrational motion and ΔS_{el}^\ddagger is the entropy arising from the reaction (non-)adiabaticity. In principle, calculation of κ_{el} subsequently allows one to correct for non-adiabaticity. Electronic factors contribute to ΔS^\ddagger when $\kappa_{el} \neq 1$. Hence, the minimum entropic barrier is realized when $\kappa_{el} = 1$ and the reaction is adiabatic. On the other hand, when $\kappa_{el} < 0.5$, the factor $k_b \ln(\kappa_{el})$ can become significant, on the order of $-6 \text{ J mol}^{-1} \text{ K}^{-1}$.

Turning now to Marcus theory, a continuum description for the influence of electronic coupling on the rate of electron transfer is given by Eq. 8.²⁶

$$k_{ET} = \frac{2\pi}{\hbar} \frac{|H_{DA}|^2}{\sqrt{4\pi\lambda k_bT}} \left[\frac{1}{1 + \kappa_A} \right] \exp \left(\frac{\Delta G^\ddagger}{k_bT} \right) \quad (8)$$

Where κ_A is the Rips-Jortner adiabaticity factor given by Eq. 9.²⁷

$$\kappa_A = \frac{4\pi\tau_L H_{DA}^2}{\hbar\lambda} \quad (9)$$

Here, τ_L , is the longitudinal solvent reorientation lifetime which is a constant for a given solvent. This adiabaticity factor, κ_A , indicates the extent to which solvent motion influences a reaction rate. When $\kappa_A \gg 1$, the electron transfer rate expression becomes independent of H_{DA} , Eq. 10,²⁸

$$k_{ET} = \frac{1}{\tau_L} \sqrt{\frac{\lambda}{16\pi k_b T}} \exp\left(-\frac{\Delta G^\ddagger}{k_b T}\right) \quad (10)$$

and the adiabatic reaction is defined as solvent-controlled.²⁹ Solvent dipole reorientation is slower than low-frequency vibrational modes, $\sim 200 \text{ cm}^{-1}$, and becomes the rate limiting factor for the reaction discussed in more detail below.³⁰

A final point lies in the temperature dependent rate constants. Prior to linear regression analysis, rate constants are temperature-normalized to account for the temperature factor within the pre-exponential term. As a result, temperature factors in Eyring, $\ln(k/T)$, and Marcus, $\ln(kT^{1/2})$, analysis vs. $1/T$ yield different slopes (and intercepts). The general relationship between Marcus and Eyring models is given by Eq. 11

$$\Delta H_M^\ddagger = \Delta H_E^\ddagger + \frac{3}{2}k_b T \quad (11)$$

where ΔH_M^\ddagger and ΔH_E^\ddagger are the Marcus and Eyring enthalpies of activation, respectively, provided they are on the order of $k_b T$ as is the present case. The relationship between the two kinetic models arises as a result of the Gibbs-Helmholtz relation. A derivation is presented in the SI analogous to the well-known relationship between Eyring and Arrhenius analysis where $E_a = \Delta H_E^\ddagger - k_b T$.³¹ Importantly, the total Gibbs Free energy of activation, ΔG^\ddagger , were

model independent. When $\kappa_A \gg 1$, the maximum pre-exponential factor for a solvent-controlled adiabatic reaction, Eq. 10, is predicted to be $7 \times 10^{13} \text{ s}^{-1}$ with $\lambda = 1 \text{ eV}$ in acetonitrile. Under Eyring analysis, the maximum is $k_b/h = 2 \times 10^{10} \text{ s}^{-1}$ – a three order of magnitude difference that is accounted for by the difference in activation enthalpies and temperature factors.

In summary, guidelines for appropriate use of pre-exponential factors from Eyring and Marcus analysis were presented. Both models have a continuum expression that link non-adiabatic and adiabatic electron transfer reactions with known values of H_{DA} , λ , ν_n , and τ_L . The intercepts from these data, as a result, properly account for the influence of non-adiabaticity on ΔS^\ddagger . Differences in ΔH^\ddagger values between the models are accounted for by the Gibbs-Helmholtz relationship with the important realization that the free energy of activation, ΔG^\ddagger , is conserved. This discussion allows for some comment on the physical manifestation of reaction adiabaticity. Adiabatic Marcus theory indicates that the reaction is limited by solvent motion, seen in the pre-exponential factor. However, the pre-exponential factor in the Eyring model arises from the vibrational and/or rotational partition functions resulting in a frequency factor of $k_b T/h$. In the following sections, the experimental data are analyzed under the Eyring formalism. Emphasis is placed on differentiating the solvent-controlled adiabatic reactions for the phenyl-bridged compounds from the non-adiabatic reactions for the xylyl-bridged compounds. Results of the kinetic analysis which yield the entropies, enthalpies and free energies of activation are discussed.

4.3.2 Entropy of activation

Electron transfer reactions for the xylyl-bridged compounds were shown to be non-adiabatic by the results of the van't Hoff analysis. In addition, the mixed-valent form of the

xylyl-bridged compounds did not display significant optical data indicative of low-energy intervalence charge transfer bands, concomitant with the weak coupling and non-adiabatic electron transfer. The degree of coupling is, however, uncertain with an upper-limit of 150 cm^{-1} likely under the experimental conditions used. Assuming $\lambda = 1$ eV (see Reorganization Energy for a detailed discussion) and $\nu_n = k_b T/h$, $\kappa_{el} = 0.56$ (from Eq. 5) which is an upper estimate at 298 K. This affords an electronic entropy contribution of $\Delta S_{el}^\ddagger = -5 \text{ J mol}^{-1} \text{ K}^{-1}$. This indicates a reasonable value for electronic coupling of $\sim 100 \text{ cm}^{-1}$, which corresponds to $\kappa_{el} = 0.32$ and $\Delta S_{el}^\ddagger = -10 \text{ J mol}^{-1} \text{ K}^{-1}$, doubling the electronic entropy contribution. Determination of the electronic entropy allowed the measured entropy of activation ΔS^\ddagger to be partitioned into the electronic and nuclear components for the forward and reverse reaction in the redox equilibrium.

Assuming $\lambda = 1$ eV with $H_{DA} = 1000 \text{ cm}^{-1}$, using Eq. 5 resulted in $\kappa_{el} = 1$ for the phenyl-bridged compounds. As a result, entropic factors measured arose solely from nuclear contributions, ΔS_n^\ddagger , as $\Delta S_{el}^\ddagger = 0 \text{ J mol}^{-1} \text{ K}^{-1}$. Inclusion of the non-adiabatic correction term allows the entropic barriers to be correctly distinguished between non-adiabatic and adiabatic electron transfer mechanisms. The standard entropy change, the total activation entropy and the deconvoluted nuclear and electronic entropy terms are presented in Table 4.3.

Table 4.3. Standard and thermodynamic activation entropies for electron transfer.

	1x		1p		2x		2p	
Rxn	k_{TPA}	k_{Ru}	k_{TPA}	k_{Ru}	k_{TPA}	k_{Ru}	k_{TPA}	k_{Ru}
ΔS^{oa}	0		-18		+2		+17	
$\Delta S_{a,c}^\ddagger$	-70	-70	-93	-75	-78	-80	-73	-90
$\Delta S_{el}^\ddagger^{a,b}$	-10	-10	0	0	-10	-10	0	0
$\Delta S_n^\ddagger^{a,c}$	-60	-60	-93	-75	-68	-70	-73	-90

^a $\text{J mol}^{-1} \text{ K}^{-1}$. ^bFrom equation 6. ^cUsing experimental data with from equation 2. ^d From equation 8.

Of particular interest in **Table 3** are the values for $\Delta S_{\text{el}}^\ddagger$, and $\Delta S_{\text{n}}^\ddagger$. The xylyl-bridged compounds have smaller $\Delta S_{\text{n}}^\ddagger$ contributions to ΔS^\ddagger than do the phenyl-bridged compounds. Further, an interesting phenomenon was observed by comparing the nuclear entropic barriers for the endergonic (k_{TPA} for **1** and k_{Ru} for **2**) and exergonic reactions of the phenyl-bridged compounds. Namely that the difference between the nuclear barriers, $|\Delta \Delta S_{\text{n}}^\ddagger| = \sim 20 \text{ J mol}^{-1} \text{ K}^{-1}$, is likely also the origin of the large values for ΔS° garnered from Arrhenius and van't Hoff analysis. Taken together, the results of the pre-exponential factor analysis support two conclusions: 1) Accounting for adiabaticity properly differentiated between the entropic barriers for adiabatic and non-adiabatic electron transfer, and 2) The barrier of the uphill reaction in the adiabatic limit is $\sim 20 \text{ J mol}^{-1} \text{ K}^{-1}$ larger relative to the downhill process as was reflected through ΔS° . These results demonstrate that the product is entropically stabilized relative to the reactant when electronic coupling is present. This analysis, however, does not characterize the molecular origin of these barriers which is discussed later.

4.3.3 Enthalpy of activation

For compounds **1x** and **2x**, the thermodynamically uphill process displayed enthalpic barriers ~ 3 times larger than the corresponding downhill process (*e.g.* $\Delta H^\ddagger = 12.3 \text{ kJ mol}^{-1}$ and 4.3 kJ mol^{-1} for k_{TPA} and k_{Ru} respectively). Because the reactions of interest occur thermally and are intramolecular, small enthalpic barriers are wholly consistent with a through bond hole-transfer mechanism where no covalent bonds are broken.^{8, 32-34}

Differences in ΔH^\ddagger between the xylyl-bridged compounds can be rationalized by the influence of either electron withdrawing ($-\text{CF}_3$) or donating ($-\text{OCH}_3$) substituents. These inductive effects modulate the energetic proximity of the bridge orbitals to either the TPA (**1x**) or Ru^{II} center (**2x**) causing electron transfer to Ru^{III} to be downhill or uphill, relative to

the TPA reduction potential.³⁵ When Ru^{II} was electrochemically oxidized prior to TPA, as in **1x** and **1p**, an inductive influence of the oxidized metal center resulted in an increased energy of the bridge-centered orbitals thus leading to a larger barrier.

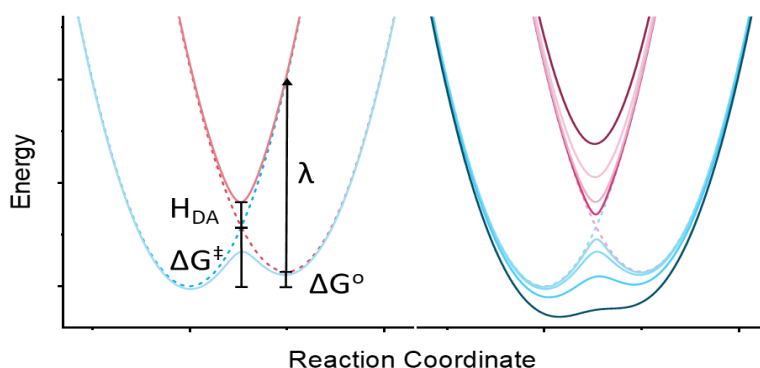
Enthalpic barriers for the phenyl-bridged compounds were surprisingly similar for the forward and reverse adiabatic reactions. For phenyl-bridged compounds the barriers in either the forward or reverse direction were, within experimental error, the same (*e.g.* $\Delta H^\ddagger = 3.0 \pm 0.3$ and 3.7 ± 0.1 kJ mol⁻¹). When $H_{DA} > 1000$ cm⁻¹, the data indicate that ΔH^\ddagger for the reverse reaction was greatly reduced, $\Delta H^\ddagger = 3$ kJ mol⁻¹, relative to the non-adiabatic compounds, $\Delta H^\ddagger = 11$ kJ mol⁻¹. On the other hand, the downhill process barrier remained essentially unchanged, $\Delta H^\ddagger \sim 3-4$ kJ mol⁻¹. Interestingly, the barriers for the forward and reverse reactions are very similar to the longitudinal relaxation of CH₃CN, with $\Delta H_L^\ddagger = 4.9$ kJ mol⁻¹.³⁶ In the adiabatic limit, the transient kinetics were similarly temperature dependent, Table 3.2 and a standard enthalpy change was not observed for redox equilibrium, $\Delta H^\circ = 0$ kJ mol⁻¹. As a result, the equilibrium constant, K_{eq} , was demonstrated by the van't Hoff analysis to be temperature independent, Figure 1. An important conclusion from combining the results of the Eyring and van't Hoff analyses is that the equilibrium concentrations of Ru^{III} and TPA⁺ were entirely dictated by enthalpy for the xylyl-bridged compounds while the nuclear entropy was the dominant factor for the phenyl-bridged compounds.

4.3.4 Free energy of activation

Evaluating the intercepts and slopes from the Eyring analysis yielded values of ΔS^\ddagger and ΔH^\ddagger . From those results, it is evident that the enthalpic barriers do not contribute significantly to the total free energy barrier, $\Delta G^\ddagger = \Delta H^\ddagger - T\Delta S^\ddagger$, at 298K. The main result arising from calculation of ΔG^\ddagger is that the free energy barriers were independent of the electronic

coupling. For the uphill reactions $\Delta G^\ddagger = 30 \text{ kJ mol}^{-1}$ across the series while for the downhill reaction $\Delta G^\ddagger = 25 \text{ kJ mol}^{-1}$. Indeed, the independence of the free energy barriers with respect to (non-)adiabaticity was surprising. Theory predicts, and some experiments have demonstrated, that a decrease in ΔG^0 and ΔG^\ddagger is expected with increased H_{DA} by virtue of the energy splitting in the transition state, Scheme 32.^{13, 37-39} The scheme also demonstrates the theoretical expectation of decreases in the activation energy in the transition state (left panel) as the electronic coupling increases. It is recognized that one-dimensional reaction coordinates are likely too simplistic to capture the 3N-6 vibrational and/or solvent modes. The approach does, however, provide a great deal of insight into how potential energy surfaces trend with factors such as λ , ΔG^0 , and H_{DA} . At a cursory level, the schematic surfaces indicate that ΔG^\ddagger decreases linearly with H_{DA} . Additionally, the splitting between the upper and lower surfaces is $2H_{DA}$ for $\Delta G^0 = 0 \text{ eV}$, and to a first approximation that holds for the compounds used in this study, $\Delta G^0 < 100 \text{ mV}$. Higher order algebraic expressions for λ , ΔG^0 , and H_{DA} are known.¹⁹

Scheme 4.2. Two-dimensional potential energy surfaces for asymmetric electron transfer.



Thus, with the large electronic coupling between the Ru^{II} and TPA centers the initial expectation is that ΔG^\ddagger would decrease and k_{ET} would approach a maximum value. The maximum rate for a barrierless reaction under the Eyring formalism is $\nu_n = k_b T/h$, while for

adiabatic Marcus theory the solvent modes ultimately dominate the reaction, $1/\tau_L \sim 5 \times 10^{12} \text{ s}^{-1}$ (for a given λ), which is the kinetic speed limit. However, the experimentally determined values were $\sim 10^4$ times slower at all temperatures investigated, even when the decrease in ΔG^0 is accounted for. Clearly, the free energy barrier still must dictate the kinetics.

Deconvolution of ΔG^\ddagger into its enthalpic and entropic components indicates that ΔH^\ddagger comprises 10-40% of ΔG^\ddagger for the xylyl-bridged compounds. By contrast for the phenyl bridged compounds, ΔH^\ddagger is just 10-15% of ΔG^\ddagger . More specifically, for all compounds studied herein, $|T\Delta S^\ddagger|$ is $>17 \text{ kJ mol}^{-1}$ on average at 298K, similar to values measured for bimolecular electron transfer in CH_3CN .⁹ Careful analysis revealed that electronic entropy did not influence the barriers for the phenyl-bridged compounds, while the opposite was observed for the xylyl-bridged compounds: non-adiabaticity effectively increased the entropic barrier. From Table 3, it is clear that the nuclear entropy of activation is critical in explaining the differences between the two mechanisms. Lastly, the observation that the free energy barrier was independent of the vastly different electronic coupling elements was unexpected. In order to compare the results directly with electron transfer models described above, we turn now to calculations of the rate constants and reorganization energies for the adiabatic and non-adiabatic regimes.

4.3.5 *A priori* rate calculations

Theoretical expectations allow for rate constants for electron transfer to be predicted using the previously presented Marcus theory continuum expression, Eq. 8, using only spectroscopic and electrochemical data with an assumed reorganization energy of $\lambda = 1 \text{ eV}$. Because electronic coupling through the xylyl-bridge was taken as 150 cm^{-1} , and $\tau_L = 0.2 \times 10^{12} \text{ s}^{-1}$ for neat CH_3CN , the Jortner adiabaticity parameter begins to contribute, at room

temperature $\kappa_A = 1.3$. For example, Figure 3 shows calculated electron transfer rate constants using Eqs. 8 and 10 as a function of electronic coupling when $\Delta G^\ddagger = 24 \text{ kJ mol}^{-1}$. These simulated data demonstrate the parabolic dependence of the rate constants when $\kappa_A = 0$. More interesting is the situation when $\kappa_A > 0$. Here, an initially non-adiabatic rate constant accelerates with H_{DA}^2 for $0 < H_{DA} < 100 \text{ cm}^{-1}$, followed by a transition into a mixed (non-)adiabatic regime, $100 < H_{DA} < 350 \text{ cm}^{-1}$, after which the rate constant becomes coupling-independent, $H_{DA} > 350 \text{ cm}^{-1}$ and $\kappa_A \gg 1$. The so-called ‘speed limit’ is calculated from Eq. 10, and is shown as the blue dashed line in Figure 4.3.

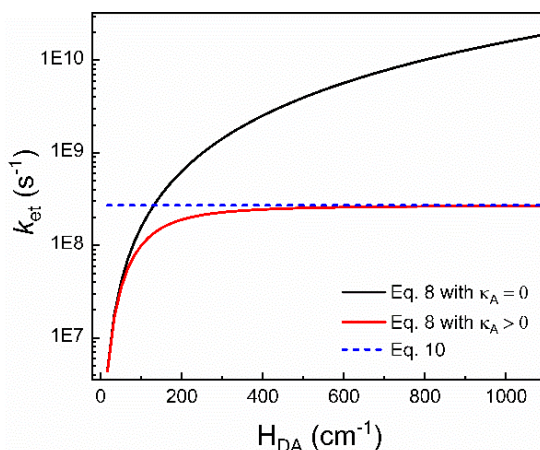


Figure 4.3 Electron transfer rates as a function of electronic coupling for a purely non-adiabatic reaction (Eq. 8, $\kappa_A = 0$, black), a non-adiabatic reaction with the adiabaticity parameter (Eq. 8, $\kappa_A > 0$, red) and a solvent-controlled adiabatic reaction (Eq. 10, dashed blue line). Parameters used in these calculations: $T = 298 \text{ K}$, $\lambda = 1 \text{ eV}$, $\tau_L = 0.2 \text{ ps}$, $\Delta G^\ddagger = 24 \text{ kJ mol}^{-1}$.

Thus, Eq. 8 is applicable to the xylyl-bridged compounds. Indeed, calculated rate constants for **1x** and **2x** show good agreement with experiment. If κ_A is ignored for the non-adiabatic electron transfer reactions, the pre-exponential term was indeed larger than would be allowed by τ_L .

Moving now to the phenyl-bridged compounds, $\kappa_A = 53$ which places the kinetics firmly in the limit $\kappa_A \gg 1$, and the reaction is adiabatic. In this limit, the electron transfer rate was

expected to be independent of the coupling and limited instead by the frequency with which the reactant approaches the transition state which depends on properties of the solvent.⁴⁰⁻⁴¹ As a result, eq. 10 becomes solely applicable. If the adiabaticity factor were ignored, predicted rate constants were found to differ by factors of 40-100 from experiment.^{27, 29} The pre-exponential term in Eq. 5 represents the kinetic speed limit for electron transfer between strongly coupled redox centers with k_{ET} governed by solvent reorientational motion, $1/\tau_L$, ($5 \times 10^{12} \text{ s}^{-1}$ for CH_3CN).⁴² Equations 8 and 10 accurately reproduced experimental rate constants to within factors of 1 to 3. Selected rate constants are presented in Table 4.4, with the remainder of the rate constants as well as the calculation methodology presented in the SI.

Table 4.4. Calculated and observed rate constants of intramolecular electron transfer at 293 K.

Rate ($\times 10^7 \text{ s}^{-1}$)		1x ^a	2x ^a	1p ^b	2p ^b
k_{TPA}	Obs. ^c	0.45	8.5	2.1	23
	Calc. ^d	0.35	4.5	1.4	22
k_{Ru}	Obs. ^c	1.0	.65	23	2.8
	Calc. ^d	0.94	.25	18	1.8

^aUsing Eq. 8. ^bUsing Eq. 10. ^cExperimentally determined. ^dCalculated from Eqs. 8 or 10.

4.3.6 Reorganization energy

The total reorganization energy was calculated by Eq. 12, which relates the activation free energies to the standard free energy and reorganization energy for an electron transfer reaction.

$$\Delta G^\ddagger = \frac{(\Delta G^0 + \lambda)^2}{4\lambda} \quad (12)$$

By definition, the reorganization energy corresponds to the vertical energy difference between the reactants and products potential energy surfaces, Scheme 3.2.¹⁹ The total reorganization energy, λ , is generally partitioned into the outer-sphere (λ_o) and inner-sphere

(λ_i) reorganization energies for solvent reorganization and bond length changes, respectively, so $\lambda = \lambda_o + \lambda_i$. Temperature dependent values of ΔG^0 and ΔG^\ddagger provided the necessary quantities to calculate λ . Solutions to Eq. 12 provided two values, $\lambda = 0.004$ eV or 1.2 eV. It is clear that the larger of the two values is a more physically appropriate number as the intramolecular reactions are well within the Marcus normal region and are certainly not activationless. Apart from Eq. 12, a value for λ at room temperature has been determined by three additional methods: the dielectric continuum approximation, spectroscopic data on intervalence charge transfer transitions, and generalized Mulliken-Hush theory.

Dielectric continuum estimates of the reorganization energy, discussed in detail in Section 4.5.1, predicts $\lambda \sim 0.9$ eV, close to the standard literature value for electron transfer reactions in acetonitrile.⁴³ Note that the dielectric continuum estimation provides a value only for λ_o . A key value for calculation of the reorganization energy is the geometric distance, r_{DA} , between the Ru and TPA centers which was taken as $r_{DA} = 14$ Å from density functional theory calculations. It is acknowledged that the geometric distance is an upper-limit for the true charge transfer distance. Analysis of intervalence charge transfer optical data for the phenyl-bridged compounds that allowed for H_{DA} to be calculated utilize band shape parameters that ultimately relate to the total reorganization energy through Eq. 13,

$$\lambda = \frac{(\Delta\nu_{1/2})^2}{16 \ln(2) RT} \quad (13)$$

where $\Delta\nu_{1/2}$ is the full-width at half-maximum of the intervalence charge transfer band.⁴⁴⁻⁴⁵ This analysis gave $\lambda = 0.9$ -1.1 eV with $\Delta\nu_{1/2} = 4100$ -4500 cm^{-1} .¹⁷ Generalized Mulliken-Hush theory, which accounts for delocalization-induced reduction of r_{DA} from the geometric distances uses computationally calculated changes in dipole moments. This analysis provided $\lambda = 0.7$ eV.^{15, 46} These three independent measures of the reorganization energy are in

reasonably good agreement with each other and are similar to commonly accepted values of for electron transfer in transition metal compounds in CH₃CN.⁴⁷⁻⁴⁹ This supports the value of 1 eV used in the previous calculations.

The inner-sphere contribution is often assumed to be zero as Ru^{II} polypyridyl complexes display the experimentally indistinguishable Ru-N bond length distortions between the 3+ and 2+ formal oxidation states.⁵⁰ It is acknowledged that the covalent cyclometalating bond is unaccounted for under this assumption and literature searches for crystal structure data, to the best of our knowledge, are notably absent. Additionally, λ_i for a series of substituted TPA⁺⁰ redox couples have been predicted to range from 0.1 and 0.25 eV.⁵¹ Thus, the calculations of λ are reasonable even when including a non-zero inner-sphere reorganization.

4.3.7 Standard thermodynamics

A critical advantage in addressing the influence of electronic coupling on the activation and reorganization energies for the compounds lies in the inherent energetic asymmetry of the Ru^{III/II} and TPA⁺⁰ redox centers, which have non-zero standard thermodynamic quantities. In self-exchange model systems, $\Delta G^\circ = 0$ kJ mol⁻¹ so moving between nonadiabatic to adiabatic regimes results in equal stabilization of the product and reactant surfaces relative to one another and critical details are lost.¹⁹ Thus, revisiting the standard thermodynamic quantities may provide some insight into the apparent thermodynamic activation parameters. Standard entropies for the xylyl-bridged compounds were $\Delta S^\circ \approx -2 \pm 2$ J mol⁻¹ K⁻¹, a negligible entropic contribution, with a predominant enthalpic incentive of +7 and -8 kJ mol⁻¹. The opposite was true in the adiabatic limit due to the apparent thermodynamically favorable entropy changes, $\Delta S^\circ = +18 \pm 2$ J mol⁻¹ K⁻¹ and a negligible enthalpic contribution. While the necessary extrapolation to infinite temperature can raise

uncertainty in the physical nature of the van't Hoff model, this analysis nevertheless provides self-consistent values to those extracted from the Eyring model and are independent of reaction adiabaticity over the range of temperatures investigated. After accounting for electronic entropy, a direct comparison between the non-adiabatic and adiabatic barriers implicates that electronic coupling manifests as nuclear entropy which is the origin of the stabilizing entropic incentive. Ultimately, the larger entropy term in the adiabatic limit result in the similar values of ΔG^\ddagger . However, the molecular origin of the nuclear entropy is not easily distinguishable.

4.3.8 Origin of entropic barriers

With the underlying activation barriers resolved and reaction adiabaticity properly accounted for the following question arises: what do the standard thermodynamic quantities ultimately indicate regarding adiabatic and nonadiabatic electron transfer? At a minimum, the large change in ΔS^0 between the xylyl- and phenyl-bridged compounds cannot adequately be explained by electronic coupling effects. Enthalpic barriers, while partially indicative of H_{DA} contributions, do not satisfactorily characterize the molecular origin, either. Comparison of the kinetic and thermodynamic data herein with prior work is helpful in defining a reasonable molecular picture. Results from this study indicated that entropic contributions to electron transfer rate constants manifest as ‘nuclear’ entropic terms, ΔS_n^\ddagger , when in an adiabatic regime. A logical starting point for discussion is the structure of the transition state.

For non-adiabatic processes the transition state structure is often invoked as the main contributor to the entropy of activation, ΔS^\ddagger .⁵² Measurement and interpretation of such barriers has been performed on Diels-Alder or condensation-type exemplar reactions, and many indicated that the loss of translational and rotational degrees of freedom are the sources

of ΔS^\ddagger .⁵³⁻⁵⁴ Compounds anchored to TiO₂ are assumed to be stationary. As such, a covalent and rigid bridge likely minimizes translational and rotational motion. Such conclusions are justifiable through comparison with enzymatic catalysis, where a bound substrate removes translation and rotational degrees of freedom and the entropic contributions have been ‘paid’ prior to any chemistry occurring.⁵⁵⁻⁵⁶

Beyond rotational and translation motion, *intermolecular* electron transfer reactions between neighboring Ru^{II}-B-TPA compounds could have occurred on a similar timescale with unusual entropic factors.⁵⁷ However, in this study intermolecular electron transfer was minimal in these studies that were performed below a critical percolation threshold – inhibiting lateral electron transfer pathways.⁵⁸⁻⁵⁹ Solvent structure or polarity also influences rates of electron transfer at a surface. The carboxylate derivatized compounds anchored onto TiO₂ are nearly insoluble in acetonitrile and may give rise to solvent exclusion effects.⁶⁰⁻⁶¹ Thus one may expect the reorganization energy to vary. Previous work has demonstrated that intermolecular and/or intramolecular reactions for the compounds anchored onto a metal oxide surface are similar to those reported in acetonitrile fluid solution.⁴⁸⁻⁴⁹ Finally, electric fields generated by electrons injected into TiO₂ are known to transiently induce a Stark-like effect on the ground state absorption spectra of compounds anchored onto the surface.⁶²⁻⁶³ Charge screening by 100 mM Li⁺ efficiently dampens the field and thus effects are expected to be minimal for the pendant TPA located nearly 20 Å away from the surface.⁶⁴ Furthermore, calculation of equilibrium constants from electrochemical data for the xylyl-bridged compounds indicated that ΔG^0 did not change. In turn, the electric field effect created by injected electrons did not significantly perturb the redox equilibrium.

Finally, significant literature precedent exists for vibrational entropic factors in transition metal complexes of Fe, Co, and Ru undergoing bimolecular (proton-coupled) electron transfer reactions. For Ru-based reactants, $\Delta S^0 = 25 \text{ J mol}^{-1} \text{ K}^{-1}$. The origin of the barriers were ascribed to low-frequency vibrational modes, $E_{\text{vib}} \leq 200 \text{ cm}^{-1}$. Careful control experiments ruled out solvent effects as well as translational and rotational entropy.^{65,66} Indeed, the importance of vibrational factors have been experimentally demonstrated for many transition metal half reactions which displayed large positive standard entropy changes and is garnered from summation over all available modes.⁶⁷ Considering that for the xylyl-bridged compounds $\Delta S^0 \sim 0 \text{ J mol}^{-1} \text{ K}^{-1}$ and implies that, even if vibrational frequencies do change, the net effect is zero.

More applicable to the adiabatic limit are bridged mixed-valent compounds with positive standard entropies. The origin of these entropic factors was a result of *decreases* in vibrational frequencies resulting from charge delocalization through the intervening bridge and charge balance between redox centers.⁶⁸ In this limit, solvent reorientation occurs over a larger volume which necessitates a more ordered solvation shell around the compound, effectively reducing the number of available solvent configurational microstates.⁶⁹⁻⁷⁰ The results presented here seemingly indicate that the ‘product state’ of the reaction becomes entropically stabilized, $\Delta S^\ddagger = -90 \text{ J mol}^{-1} \text{ K}^{-1}$ while the initial state remains relatively unchanged, $\Delta S^\ddagger = -70 \text{ J mol}^{-1} \text{ K}^{-1}$, consistent with previous work.⁶⁸ Ultimately, this provides the standard entropy change garnered from the van’t Hoff analysis.

As a final point, electron transfer reactions that are adiabatic contain a unique set of theoretical challenges. Under adiabatic assumptions, solvent-controlled electron transfer rates represent exceptions to the traditional Born-Oppenheimer approximation as the electronic

structure dynamics, rate-limited by solvent, exists in a steady-state with the solvent dielectric as it traverses the potential energy surface.⁷¹⁻⁷³ The fact that such violations occur, and as a consequence solvent-controlled rates begin to arise, may explain the origin of the enthalpic barriers observed for the adiabatic reactions closely matching the barrier for solvent longitudinal motion, ΔH_L^\ddagger .³⁶ An additional concern for an adiabatic electron transfer reaction is that motion through the transition state is repeated or initial crossing of the barrier fails as a result of solvent influence – an effect not typically observed for non-adiabatic electron transfer.⁷⁴ This would also manifest through a more negative activation entropy as a specific local solvent arrangement of orbitals facilitates the reaction, an entropically unfavorable event.

4.4 Conclusions

In summary, the kinetics for electron transfer reactions in a strong (adiabatic) and weak (non-adiabatic) electronic coupling regime were analyzed with Eyring and Marcus continuum theories. Placed into context, the results indicate that even though coupling accelerates the electron transfer rate constant by allowing a rapid approach to the transition state, a substantial entropic penalty is imposed despite smaller ΔH^\ddagger for thermodynamically uphill reactions. Entropies of activation were dissected into nuclear and electronic components and the degree of (non-)adiabaticity was accounted for through the transmission coefficient (κ_{el} , Eyring) or Jortner adiabaticity parameter, (κ_a , Marcus). Free energy barriers were found to be independent of the coupling, despite a theoretical expectation that H_{DA} reduces the barrier. Finally, ΔS^\ddagger was found to be a significant contributor to the activation energy. The thermodynamic quantities were placed into context using previous studies on bimolecular, biological, and bridged inter- and intramolecular electron transfer. The work

presented here is an early example of explicit characterization of both forward and reverse rates of thermal electron transfer reactions that lie in extreme regimes of electron transfer theory and which are relevant to energy conversion schemes.

4.5 Additional content

4.5.1 Calculation of the reorganization energy

The dielectric continuum equation for the reorganization energy is given by Eq. 14,

$$\lambda = \frac{e^2}{4\pi\epsilon_o} \left(\frac{1}{2r_A} + \frac{1}{2r_B} - \frac{1}{R} \right) \left(\frac{1}{\epsilon_{op}} - \frac{1}{\epsilon_s} \right) \quad (14)$$

Where e is elementary charge, ϵ_o is the permittivity of vacuum, r_A is the radius of the Ru^{II} center, r_B is the TPA radius, R is the distance between the centers of the two spheres, and ϵ_{op} and ϵ_s are the optical (2.26) and static (35.9) dielectric constants of acetonitrile, respectively.²⁸ Computational calculations were done using a mixed LANL2DZ (for Ru only) and 6-31G(d) with either a B3LYP or M06 functional and provided distances to approximate r_A , r_B , and R , Figure 4.4.¹⁵

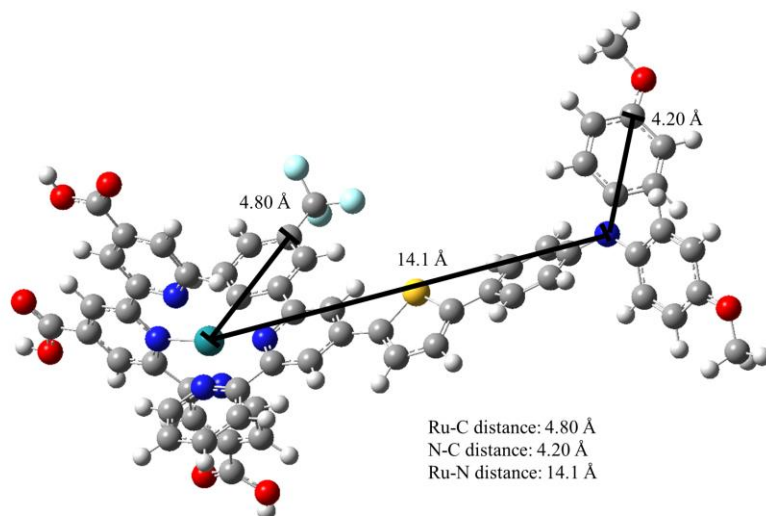


Figure 4.4. TD-DFT optimized structure of **2p** used to determine geometric distances for estimation of the reorganization energy.

The radius of the Ru^{II} center was taken from the Ru atom to the para carbon atom of the cyclometalating ligand, $r_A = 4.8 \text{ \AA}$. In a similar way the radius of TPA was taken from the N atom to the para carbon atom of the phenyl, $r_B = 4.2 \text{ \AA}$. The geometric distance R was taken as the distance between the Ru and N atoms and $R = 14.1 \text{ \AA}$. This results in $\lambda = 0.9 \text{ eV}$. It is recognized that the geometric distance between the redox centers, R , is an upper estimate.

Generalized Mulliken-Hush theory calculations have provided means to calculate the effective charge transfer distance, which accounts for delocalization to give $R_{del} = 9.5 \text{ \AA}$ so $\lambda = 0.7 \text{ eV}$.¹⁵

4.5.2 Temperature dependence of the reorganization energy and adiabaticity factor

Electron transfer rate expressions used in this work have five nominally temperature dependent variables, namely, λ , ΔG° , H_{DA} , τ_L , and $k_b T$. In the present analysis, only H_{DA} is assumed to be strictly temperature independent. In this section, the possible temperature dependence of λ is examined to justify the assumption of temperature independence used herein. In order to accomplish this task and fully compare the calculated and measured rate

constants, the temperature dependence of the reorganization energy was evaluated for **2x** as the case-study. Temperature dependent values of λ were evaluated from Eq. 11 in the main text with ΔG° from the van't Hoff analysis and ΔG^\ddagger from the analysis of the barriers by solving for λ at each temperature. Correspondingly, rate constants were calculated as described below for **2x**. For comparison and simplicity of the model, rates were also calculated at room temperature ($T = 298$ K) using either 1.2 eV or 1.1 eV for k_{Ru} or k_{TPA} , respectively, as explained in the main text. Results of this comparative calculation are provided in Table 4.5. Errors for the experimentally measured rate constants are approximately $\pm 5\%$ and these errors were propagated throughout the analysis.

Table 4.5. Rate constants for 2x calculated with reorganization energy as a temperature dependent and independent value.

2x		$k_{Ru} \times 10^6 \text{ s}^{-1}$ (calc)		$k_{TPA} \times 10^7 \text{ s}^{-1}$ (calc)		
		$\lambda(T)$	$\lambda = 1.2 \text{ eV}$	$\lambda(T)$	$\lambda = 1.1 \text{ eV}$	
Temp. (K)	$\lambda \text{ (kJ mol}^{-1}\text{)}$ [eV]	$k_{et}(\lambda(T), T)$	$k_{et}(T)$	$\lambda \text{ (kJ mol}^{-1}\text{)}$ [eV]	$k_{et}(\lambda(T), T)$	$k_{et}(T)$
233	97.0 [1.00]	0.7	0.7	97.5 [1.01]	2.6	2.6
243	100.0 [1.04]	0.9	0.9	99.6 [1.03]	2.9	2.9
253	104.0 [1.07]	1.2	1.2	102.0 [1.06]	3.2	3.3
263	107.0 [1.11]	1.5	1.5	104.0 [1.08]	3.6	3.6
273	110.0 [1.15]	1.8	1.8	106.0 [1.10]	3.9	3.9
283	114.0 [1.18]	2.1	2.1	109.0 [1.13]	4.2	4.2
293	118.0 [1.22]	2.5	2.5	111.0 [1.15]	4.5	4.5
303	121.0 [1.25]	3.0	3.0	114.0 [1.18]	4.8	4.7
313	124.0 [1.28]	3.4	3.4	116.0 [1.20]	5.0	5.0
323	127.0 [1.32]	3.9	3.9	118.0 [1.23]	5.3	5.3

The pertinent results of this analysis support an assumption that the temperature-dependence of the reorganization energy does not critically influence the calculated rate constants outside of the experimental uncertainty. Hence, in the following calculations λ will be taken as 1.15 eV for the exergonic and endergonic reactions respectively.

With the assumption of temperature independent reorganization energies, the adiabaticity factor, κ_A , was also determined, Table 4.6. An average value of $\lambda = 1.15$ eV was used and H_{DA} was assumed to be constant. Values for κ_A within the adiabatic and non-adiabatic limit is differentiated predominately by the electronic coupling term which provides a factor of >40 when moving between the two limits.

Table 4.6. Temperature dependence of the adiabaticity parameter, κ_A , at $\lambda = 1.15$ eV.

Temp. (K)	$H_{DA}(\text{cm}^{-1})$	
	150	1000
	κ_A	
233	1.95	86.7
243	1.77	78.6
253	1.62	71.9
263	1.49	66.1
273	1.38	61.2
283	1.28	57.0
293	1.20	53.3
303	1.13	50.1
313	1.06	47.3
323	1.00	44.7

4.5.3 Nonadiabatic kinetics

The rate constants for nonadiabatic intramolecular electron transfer between Ru^{II} and TPA were modeled from Eq. 15,^{19, 32}

$$k_{ET} = \frac{2\pi}{\hbar} \frac{|H_{DA}|^2}{\sqrt{4\pi\lambda k_b T}} \left[\frac{1}{1+\kappa_A} \right] \exp\left(-\frac{\Delta G^\ddagger}{k_b T}\right) \quad (15)$$

Where \hbar is the reduced Planck's constant, k_b is the Boltzmann constant, T is the temperature, H_{DA} is the electronic coupling matrix element, ΔG^\ddagger is the Gibbs energy of activation, and λ is the reorganization energy, and κ_A is an adiabaticity factor. The free energy of activation was calculated from $\Delta G^\ddagger = \Delta H^\ddagger - T\Delta S^\ddagger$ from Eyring analysis. Recall that the main text details

the relationships between the Marcus and Eyring models that yield the different enthalpic and entropic barriers while maintain an similar free energy barrier. For reference, see Equations S14 and S15 below or the ‘Pre-exponential factors’ section in the main text.

With the typical assumption of temperature-independence, H_{DA} was taken as the upper limit from spectroelectrochemical experiments, $H_{DA} \approx 150 \text{ cm}^{-1}$. Reorganizational energies were also assumed to be temperature independent while the adiabaticity factor was calculated for each temperature used experimentally, *vide supra*. Temperature dependent changes in ΔG^0 were accounted for through the van’t Hoff analysis in the main text elsewhere.¹⁵ The resulting calculated rate constants are displayed compared to the measured rate constants with the ratio being defined as $k_{\text{obs}}/k_{\text{calc}}$.

Reasonable agreement between the rate constants were found for **1x** (Table 4.7) and **2x** (Table 4.8), within factors of 1 to 2. Thermodynamically uphill and downhill reactions were modeled by adjusting the sign of the relevant thermodynamic quantities thus modifying the free energy of activation, ΔG^\ddagger . Deviations were observed at higher temperatures, $T > 290 \text{ K}$, which possibly result from increased electronic coupling as a result of thermal energy providing access to rotational states that approach the adiabatic (phenyl-bridged) limit similar to conformational gating effects.⁸

Table 4.7. Experimental and calculated rate constants for electron transfer in the nonadiabatic limit in compound **1x**.

1x						
Temp	k_{TPA}			k_{Ru}		
	rate (obs)	rate (calc)	rati	rate (obs)	rate (calc)	rati
223	1.00	0.57	1.8	6.00	4.3	1.4
233	1.60	0.79	2.0	7.20	4.9	1.5
243	2.00	1.10	1.9	8.00	5.7	1.4
253	2.40	1.40	1.7	8.70	6.4	1.4
263	2.90	1.80	1.6	9.00	7.2	1.3

273	3.20	2.30	1.4	9.20	7.9	1.2
283	3.80	2.90	1.3	9.50	8.7	1.1
293	4.50	3.50	1.3	10.00	9.4	1.1
303	6.00	4.30	1.4	12.00	10.2	1.2

Table 4.8. Experimental and calculated rate constants for electron transfer in the nonadiabatic limit for compound **2x**.

2x						
<i>k_{TPA}</i>				<i>k_{RU}</i>		
Temp (K)	rate (obs) x10 ⁷	rate (calc) x10 ⁷	ratio	rate (obs) x10 ⁶	rate (calc) x10 ⁶	ratio
233	5.0	2.6	1.9	2.00	0.7	2.7
243	5.5	2.9	1.9	2.50	0.9	2.7
253	6.0	3.3	1.8	3.00	1.2	2.5
263	7.0	3.6	2.0	3.50	1.5	2.4
273	7.5	3.9	1.9	4.00	1.8	2.3
283	8.0	4.2	1.9	5.00	2.1	2.6
293	8.5	4.5	1.9	6.50	2.5	2.9
303	9.0	4.7	1.9	8.50	3.0	2.6
313	9.5	5.0	2.3	9.00	3.4	3.3
323	12.0	10.1	1.2	13.00	7.7	1.7

4.5.4 Adiabatic kinetics

When the coupling is very large, the kinetics of electron transfer are instead expected to be controlled by solvent reorientational relaxation, τ_L , by Eq. 16 (Eq. 6 in the main text).^{26, 28}

$$k_{ET} = \frac{1}{\tau_L} \sqrt{\frac{\lambda}{16\pi k_b T}} \exp\left(-\frac{\Delta G^\ddagger}{k_b T}\right) \quad (16)$$

The other constants retain the previously defined meanings. For acetontirile, $\tau_L^{-1} = 5 \times 10^{12} \text{ s}^{-1}$. However, the reorientational motion is also temperature dependent as defined by

$$\frac{1}{\tau_L} = \frac{1}{\tau_o} \exp\left(-\frac{\Delta H_L}{k_b T}\right) \quad (17)$$

where $\tau_0^{-1} = 3.2 \times 10^{13} \text{ s}^{-1}$ is the pre-exponential ‘frequency’ factor and, $\Delta H_L = 4.6 \pm 0.4 \text{ kJ mol}^{-1}$, is the barrier for solvent reorientational motion.^{36, 65} Notably, over the temperature ranges studied here the value of τ_L is weakly temperature dependent, changing only by a factor of 2 between 220 and 310 K. The rate constants were calculated in the same fashion as above with ratios ranging from factors of 1.4-2.0. Data are tabulated in tables 4.9 and 4.10.

Table 4.9 Experimental and calculated rate constants for electron transfer in the adiabatic limit in compound **1p**.

1p						
<i>k_{Ru}</i>				<i>k_{TPA}</i>		
Temp (K)	rate (obs) $\times 10^8$	rate (calc) $\times 10^8$	ratio	rate (obs) $\times 10^7$	rate (calc) $\times 10^7$	ratio
223	1.2	0.75	1.5	1.0	0.60	1.6
233	1.4	0.89	1.6	1.2	0.70	1.7
243	1.6	1.02	1.6	1.3	0.81	1.6
253	1.7	1.30	1.5	1.5	0.93	1.6
263	1.9	1.43	1.5	1.7	1.10	1.6
273	2.0	1.57	1.4	1.8	1.17	1.5
283	2.2	1.72	1.4	1.9	1.29	1.5
293	2.3	1.86	1.3	2.1	1.42	1.5
303	2.5	2.0	1.2	2.2	1.6	1.4

Table 4.10. Experimental and calculated rate constants for electron transfer in the adiabatic limit in compound **2p**.

2p						
<i>k_{TPA}</i>				<i>k_{Ru}</i>		
Temp (K)	rate (obs) $\times 10^8$	rate (calc) $\times 10^8$	ratio	rate (obs) $\times 10^7$	rate (calc) $\times 10^7$	ratio
223	1.30	0.87	1.49	1.50	0.70	2.1
233	1.35	1.03	1.31	1.60	0.84	1.9
243	1.40	1.20	1.17	1.65	0.97	1.7
253	1.50	1.37	1.09	1.70	1.13	1.5
263	1.70	1.56	1.09	1.90	1.30	1.5
273	2.00	1.76	1.14	2.40	1.45	1.7
293	2.30	2.17	1.06	2.80	1.80	1.6
313	3.00	2.59	1.16	3.90	2.17	1.8

The thermodynamic quantities found by the van't Hoff analysis errors are presented below in Table 4.11.

Table 4.11. Errors for standard thermodynamic quantities from the van't Hoff analysis.

Compd	ΔH^{0a}	ΔS^{0b}	$\Delta G^{0a,c}$
1x	± 0.2	± 1	± 0.2
2x	± 0.6	± 2	± 0.7
1p	± 0.2	± 1	± 0.2
2p	± 0.2	± 2	± 0.2

^ain kJ mol⁻¹. ^bin J mol⁻¹ K⁻¹. ^cat T = 298K.

4.5.5 Marcus and Eyring model equivalence

The present derivation is based roughly on the initial relationship between the Eyring and Arrhenius equation.³¹ The relationship between the Marcus and Eyring enthalpies of activation can be addressed beginning with the definition Gibbs-Helmholtz equation, Eq. 18,

$$\frac{\delta \left(\frac{G}{T} \right)}{\delta T} = -\frac{H}{T^2} \quad (18)$$

Where G is the Gibbs energy, H is the enthalpy, and T is the temperature. The expression can be recast in terms of the equilibrium constant, $\ln(K^\ddagger) = -\Delta G^\ddagger/k_bT$. For chemical reactions, the equilibrium constant for the transition state is a function of free energy of activation,

$$K^\ddagger = \exp \left(-\frac{\Delta G^\ddagger}{k_bT} \right) = \exp \left(-\frac{\Delta H^\ddagger - T\Delta S^\ddagger}{k_bT} \right) = \exp \left(-\frac{\Delta H^\ddagger}{k_bT} + \frac{\Delta S^\ddagger}{k_b} \right) \quad (19)$$

Substituting $G/T = -k_b\ln(K)$ results in Eq. 20,

$$\frac{\delta}{\delta T} \left(\frac{\Delta G^\ddagger}{T} \right) = \frac{\delta}{\delta T} \left(-k_b\ln(K^\ddagger) \right) = \frac{\delta}{\delta T} \left(\frac{\Delta H^\ddagger}{T} - \Delta S^\ddagger \right) = -\frac{\Delta H^\ddagger}{T^2} \quad (20)$$

Note that the entropy of activation term is absent as it is assumed to be temperature independent.

The next point of interest is the temperature dependence of the electron transfer rate constants. Beginning with the Eyring equation, k_E ,

$$k_E = \frac{k_b T}{h} \exp\left(-\frac{\Delta G^\ddagger}{k_b T}\right) \quad (21)$$

Which is familiar to the definition in Eq. 19. The derivative of the electron transfer rate with respect to temperature is Eq. 22,

$$\frac{\delta}{\delta T} \ln(k_E) = \frac{\delta}{\delta T} \left[\ln\left(\frac{k_b T}{h}\right) - \frac{\Delta G^\ddagger}{k_b T} \right] = \frac{1}{T} + \frac{\Delta H^\ddagger_E}{k_b T^2} \quad (22)$$

Where the results of Eq. 20 were used. It is now useful to distinguish the enthalpy of activation for the Eyring equation as ΔH^\ddagger_E . The rate expression for either the non-adiabatic or adiabatic expression for Marcus theory is given generally by

$$k_M = \frac{C}{\sqrt{T}} \exp\left(-\frac{\Delta G^\ddagger}{k_b T}\right) \quad (23)$$

With C given by Eq. 8 or 10 in the manuscript. Nevertheless, the temperature dependence scales with $T^{1/2}$.

Applying the same procedure as the Eyring expression above, the derivative of the Marcus rate constant with respect to temperature is Eq. 24.

$$\frac{\delta}{\delta T} \ln(k_M) = \frac{\delta}{\delta T} \left[\ln\left(\frac{C}{\sqrt{T}}\right) - \frac{\Delta G^\ddagger}{k_b T} \right] = -\frac{1}{2T} + \frac{\Delta H^\ddagger_M}{k_b T^2} \quad (24)$$

Note that the temperature term is now $-1/2T$. Since the rate constants determined experimentally are independent of the approach with which they are analyzed, the rate expressions should, in principle, be equivalent and differ only by the temperature dependent term in the pre-exponential factor as Eq. 25.

$$\frac{\delta}{\delta T} \ln(k_M) = \frac{\delta}{\delta T} \ln(k_E) \quad (25)$$

Using the results of the expressions above, equality becomes

$$-\frac{1}{2T} + \frac{\Delta H^\ddagger_M}{k_b T^2} = \frac{1}{T} + \frac{\Delta H^\ddagger_E}{k_b T^2} \quad (26)$$

Which allows for a general relationship between the enthalpies of activation from Marcus and Eyring analysis to be related explicitly. In this case, we wish to look at the relationship of the Eyring enthalpies of activation, ΔH^\ddagger_E , with respect to those of the Marcus expression. Moving ΔH^\ddagger_E and other temperature terms to one side, and multiplying through by $k_b T^2$ a final relationship between the slopes of the kinetic expressions is given by Eq. 27.

$$\Delta H^\ddagger_E = \Delta H^\ddagger_M - \frac{3}{2} k_b T \quad (27)$$

Indeed, this result is nearly identical to the common mathematical relationship between Eyring and Arrhenius analysis, $E_a = \Delta H^\ddagger_E + k_b T$, because the pre-exponential factor is assumed to be temperature independent and so only the $1/T$ term is relevant. The results of this exercise indicate that when plotting rate constants as $\ln(k/T)$ vs. $1/T$ or $\ln(kT^{1/2})$ vs. $1/T$ different enthalpic barriers (slopes) will result. Using this analysis on our experimental data, the $3/2k_b T$ term moves the slopes to within 0.4 kJ mol^{-1} of each other, within the

experimental errors from the linear regression analysis. Though, some comments on the underlying assumptions are necessary at this point.

First, we begin with the missing term: the entropy of activation. This quantity is notably absent from the temperature derivatives of the rate expressions under a basic assumption is that ΔS^\ddagger is independent of temperature. Indeed, the slopes being different by $3/2k_bT$ would result in very different intercepts and values for ΔS^\ddagger . As an example, consider the kinetic data for **2p**. Analysis with Marcus theory yields an intercept of 24.8 whereas Eyring yields 14.9, corresponding to ΔS^\ddagger values of -60 and -73 J mol⁻¹. Where, mathematically, does the difference arise? To begin, an important point is that the rate constants have already been temperature normalized, so now the explicit forms of the pre-exponential factors matter and yield different values of ΔS^\ddagger . Because the free energy of activation is the same by definition, substitution of Eq. S14 into $\Delta G^\ddagger = \Delta H^\ddagger - T\Delta S^\ddagger$ with either ΔH^\ddagger_E or ΔH^\ddagger_M to solve for ΔS^\ddagger yields Eq. 28, which provides the relationship between the entropies of activation.

$$\Delta S^\ddagger_E = \Delta S^\ddagger_M - \frac{3}{2}k_b$$

Then, in general, the Eyring and Marcus entropies are different by -12 J mol⁻¹, (28) consistent with the values from analysis of **2p**. Non-adiabaticity may play an important role in this relationship, however the effects should be small nearly cancel out.

Some minor details in the assumptions for this derivation is that the temperature dependence of the reorganization energy, λ , and solvent reorientational time, τ_L , are assumed to be small enough to be considered constant. Our experimental results indicate that the values change by no more than 15% over the temperature range investigated, which may shed some light as to why the $3/2k_bT$ term does not match precisely the values between the two methods.

4.6 Acknowledgements

The authors gratefully acknowledge support from the Division of Chemical Sciences, Office of Basic Energy Sciences, Office of Energy Research, US Department of Energy (Grant DE-SC0013461). L.T.-G. acknowledges the Belgian American Educational Foundation as well as the Bourse d'excellence Wallonie-Bruxelles International for postdoctoral funding.

REFERENCES

1. Groot, M.-L.; van Mourik, F.; Eijkelhoff, C.; van Stokkum, I. H. M.; Dekker, J. P.; van Grondelle, R., Charge separation in the reaction center of photosystem ii studied as a function of temperature. *Proceedings of the National Academy of Sciences* **1997**, *94* (9), 4389-4394.
2. Veldkamp, B. S.; Han, W.-S.; Dyar, S. M.; Eaton, S. W.; Ratner, M. A.; Wasielewski, M. R., Photoinitiated multi-step charge separation and ultrafast charge transfer induced dissociation in a pyridyl-linked photosensitizer–cobaloxime assembly. *Energy & Environmental Science* **2013**, *6* (6), 1917-1928.
3. Lewis, F. D.; Wu, T.; Liu, X.; Letsinger, R. L.; Greenfield, S. R.; Miller, S. E.; Wasielewski, M. R., Dynamics of photoinduced charge separation and charge recombination in synthetic DNA hairpins with stilbenedicarboxamide linkers. *J. Am. Chem. Soc.* **2000**, *122* (12), 2889-2902.
4. Troian-Gautier, L.; DiMarco, B. N.; Sampaio, R. N.; Marquard, S. L.; Meyer, G. J., Evidence that δs^\ddagger controls interfacial electron transfer dynamics from anatase tio₂ to molecular acceptors. *J. Am. Chem. Soc.* **2018**, *140* (8), 3019-3029.
5. Marcus, R. A.; Sutin, N., Electron transfers in chemistry and biology. *Biochimica et Biophysica Acta (BBA) - Reviews on Bioenergetics* **1985**, *811* (3), 265-322.
6. Natali, M.; Campagna, S.; Scandola, F., Photoinduced electron transfer across molecular bridges: Electron- and hole-transfer superexchange pathways. *Chem. Soc. Rev.* **2014**, *43* (12), 4005-4018.
7. Isied, S. S.; Kuehn, C.; Worosila, G., Ruthenium-modified cytochrome c: Temperature dependence of the rate of intramolecular electron transfer. *J. Am. Chem. Soc.* **1984**, *106* (6), 1722-1726.
8. Weiss, E. A.; Tauber, M. J.; Kelley, R. F.; Ahrens, M. J.; Ratner, M. A.; Wasielewski, M. R., Conformationally gated switching between superexchange and hopping within oligo-p-phenylene-based molecular wires. *J. Am. Chem. Soc.* **2005**, *127* (33), 11842-11850.
9. Roth, J. P.; Lovell, S.; Mayer, J. M., Intrinsic barriers for electron and hydrogen atom transfer reactions of biomimetic iron complexes. *J. Am. Chem. Soc.* **2000**, *122* (23), 5486-5498.
10. Closs, G. L.; Miller, J. R., Intramolecular long-distance electron transfer in organic molecules. *Science* **1988**, *240* (4851), 440-447.
11. Nocera, D. G.; Winkler, J. R.; Yocom, K. M.; Bordignon, E.; Gray, H. B., Kinetics of intermolecular and intramolecular electron transfer from ruthenium(ii) complexes to ferricytochrome c. *J. Am. Chem. Soc.* **1984**, *106* (18), 5145-5150.
12. Turró, C.; Zaleski, J. M.; Karabatsos, Y. M.; Nocera, D. G., Bimolecular electron transfer in the marcus inverted region. *J. Am. Chem. Soc.* **1996**, *118* (25), 6060-6067.

13. Lear, B. J.; Glover, S. D.; Salsman, J. C.; Londergan, C. H.; Kubiak, C. P., Solvent dynamical control of ultrafast ground state electron transfer: Implications for class ii–iii mixed valency. *J. Am. Chem. Soc.* **2007**, *129* (42), 12772-12779.
14. Londergan, C. H.; Salsman, J. C.; Ronco, S.; Dolkas, L. M.; Kubiak, C. P., Solvent dynamical control of electron-transfer rates in mixed-valence complexes observed by infrared spectral line shape coalescence. *J. Am. Chem. Soc.* **2002**, *124* (22), 6236-6237.
15. Sampaio, R. N.; Piechota, E. J.; Troian-Gautier, L.; Maurer, A. B.; Hu, K.; Schauer, P. A.; Blair, A. D.; Berlinguette, C. P.; Meyer, G. J., Kinetics teach that electronic coupling lowers the free-energy change that accompanies electron transfer. *Proceedings of the National Academy of Sciences* **2018**, *115* (28), 7248-7253.
16. Robson, K. C. D.; Sporinova, B.; Koivisto, B. D.; Schott, E.; Brown, D. G.; Berlinguette, C. P., Systematic modulation of a bichromic cyclometalated ruthenium(ii) scaffold bearing a redox-active triphenylamine constituent. *Inorg. Chem.* **2011**, *50* (13), 6019-6028.
17. Piechota, E. J.; Troian-Gautier, L.; Sampaio, R. N.; Brennaman, M. K.; Hu, K.; Berlinguette, C. P.; Meyer, G. J., Optical intramolecular electron transfer in opposite directions through the same bridge that follows different pathways. *J. Am. Chem. Soc.* **2018**, *140* (23), 7176-7186.
18. Brunschwig, B. S.; Creutz, C.; Sutin, N., Optical transitions of symmetrical mixed-valence systems in the class ii–iii transition regime. *Chem. Soc. Rev.* **2002**, *31* (3), 168-184.
19. Brunschwig, B. S.; Sutin, N., Energy surfaces, reorganization energies, and coupling elements in electron transfer. *Coord. Chem. Rev.* **1999**, *187* (1), 233-254.
20. Hu, K.; Blair, A. D.; Piechota, E. J.; Schauer, P. A.; Sampaio, R. N.; Parlane, F. G. L.; Meyer, G. J.; Berlinguette, C. P., Kinetic pathway for interfacial electron transfer from a semiconductor to a molecule. *Nat Chem* **2016**, *8* (9), 853-859.
21. Frauenfelder, H.; Wolynes, P., Rate theories and puzzles of hemeprotein kinetics. *Science* **1985**, *229* (4711), 337-345.
22. Hupp, J. T.; Weaver, M. J., Entropic driving-force effects upon preexponential factors for intramolecular electron transfer: Implications for the assessment of nonadiabaticity. *Inorg. Chem.* **1984**, *23* (2), 256-258.
23. Creutz, C., Nonadiabatic, short-range, intramolecular electron transfer from ruthenium(ii) to cobalt(iii) complexes. *J. Phys. Chem. B* **2007**, *111* (24), 6713-6717.
24. Brunschwig, B. S.; Logan, J.; Newton, M. D.; Sutin, N., A semiclassical treatment of electron-exchange reactions. Application to the hexaaquoiron(ii)-hexaaquoiron(iii) system. *J. Am. Chem. Soc.* **1980**, *102* (18), 5798-5809.

25. Brown, G. M.; Sutin, N., A comparison of the rates of electron exchange reactions of ammine complexes of ruthenium(ii) and -(iii) with the predictions of adiabatic, outer-sphere electron transfer models. *J. Am. Chem. Soc.* **1979**, *101* (4), 883-892.
26. Bolton, J. R.; Archer, M. D., Basic electron-transfer theory. In *Electron transfer in inorganic, organic, and biological systems*, American Chemical Society: 1991; Vol. 228, pp 7-23.
27. Rips, I.; Jortner, J., Dynamic solvent effects on outer-sphere electron transfer. *J. Chem. Phys.* **1987**, *87* (4), 2090-2104.
28. Fawcett, W. R.; Fawcett, W. R., *Liquids, solutions, and interfaces : From classical macroscopic descriptions to modern microscopic details*. Oxford University Press: Cary, UNITED STATES, 2004.
29. Jortner, J.; Bixon, M., Intramolecular vibrational excitations accompanying solvent-controlled electron transfer reactions. *J. Chem. Phys.* **1988**, *88* (1), 167-170.
30. Sutin, N., Theory of electron transfer reactions: Insights and hindsight. In progress in inorganic chemistry. In *Progress in inorganic chemistry*, Lippard, S. J., Ed. 2007.
31. Steinfeld, J. I. F., J. S.; Hase, W. L., *Chemical kinetics and dynamics*. 2nd ed.; Prentice Hall: New Jersey, 1998.
32. Kuss-Petermann, M.; Wenger, O. S., Electron transfer rate maxima at large donor–acceptor distances. *J. Am. Chem. Soc.* **2016**, *138* (4), 1349-1358.
33. Farver, O.; Pecht, I., Low activation barriers characterize intramolecular electron transfer in ascorbate oxidase. *Proceedings of the National Academy of Sciences* **1992**, *89* (17), 8283-8287.
34. Larsen, C. B.; Wenger, O. S., Circular photoinduced electron transfer in a donor-acceptor-acceptor triad. *Angewandte Chemie International Edition* **2018**, *57* (3), 841-845.
35. Zhong, Y.-W.; Gong, Z.-L.; Shao, J.-Y.; Yao, J., Electronic coupling in cyclometalated ruthenium complexes. *Coord. Chem. Rev.* **2016**, *312*, 22-40.
36. Manbeck, G. F.; Fujita, E.; Concepcion, J. J., Proton-coupled electron transfer in a strongly coupled photosystem ii-inspired chromophore–imidazole–phenol complex: Stepwise oxidation and concerted reduction. *J. Am. Chem. Soc.* **2016**, *138* (36), 11536-11549.
37. Schäfer, J.; Holzapfel, M.; Mladenova, B.; Kattnig, D.; Krummenacher, I.; Braunschweig, H.; Grampp, G.; Lambert, C., Hole transfer processes in meta- and para-conjugated mixed valence compounds: Unforeseen effects of bridge substituents and solvent dynamics. *J. Am. Chem. Soc.* **2017**, *139* (17), 6200-6209.

38. Londergan, C. H.; Salsman, J. C.; Lear, B. J.; Kubiak, C. P., Observation and dynamics of “mixed-valence isomers” and a thermodynamic estimate of electronic coupling parameters. *Chem. Phys.* **2006**, *324* (1), 57-62.
39. Salsman, J. C.; Kubiak, C. P.; Ito, T., Mixed valence isomers. *J. Am. Chem. Soc.* **2005**, *127* (8), 2382-2383.
40. Maroncelli, M.; MacInnis, J.; Fleming, G. R., Polar solvent dynamics and electron-transfer reactions. *Science* **1989**, *243* (4899), 1674-1681.
41. Weaver, M. J., Dynamical solvent effects on activated electron-transfer reactions: Principles, pitfalls, and progress. *Chem. Rev.* **1992**, *92* (3), 463-480.
42. Liu, M.; Ito, N.; Maroncelli, M.; Waldeck, D. H.; Oliver, A. M.; Paddon-Row, M. N., Solvent friction effect on intramolecular electron transfer. *J. Am. Chem. Soc.* **2005**, *127* (50), 17867-17876.
43. M D Newton, a.; Sutin, N., Electron transfer reactions in condensed phases. *Annual Review of Physical Chemistry* **1984**, *35* (1), 437-480.
44. Demadis, K. D.; Hartshorn, C. M.; Meyer, T. J., The localized-to-delocalized transition in mixed-valence chemistry. *Chem. Rev.* **2001**, *101* (9), 2655-2686.
45. Hush, N. S., Intervalence-transfer absorption. Part 2. Theoretical considerations and spectroscopic data. In *Progress in inorganic chemistry*, 2007.
46. Cave, R. J.; Newton, M. D., Generalization of the mulliken-hush treatment for the calculation of electron transfer matrix elements. *Chemical Physics Letters* **1996**, *249* (1), 15-19.
47. Yonemoto, E. H.; Riley, R. L.; Kim, Y. I.; Atherton, S. J.; Schmehl, R. H.; Mallouk, T. E., Photoinduced electron transfer in covalently linked ruthenium tris(bipyridyl)-viologen molecules: Observation of back electron transfer in the marcus inverted region. *J. Am. Chem. Soc.* **1992**, *114* (21), 8081-8087.
48. Fox, L. S.; Kozik, M.; Winkler, J. R.; Gray, H. B., Gaussian free-energy dependence of electron-transfer rates in iridium complexes. *Science* **1990**, *247* (4946), 1069-1071.
49. Moia, D.; Vaissier, V.; López-Duarte, I.; Torres, T.; Nazeeruddin, M. K.; O'Regan, B. C.; Nelson, J.; Barnes, P. R. F., The reorganization energy of intermolecular hole hopping between dyes anchored to surfaces. *Chemical Science* **2014**, *5* (1), 281-290.
50. Biner, M.; Buergi, H. B.; Ludi, A.; Roehr, C., Crystal and molecular structures of [ru(bpy)3](pf6)3 and [ru(bpy)3](pf6)2 at 105 k. *J. Am. Chem. Soc.* **1992**, *114* (13), 5197-5203.
51. Cias, P.; Slugovc, C.; Gescheidt, G., Hole transport in triphenylamine based oled devices: From theoretical modeling to properties prediction. *J. Phys. Chem. A* **2011**, *115* (50), 14519-14525.

52. Åqvist, J.; Kazemi, M.; Isaksen, G. V.; Brandsdal, B. O., Entropy and enzyme catalysis. *Acc. Chem. Res.* **2017**, *50* (2), 199-207.
53. Armstrong, A. A.; Amzel, L. M., Role of entropy in increased rates of intramolecular reactions. *J. Am. Chem. Soc.* **2003**, *125* (47), 14596-14602.
54. Page, M. I.; Jencks, W. P., Entropic contributions to rate accelerations in enzymic and intramolecular reactions and the chelate effect. *Proceedings of the National Academy of Sciences* **1971**, *68* (8), 1678-1683.
55. Bruice, T. C.; Lightstone, F. C., Ground state and transition state contributions to the rates of intramolecular and enzymatic reactions. *Acc. Chem. Res.* **1999**, *32* (2), 127-136.
56. Villà, J.; Štrajbl, M.; Glennon, T. M.; Sham, Y. Y.; Chu, Z. T.; Warshel, A., How important are entropic contributions to enzyme catalysis? *Proc. Natl. Acad. Sci USA.* **2000**, *97* (22), 11899-11904.
57. Motley, T. C.; Meyer, G. J., Intramolecular electronic coupling enhances lateral electron transfer across semiconductor interfaces. *J. Phys. Chem. C* **2018**, *122* (26), 14420-14424.
58. DiMarco, B. N.; Motley, T. C.; Balok, R. S.; Li, G.; Siegler, M. A.; O'Donnell, R. M.; Hu, K.; Meyer, G. J., A distance dependence to lateral self-exchange across nanocrystalline tio₂. A comparative study of three homologous ruiii/ii polypyridyl compounds. *J. Phys. Chem. C* **2016**, *120* (26), 14226-14235.
59. Hu, K.; Meyer, G. J., Lateral intermolecular self-exchange reactions for hole and energy transport on mesoporous metal oxide thin films. *Langmuir* **2015**, *31* (41), 11164-11178.
60. Vaissier, V.; Barnes, P.; Kirkpatrick, J.; Nelson, J., Influence of polar medium on the reorganization energy of charge transfer between dyes in a dye sensitized film. *Phys. Chem. Chem. Phys.* **2013**, *15* (13), 4804-4814.
61. Brennan, B. J.; Regan, K. P.; Durrell, A. C.; Schmuttenmaer, C. A.; Brudvig, G. W., Solvent dependence of lateral charge transfer in a porphyrin monolayer. *ACS Energy Letters* **2017**, *2* (1), 168-173.
62. Cappel, U. B.; Feldt, S. M.; Schöneboom, J.; Hagfeldt, A.; Boschloo, G., The influence of local electric fields on photoinduced absorption in dye-sensitized solar cells. *J. Am. Chem. Soc.* **2010**, *132* (26), 9096-9101.
63. Ardo, S.; Sun, Y.; Staniszewski, A.; Castellano, F. N.; Meyer, G. J., Stark effects after excited-state interfacial electron transfer at sensitized tio₂ nanocrystallites. *J. Am. Chem. Soc.* **2010**, *132* (19), 6696-6709.
64. O'Donnell, R. M.; Sampaio, R. N.; Barr, T. J.; Meyer, G. J., Electric fields and charge screening in dye sensitized mesoporous nanocrystalline tio₂ thin films. *J. Phys. Chem. C* **2014**, *118* (30), 16976-16986.

65. Gennett, T.; Milner, D. F.; Weaver, M. J., Role of solvent reorganization dynamics in electron-transfer processes. Theory-experiment comparisons for electrochemical and homogeneous electron exchange involving metallocene redox couples. *J. Phys. Chem.* **1985**, *89* (13), 2787-2794.
66. Mader, E. A.; Manner, V. W.; Markle, T. F.; Wu, A.; Franz, J. A.; Mayer, J. M., Trends in ground-state entropies for transition metal based hydrogen atom transfer reactions. *J. Am. Chem. Soc.* **2009**, *131* (12), 4335-4345.
67. Hupp, J. T.; Weaver, M. J., Solvent, ligand, and ionic charge effects on reaction entropies for simple transition-metal redox couples. *Inorg. Chem.* **1984**, *23* (22), 3639-3644.
68. Neyhart, G. A.; Timpson, C. J.; Bates, W. D.; Meyer, T. J., Solvent-induced electron transfer and electronic delocalization in mixed-valence complexes. Spectral properties. *J. Am. Chem. Soc.* **1996**, *118* (15), 3730-3737.
69. Marcus, R. A.; Siders, P., Theory of highly exothermic electron transfer reactions. *J. Phys. Chem.* **1982**, *86* (5), 622-630.
70. Neyhart, G. A.; Hupp, J. T.; Curtis, J. C.; Timpson, C. J.; Meyer, T. J., Solvent-induced electron transfer and delocalization in mixed-valence complexes. Electrochemistry. *J. Am. Chem. Soc.* **1996**, *118* (15), 3724-3729.
71. Hynes, J. T., Outer-sphere electron-transfer reactions and frequency-dependent friction. *J. Phys. Chem.* **1986**, *90* (16), 3701-3706.
72. Hynes, J. T., Chemical reaction dynamics in solution. *Annual Review of Physical Chemistry* **1985**, *36* (1), 573-597.
73. Chen, P.; Meyer, T. J., Medium effects on charge transfer in metal complexes. *Chem. Rev.* **1998**, *98* (4), 1439-1478.
74. Hans, H., Dynamic solvent effects on electron-transfer reactions. *Angewandte Chemie International Edition in English* **1993**, *32* (3), 359-377.

Chapter 5. A kinetic pathway for interfacial electron transfer from a semiconductor to a molecule⁴

5.1 Introduction

The ability to control charge transfer events at illuminated semiconductor interfaces with precision like that known in molecular donor-bridge-acceptor compounds represents a goal of both practical importance and fundamental significance. In molecular compounds, superexchange can mediate electron transfer over long distances,¹⁻² while conjugated and/or redox active bridges provide opportunities for electron hopping.³⁻⁴ When the donor is a semiconductor and the acceptor is a molecule the corresponding bridge chemistry remains unknown, even though control of this reaction is important for solar cell optimization.⁵ A distance dependence for this interfacial reaction has in fact been demonstrated with molecular bridges,⁶⁻⁸ or insulating thin films in core-shell nanoparticles,⁹⁻¹⁰ and understood as an exponential decrease in the donor-acceptor electronic coupling, $H_{AB} = H_{AB}^0 \exp[-\beta(R - R^0)/2]$, where H_{AB}^0 is the value of H_{AB} at the van der Waals separation R^0 , and β is a constant scaling the distance dependence.¹ However, the abstracted β values do not address whether the bridge simply fixes the distance over which the injected electron tunnels or whether specific pathways are operative. Reported herein is clear evidence of a specific electron transfer *pathway* for interfacial electron transfer from a semiconductor to a molecule.

The question of whether specific electron transfer pathways exist through the intervening matter that separates a donor from an acceptor has been considered for some time.¹¹ In some cases, it is now known that pathways do indeed exist.¹²⁻¹⁴ For example, nature provides

⁴ This work was previously published in Nature Chemistry, 8, 853 with contributions from Ke Hu, Amber D. Blair, Eric J. Piechota, Phil A. Schauer, Renato N. Sampaio, Fraser G. L. Parlane, Gerald J. Meyer, and Curtis P. Berlinguette. Reproduced with permission. Copyright 2019.

kinetic pathways for biological electron transfer that are now understood with a high level of sophistication.^{12-13, 15-16} While a protein continuum β value of 1.4 \AA^{-1} provided reasonable estimates of long range electron transfer in reaction centers,¹⁵⁻¹⁶ it is now understood that the details of the polypeptide structure as well as the presence of specific water clusters must be taken into account to fully rationalize experimental data.¹²⁻¹³ A *tunneling pathway model* emerged for electron transfer in proteins and its educated use at molecular-semiconductor interfaces requires some experimental verification that such interfacial ‘pathways’ do indeed exist. To date, models for electron transfer in molecular solar cells are based solely on thermodynamics and do not account for specific kinetic pathways that might exist. This is unfortunate as solar cell efficiency is generally governed by kinetics and the identification of pathways that promote desired electron transfers while inhibiting unwanted reactions is most impactful.

How can specific electron transfer *pathways* be identified at molecular-semiconductor interfaces? It is non-trivial and is not easily garnered from the previously mentioned ‘distance dependent’ studies where abstracted β values were subject to large uncertainties due to the limited range of distances possible in mesoporous TiO_2 thin films.^{6-7, 9-10, 17} A further complication is that observed rate constants may not unambiguously report on the interfacial electron transfer of interest.¹⁸ The acute sensitivity of this reaction to the number of TiO_2 electrons present in the nanocrystallite¹⁷ and the very weak driving force dependence reported by most,¹⁹⁻²² but not all,²³ has led many to conclude that observed rate constants report only on diffusional encounters of the TiO_2 electrons with the molecular acceptors.²⁴⁻²⁷ Clifford et. al. found that interfacial electron transfer was most easily understood when the physical location of the acceptor frontier molecular orbitals were taken into account,¹⁹ that

has been exploited to optimize interfacial electron transfer with highly doped degenerate semiconductors.²⁸ Collectively, the prior literature is in line with the view point that electron transfer from a semiconductor to a molecular acceptor is sensitive to distance, which naturally raises the question of whether specific interfacial pathways exist.

The experimental approach described here utilizes four bis-tridentate cyclometalated ruthenium(II) compounds linked to a pendent triphenylamine (TPA) group through either a xylyl- or a phenyl-thiophene bridge. When anchored to mesoporous nanocrystalline TiO₂ thin films, pulsed light excitation is known to result in rapid excited state electron transfer to TiO₂.^{22, 29} The desired reaction of the TiO₂(e⁻) with Ru^{III} and TPA⁺ can then be quantified on nanosecond and longer time scales, Figure 5.1.

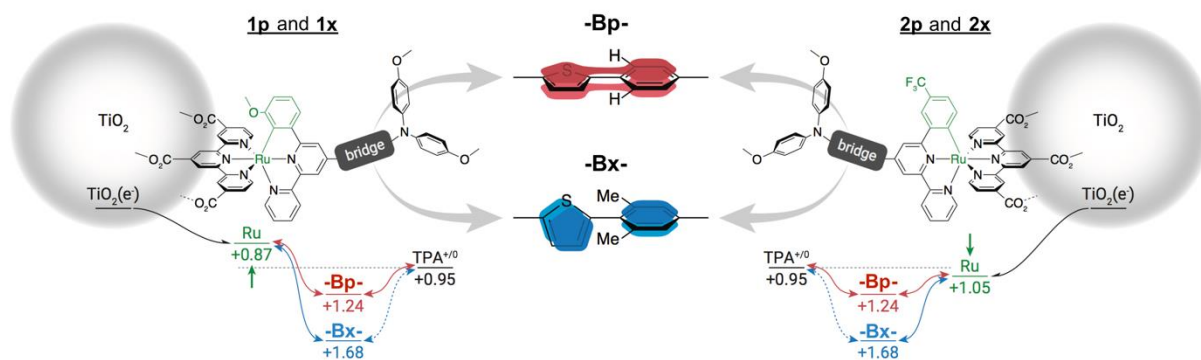


Figure 5.1. The strategy utilized to demonstrate an electron transfer **pathway** from TiO₂ to a molecule. Pulsed laser excitation initiates excited state injection that yields an electron in TiO₂, TiO₂(e⁻), and an oxidized molecule (not shown). The subsequent reaction of the TiO₂(e⁻) with the oxidized molecule shown is then quantified on nanosecond and longer time scales. The exceptional aspect of these molecules is that they vary only in the geometric torsion about the aromatic bridge (black), Bx = xylyl- or Bp = phenyl- thiophene. Hence a bridge dependence for this reaction cannot be attributed to distance or driving force and must result from an interfacial electron transfer pathway that utilizes the bridge orbitals.

Substituents on the carbene ligand were used to tune the Ru^{III/II} potential in two series of compounds that differed only in the bridging ligand, **1x** vs. **1p** and **2x** vs. **2p** where the **x** and **p** abbreviations indicate the **xylyl** and **phenyl** bridges. Within these series the distance and

driving force is held essentially constant while the nature of the bridge is varied. This approach was successful and the comparative study provided the first compelling evidence for an interfacial *pathway* and a clear demonstration that electron transfer kinetics can be optimized through judicious choice of the bridge. Such insights could not have been garnered had the distance and/or driving forces been changed.

5.2 Results

5.2.1 Spectroscopic and redox properties

The visible absorption spectra of the molecules anchored to the TiO₂ thin films were very similar to those measured for the carboxylate forms of the compounds in fluid solution. The materials absorb light through the visible region to beyond 800 nm in all cases. Due to differences in the electronic coupling described further below, **1p** and **2p** have about twice the extinction coefficients of **1x** and **2x**.

Spectro-electrochemistry was used to quantify the interfacial energetics in 0.5 M LiClO₄/CH₃CN electrolyte, Figure 5.2.

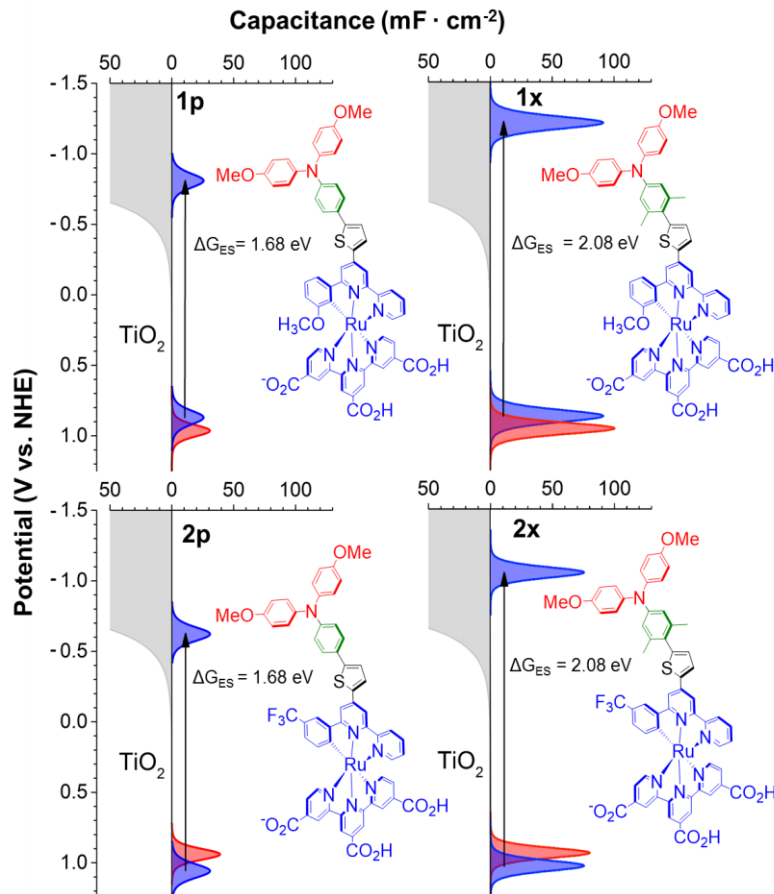


Figure 5.2. The interfacial density of states for **1x/TiO₂**, **1p/TiO₂**, **2x/TiO₂**, **2p/TiO₂** in 0.5 M LiClO₄/CH₃CN. The distributions shaded in blue correspond to Ru^{III/II} redox equilibria and that shaded in red corresponds to TPA^{+/0}.

Raising the Fermi level toward the vacuum level resulted in reduction of TiO₂ with the characteristic appearance of the TiO₂(e⁻) absorption spectrum, as well as small shifts in the molecular absorption spectrum due to an electric field effect.³⁰ Positive applied potentials resulted in absorption changes consistent with the sequential and reversible oxidation of the Ru center and the TPA group; maintenance of isosbestic points enabled determination of the absorption spectra of the one- and two-electron oxidized states of these molecules. The integrated concentration change measured spectroscopically after a potential step of 15-25 mV has been plotted as a capacitance in Figure 2. The electron donating -OCH₃ group on the aryl ring of the cyclometalating ligand for **1x** and **1p** lowered the Ru^{III/II} reduction potential

while the electron withdrawing -CF₃ group for **2x** and **2p** had the opposite effect. The TPA⁺⁰ reduction potentials were held constant by maintaining the same substituents for the entire series under evaluation. For **1x/TiO₂** the Ru metal center was oxidized prior to the TPA group while for **2x/TiO₂** the TPA donor was oxidized prior to the metal center. The potential at which equal concentrations of the reduced and oxidized forms were present was taken as the Ru^{III/II} and TPA⁺⁰ formal reduction potentials. The bridge unit had no measurable influence on the reduction potentials of **1x/TiO₂** relative to **1p/TiO₂**, and only a small 30 mV shift in the Ru^{III/II} reduction potentials for **2x/TiO₂** relative to **2p/TiO₂**, Table 5.1.

Table 5.1. Reduction Potentials^a and Rate Constants for 1-2/TiO₂.

Dyad	R	E _{1/2} ^a	E _{1/2} ^a	K _{Ru(III)} (10 ⁵ s ⁻)	k _{TPA+} (10 ⁵ s ⁻)	H _{AB} ^f (cm ⁻)
1x/TiO₂	-OMe	870	960	5.4 ^d	0.51 ^d	< 100
1p/TiO₂	-OMe	870	960	0.19 ^e	0.19 ^e	1800
2x/TiO₂	-CF ₃	1030	940	6.2 ^d	0.17 ^d	< 100
2p/TiO₂	-CF ₃	1060	940	0.19 ^e	0.19 ^e	1000

^aPotentials are in mV versus NHE. ^bDetermined from electrochemical potentials. ^cMeasured 20 ns after pulsed laser excitation.. ^dValues abstracted from fits to Equation 2 with $\beta = 0.19$. ^eCalculated with $\beta = 0.26$ that correspond to recombination to the equilibrium system (see text). ^fThe values for **1p/TiO₂** and **2p/TiO₂** were abstracted from IVCT analysis of the mixed-valent form of the compound, the values for the xylyl-bridged sensitizers were set as lower limits.

5.2.2 Bridge-mediated electronic coupling

Analysis of the absorption spectra of the mixed-valent forms of these compounds generated by one-electron electrochemical oxidation was revealing. The appearance of an absorption band that was absent in the spectra of the ground and two-electron oxidized states was assigned to an intervalence charge transfer (IVCT) type transition. A weak absorption feature was observed for the mixed-valent form of **2x/TiO₂** at approximately the same energy as **2p/TiO₂**, but no IVCT band could be identified for **1x/TiO₂**. Operating within the approximations of classical Marcus-Hush theory, the value of H_{AB} was calculated directly from the spectral bandshape through the Mulliken-Hush expression, Equation 1,

$$H_{AB} = [(4.2 \cdot 10^{-4})\epsilon_{max}\Delta\bar{\nu}_{1/2}E_{abs})^{1/2}]/d \quad (1)$$

where ϵ_{max} ($M^{-1} cm^{-1}$) is the extinction coefficient of the IVCT band, $\Delta\bar{\nu}_{1/2}$ (cm^{-1}) is the full-width at half-max of the Gaussian-shaped band, E_{abs} (cm^{-1}) is the energy of the transition maximum, and d (\AA) is the calculated 14 \AA distance between the redox active Ru and TPA centers.³¹⁻³² This analysis revealed an H_{AB} value of about $1800 \pm 200 cm^{-1}$ for **1p/TiO₂**, $1000 \pm 300 cm^{-1}$ for **2p/TiO₂**, and $< 100 cm^{-1}$ for **2x/TiO₂**. The inability to resolve the IVCT band for **2x/TiO₂** also implies weak electronic coupling with $H_{AB} < 100 cm^{-1}$. While details of the IVCT energies and band shapes deserve further study, this analysis supports the hypothesis that the methyl substituents in the xylyl bridge disrupt aryl-thiophene bridge conjugation and thereby decrease H_{AB} .

5.2.3 Time-resolved absorption spectroscopy

Figure 5.3A displays absorption difference spectra measured at the indicated delay times after pulsed laser excitation of **2x/TiO₂**. The absorption band centered at 740 nm was characteristic of TPA^+ and the metal-to-ligand charge transfer (MLCT) bleach was diagnostic of the oxidized Ru chromophore. Contributions from the excited states were negligible and spectral simulations based on the spectro-electrochemical data were found to accurately model the transient data, which allowed the relative concentrations of Ru^{III} and TPA^+ to be quantified at all times after laser excitation.

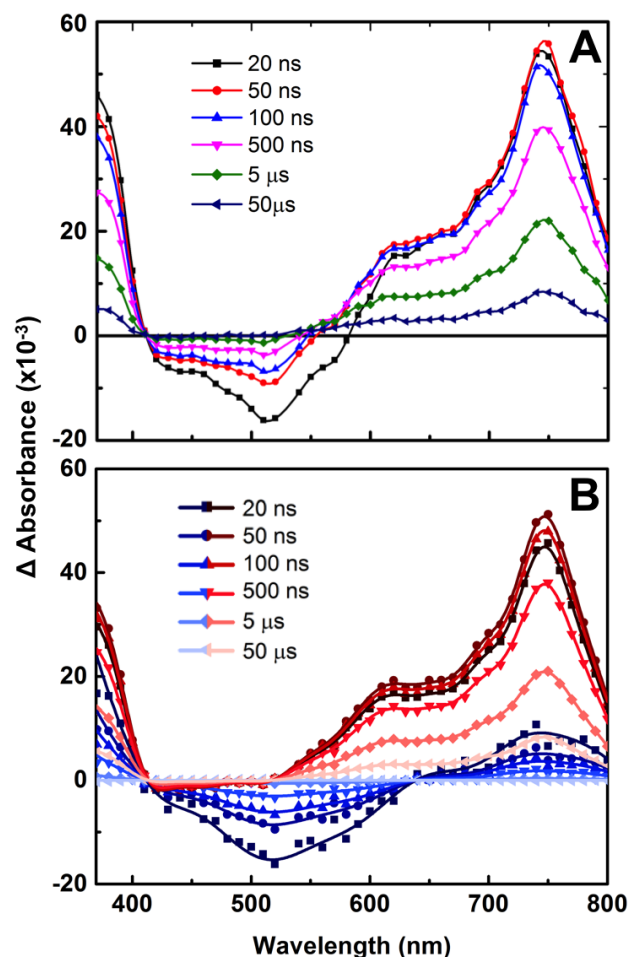


Figure 5.3. The spectroscopic evidence for preferential interfacial electron transfer from TiO_2 to the Ru^{III} center through the xylyl bridge. (A) The transient absorption difference spectra measured at the indicated delay times after pulsed 532 nm excitation (0.2 mJ/cm^2) of **2x**/ TiO_2 in 0.5 M $\text{LiClO}_4/\text{CH}_3\text{CN}$; and (b) the decay associated spectra (B) that show how the concentrations of Ru^{III} (blue) and of TPA^+ (red) change with time.

The prompt appearance of the oxidized molecules indicated rapid excited state electron injection $k_{\text{inj}} > 10^8 \text{ s}^{-1}$ in all cases. Comparative studies with *cis*- $\text{Ru}(\text{dcb})_2(\text{NCS})_2$ sensitized TiO_2 , where dcb is 2,2'-bipyridine-4,4'-dicarboxylic acid, revealed that the injection yields were near unity. For the xylyl bridged sensitizers, about 15% of the TPA^+ was time resolved, consistent with nanosecond $\text{Ru}^{\text{III}} \rightarrow \text{TPA}$ hole transfer $k_{\text{ht}} = 2 \times 10^8 \text{ s}^{-1}$. The appearance of TPA^+ for the phenyl bridged molecules required picosecond time resolution and were about an order of magnitude faster, $k_{\text{ht}} = 4 \times 10^9 \text{ s}^{-1}$.

5.2.4 Electron transfer kinetics

Visual inspection of the data in Figure 3A reveals that the bleach associated with Ru^{III} returns to pre-excitation levels on a faster time scale than does the long wavelength absorption due to TPA⁺. Similar observations were made after pulsed light excitation of **1x/TiO₂**. In contrast for the phenyl bridged sensitizers, recombination to Ru^{III} and TPA⁺ occurred simultaneously such that the normalized absorption difference spectra were time independent.

The kinetics for interfacial electron transfer to yield ground state products were non-exponential and were satisfactorily fit to a sum of two Kohlrausch-Williams-Watts (KWW) functions, equation 2.³³

$$\Delta A(\lambda, t) = A_{Ru^{III}}(\lambda) \cdot e^{-(k_{Ru^{III}}t)^\beta} + A_{TPA^+}(\lambda) \cdot e^{-(k_{TPA^+}t)^\beta} \quad (2)$$

$$\bar{k} = \left[\frac{1}{k\beta} \times \Gamma\left(\frac{1}{\beta}\right) \right]^{-1} \quad (3)$$

In this expression β is related to the breadth of an underlying Lévy distribution of rate constants. The average rate constant \bar{k} was calculated as the first moment, equation 3.³⁴ The time dependent amplitudes $A_{Ru^{III}}$ and A_{TPA^+} were linked to a specific rate constant and plotted against the observation wavelength to yield decay associated spectra (DAS) for the two components.³⁵ Typical DAS are given in Figure 2B with $\bar{k}_{Ru^{III}} = 6.2 \pm 0.6 \times 10^5 \text{ s}^{-1}$ and $\bar{k}_{TPA^+} = 1.7 \pm 0.2 \times 10^4 \text{ s}^{-1}$. The DAS spectra thus provided clear evidence that the two kinetic processes were reduction of the Ru^{III} or TPA⁺ groups. Charge recombination to a Ru model compound that did not contain a pendant TPA donor occurred with an average rate constant $\bar{k}_{Ru^{III}} = 1.9 \pm 0.2 \times 10^4 \text{ s}^{-1}$

Single wavelength kinetics monitored at the peak maximum of 750 nm for TPA⁺ and 510 (or 540) nm for Ru^{III} with overlaid fits are given in Figure 4. Note that the kinetic data measured

between 510 and 540 nm represented a bleach that was inverted in the figure to aid comparisons. This kinetic data is distinctly different to that of **1p/TiO₂** and **2p/TiO₂** where the abstracted rate constants were the same within experimental error, Figure 5.4 insets.²⁹

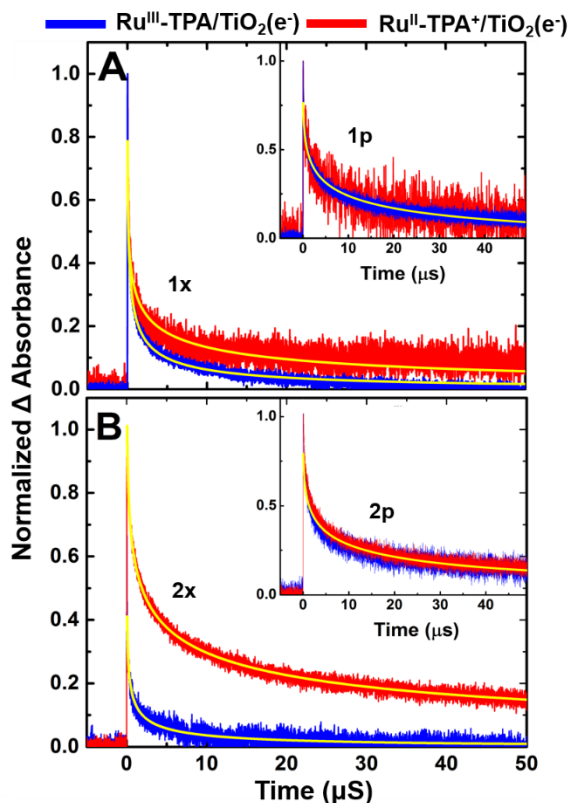


Figure 5.4. Comparative kinetic analysis showing that reduction of TPA⁺ and Ru^{III} were the same for the phenyl bridge, $\bar{k}_{\text{Ru}^{\text{III}}}/\bar{k}_{\text{TPA}^+} = 1$, and were significantly influenced by the xylyl bridge, $\bar{k}_{\text{Ru}^{\text{III}}}/\bar{k}_{\text{TPA}^+} > 10$. Single wavelength kinetic data measured after pulsed 532-nm excitation (0.2 mJ/cm²) of A) 2x/TiO₂ and B) 1x/TiO₂ immersed in 0.5 M LiClO₄/CH₃CN solution at wavelengths that correspond mainly to recombination to Ru^{III} (blue), monitored at 510 nm, and TPA⁺ (red) monitored at 750 nm. The insets show recombination data for 2p/TiO₂ and 1p/TiO₂, of Ru^{III} and TPA⁺ monitored at 550 nm and 740 nm, respectively.

5.3 Discussion

The spectroscopic and electrochemical data clearly indicate that the approach described in the Introduction section for identification of an interfacial electron transfer pathway was successful. To a very good approximation the thermodynamics and distance for interfacial electron transfer were held at parity, with only the nature of the intervening bridge being

altered. Significantly the $E^0(\text{TPA}^{+/0})$ reduction potentials were the same for all the compounds studied. Density functional theory indicated that the methyl substituents in the xylyl bridge destabilized the planar configuration of the aryl-thiophene moiety by about 40 kJ/mole relative to the phenyl bridge. The extinction coefficients of the xylyl bridged compounds were about $\frac{1}{2}$ that of those with phenyl bridges, behavior that is also consistent with decreased conjugation.³⁶⁻³⁷ Marcus-Hush analysis of the absorption spectra of the one-electron oxidized forms of these molecules revealed an approximate 10 fold decrease in electronic coupling (H_{AB}) through the xylyl bridge. The important role that electronic coupling plays on interfacial electron transfer was revealed by kinetic experiments where a laser pulse was used to inject electrons into TiO_2 and the subsequent electron transfer to the singly oxidized molecules was quantified.

For the phenyl bridged molecules, electron transfer to the remote TPA^+ and the more proximate Ru^{III} center were identical. The kinetics were non-exponential, yet overlaid raw transient data as well as average rate constants revealed that electron transfer to both acceptors was the same, $\bar{k}_{\text{Ru}^{\text{III}}}/\bar{k}_{\text{TPA}^+} = 1$. Strong electronic coupling, $H_{AB} > 1000 \text{ cm}^{-1}$, provides highly delocalized molecular orbitals that promote rapid adiabatic electron transfer. At such a strongly coupled interface there is no kinetic advantage for $\text{Ru}^{\text{III}} \rightarrow \text{TPA}$ hole transfer, however the larger surface dipole formed when the TPA is oxidized is known to enhance open circuit photovoltages.²²

In contrast to the phenyl bridged molecules, electron transfer to the remote TPA^+ was slow relative to electron transfer to Ru^{III} for the xylyl bridge compounds, $\bar{k}_{\text{Ru}^{\text{III}}}/\bar{k}_{\text{TPA}^+} > 10$. Indeed, after pulsed laser excitation of **2x**/ TiO_2 electron transfer to the remote TPA^+ was the only kinetic process observed at long observation times. Theoretical calculations indicate that

the xylyl-thiophene bridge molecular orbitals were further removed from the $\text{Ru}^{\text{III/II}}$ and $\text{TPA}^{+/0}$ reduction potentials than were the phenyl-thiophene bridge resulting in decreased mixing and more localized molecular orbitals. Marcus-Hush analysis of the mixed valent forms directly indicates weak electronic coupling, $H_{\text{AB}} < 100 \text{ cm}^{-1}$, through the xylyl bridge that likely underlie the temporal data.

The kinetic data indicates that observed rate constants do indeed report on interfacial electron transfer and are not rate limited by diffusional encounters of the injected electron and the oxidized sensitizer. A preliminary temperature dependent study revealed a significant barrier, the details of which will be discussed in Chapter 6. Given the homologous nature of these molecules and the parity of the $\text{TPA}^{+/0}$ reduction potentials, it is clear that the pathway for electrons includes transfer through the bridge orbitals. The use of methyl substituents that sterically prevent planarization and lower electronic couplings in molecular donor-bridge-acceptor compounds has previously been exploited in molecular energy transfer,³⁸ thermal electron transfer,³⁹ and light driven electron transfer.⁴⁰⁻⁴³ This is the first example at an interface and is important for controlling electron transfer at illuminated semiconductor interfaces that does not necessitate the loss of free energy or rely on distance.

Prior reports and DFT analysis indicate that the direct oxidation or reduction of the bridge through a ‘hopping mechanism’ can be ruled out under these experimental conditions.⁴⁴ The lowest energy bridge-dominated *unfilled* molecular orbitals are $>3 \text{ eV}$ s, while the *filled* molecular orbitals are within 1 eV of the $\text{Ru}^{\text{III/II}}$ and $\text{TPA}^{+/0}$ reduction potentials. This suggests that electron transfer occurs by a ‘hole’ transfer superexchange mechanism with the filled bridge orbitals. This mechanism is well established in purely molecular compounds and

has recently been shown to support long-range electronic communication over distances of $> 27 \text{ \AA}$ through an oligophenylene bridge that provides electronic coupling intermediate to that reported here for the xylyl- and phenyl-thiophene bridges.⁴⁴ While there would be no kinetic advantage to hole super-exchange through an oligophenylene bridge immobilized on semiconductor surfaces, the data reported here indicates that this bridge would also provide a pathway for electron transfer over large distances.

5.4 Conclusions

The spectroscopic and redox behavior of a homologous series of four rigid molecules anchored to semiconducting mesoporous TiO_2 thin films were quantified. The electronic coupling was tuned by introduction of methyl groups that inhibited planarization of a thiophene bridge with an aromatic ring of a tri-aryl amine donor. Density functional theory indicated that the coplanar geometry was destabilized by 40 kJ/mol; Marcus-Hush analysis of the intervalence charge transfer absorption bands revealed that H_{AB} was decreased by about a factor of ten. The orientation of the aryl-thiophene bridge was found to significantly influence electron transfer from TiO_2 to a distal acceptor thereby providing the first compelling evidence of a *pathway* for this important interfacial reaction. This data reveals that through-bond pathways need to be considered in the development of fundamental mechanistic models for interfacial electron transfer at molecular-semiconductor interfaces. Furthermore, the molecular arrangement of the bridge atoms can have a dramatic influence on interfacial electron transfer that can be exploited to optimize solar energy conversion efficiency. While enhancing conjugation in donor-bridge-acceptor sensitizers has been a uniform goal of practitioners seeking state-of-the-art devices over the past half-decade, this work shows for the first time the possible benefit of disrupting said conjugation.

5.5 Additional content and experimental details

5.5.1 Sensitized thin films

Mesoporous nanocrystalline TiO₂ thin films were prepared as described previously.⁴⁵ The as prepared TiO₂ thin films were immersed in $\sim 1 \times 10^{-4}$ M of dye loading solutions over 12 hours for saturation surface coverage for spectroelectrochemistry or the absorbance of the film was controlled at ~ 0.4 at 532 nm for transient absorption measurements in the transmission mode. All samples were purged with argon gas for at least 30 min prior to experimentation.

5.5.2 Spectroelectrochemistry

Steady state UV-vis absorption measurements were carried out on a Varian Cary 50 spectrophotometer at room temperature. Potential steps were applied by a BAS model CV-50W potentiostat. Sensitized TiO₂ thin films on FTO glass (fluorine doped tin oxide, 15 Ω/sq) were used as the working electrodes along with a AgCl/Ag pseudo-reference electrode, and a platinum disk counter electrode; the electrodes were positioned in a 1 cm quartz cuvette and used as the standard three electrode cell. The pseudo-reference electrode was calibrated against ferrocenium/ferrocene (Fc^+/Fc) standard before and after experiments and was converted to normal hydrogen electrode (NHE) with the Fc^+/Fc half wave potential of +630 mV vs. NHE.⁴⁶

5.5.3 Transient absorption spectroscopy

Nanosecond transient absorption measurements were obtained on an apparatus similar to the one that has been described previously.⁴⁵ Briefly, samples were excited by a frequency-doubled Q-switched, pulsed Nd:YAG laser (Quatel USA (BigSky) Brilliant B; 532 nm, 5-6 ns full width at half-maximum (fwhm), 1 Hz, ~ 1 cm in diameter) at $\sim 45^\circ$ angle to the thin

film substrate surface. A 150 W Xe arc lamp (Applied Photophysics) was served as the probe beam orthogonal to the excitation direction. Detection was achieved by a R928 photomultiplier tube (Hamamatsu) optically coupled to a monochromator (Spex 1702/04). Transient data were acquired using a computer interfaced digital oscilloscope (LeCroy 9450, Dual 350 MHz). Transient signals were typically averaged with 30-50 laser pulses. Kinetic data fitting was performed in Origin 9 using Levenberg-Marquardt iteration method for least-squares error minimization and spectral modeling was performed using a code written in Mathematica 10. Excited state injection yields for all compounds were determined by comparative actinometry using N3 as the reference with injection yield equal to 1, Table S1.⁴⁷

5.5.4 Density functional theory calculations

Ground state geometries of xylyl- and phenyl- thiophene bridges were optimized and orbital energies were calculated using B3LYP and 6-31G(d) basis set. Calculation was carried using Gaussian 09 Package.⁴⁸

5.5.5 H_{DA} calculations

Using Equation 1 in the text, H_{AB} was calculated for both **1p** and **2p** individually. Beginning with **2p**, the growth and recession of a CT band was evident in the steady-state UV-Visible spectro-electrochemical data, but was analyzed explicitly by subtracting the ground state spectrum at an applied potential that could not oxidize TPA or the Ru^{II} center, see text (Figure 1). After referencing the various spectra at higher applied potentials to the ground state, we observe a bleach of the Ru^{II} absorbance at 530 nm and a growth of TPA⁺ absorbance occurring around 730 nm. There was a significant growth and decay of an absorbance peak to the high energy side of the formal TPA⁺ absorbance attributed to an

IVCT band. This band, centered at 15500 cm^{-1} (645 nm), reached a maximum at $V_{\text{app}} = 995$ mV vs. NHE. Five unique Gaussian fits of the band yielded values for E_{abs} (*vide supra*) and $\Delta\bar{\nu}_{1/2} \cdot \epsilon_{\text{max}}$ was estimated from the extinction coefficient of a structurally similar compound at 19230 cm^{-1} (520 nm) and 23200 cm^{-1} (431 nm) with extinction coefficients of 41.5×10^3 and $39.1 \times 10^3\text{ M}^{-1}\text{ cm}^{-1}$, respectively.⁴⁹ Under the assumption that the number of **2p** molecules that are in the intervalence state is equal to the number in the ground state (i.e. complete 1 e^- oxidation to the mixed valence state), a ratio of absorbance values and extinction coefficients was employed, and ten values of H_{AB} were calculated. The average of these values is reported in Table 1.

A similar analysis was performed for **1p**. The growth occurred at energies similar to the bleach of the ground state of **1p** which complicated the analysis when the ground state was used as a reference spectrum. To circumvent this, the *fully oxidized spectrum* was treated as the ground state of the system. A depletion of TPA^+ absorbance at 740 nm and a growth of the Ru^{II} -centered absorbance at 530 nm were observed. Similar to **2p**, the growth and recession of a band was attributed to an IVCT transition. The band maximum was observed at $V_{\text{app}} = 905$ mV vs. NHE, and was centered at 20620 cm^{-1} (485 nm). The extinction coefficients used for the structural analog of **1p** were observed at 18800 cm^{-1} (532 nm) and 22780 cm^{-1} (439 nm) with reported values of 32.8×10^3 and $44.9 \times 10^3\text{ M}^{-1}\text{ cm}^{-1}$, respectively.⁴⁹ The same approach to calculate the CT extinction was used for **1p**. The average value is given in Table 1.

5.6 Acknowledgements

GJM gratefully acknowledge support by a grant from the Division of Chemical Sciences, Office of Basic Energy Sciences, Office of Energy Research, U.S. Department of Energy

(DE-SC0013461). The authors thank Ms. Melissa Gish and the Papanikolas group at UNC for the ultrafast measurements.

REFERENCES

1. Closs, G. L.; Miller, J. R., Intramolecular long-distance electron transfer in organic molecules. *Science* **1988**, *240* (4851), 440-447.
2. Davis, W. B.; Svec, W. A.; Ratner, M. A.; Wasielewski, M. R., Molecular-wire behaviour in p -phenylenevinylene oligomers. *Nature* **1998**, *396* (6706), 60-63.
3. Lambert, C.; Noll, G.; Schelter, J., Bridge-mediated hopping or superexchange electron-transfer processes in bis(triarylamine) systems. *Nat. Mater.* **2002**, *1* (1), 69-73.
4. Vura-Weis, J.; Abdelwahed, S. H.; Shukla, R.; Rathore, R.; Ratner, M. A.; Wasielewski, M. R., Crossover from single-step tunneling to multistep hopping for molecular triplet energy transfer. *Science* **2010**, *328* (5985), 1547-1550.
5. Ardo, S.; Meyer, G. J., Photodriven heterogeneous charge transfer with transition-metal compounds anchored to TiO₂ semiconductor surfaces. *Chem. Soc. Rev.* **2009**, *38* (1), 115-164.
6. Abrahamsson, M.; Johansson, P. G.; Ardo, S.; Kopecky, A.; Galoppini, E.; Meyer, G. J., Decreased interfacial charge recombination rate constants with N₃-type sensitizers. *J. Phys. Chem. Lett.* **2010**, *1* (11), 1725-1728.
7. Asbury, J. B.; Hao, E. C.; Wang, Y. Q.; Lian, T. Q., Bridge length-dependent ultrafast electron transfer from re polypyridyl complexes to nanocrystalline tio2 thin films studied by femtosecond infrared spectroscopy. *J. Phys. Chem. B* **2000**, *104* (50), 11957-11964.
8. Haque, S. A.; Handa, S.; Peter, K.; Palomares, E.; Thelakkat, M.; Durrant, J. R., Supramolecular control of charge transfer in dye-sensitized nanocrystalline tio2 films: Towards a quantitative structure–function relationship. *Angew. Chemie. Int. Ed.* **2005**, *44* (35), 5740-5744.
9. Cameron, P. J.; Peter, L. M., Characterization of titanium dioxide blocking layers in dye-sensitized nanocrystalline solar cells. *J. Phys. Chem. B* **2003**, *107* (51), 14394-14400.
10. Palomares, E.; Clifford, J. N.; Haque, S. A.; Lutz, T.; Durrant, J. R., Control of charge recombination dynamics in dye sensitized solar cells by the use of conformally deposited metal oxide blocking layers. *J. Am. Chem. Soc.* **2003**, *125* (2), 475-482.
11. Taube, H.; Myers, H., Evidence for a bridged activated complex for electron transfer reactions. *J. Am. Chem. Soc.* **1954**, *76* (8), 2103-2111.
12. Beratan, D. N.; Betts, J. N.; Onuchic, J. N., Protein electron transfer rates set by the bridging secondary and tertiary structure. *Science* **1991**, *252* (5010), 1285-1288.
13. Beratan, D. N.; Onuchic, J.; xe; Nelson; Winkler, J. R.; Gray, H. B., Electron-tunneling pathways in proteins. *Science* **1992**, *258* (5089), 1740-1741.

14. Wenger, O. S., Photoinduced electron and energy transfer in phenylene oligomers. *Chem. Soc. Rev.* **2011**, *40* (7), 3538-3550.
15. Hopfield, J. J., Electron transfer between biological molecules by thermally activated tunneling. *Proc. Natl. Acad. Sci. USA* **1974**, *71* (9), 3640-3644.
16. Moser, C.; Page, C.; Farid, R.; Dutton, P. L., Biological electron transfer. *J. Bioeng. Biomem.* **1995**, *27* (3), 263-274.
17. Haque, S. A.; Tachibana, Y.; Klug, D. R.; Durrant, J. R., Charge recombination kinetics in dye-sensitized nanocrystalline titanium dioxide films under externally applied bias. *J. Phys. Chem. B* **1998**, *102* (10), 1745-1749.
18. Brigham, E. C.; Meyer, G. J., Ostwald isolation to determine the reaction order for $\text{TiO}_2(e^-)/\text{S}^+ \rightarrow \text{TiO}_2$ is charge recombination at sensitized TiO_2 interfaces. *J. Phys. Chem. C* **2014**, *118* (15), 7886-7893.
19. Clifford, J. N.; Palomares, E.; Nazeeruddin, K.; Thampi, R.; Gratzel, M.; Durrant, J. R., Multistep electron transfer processes on dye co-sensitized nanocrystalline TiO_2 films. *J. Am. Chem. Soc.* **2004**, *126* (18), 5670-5671.
20. Hasselmann, G. M.; Meyer, G. J., Diffusion-limited interfacial electron transfer with large apparent driving forces. *J. Phys. Chem. B* **1999**, *103* (36), 7671-7675.
21. Maggio, E.; Troisi, A., Theory of the charge recombination reaction at the semiconductor-adsorbate interface in the presence of defects. *J. Phys. Chem. C* **2013**, *117* (46), 24196-24205.
22. Hu, K.; Robson, K. C. D.; Beauvilliers, E. E.; Schott, E.; Zarate, X.; Arratia-Perez, R.; Berlinguette, C. P.; Meyer, G. J., Intramolecular and lateral intermolecular hole transfer at the sensitized TiO_2 interface. *J. Am. Chem. Soc.* **2014**, *136* (3), 1034-1046.
23. Kuciauskas, D.; Freund, M. S.; Gray, H. B.; Winkler, J. R.; Lewis, N. S., Electron transfer dynamics in nanocrystalline titanium dioxide solar cells sensitized with ruthenium or osmium polypyridyl complexes. *J. Phys. Chem. B* **2001**, *105* (2), 392-403.
24. Ashford, D. L.; Song, W. J.; Concepcion, J. J.; Glasson, C. R. K.; Brennaman, M. K.; Norris, M. R.; Fang, Z.; Templeton, J. L.; Meyer, T. J., Photoinduced electron transfer in a chromophore-catalyst assembly anchored to TiO_2 . *J. Am. Chem. Soc.* **2012**, *134* (46), 19189-19198.
25. Barzykin, A. V.; Tachiya, M., Mechanism of molecular control of recombination dynamics in dye-sensitized nanocrystalline semiconductor films. *J. Phys. Chem. B* **2004**, *108* (24), 8385-8389.
26. Hanson, K.; Brennaman, M. K.; Ito, A.; Luo, H.; Song, W.; Parker, K. A.; Ghosh, R.; Norris, M. R.; Glasson, C. R. K.; Concepcion, J. J.; Lopez, R.; Meyer, T. J., Structure-property relationships in phosphonate-derivatized, Ru(II) polypyridyl dyes on metal oxide surfaces in an aqueous environment. *J. Phys. Chem. C* **2012**, *116* (28), 14837-14847.

27. Nelson, J., Continuous-time random-walk model of electron transport in nanocrystalline TiO_2 electrodes. *Phys. Rev. B* **1999**, *59* (23), 15374-15380.
28. Huang, Z. J.; He, M. F.; Yu, M. Z.; Click, K.; Beauchamp, D.; Wu, Y. Y., Dye-controlled interfacial electron transfer for high-current indium tin oxide photocathodes. *Angew. Chemie. Intd. Ed.* **2015**, *54* (23), 6857-6861.
29. Hu, K.; Robson, K. C. D.; Johansson, P. G.; Berlinguette, C. P.; Meyer, G. J., Intramolecular hole transfer at sensitized TiO_2 interfaces. *J. Am. Chem. Soc.* **2012**, *134* (20), 8352-8355.
30. Ardo, S.; Sun, Y.; Staniszewski, A.; Castellano, F. N.; Meyer, G. J., Stark effects after excited-state interfacial electron transfer at sensitized TiO_2 nanocrystallites. *J. Am. Chem. Soc.* **2010**, *132* (19), 6696-6709.
31. Brunschwig, B. S.; Creutz, C.; Sutin, N., Optical transitions of symmetrical mixed-valence systems in the class ii-iii transition regime. *Chem. Soc. Rev.* **2002**, *31* (3), 168-184.
32. Chen, P. Y.; Meyer, T. J., Medium effects on charge transfer in metal complexes. *Chem. Rev.* **1998**, *98* (4), 1439-1477.
33. Williams, G.; Watts, D. C., Non-symmetrical dielectric relaxation behaviour arising from a simple empirical decay function. *Trans. Farad. Soc.* **1970**, *66* (0), 80-85.
34. Lindsey, C. P.; Patterson, G. D., Detailed comparison of the williams–watts and cole–davidson functions. *J. Chem. Phys.* **1980**, *73* (7), 3348-3357.
35. Knutson, J. R.; Walbridge, D. G.; Brand, L., Decay-associated fluorescence-spectra and the heterogeneous emission of alcohol-dehydrogenase. *Biochemistry* **1982**, *21* (19), 4671-4679.
36. Robson, K. C. D.; Koivisto, B. D.; Gordon, T. J.; Baumgartner, T.; Berlinguette, C. P., Triphenylamine-modified ruthenium(II) terpyridine complexes: Enhancement of light absorption by conjugated bridging motifs. *Inorg. Chem.* **2010**, *49* (12), 5335-5337.
37. Chen, C.-Y.; Chen, J.-G.; Wu, S.-J.; Li, J.-Y.; Wu, C.-G.; Ho, K.-C., Multifunctionalized ruthenium-based supersensitizers for highly efficient dye-sensitized solar cells. *Angew. Chemie. Int. Ed.* **2008**, *47* (38), 7342-7345.
38. Song, H. E.; Taniguchi, M.; Diers, J. R.; Kirmaier, C.; Bocian, D. F.; Lindsey, J. S.; Holten, D., Linker dependence of energy and hole transfer in neutral and oxidized multiporphyrin arrays. *J. Phys. Chem. B* **2009**, *113* (52), 16483-16493.
39. Chen, P. Y.; Curry, M.; Meyer, T. J., Effects of conformational change in the acceptor on intramolecular electron-transfer. *Inorg. Chem.* **1989**, *28* (12), 2271-2280.
40. Hanss, D.; Walther, M. E.; Wenger, O. S., Importance of covalence, conformational effects and tunneling-barrier heights for long-range electron transfer: Insights from dyads with oligo-p-phenylene, oligo-p-xylene and oligo-p-dimethoxybenzene bridges. *Coord. Chem. Rev.* **2010**, *254* (21–22), 2584-2592.

41. Laine, P. P.; Bedioui, F.; Loiseau, F.; Chiorboli, C.; Campagna, S., Conformationally gated photoinduced processes within photosensitizer-acceptor dyads based on osmium(II) complexes with triarylpyridinio-functionalized terpyridyl ligands: Insights from experimental study. *J. Am. Chem. Soc.* **2006**, *128* (23), 7510-7521.
42. Meylemans, H. A.; Lei, C. F.; Damrauer, N. H., Ligand structure, conformational dynamics, and excited-state electron delocalization for control of photoinduced electron transfer rates in synthetic donor-bridge-acceptor systems. *Inorg. Chem.* **2008**, *47* (10), 4060-4076.
43. Sun, D. L.; Rosokha, S. V.; Lindeman, S. V.; Kochi, J. K., Intervalence (charge-resonance) transitions in organic mixed-valence systems. Through-space versus through-bond electron transfer between bridged aromatic (redox) centers. *J. Am. Chem. Soc.* **2003**, *125* (51), 15950-15963.
44. Shen, J.-J.; Zhong, Y.-W., Long-range ruthenium-amine electronic communication through the para-oligophenylene wire. *Sci. Rep.* **2015**, *5*, 13835.
45. Argazzi, R.; Bignozzi, C. A.; Heimer, T. A.; Castellano, F. N.; Meyer, G. J., Enhanced spectral sensitivity from ruthenium(II) polypyridyl based photovoltaic devices. *Inorg. Chem.* **1994**, *33* (25), 5741-5749.
46. Pavlishchuk, V. V.; Addison, A. W., Conversion constants for redox potentials measured versus different reference electrodes in acetonitrile solutions at 25°C. *Inorg. Chimica Acta* **2000**, *298* (1), 97-102.
47. Johansson, P. G.; Rowley, J. G.; Taheri, A.; Meyer, G. J.; Singh, S. P.; Islam, A.; Han, L., Long-wavelength sensitization of TiO₂ by ruthenium diimine compounds with low-lying π^* orbitals. *Langmuir* **2011**, *27* (23), 14522-14531.
48. Frisch, M. J.; Trucks, G. W.; Schlegel, H. B.; Scuseria, G. E.; Robb, M. A.; Cheeseman, J. R.; Scalmani, G.; Barone, V.; Mennucci, B.; Petersson, G. A.; Nakatsuji, H.; Caricato, M.; Li, X.; Hratchian, H. P.; Izmaylov, A. F.; Bloino, J.; Zheng, G.; Sonnenberg, J. L.; Hada, M.; Ehara, M.; Toyota, K.; Fukuda, R.; Hasegawa, J.; Ishida, M.; Nakajima, T.; Honda, Y.; Kitao, O.; Nakai, H.; Vreven, T.; Montgomery Jr., J. A.; Peralta, J. E.; Ogliaro, F. o.; Bearpark, M. J.; Heyd, J.; Brothers, E. N.; Kudin, K. N.; Staroverov, V. N.; Kobayashi, R.; Normand, J.; Raghavachari, K.; Rendell, A. P.; Burant, J. C.; Iyengar, S. S.; Tomasi, J.; Cossi, M.; Rega, N.; Millam, N. J.; Klene, M.; Knox, J. E.; Cross, J. B.; Bakken, V.; Adamo, C.; Jaramillo, J.; Gomperts, R.; Stratmann, R. E.; Yazyev, O.; Austin, A. J.; Cammi, R.; Pomelli, C.; Ochterski, J. W.; Martin, R. L.; Morokuma, K.; Zakrzewski, V. G.; Voth, G. A.; Salvador, P.; Dannenberg, J. J.; Dapprich, S.; Daniels, A. D.; Farkas, A. d. n.; Foresman, J. B.; Ortiz, J. V.; Cioslowski, J.; Fox, D. J. *Gaussian 09*, Gaussian, Inc.: Wallingford, CT, USA, 2009.
49. Robson, K. C. D.; Spornova, B.; Koivisto, B. D.; Schott, E.; Brown, D. G.; Berlinguette, C. P., Systematic modulation of a bichromic cyclometalated ruthenium(II) scaffold bearing a redox-active triphenylamine constituent. *Inorg. Chem.* **2011**, *50* (13), 6019-6028.

Chapter 6. Barriers for interfacial back-electron transfer: a comparison between TiO₂ and SnO₂/TiO₂ core/shell structures⁵

6.1 Introduction

Mesoporous thin films of wide bandgap metal oxide semiconductors, such as TiO₂ and SnO₂, are commonly utilized for dye-sensitized solar energy conversion and storage applications.¹⁻¹⁴ Dye-sensitized water oxidation with these materials requires catalysts that accept redox equivalents from the oxidized dyes and accumulate them for O₂(g) production while avoiding recombination with the injected electrons.^{1, 3-4, 10-13, 15} To this extent, the lifetime of electrons injected into TiO₂ and related metal oxide (MO_x) thin films is critically important. The microsecond lifetimes that are typical for anatase TiO₂ used in regenerative dye-sensitized solar cells are often insufficient for the much slower water oxidation reactions. In an attempt to circumvent this kinetic limitation, core/shell SnO₂/TiO₂ architectures have been utilized that inhibit interfacial charge recombination, termed hereafter “back-electron transfer” (BET), and greatly extend the lifetime of the injected electron relative to TiO₂ alone.^{5-9, 16-20} As a result, the core/shell SnO₂/TiO₂ thin films exhibit higher water oxidation efficiencies when compared to their SnO₂ or TiO₂ counterparts.^{11, 21-24}

Although core/shell metal oxides are commonly utilized for dye-sensitized water oxidation, the origin of the enhanced water oxidation performance and longer lifetimes of the injected electrons are still debated.^{5, 16, 25} Two models have been proposed. In the first, the

⁵This work was previously published in *The Journal of Chemical Physics*, 150 (4), 041719 with contributions from Ludovic Troian-Gautier, Renato N. Sampaio, Eric J. Piechota, Matthew D. Brady, and Gerald J. Meyer. Reproduced with permission. Copyright 2019.

~300 meV (29 kJ mol⁻¹) lower conduction band edge expected for single crystal SnO₂ relative to TiO₂ has been proposed to provide to exist within the core/shell materials thereby providing a barrier for electrons residing in the core to enter the shell.¹⁶ In the second model, an interfacial Sn_xTi_yO₂ species has been proposed to be present between the core and the shell which provides a low energy trap for injected electrons.²⁵

Temperature dependent back-electron transfer kinetics provide estimates of the intrinsic barrier for the rate determining BET step and hence insights into the mechanism. Standard Arrhenius analysis has previously provided activation energies (E_a) for back-electron transfer that ranged between 11 kJ mol⁻¹ and 27 kJ mol⁻¹ depending on the nature of the mediator or sensitizer as well as the distance between the redox center and the TiO₂ nanocrystallites.²⁶⁻²⁹

Herein, the underlying thermodynamic barriers for back-electron transfer for both TiO₂ and core/shell SnO₂/TiO₂ thin films are reported. The sensitizers utilized were bis(tridentate) cyclometalated Ru^{II} centers, CF₃-**x** and CF₃-**p**, covalently bound through a phenyl- or xylyl-thiophene bridge to a pendant triphenylamine (TPA) unit (Figure 6.1). Substitutions on the bridge allowed the electronic coupling, H_{DA} , to be modulated. The phenyl bridge ($R = H$) facilitated strong electronic coupling and adiabatic electron transfer, $H_{DA} > 1000 \text{ cm}^{-1}$, whereas the xylyl bridge ($R = CH_3$) resulted in smaller coupling, $H_{DA} < 150 \text{ cm}^{-1}$.³⁰⁻³¹ The kinetic analysis provided the equilibrium constants for the Ru^{III/II}-B-TPA^{+ /0} and the values were found to be closer to unity for the adiabatic equilibrium, *i.e.* $|\Delta G^0_{ad}| < |\Delta G^0|$.³¹ The data also showed that the activation energies for back-electron transfer from electrons in SnO₂/TiO₂ core/shell to Ru^{III} or TPA⁺ were consistently larger than those measured for TiO₂.

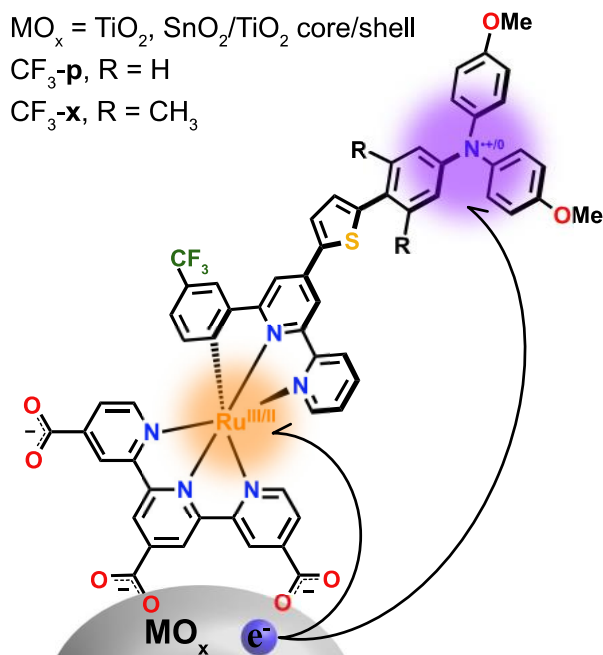


Figure 6.1: Structure of the D-B-A sensitizers bearing either a xyllyl bridge ($\text{R} = \text{CH}_3, \text{CF}_3\text{-x}$) or a phenyl bridge ($\text{R} = \text{H}, \text{CF}_3\text{-p}$) anchored on different metal oxides (TiO_2 or $\text{SnO}_2/\text{TiO}_2$ core/shell). The recombination reaction from electrons in the metal oxides to the oxidized Ru^{III} or the oxidized TPA^+ is highlighted.

6.2 Results

Experimental procedures for thin film fabrication are presented in Section 6.5. The $\text{CF}_3\text{-x}$ and $\text{CF}_3\text{-p}$ sensitizers were synthesized following published procedures and were anchored on TiO_2 or $\text{SnO}_2/\text{TiO}_2$ core/shell (CS) thin films (abbreviated hereafter $\text{TiO}_2|\text{CF}_3\text{-x/p}$ and $\text{CS}|\text{CF}_3\text{-x/p}$) by soaking in a concentrated methanol solution.³² The thin films were immersed in the desired sensitizer solution until absorbance values reached 0.3-0.6 at 430 nm. Low sensitizer surface coverages were utilized to inhibit dye to oxidized dye intermolecular electron transfer (also known as lateral hole-hopping).³³⁻³⁷

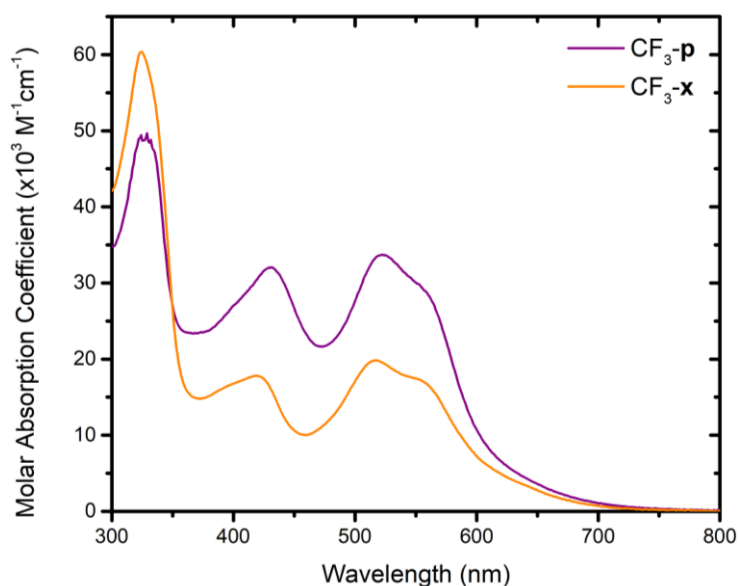


Figure 6.2: Absorption spectra of CF₃-**p** and CF₃-**x** recorded in methanol at room temperature.

Typical absorption spectra of CF₃-**x/p** in methanol solution are represented in Figure 6.2. The ground-state UV-vis spectra exhibited three major spectral features. First, the absorption bands at lower energy, centered around 510 nm and 600 nm, were attributed to metal-to-ligand charge transfer (MLCT) transitions. Second, the higher energy band, centered around 450 nm, was characteristic of an intra-ligand charge transfer (ILCT) transition between the cyclometalating ligand and the triphenylamine moiety. Third, the absorption features below 400 nm, which were attributed to π to π^* transitions of terpyridine, triphenylamine and the cyclometalating ligand. Detailed oxidative spectroelectrochemical studies of the sensitizers CF₃-**x** and CF₃-**p** have been previously reported in solution and anchored to metal oxide thin films.³⁰⁻³² Briefly, upon surface immobilization, CF₃-**x** and CF₃-**p** exhibited a TPA-centered oxidation with $E^\circ(\text{TPA}^{+/0}) = 945$ mV and 955 mV vs NHE respectively, which were concomitant with the appearance of TPA⁺ absorption features around 700 nm. Applying a more positive potential led to Ru^{III/II} oxidation and a MLCT bleach with $E^\circ(\text{Ru}^{\text{III/II}}) = 1010$ mV and 1050 mV vs NHE for CF₃-**x** and CF₃-**p** respectively.³⁰

The transient absorption difference spectra of $\text{TiO}_2|\text{CF}_3\text{-x/p}$ and $\text{CS}|\text{CF}_3\text{-x/p}$ after pulsed 532 nm light excitation in 0.1 M LiClO_4 CH_3CN electrolyte are represented in Figure 6.3. Pulsed light excitation led to rapid electron injection, that could not be time-resolved, from the cyclometalated Ru excited-state into the metal oxide, $\text{MO}_x|\text{Ru}^{\text{II}*} - \text{B} - \text{TPA} \rightarrow \text{MO}_x(\text{e}^-)|\text{Ru}^{\text{III}} - \text{B} - \text{TPA}$, where $\text{Ru}^{\text{II}}\text{-B-TPA}$ denotes either $\text{CF}_3\text{-x}$ or $\text{CF}_3\text{-p}$ and MO_x is either TiO_2 or $\text{SnO}_2/\text{TiO}_2$ core/shell thin films. The nature of the bridge (B), *i.e.* thiophene-xylyl or thiophene-phenyl, controlled the extent of electronic coupling between Ru^{III} and TPA, $\text{MO}_x(\text{e}^-)|\text{Ru}^{\text{III}} - \text{B} - \text{TPA} \rightleftharpoons \text{MO}_x(\text{e}^-)|\text{Ru}^{\text{II}} - \text{B} - \text{TPA}^+$.³¹ Oxidized triphenylamine (TPA^+) exhibited very distinct absorption features above 600 nm.³⁸ Back-electron transfer from electrons in the metal oxide thin films to TPA^+ was monitored at 750 nm, $\text{MO}_x(\text{e}^-)|\text{Ru}^{\text{II}} - \text{B} - \text{TPA}^+ \rightarrow \text{MO}_x|\text{Ru}^{\text{II}} - \text{B} - \text{TPA}$. The corresponding back-electron transfer from $\text{CS}(\text{e}^-)$ to TPA^+ occurred 1-2 orders of magnitude slower than for $\text{TiO}_2(\text{e}^-)$. Indeed, the TPA^+ transient signal returned to pre-excitation levels within several hundreds of microseconds for sensitizers anchored to TiO_2 whereas it took around 0.1 seconds on $\text{SnO}_2/\text{TiO}_2$ core/shell nanoparticles.

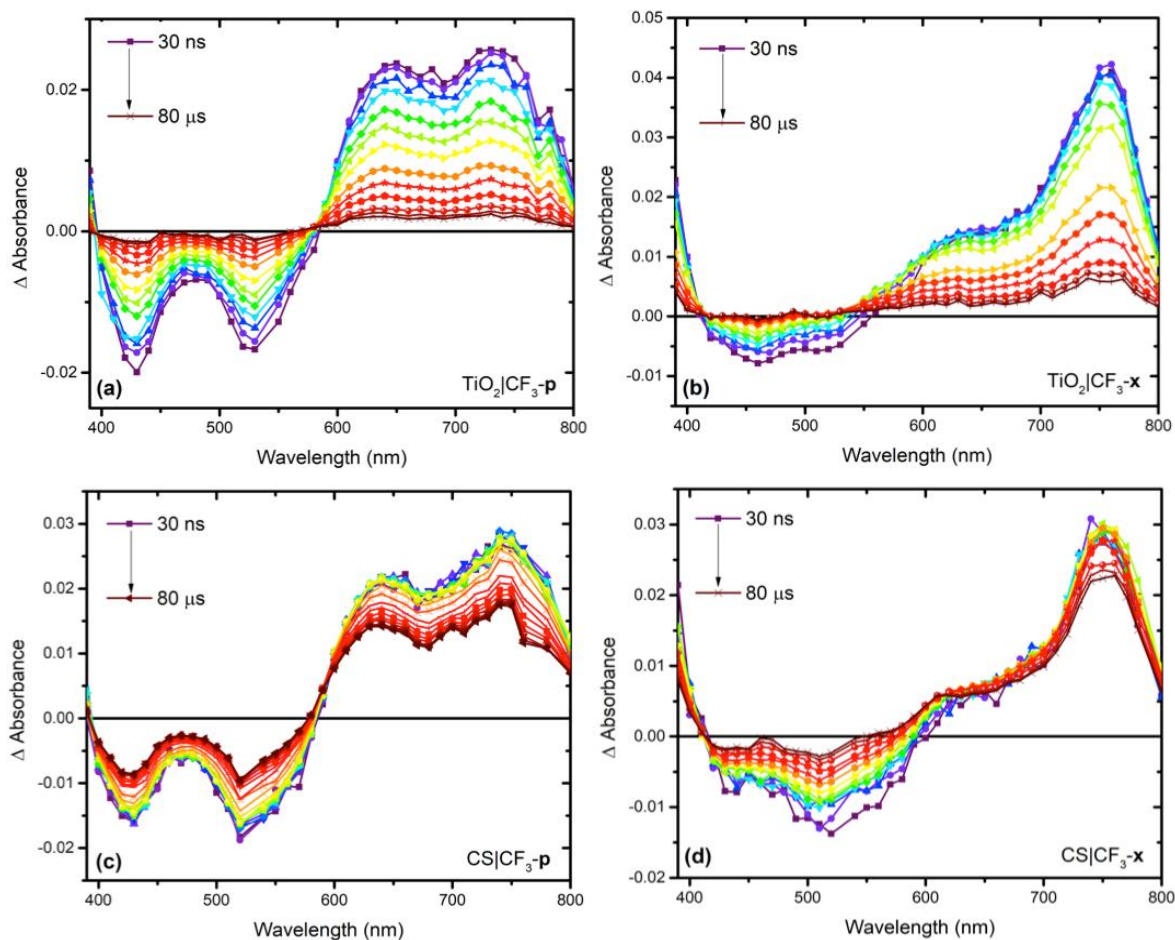


Figure 6.3: Transient absorption difference spectra measured over the indicated time range after pulsed 532 nm light excitation of $\text{TiO}_2|\text{CF}_3\text{-p}$ (a), $\text{TiO}_2|\text{CF}_3\text{-x}$ (b), $\text{CS}|\text{CF}_3\text{-p}$ (c) and $\text{CS}|\text{CF}_3\text{-x}$ (d) thin films submerged in argon purged 0.1M LiClO_4 CH_3CN electrolyte.

To gain further insight into the barriers for back-electron transfer, single wavelength absorption changes were recorded at 730 nm over a temperature range that spanned 110° (from -40°C to +70°C). Representative data for $\text{TiO}_2|\text{CF}_3\text{-x/p}$ and $\text{CS}|\text{CF}_3\text{-x/p}$ are represented in Figure 6.4.

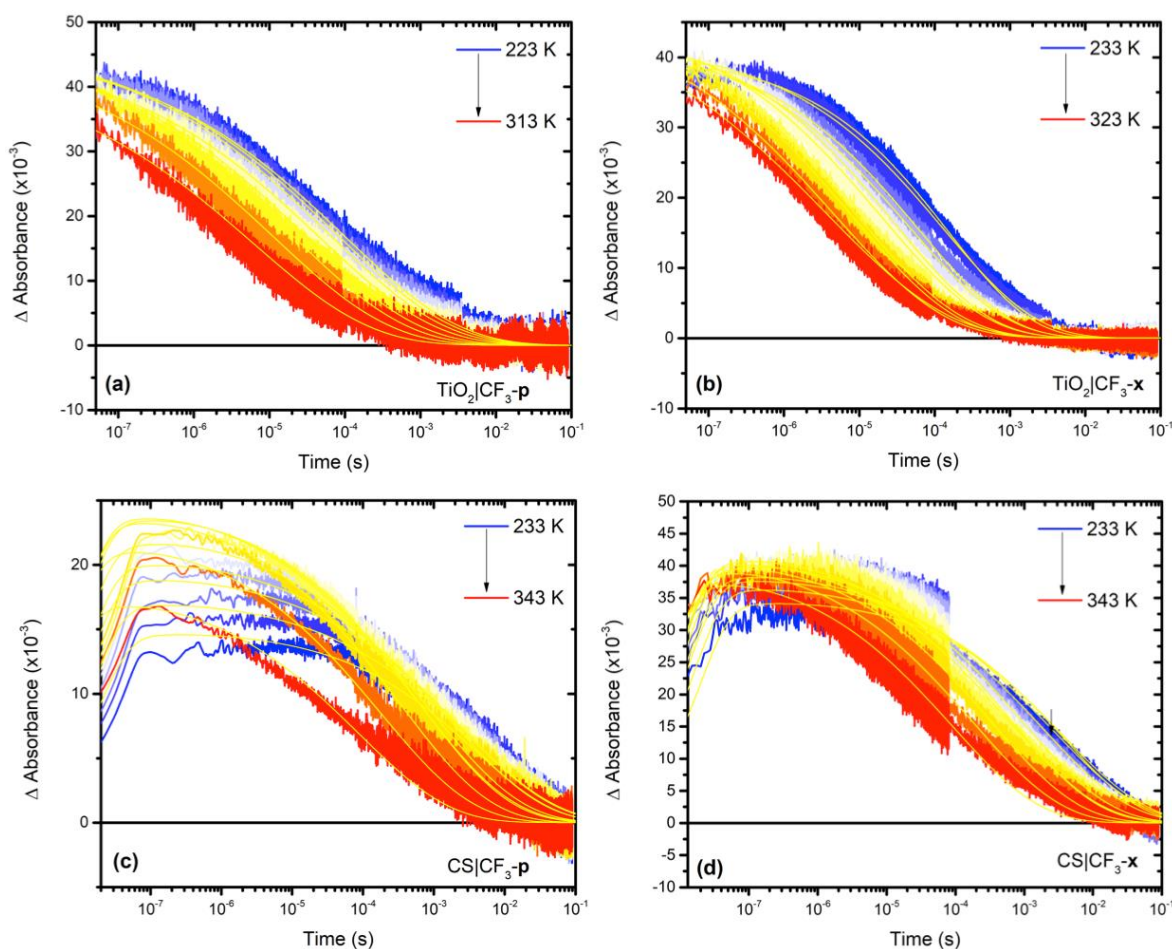


Figure 6.4: The absorption change monitored at 730 nm after pulsed 532 nm excitation of $\text{TiO}_2|\text{CF}_3\text{-p}$ (a), $\text{TiO}_2|\text{CF}_3\text{-x}$ (b), $\text{CS}|\text{CF}_3\text{-p}$ (c) and $\text{CS}|\text{CF}_3\text{-x}$ (d) over the temperature ranges indicated. The dye-sensitized thin films were immersed in an argon purged 0.1M LiClO_4 CH_3CN electrolyte solution.

A previously described kinetic model³¹ (*vide infra*), that accounts for both intramolecular electron transfer equilibrium between the oxidized sensitizer and the triphenylamine moiety as well as interfacial back-electron transfer to a discrete redox center, either TPA^+ or Ru^{III} , was used to quantify the experimental data. The forward and reverse rate constants for the intramolecular equilibrium extracted from this analysis were used to calculate the equilibrium constant between $[\text{Ru}^{\text{II}}\text{-B-TPA}^+]$ and $[\text{Ru}^{\text{III}}\text{-B-TPA}]$. Consistent with previous studies, a van't Hoff plot of this data (**Figure 5**) revealed an adiabatic electron transfer mechanism for $\text{CF}_3\text{-p}$ on both oxides, i.e. $\Delta H^0 = q_p = 0$, and a smaller equilibrium constant

for the adiabatic pathway.³¹ In contrast, larger equilibrium constants with a marked temperature dependence revealed a non-adiabatic pathway for CF₃-**x**, $\Delta H^\circ = -7$ kJ/mol.

A challenge often encountered in kinetic analysis of interfacial electron transfer lies in the non-exponential nature of the back-electron transfer reaction. There are indeed only limited examples when back-electron transfer from TiO₂ was first-order.^{26, 39} A “stretched exponential” function, known as the Kohlrausch-William-Watts (KWW) function (Equation 1) was used to fit the data, from which average rate constant k_{kww} was calculated (Equation 2) with the Gamma function (Γ).

$$\Delta A = \sum_{i=1} \Delta A_i e^{-(kt)^\beta} \quad (1)$$

$$k_{kww} = \frac{k_i \beta}{\Gamma(1/\beta)} \quad (2)$$

Scher and Montroll initially derived the KWW function based on a random walk model that is nowadays an archetype for modelling charge transport in disordered media.⁴⁰ In this model, β was inversely related to the width of the underlying Lévy distribution of rate constants, $0 < \beta < 1$, A_0 is the initial absorbance, k is the characteristic rate constant and k_{kww} is the average rate constant. A first-order reaction is recovered when $\beta = 1$.²⁶ In the present case, back-electron transfer from injected electrons to oxidized triphenylamine was fit with a β value of 0.35-0.4, and was independent of the chemical nature of the MO_x thin film.

The average rate constant, k_{kww} , extracted at each temperature for TiO₂|CF₃-**x/p** and CS|CF₃-**x/p** were used to determine the activation energy E_a for back-electron transfer through an Arrhenius analysis, equation 3 (Figure 6.5). Results from the Arrhenius analysis, Equation 3, are gathered in Table 6.2.

$$\ln k = \frac{-E_a}{R} \frac{1}{T} + \ln A \quad (3)$$

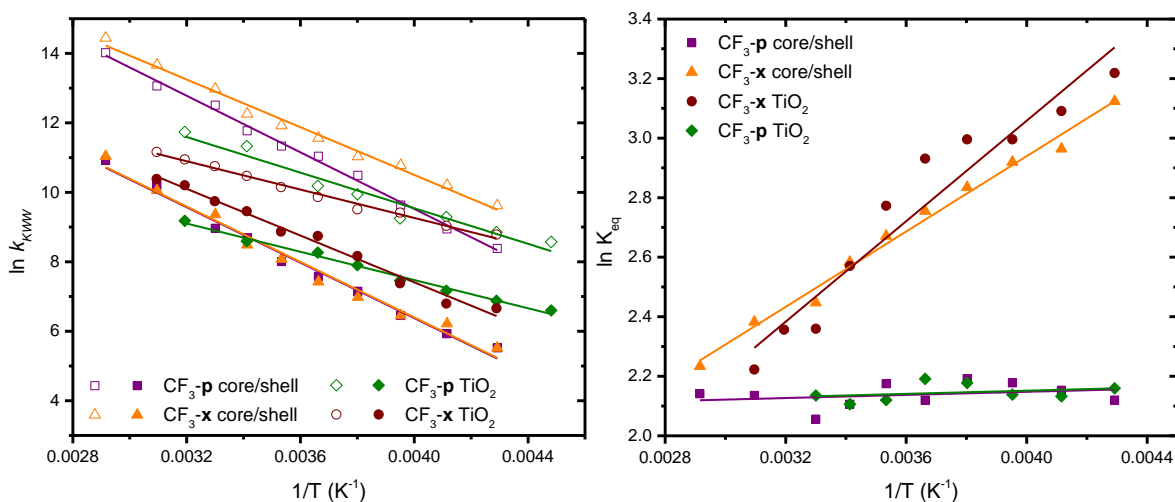


Figure 6.5: Arrhenius (left) analysis of back-electron transfer at the indicated dye-sensitized interfaces. The open shapes correspond to back-electron transfer from $\text{MO}_x(\text{e}^-)$ to Ru^{III} whereas the solid shapes correspond to back-electron transfer from $\text{MO}_x(\text{e}^-)$ to TPA^+ . A van't Hoff plot (right) obtained from the intramolecular equilibrium between $\text{MO}_x(\text{e}^-)|\text{Ru}^{\text{III}}\text{-B-TPA}$ and $\text{MO}_x(\text{e}^-)|\text{Ru}^{\text{II}}\text{-B-TPA}^+$.

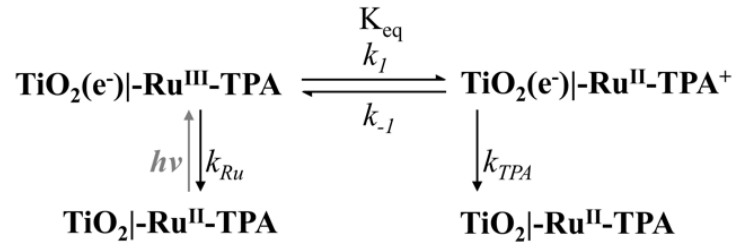
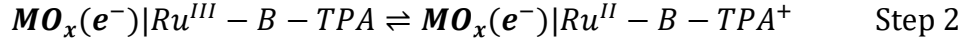
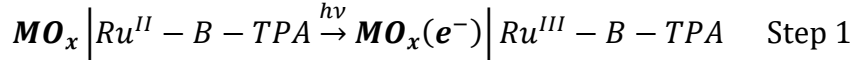
Table 6.1: Activation parameters for the back-electron transfer reaction from TiO_2 and $\text{SnO}_2/\text{TiO}_2$ core/shell (CS) to the oxidized form of the indicated sensitizer.

	Ru^{III}		TPA^+	
	$\ln(A)$	E_a (kJ mol $^{-1}$)	$\ln(A)$	E_a (kJ mol $^{-1}$)
$\text{TiO}_2 \text{CF}_3\text{-x}$	17	17 ± 1	21	28 ± 1
$\text{TiO}_2 \text{CF}_3\text{-p}$	19	21 ± 1	18	21 ± 1
$\text{CS} \text{CF}_3\text{-x}$	24	29 ± 1	22	33 ± 1
$\text{CS} \text{CF}_3\text{-p}$	26	34 ± 1	23	34 ± 1

6.3 Discussion

Two donor-bridge-acceptor sensitizers, $\text{CF}_3\text{-p}$ and $\text{CF}_3\text{-x}$, were used to investigate the back-electron transfer from electrons injected into TiO_2 (or core/shell $\text{SnO}_2/\text{TiO}_2$) to oxidized triphenylamine moieties. Light excitation of $\text{TiO}_2|\text{CF}_3\text{-x/p}$ and $\text{CS}|\text{CF}_3\text{-x/p}$ led to electron

injection into the metal oxide and formation of the oxidized sensitizer (Step 1). After excited-state electron transfer into the metal oxide thin film, intramolecular electron transfer from TPA to Ru^{III} was thermodynamically downhill.



A kinetic model that incorporates both the intramolecular electron transfer equilibrium (step 2) as well as interfacial back-electron transfer to a discrete redox center was used.³¹ Rate constants for back-electron transfer were measured over a 110° temperature range. Arrhenius analyses were of importance to determine the activation parameters that govern back-electron transfer from TiO_2 (or $\text{SnO}_2/\text{TiO}_2$ core/shell materials) to oxidized sensitizers.

6.3.1 The kinetic model

The kinetic model used to extract the rate constant for back-electron transfer has been previously published and is described as follows.³¹ Excited-state electron injection $\text{MO}_x | \text{Ru}^{\text{II}*} - \text{B} - \text{TPA} \rightarrow \text{MO}_x(e^-) | \text{Ru}^{\text{III}} - \text{B} - \text{TPA}$ generates the oxidized Ru sensitizer that triggers the dynamic intramolecular electron transfer equilibrium between the $\text{Ru}^{\text{III/II}}$ and $\text{TPA}^{+/0}$ redox centers, where k_1 and k_{-1} are the forward and reverse rate constants, respectively. The ground state recovery proceeds via back-electron transfer from the photo-injected electrons

to either Ru^{III} (k_{Ru}) or TPA^+ (k_{TPA}). The coupled differential rate equations that mathematically describes the kinetic model are given by:

$$\frac{d[\text{Ru}^{\text{III}}]}{dt} = -(k_{\text{Ru}} + k_1)[\text{Ru}^{\text{III}}] + k_{-1}[\text{TPA}^+] \quad (6)$$

$$\frac{d[\text{TPA}^+]}{dt} = -(k_{\text{TPA}} + k_{-1})[\text{TPA}^+] + k_1[\text{Ru}^{\text{III}}] \quad (7)$$

For simplicity, $\text{MO}_x(\text{e}^-)|\text{Ru}^{\text{III}}\text{-B-TPA}$ and $\text{MO}_x(\text{e}^-)|\text{Ru}^{\text{II}}\text{-B-TPA}^+$ were abbreviated to **Ru^{III}** and **TPA⁺**. Equations 6 and 7 are based on first-order kinetic behavior that are appropriate for many quasi-equilibria, such as for photoacids and photobases, but may not be appropriate for charge recombination at TiO_2 interfaces when the back-electron transfer kinetics often display higher-order reaction kinetics.⁴¹⁻⁴³ The Kohlrausch-Williams-Watts (KWW) function was used to account for the non-exponential behavior, Equation 8,

$$f(t) = Ae^{-(k t)^\beta} \quad (8)$$

where β is inversely related to the width of an underlying Lévy distribution of rate constants. Rewriting equation 6 and 7 to consider the non-exponential nature of back-electron transfer kinetics resulted in equations 9 and 10.

$$\frac{d[\text{Ru}^{\text{III}}]}{dt} = -(\beta_{\text{Ru}}(k_{\text{Ru}})^{\beta_{\text{Ru}}} t^{\beta_{\text{Ru}}-1} + k_1)[\text{Ru}^{\text{III}}] + k_{-1}[\text{TPA}^+] \quad (9)$$

$$\frac{d[\text{TPA}^+]}{dt} = -(\beta_{\text{TPA}}(k_{\text{TPA}})^{\beta_{\text{TPA}}} t^{\beta_{\text{TPA}}-1} + k_{-1})[\text{TPA}^+] + k_1[\text{Ru}^{\text{III}}] \quad (10)$$

The time-dependent concentrations of $[\text{Ru}^{\text{III}}]$ and $[\text{TPA}^+]$ were correlated with the absorption changes on the metal oxide thin films through a modified Beer-Lambert law, $\Delta A = \Gamma \Delta \epsilon / 1000$, where Γ is the surface coverage (mol/cm^2) and $\Delta \epsilon$ is the extinction coefficient difference ($\text{M}^{-1} \text{cm}^{-1}$) between the transient state and the initial ground-state.⁴⁴

6.3.2 Models for back-electron transfer

Back-electron transfer plays a paramount role in the overall efficiency of dye-sensitized solar cells (DSSCs) and dye-sensitized photoelectrosynthesis cells (DPSECs). The 1 to 2 orders of magnitude decrease in back-electron transfer timescale from electrons in core/shell $\text{SnO}_2/\text{TiO}_2$ compared to electrons in TiO_2 points towards drastic differences in the intrinsic electron transfer barriers for these materials. Two models proposed for back-electron transfer from core/shell are represented in Figure 6.6.

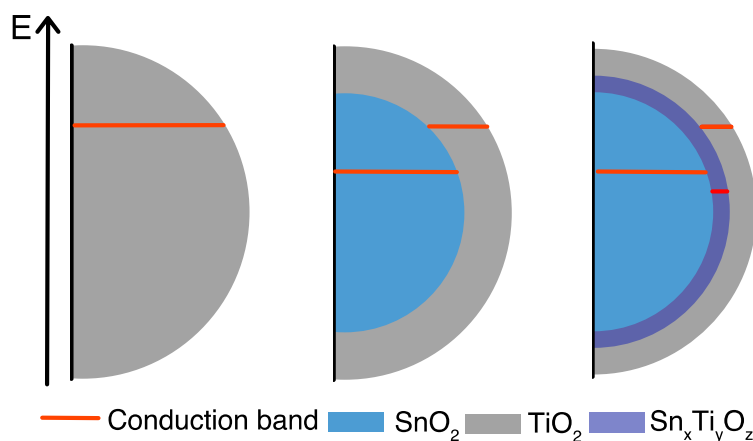


Figure 6.6: Representation of two models previously used to rationalize the kinetics for back-electron transfer from $\text{SnO}_2/\text{TiO}_2$ core/shell nanoparticles to oxidized sensitizers or redox mediators. On the left, the conduction band edge band edge potential of TiO_2 is represented for illustration purposes as a solid red line. The band edge offset model between SnO_2 and TiO_2 is represented in the middle while the formation of a low energy $\text{Sn}_x\text{Ti}_y\text{O}_z$ electronic state at the interface between the SnO_2 core and the TiO_2 shell is represented on the right.

The enhanced performance of SnO₂/TiO₂ core/shell mesoporous thin films for water splitting has previously been attributed to the 300mV band edge offset between SnO₂ and TiO₂.^{10, 16, 19, 22, 45} Electrons photo-injected into the TiO₂ shell migrate into the SnO₂ core and back-electron transfer is inhibited by the more negative position of the TiO₂ shell conduction band edge.¹⁶ A second model was recently proposed based on a comparative spectroelectrochemical study of mesoporous TiO₂, SnO₂ and SnO₂/TiO₂ core/shell nanocrystallites thin films.²⁵ No spectroscopic evidence of electrons located either in the SnO₂ core or in the TiO₂ shell were obtained. Instead, a single reduced state was detected spectroscopically and assigned to a Sn_xTi_yO₂ species that formed initially in the atomic layer deposition procedure.²⁵ These authors also found that annealing the core/shell structures created a rutile TiO₂ shell.²⁵ Due to the lack of singular TiO₂ or SnO₂ absorption spectra for the reduced materials, it was suggested that the electrons were predominantly located in a discrete mixed acceptor state located at the oxide junction between the SnO₂ core and the TiO₂ shell.

The pre-exponential factor, $\ln(A)$ in the Arrhenius equation, *i.e* the frequency factor, corresponds physically to an “attempt” frequency with which the injected electrons approach the transition state imposed by the activation barrier for back-electron transfer with the oxidized sensitizer. The pre-exponential factors reported here were consistently larger for SnO₂/TiO₂ core/shell than for TiO₂. From these results, it did not seem that a slower back-electron transfer observed for SnO₂/TiO₂ core/shell originated from the “attempt” frequency. We note that the required extrapolation to infinite temperature may provide unreliable estimates of the frequency factors for BET mechanisms.

Temperature dependent back-electron transfer kinetic measurements have also proven to be useful for determination of the thermodynamic barriers for electron transfer based on spectroscopic²⁶⁻²⁸ or photoelectrochemical assays.⁴⁶⁻⁴⁷ Here, activation energies for back-electron transfer of $\text{TiO}_2(\text{e}^-)$ to the TPA^+ moiety in $\text{CF}_3\text{-x}$ and $\text{CF}_3\text{-p}$ were measured to be 28 kJ mol^{-1} and 21 kJ mol^{-1} , respectively. These values are larger than those reported for recombination to oxidized triphenylamine mediators in solution^{26, 28} as well as for electron transport between $\text{Ti}^{\text{IV/III}}$ sites in TiO_2 (0.13 eV, about 12 kJ mol^{-1}),⁴⁸ and for Li^+ transfer in $\text{Li}_{10}\text{SnP}_2\text{S}_{12}$ -based composites.⁴⁹ Activation energies for electron transport in nanocrystalline TiO_2 in the range between 0.1 and 0.27 eV have also been reported.^{46-47, 50-53} The activation energies for $\text{CF}_3\text{-x}$ and $\text{CF}_3\text{-p}$ were however in line with those usually reported for surface anchored molecular acceptors and oxidized sensitizers.²⁶⁻²⁸ Indeed, back-electron transfer from $\text{TiO}_2(\text{e}^-)$ to a related “Ru-TPA” oxidized sensitizer (**Figure 7**) was determined to be 27 kJ mol^{-1} .²⁸ Furthermore, back-electron transfer to the oxidized ruthenium centers occurred with activation energies of 17 kJ mol^{-1} and 21 kJ mol^{-1} for $\text{CF}_3\text{-x}$ and $\text{CF}_3\text{-p}$, respectively. These values were within the same order of magnitude as those reported for Ru^{II} polypyridyl complexes anchored on TiO_2 interfaces.²⁷

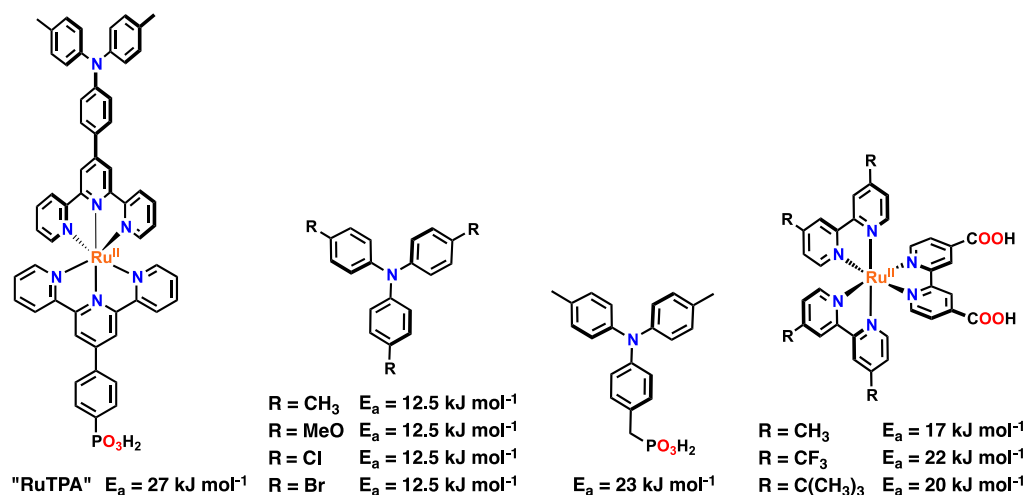


Figure 6.7: Activation energies for back-electron transfer from $\text{TiO}_2(e^-)$ to oxidized RuTPA,²⁸ triphenylamine derivatives

^{26, 28} and ruthenium sensitizers²⁷ in 0.1M LiClO_4 CH_3CN electrolytes.

Back-electron transfer from $\text{CS}(e^-)$ to $\text{CF}_3\text{-x}$ and $\text{CF}_3\text{-p}$ occurred with activation energies that were 5 - 13 kJ mol^{-1} higher than the corresponding values obtained on TiO_2 (Table 6.1). Both models described in Figure 6.6 were expected to provide significantly different activation energies than those measured for the back-electron transfer from TiO_2 and were consistent with this data. An explanation for the slower back-electron transfer from CS materials may arise from a combination of different polymorphs that arose from preparative methods of the mesoporous films and shell thickness as discussed in Chapter 6.1. Indeed, rutile and anatase polymorphs of SnO_2 and TiO_2 are known have different dielectric constants and band-gaps necessary for understanding charge recombination reactions. Film thickness is also critical as Dempsey *et al.* have concluded that electrons injected into $\text{SnO}_2/\text{TiO}_2$ core/shell do not reach the core when using $\sim 4.5 \text{ nm}$ shell thickness as were employed here.¹⁶ Hence under open circuit conditions, it is possible that the injected electrons do not make it to the core or the interfacial states proposed in the two models. The TiO_2 thin films are comprised of the anatase nanocrystallites whereas a rutile TiO_2 polymorph shell is

formed upon annealing of the SnO₂/TiO₂ core/shell thin films due to the rutile SnO₂ core. Swierk and Schmittenmaer have recently shown that rutile TiO₂ was a better material for water-splitting dye-sensitized photoelectrochemical cells (WS-DSPEC) than anatase TiO₂.⁵⁴ Back-electron transfer from rutile-TiO₂(e⁻) to oxidized sensitizer was an order of magnitude slower than for anatase-TiO₂(e⁻). Similar behavior has also been recently reported by Durrant *et al.* of anatase:rutile heterojunctions.⁵⁵ Although temperature dependent studies of back-electron transfer with the rutile polymorph of TiO₂ has not to our knowledge been conducted, the sluggish rates reported by Swierk and Durrant suggest a higher activation energy than that for anatase TiO₂, as was measured in this work.

6.4 Conclusion

The data gathered herein provide the barriers for back-electron transfer from electrons photo-injected into metal oxide thin films to two different oxidized sensitizers. This study utilized two structurally similar Ru-B-TPA sensitizers, CF₃-**p** and CF₃-**x**, that varied only by the nature of the bridge. The phenyl-thiophene bridge allowed for strong electronic coupling between the two redox active centers while the xylyl-thiophene bridge decreased electronic coupling. A van't Hoff analysis of the equilibrium revealed an adiabatic pathway for the phenyl bridge and a non-adiabatic pathway for xylyl-bridge, where the latter preserved more Gibbs free energy. These two sensitizers were anchored onto two different MO_x thin films, TiO₂ or SnO₂/TiO₂ core/shell films. Back-electron transfer from core/shell thin films to oxidized redox active molecules was slower than from TiO₂, with higher activation energies. These observations were qualitatively consistent with a band-edge offset model discussed in Section 6.5.2. Furthermore, as previous studies have indicated²⁵ electrons reside in a mixed

metal oxide layer with spectroscopic data indicating that at thicker TiO₂ shells, formation of the rutile polymorph is present once SnO₂/TiO₂ core/shell thin films were annealed.

6.5 Additional details

6.5.1 Materials

The following reagents were used as received: titanium(IV) isopropoxide (Sigma-aldrich, 97%), polyethyleneglycol Bisphenol A Epichlorohydrin Copolymer (M. W. = 15,000-20,000 Da, Sigma-Aldrich), SnO₂ nanoparticles (15% w/v, 15 nm diameter, Alfa-Aesar), poly(ethylene oxide) (M. W. = 100,000), tetrakis(dimethylamido) titanium (IV) (Sigma-Aldrich, 99.999%), Lithium perchlorate (Sigma Aldrich, 99.99%), Argon gas (Airgas, 99.998%), Oxygen gas (Airgas, Industrial grade), fluorine-doped tin oxide-coated glass (FTO, Hartford Glass Co., Inc, 2.3 mm thick, 15 Ω/\square). The sensitizers CF₃-**x** and CF₃-**p** were synthesized following published procedures.³²

6.5.2 Preparation of SnO₂ and TiO₂ colloidal suspensions.

Colloidal TiO₂ and SnO₂ solutions were obtained following published procedures.⁵⁶⁻⁵⁸ For SnO₂, 30 mL of SnO₂ colloid (15 wt% in H₂O) were placed in a 125 mL Erlenmeyer flask. Glacial acetic acid (1mL) was added dropwise with vigorous stirring. The mixture was stirred until the white solution became homogeneous (approximately 8h). The mixture was transferred to a 45 mL Parr reaction vessel and sealed. The reaction vessel was heated to 240°C in 1h and held at that temperature for 60h. After hydrothermal treatment, the reaction was brought to room temperature in one hour and the mixture was transferred in a vial and sonicated. PEO [poly(ethylene oxide) (M.W = 100,000)] and PEG [poly(ethylene glycol) (M.W = 15,000)] were added to reach a final concentration of 2.5 wt% of PEO and 2.5 wt% of PEG.

For TiO₂, 60 mL of deionized water were poured in a 125 mL Erlenmeyer flask. Concentrated nitric acid (70%, 0.42 mL) was then added. The solution was stirred vigorously under protection from light. Titanium (IV) isopropoxide (10 mL) was then added dropwise to that mixture. After addition, the mixture was heated at 95°C for several hours until the final volume reached 20 mL. The slurry was then transferred to a 25 mL acid digestion bomb and heated at 200°C for 12h. After digestion, the mixture was brought to room temperature and transferred into a vial. Finely ground Polyethyleneglycol Bisphenol A Epichlorohydrin Copolymer 15,000-20,000 Da (Carbowax, 1g) was then added and the mixture was stirred until complete dissolution of the carbowax occurred.

6.5.3 Preparation of TiO₂ and SnO₂/TiO₂ core/shell thin films.

The mesoporous TiO₂ and SnO₂ thin films were obtained following published procedures.^{1-2, 25, 57} TiO₂ or SnO₂ colloidal suspensions described above were doctor-bladed onto a fluorine-doped tin oxide (FTO) substrate to reach a thickness of approximately 3 μm and a width of 1 cm. The substrates were allowed to stand in the dark for 30 minutes prior to being heated at 450°C under a flow of O₂. The thin films were then stored in an oven kept at 70°C until needed. For core/shell SnO₂/TiO₂ thin films, the SnO₂ thin films previously prepared were modified by atomic layer deposition (ALD) of tetrakis(dimethylamido) titanium (IV) (Ti(NMe₂)₄, TDMAT) held at 75°C, using an Ultratech/Cambridge Nanotech Savannah S200 instrument. The chamber was kept at 130°C under 20 sccm of N₂ carrier gas flow with a deposition sequence that was as follows: 0.3 s TDMAT pulse, 30 s hold, 60 s N₂ purge, 0.02 s H₂O pulse, 30 s hold, and 60 s N₂ purge. After deposition of 75 cycles of ALD TiO₂ on SnO₂ (~ 4.5 nm, 0.06 nm/cycle), the as prepared core/shell structures were annealed at 450 °C under 1 atm O₂ for 30 min.

6.5.4 UV–Vis Absorption

The UV–vis absorption spectra were recorded on a Varian Cary 60 UV–Vis spectrophotometer with a resolution of 1 nm.

6.5.5 Transient absorption

Nanosecond transient absorption measurements were acquired on a previously described apparatus.⁵⁹ Briefly, a Q-switched, pulsed Nd:YAG laser (Quantel U.S.A. (BigSky) Brilliant B 5-6 ns full width at half-maximum (fwhm), 1 Hz, ~10 mm in diameter) doubled to 532 nm with appropriate non-linear optics was utilized. The laser irradiance at the sample was attenuated to 0.5 mJ/pulse. The probe lamp consisted of a 150 W Xenon arc lamp that was often pulsed at 1 Hz. Signal detection was achieved using a monochromator (SPEX 1702/04) optically coupled to an R928 photomultiplier tube (Hamamatsu) at a right angle to the excitation laser. Transient data were acquired with a computer-interfaced digital oscilloscope (LeCroy 9450, Dual 330 MHz) with an overall instrument response time of ~10 ns. An average of 90 laser pulses was averaged at each wavelength of interest over the 370-800 nm range. Intervals of 10 nm were used between 390 and 800 nm.

REFERENCES

1. Alibabaei, L.; Brennaman, M. K.; Norris, M. R.; Kalanyan, B.; Song, W.; Losego, M. D.; Concepcion, J. J.; Binstead, R. A.; Parsons, G. N.; Meyer, T. J., Solar water splitting in a molecular photoelectrochemical cell. *P. Natl. Acad. Sci. USA* **2013**, *110* (50), 20008-20013.
2. Alibabaei, L.; Farnum, B. H.; Kalanyan, B.; Brennaman, M. K.; Losego, M. D.; Parsons, G. N.; Meyer, T. J., Atomic layer deposition of TiO₂ on mesoporous nanoITO: Conductive core-shell photoanodes for dye-sensitized solar cells. *Nano Lett.* **2014**, *14* (6), 3255-3261.
3. Brennaman, M. K.; Dillon, R. J.; Alibabaei, L.; Gish, M. K.; Dares, C. J.; Ashford, D. L.; House, R. L.; Meyer, G. J.; Papanikolas, J. M.; Meyer, T. J., Finding the way to solar fuels with dye-sensitized photoelectrosynthesis cells. *J. Am. Chem. Soc.* **2016**, *138* (40), 13085-13102.
4. Concepcion, J. J.; House, R. L.; Papanikolas, J. M.; Meyer, T. J., Chemical approaches to artificial photosynthesis. *P. Natl. Acad. Sci. USA* **2012**, *109* (39), 15560-15564.
5. Gish, M. K.; Lapides, A. M.; Brennaman, M. K.; Templeton, J. L.; Meyer, T. J.; Papanikolas, J. M., Ultrafast recombination dynamics in dye-sensitized SnO₂/TiO₂ core/shell films. *J. Phys. Chem. Lett.* **2016**, *7* (24), 5297-5301.
6. Kapilashrami, M.; Zhang, Y.; Liu, Y.-S.; Hagfeldt, A.; Guo, J., Probing the optical property and electronic structure of tio2 nanomaterials for renewable energy applications. *Chem. Rev.* **2014**, *114* (19), 9662-9707.
7. Karlsson, M.; Jögi, I.; Eriksson, S. K.; Rensmo, H.; Boman, M.; Boschloo, G.; Hagfeldt, A., Dye-sensitized solar cells employing a SnO₂-TiO₂ core-shell structure made by atomic layer deposition. *CHIMIA International Journal for Chemistry* **2013**, *67* (3), 142-148.
8. Palomares, E.; Clifford, J. N.; Haque, S. A.; Lutz, T.; Durrant, J. R., Slow charge recombination in dye-sensitised solar cells (dssc) using Al₂O₃ coated nanoporous TiO₂ films. *Chem. Commun.* **2002**, (14), 1464-1465.
9. Palomares, E.; Clifford, J. N.; Haque, S. A.; Lutz, T.; Durrant, J. R., Control of charge recombination dynamics in dye sensitized solar cells by the use of conformally deposited metal oxide blocking layers. *J. Am. Chem. Soc.* **2003**, *125* (2), 475-482.
10. Sherman, B. D.; Ashford, D. L.; Lapides, A. M.; Sheridan, M. V.; Wee, K.-R.; Meyer, T. J., Light-driven water splitting with a molecular electroassembly-based core/shell photoanode. *J. Phys. Chem. Lett.* **2015**, *6* (16), 3213-3217.
11. Swierk, J. R.; Mallouk, T. E., Design and development of photoanodes for water-splitting dye-sensitized photoelectrochemical cells. *Chem. Soc. Rev.* **2013**, *42* (6), 2357-2387.
12. Xu, P.; Huang, T.; Huang, J.; Yan, Y.; Mallouk, T. E., Dye-sensitized photoelectrochemical water oxidation through a buried junction. *Proc. Natl. Acad. Sci. USA* **2018**.

13. Zhao, Y.; Swierk, J. R.; Megiatto, J. D.; Sherman, B.; Youngblood, W. J.; Qin, D.; Lentz, D. M.; Moore, A. L.; Moore, T. A.; Gust, D.; Mallouk, T. E., Improving the efficiency of water splitting in dye-sensitized solar cells by using a biomimetic electron transfer mediator. *P. Natl. Acad. Sci. USA* **2012**, *109* (39), 15612-15616.
14. Grätzel, M., Photoelectrochemical cells. *Nature* **2001**, *414*, 338.
15. Hu, K.; Sampaio, R. N.; Marquard, S. L.; Brennaman, M. K.; Tamaki, Y.; Meyer, T. J.; Meyer, G. J., A high-valent metal-oxo species produced by photoinduced one-electron, two-proton transfer reactivity. *Inorg. Chem.* **2018**, *57* (1), 486-494.
16. Knauf, R. R.; Kalanyan, B.; Parsons, G. N.; Dempsey, J. L., Charge recombination dynamics in sensitized SnO₂/TiO₂ core/shell photoanodes. *J. Phys. Chem. C* **2015**, *119* (51), 28353-28360.
17. Brady, M. D.; Sampaio, R. N.; Wang, D.; Meyer, T. J.; Meyer, G. J., Dye-sensitized hydrobromic acid splitting for hydrogen solar fuel production. *J. Am. Chem. Soc.* **2017**, *139* (44), 15612-15615.
18. Brady, M. D.; Troian-Gautier, L.; Sampaio, R. N.; Motley, T. C.; Meyer, G. J., Optimization of photocatalyst excited- and ground-state reduction potentials for dye-sensitized hbr splitting. *ACS Appl. Mater. Interfaces* **2018**, *10* (37), 31312-31323.
19. Chappel, S.; Chen, S.-G.; Zaban, A., TiO₂-coated nanoporous SnO₂ electrodes for dye-sensitized solar cells. *Langmuir* **2002**, *18* (8), 3336-3342.
20. Li, W.; Elzatahry, A.; Aldhayan, D.; Zhao, D., Core-shell structured titanium dioxide nanomaterials for solar energy utilization. *Chem. Soc. Rev.* **2018**.
21. Alibabaei, L.; Sherman, B. D.; Norris, M. R.; Brennaman, M. K.; Meyer, T. J., Visible photoelectrochemical water splitting into H₂ and O₂ in a dye-sensitized photoelectrosynthesis cell. *P. Natl. Acad. Sci. USA* **2015**, *112* (19), 5899-5902.
22. Sheridan, M. V.; Sherman, B. D.; Coppo, R. L.; Wang, D.; Marquard, S. L.; Wee, K.-R.; Murakami Iha, N. Y.; Meyer, T. J., Evaluation of chromophore and assembly design in light-driven water splitting with a molecular water oxidation catalyst. *ACS Energy Lett.* **2016**, *1* (1), 231-236.
23. Wang, D.; Sheridan, M. V.; Shan, B.; Farnum, B. H.; Marquard, S. L.; Sherman, B. D.; Eberhart, M. S.; Nayak, A.; Dares, C. J.; Das, A. K.; Bullock, R. M.; Meyer, T. J., Layer-by-layer molecular assemblies for dye-sensitized photoelectrosynthesis cells prepared by atomic layer deposition. *J. Am. Chem. Soc.* **2017**, *139* (41), 14518-14525.
24. Xu, P.; McCool, N. S.; Mallouk, T. E., Water splitting dye-sensitized solar cells. *Nano Today* **2017**, *14*, 42-58.

25. James, E. M.; Barr, T. J.; Meyer, G. J., Evidence for an electronic state at the interface between the SnO₂ core and the TiO₂ shell in mesoporous SnO₂/TiO₂ thin films. *ACS Applied Energy Materials* **2018**, *1* (2), 859-867.
26. DiMarco, B. N.; Troian-Gautier, L.; Sampaio, R. N.; Meyer, G. J., Dye-sensitized electron transfer from TiO₂ to oxidized triphenylamines that follows first-order kinetics. *Chem. Sci.* **2018**, *9* (4), 940-949.
27. Sampaio, R. N.; DiMarco, B. N.; Meyer, G. J., Activation energies for electron transfer from TiO₂ to oxidized dyes: A surface coverage dependence correlated with lateral hole hopping. *ACS Energy Lett.* **2017**, *2* (10), 2402-2407.
28. Troian-Gautier, L.; DiMarco, B. N.; Sampaio, R. N.; Marquard, S. L.; Meyer, G. J., Evidence that ΔS^\ddagger controls interfacial electron transfer dynamics from anatase TiO₂ to molecular acceptors. *J. Am. Chem. Soc.* **2018**, *140* (8), 3019-3029.
29. Kuciauskas, D.; Freund, M. S.; Gray, H. B.; Winkler, J. R.; Lewis, N. S., Electron transfer dynamics in nanocrystalline titanium dioxide solar cells sensitized with ruthenium or osmium polypyridyl complexes. *J. Phys. Chem. B* **2001**, *105* (2), 392-403.
30. Piechota, E. J.; Troian-Gautier, L.; Sampaio, R. N.; Brennaman, M. K.; Hu, K.; Berlinguette, C. P.; Meyer, G. J., Optical intramolecular electron transfer in opposite directions through the same bridge that follows different pathways. *J. Am. Chem. Soc.* **2018**, *140* (23), 7176-7186.
31. Sampaio, R. N.; Piechota, E. J.; Troian-Gautier, L.; Maurer, A. B.; Hu, K.; Schauer, P. A.; Blair, A. D.; Berlinguette, C. P.; Meyer, G. J., Kinetics teach that electronic coupling lowers the free-energy change that accompanies electron transfer. *Proceedings of the National Academy of Sciences* **2018**, *115* (28), 7248-7253.
32. Hu, K.; Blair, A. D.; Piechota, E. J.; Schauer, P. A.; Sampaio, R. N.; Parlane, F. G. L.; Meyer, G. J.; Berlinguette, C. P., Kinetic pathway for interfacial electron transfer from a semiconductor to a molecule. *Nature Chem.* **2016**, *8*, 853.
33. DiMarco, B. N.; Motley, T. C.; Balok, R. S.; Li, G.; Siegler, M. A.; O'Donnell, R. M.; Hu, K.; Meyer, G. J., A distance dependence to lateral self-exchange across nanocrystalline tio₂. A comparative study of three homologous Ru(III/II) polypyridyl compounds. *J. Phys. Chem. C* **2016**, *120* (26), 14226-14235.
34. Moia, D.; Szumska, A.; Vaissier, V.; Planells, M.; Robertson, N.; O'Regan, B. C.; Nelson, J.; Barnes, P. R. F., Interdye hole transport accelerates recombination in dye sensitized mesoporous films. *J. Am. Chem. Soc.* **2016**, *138* (40), 13197-13206.
35. Motley, T. C.; Meyer, G. J., Intramolecular electronic coupling enhances lateral electron transfer across semiconductor interfaces. *J. Phys. Chem. C* **2018**, *122* (26), 14420-14424.
36. Nelson, J.; Chandler, R. E., Random walk models of charge transfer and transport in dye sensitized systems. *Coord. Chem. Rev.* **2004**, *248* (13), 1181-1194.

37. Hu, K.; Meyer, G. J., Lateral intermolecular self-exchange reactions for hole and energy transport on mesoporous metal oxide thin films. *Langmuir* **2015**, *31* (41), 11164-11178.
38. Sreenath, K.; Suneesh, C. V.; Gopidas, K. R.; Flowers, R. A., Generation of triarylamine radical cations through reaction of triarylamines with cu(ii) in acetonitrile. A kinetic investigation of the electron-transfer reaction. *J. Phys. Chem. A* **2009**, *113* (23), 6477-6483.
39. Barr, T. J.; Meyer, G. J., Evidence for first-order charge recombination in dye-sensitized solar cells. *ACS Energy Lett.* **2017**, *2* (10), 2335-2340.
40. Scher, H.; Montroll, E. W., Anomalous transit-time dispersion in amorphous solids. *Phys. Rev. B* **1975**, *12* (6), 2455-2477.
41. Kelly, C. A.; Farzad, F.; Thompson, D. W.; Meyer, G. J., Excited-state deactivation of ruthenium(II) polypyridyl chromophores bound to nanocrystalline tio2 mesoporous thin films. *Langmuir* **1999**, *15* (3), 731-737.
42. Demas, J. N., Chapter 4 - more complex systems. In *Excited state lifetime measurements*, Demas, J. N., Ed. Academic Press: 1983; pp 43-69.
43. O'Donnell, R. M.; Sampaio, R. N.; Li, G.; Johansson, P. G.; Ward, C. L.; Meyer, G. J., Photoacidic and photobasic behavior of transition metal compounds with carboxylic acid group(s). *J. Am. Chem. Soc.* **2016**, *138* (11), 3891-3903.
44. Trammell, S. A.; Meyer, T. J., Diffusional mediation of surface electron transfer on TiO₂. *J. Phys. Chem. B* **1998**, *103* (1), 104-107.
45. Kavan, L.; Grätzel, M.; Gilbert, S. E.; Klemenz, C.; Scheel, H. J., Electrochemical and photoelectrochemical investigation of single-crystal anatase. *J. Am. Chem. Soc.* **1996**, *118* (28), 6716-6723.
46. O'Regan, B. C.; Durrant, J. R., Calculation of activation energies for transport and recombination in mesoporous TiO₂/dye/electrolyte filmstaking into account surface charge shifts with temperature. *J. Phys. Chem. B* **2006**, *110* (17), 8544-8547.
47. Savenije, T. J.; Huijser, A.; Vermeulen, M. J. W.; Katoh, R., Charge carrier dynamics in TiO₂ nanoparticles at various temperatures. *Chem. Phys. Lett.* **2008**, *461* (1), 93-96.
48. Boschloo, G.; Hagfeldt, A., Activation energy of electron transport in dye-sensitized tio2 solar cells. *J. Phys. Chem. B* **2005**, *109* (24), 12093-12098.
49. Kaus, M.; Stöffler, H.; Yavuz, M.; Zinkevich, T.; Knapp, M.; Ehrenberg, H.; Indris, S., Local structures and Li ion dynamics in a Li₁₀SnP₂S₁₂-based composite observed by multinuclear solid-state nmr spectroscopy. *J. Phys. Chem. C* **2017**, *121* (42), 23370-23376.
50. Goossens, A.; van der Zanden, B.; Schoonman, J., Single-electron migration in nanostructured TiO₂. *Chem. Phys. Lett.* **2000**, *331* (1), 1-6.

51. Greijer Agrell, H.; Boschloo, G.; Hagfeldt, A., Conductivity studies of nanostructured TiO₂ films permeated with electrolyte. *J. Phys. Chem. B* **2004**, *108* (33), 12388-12396.
52. Kopidakis, N.; Benkstein, K. D.; van de Lagemaat, J.; Frank, A. J.; Yuan, Q.; Schiff, E. A., Temperature dependence of the electron diffusion coefficient in electrolyte-filled TiO₂ nanoparticle films: Evidence against multiple trapping in exponential conduction-band tails. *Phys. Rev. B* **2006**, *73* (4), 045326.
53. Peter, L. M.; Walker, A. B.; Boschloo, G.; Hagfeldt, A., Interpretation of apparent activation energies for electron transport in dye-sensitized nanocrystalline solar cells. *J. Phys. Chem. B* **2006**, *110* (28), 13694-13699.
54. Swierk, J. R.; Regan, K. P.; Jiang, J.; Brudvig, G. W.; Schmittenmaer, C. A., Rutile tio₂ as an anode material for water-splitting dye-sensitized photoelectrochemical cells. *ACS Energy Lett.* **2016**, *1* (3), 603-606.
55. Kafizas, A.; Wang, X.; Pendlebury, S. R.; Barnes, P.; Ling, M.; Sotelo-Vazquez, C.; Quesada-Cabrera, R.; Li, C.; Parkin, I. P.; Durrant, J. R., Where do photogenerated holes go in anatase:Rutile TiO₂? A transient absorption spectroscopy study of charge transfer and lifetime. *J. Phys. Chem. A* **2016**, *120* (5), 715-723.
56. Chappel, S.; Zaban, A., Nanoporous sno₂ electrodes for dye-sensitized solar cells: Improved cell performance by the synthesis of 18nm sno₂ colloids. *Sol. Energ. Mat. Sol. C.* **2002**, *71* (2), 141-152.
57. Heimer, T. A.; D'Arcangelis, S. T.; Farzad, F.; Stipkala, J. M.; Meyer, G. J., An acetylacetonate-based semiconductor-sensitizer linkage. *Inorg. Chem.* **1996**, *35* (18), 5319-5324.
58. O'Regan, B.; Moser, J.; Anderson, M.; Graetzel, M., Vectorial electron injection into transparent semiconductor membranes and electric field effects on the dynamics of light-induced charge separation. *J. Phys. Chem* **1990**, *94* (24), 8720-8726.
59. Argazzi, R.; Bignozzi, C. A.; Heimer, T. A.; Castellano, F. N.; Meyer, G. J., Enhanced spectral sensitivity from ruthenium(II) polypyridyl based photovoltaic devices. *Inorg. Chem.* **1994**, *33* (25), 5741-5749.